ARRAY PROCESSING TECHNIQUES FOR ESTIMATION AND TRACKING OF AN ICE-SHEET BOTTOM

By

Mohanad Ahmed Abdulkareem Al-Ibadi

Submitted to the Department of Electrical Engineering and Computer Science and the
Graduate Faculty of the University of Kansas
in partial fulfillment of the requirements for the degree of
Doctor of Philosophy

Committee members

Shannon Blunt, Chairperson

John Paden, Co-chair

James Stiles

Erik Perrins

Christopher Allen

Huazhen Fang

Date defended: May 10, 2019

The Dissertation Committee for Mohanad Ahmed Abdulkareem Al-Ibadi certifies
that this is the approved version of the following dissertation :

ARRAY PROCESSING TECHNIQUES FOR ESTIMATION AND TRACKING OF AN ICE-SHEET BOTTOM

Shannon Blunt, Chairperson

John Paden, Co-chair

Date approved:

Abstract

Ice bottom topography layers are an important boundary condition required to model the flow dynamics of an ice sheet. In this work, using low frequency multichannel radar data, we locate the ice bottom using two types of automatic trackers.

First, we use the multiple signal classification (MUSIC) beamformer to determine the pseudo-spectrum of the targets at each range-bin. The result is passed into a sequential tree-reweighted message passing belief-propagation algorithm to track the bottom of the ice in the 3D image. This technique is successfully applied to process data collected over the Canadian Arctic Archipelago ice caps in 2014, and produce digital elevation models (DEMs) for 102 data frames. We perform crossover analysis to self-assess the generated DEMs, where flight paths cross over each other and two measurements are made at the same location. Also, the tracked results are compared before and after manual corrections. We found that there is a good match between the overlapping DEMs, where the mean error of the crossover DEMs is 38 ± 7 m, which is small relative to the average ice-thickness, while the average absolute mean error of the automatically tracked ice-bottom, relative to the manually corrected ice-bottom, is 10 range-bins.

Second, a direction of arrival (DOA)-based tracker is used to estimate the DOA of the backscatter signals sequentially from range bin to range bin using two methods: a sequential maximum a posterior probability (S-MAP) estimator and one based on the particle filter (PF). A dynamic flat earth transition model is used to model the flow of information between range bins. A simulation study is performed to evaluate the performance of these two DOA trackers. The results show that the PF-based tracker can handle low-quality data better than S-MAP, but, unlike S-MAP, it saturates quickly with increasing numbers of snapshots. Also, S-MAP is successfully applied to track the ice-bottom of several data frames collected over Russell glacier in 2011. Several tracker bounding models with uniform and Gaussian priors are proposed and compared as well. The results show that uniform prior pdf with not-too-tight bounds give the best tracking results. The results of the DOA-based techniques are the final tracked surfaces, so there is no need for an additional tracking stage as there is with the beamformer technique.

In addition, a machine learning (ML) based solution to the wideband model order estimation (MOE) problem is proposed and compared to six other standard MOE methods as well as a numerically tuned method. The results show a substantial improvement in the percentage of estimating the correct number of targets, especially in the more challenging scenario of wideband data with large number of targets relative to the number of sensors. Also, we found that the standard MOE methods work well on real wideband if the log-likelihood term of the cost function is corrected to account for the narrowband model mismatch when the number of targets is small.

Acknowledgements

I would like to thank my wife, Dumooa, for her love and support during the many years of my PhD, and for taking care of my two little daughters as well. She was, and still is, the source of joy and happiness in the family all the time. I also would like to thank my great mother for her encouragement and support and for her smile and reassuring words whenever I feel homesick. Many thanks to my father as well for his big love and support.

I am indebted to my advisor, Dr. John Paden, for his help and patience with my slow learning process and for the too much time he dedicated to me and the data processing group. All the words can't express my deep gratitude to him.

I'm also grateful to Dr. Shannon Blunt and Dr. James Stiles for the great courses that I took with them. These courses increased my love to the radar signal processing field.

I also want to thank my dearest friends in the data processing group in CReSIS. Many thanks to Victor Berger and Sravya Athinarapu for the long discussions we had about different parts of our research. I'm really proud of being surrounded by such a great colleagues, friends, and collaborators.

I also acknowledge my sponsor, the Higher Committee for Education Development in Iraq (HCED), NSF (ACI-1443054), and NASA (NNX16AH54G).

Contents

List of Figures

List of Tables

Chapter 1

Introduction and Literature Review

1.1 Motivation and Literature Review

The increased melting rate of ice-sheets has been a major concern to scientists over the last couple of decades due to several reasons including their contribution to the mean sea-level rise [2, 3, 4] and their role in climate change [5]. The ice mass measurements from the National Aeronautics and Space Administration (NASA) GRACE satellite have revealed that both the Antarctic and Greenland ice sheets have accelerating ice mass loss since 2009, where the rate of change in ice mass was reported as 127 ± 39 Gt in Antarctica and 286 ± 21 Gt in Greenland based on data collected between April 2002 and June 2017 [6].

The ice mass loss varies over time due to ice flow and discharge dynamics. Since the time over which ice-sheet measurements are taken is small compared to the response times of the ice-sheet dynamics, ice-sheet models provide the ability to decipher between short and long-term trends and identify feedback mechanisms, and thereby predict future mass balance changes [7] as well as understand present ice dynamics. The input boundary conditions to these ice-dynamics models are the ice-surface (i.e. air-ice interface) and ice-bottom (i.e. ice-bed interface). We use multichannel sounding radars [8] to collect data to estimate these boundaries and map the basal topography of the glaciers and ice sheets to produce a digital elevation model (DEM) that shows the location of the ice-surface and ice-bottom for the areas where the data were collected. Ice-surface measurements are available from satellite data, but ice-bottom measurements are not due to the large attenuation of the high-frequency satellite signals when they propagate through the ice. Thus, in this work we focus on estimating the ice-bottom DEMs only and use the available ice-surface DEMs for validation and algorithm training purposes.

Several methods have been proposed in the literature to estimate the bed of ice-sheets. In [9], the ice thickness was estimated using an estimate of the ice flux, where the continuity equation is solved between adjacent flow lines, and the method was tested on data from Colombia Glacier in Alaska, USA. This method works only for glaciers for which ice-surface data are available, and tracking the ice-bed in the cross-track dimension is not studied. In [10], the authors developed a method for estimating the ice thickness along glacier flow lines using the "perfect-plasticity" rheological assumption that relates the thickness and surface slope to yield stress. The method was tested on five glaciers in northwest China where thickness data are available from radio echo soundings, but no DEMs were generated.

Another approach to generate the DEMs is to digitally process the radar data collected in along-track, range, and elevation angle dimensions using signal processing techniques to resolve the ground targets along each of these three dimensions. Then a tracker is applied to extract the surface and bottom of the ice-sheet. The combination of these 2D images constitutes the final 3D image of the scene.

Several DoA estimation techniques can be applied to resolve the elevation angle of targets and generate tomographic SAR images. In [11], the multiple signal classification (MUSIC) was applied for ice-bed mapping using data collected by the Center for Remote Sensing of Ice-Sheets (CReSIS) radars. In [12], MUSIC was compared against interferometric SAR (InSAR) technique for tomographic DEM generation and it was shown that applying MUSIC to resolve near-nadir targets would give better results owing to the difficulty in separating the returns by beam steering near nadir in the case of InSAR. Other narrowband and wideband methods, such as maximum likelihood estimation (MLE) and wideband MLE, have also been discussed in [13, 14, 15]. It is worth noting that compressive sensing has also been used for tomographic imaging purposes in several applications, such as resolving two targets in a SAR pixel using orbital information from RADARSAT-2 [16], exploring the potentials of very high resolution SAR data for urban infrastructure mapping [17], and for spaceborne tomographic reconstruction [18].

After estimating the direction of arrival (DoA) of the received signals, the surface and bottom of the ice-sheets can be estimated. This problem can be formulated as a target tracking problem, where different tracking and learning algorithms can be used to estimate the ice-sheet boundaries. In [19], the authors proposed an automatic technique for identifying the ice boundaries by posing the problem as a Hidden Markov Model (HMM) inference problem and solving it using the Viterbi algorithm. The input tensor to this method is the result of the MUSIC beamformer, where each pixel in the DoA-range grid is the pseudo-spectrum of the corresponding DoA bin center [11]. This work was extended in [20], where a Markov-Chain Monte Carlo (MCMC) method was used to sample from the joint distribution over all possible layers conditioned on an image, and then estimate the ice-layers boundaries by taking the expectation over this distribution. Another extension to [19] was also published in [21] to extract 3D ice-bottom surfaces using Sequential Tree-reweighted Message Passing (TRW-S) algorithm, which is a belief propagation based technique. The authors in [22] proposed a semi-automatic approach for tracing near surface internal layers in snow radar echogram imagery, where curve point classification was used for this purpose, followed by a refining step. Further improvements were applied in [23] to the TRW-S and Viterbi algorithms used in the aforementioned references by incorporating domain-specific knowledge to the cost-functions. Even though these methods have produced acceptable results so far in terms of tracking accuracy, the main drawback is that the trackers work on an intensity image where the continuous spacial field of view of the radar is discretized into a small set of bins to form image pixels (or voxels) rather than working on the continuous space directly.

A point cloud based surface tracker is also possible, where the arrival angles of the received signals are estimated adaptively so that there is no need for the tracking step. However, for the ice-sheet airborne radar imaging application, there is very little about this approach in the literature relative to the voxel-based approaches mentioned previously. Also, this method requires the number of targets in each range-bin to be estimated beforehand, which is a problem known as the model order estimation (MOE) problem in signal processing literature. Errors in the model order (or number of targets) can change the tracker decision about the best surface that fits the estimated DoAs. Another issue with these approaches is that they are more sensitive to array errors, such as phase, location, and gain errors, than voxel based methods (e.g. MUSIC beamformer). In [13], an MLE-based method was used to sequentially track the elevation angles of the signals received from the surface and bottom of the ice-sheet, but there are no details about the technique. However, from a personal communication with the first author, X. Wu, they have imposed some constraints on the estimated signal directions in one range-bin based on the previous range-bin. In spaceborne SAR tomography literature, there is some work on using neural networks to fit surfaces to 3D SAR tomography point clouds, such as [24, 25, 26, 27]. In this thesis we will explore more about the point cloud trackers and suggest new solutions to the ice boundaries estimation problem.

Multiple other approaches were also presented in the literature recently. A level-set approach was used in [28] to detect the ice-layer topology by evolving an initial curve using distance-regularized level set. The main idea is that the algorithm is fed by an initial surface (zero-level surface or contour at a given time, t), then the changes in the surface are tracked as the 3D shape evolves at each iteration. In [29], the authors used a multi-task spatiotemporal neural network that combines 3D ConvNets and Recurrent Neural Networks (RNN) to estimate ice surface boundaries from sequences of tomographic radar images. This approach has the ability to estimate ice-surface and ice-bottom simultaneously with higher speed relative to the belief propagation based techniques mentioned above. Another neural network (NN) based detection approach was proposed in [30], where surface boundaries are tracked using a convolutional NN model that takes advantage of an undecimated Wavelet transform to provide the highest level of information from radar images, as well as a multilayer and multi-scale optimized architecture. These recent approaches are promising directions for better ice-layer detection results although both are only demonstrated on 2D imagery with no elevation angle dimension.

The algorithms and methods discussed in the subsequent chapters are used to process data collected by CReSIS radars. These radars operate on a wide range of frequencies ranging from VHF to SHF [8]. The higher frequency radars, such as the Snow Radar and Accumulation Radar, are used for near-surface radar imaging. The lower frequency radars, such as MCoRDS radar, are used for surface and basal ice-sheet imaging. Since our purpose in this work is to generate 3D ice-bed tomography images, we use the MCoRDS radar data collected from Greenland and Antarctica. Specifically, we have processed several missions collected by the P-3 airborne radar from the 2014 Greenland mission (102 data frames) [31]. Also, we processed data collected over Russell glacier during the 2011 arctic campaign.

1.2 Thesis Outline

In the following chapters, we study the ice-bottom tracking problem from different perspectives. In chapter 2, we lay the ground for the following three chapters by providing a necessary theoretical background that covers the basic theory of synthetic aperture radar (SAR) tomography imaging, narrowband and wideband signal models, and multiple direction finding techniques, among other topics.

In chapter 3, we explore the problem of estimating the signal subspace dimension (or number of targets). We propose a machine learning-based method to solve this problem in the case of wideband data with large number of targets relative to the number of sensors.

Particle filter (PF) and sequential maximum a posterior estimation (S-MAP) algorithms are studied and compared for the ice-surface tracking problem using 2D simulation data in chapter 4.

Chapter 5 is dedicated to the application of beamformer-based and direction of arrival (DOA)-based trackers into real wideband radar data, where we elaborate on the steps that led to the generation of tracked surfaces and, eventually, digital elevation models (DEMs).

We conclude this work in chapter 6 and we list few possible future research directions that can be extended from this work.

Chapter 2

Array Signal Processing for Ice-Sheet Imaging: Theory and Background

2.1 Introduction

In airborne radar sounder signal processing, the collected data are most naturally represented in a cylindrical coordinate system: along-track (or slow-time dimension), range (or fast-time dimension), and elevation angle. Generally, the data are processed in each of these dimensions sequentially using proper signal processing techniques [32, 33], as shown in figure 2.1. The goal of each step is to focus or resolve the data in the corresponding dimension such that a 3D image of the scene can be formulated. SAR processing algorithms, such as the frequency-wavenumber (f-k) migration algorithm [34], are used to process the data in along-track, pulse-compression or matched filtering is used to process the range dimension, and array-processing techniques are used for the elevation angle dimension.

After the first two steps, the 3D scene is dissected into toroids parallel to the cross-track dimension, where the common-range targets need to be resolved using their arrival direction. In this work, we focus on the array processing step, with the goal of using these results to form 3D images of the ice-bed. Several direction of arrival (DOA) estimation methods can be used to resolve the elevation angle of the targets, such as MUltiple Signal Classification (MUSIC) and maximum-likelihood estimation (MLE), which are two techniques, among others, utilized in this work. Other wideband DOA estimators are also possible, such as wideband MLE. A class of adaptive DOA estimators is also discussed in this chapter. These array processing techniques are detailed in Section 2.6. Sections 2.2 to 2.5 will be dedicated to the general background theory needed to understand the following sections.

In section 2.7, we discuss another practical issue with DOA estimation, which is the array calibration problem, where we account for the mismatch between the ideal and actual beam pattern of the sensors and the array. The types of the radars and data used in this work are introduced in section 2.8. The chapter ends in section 2.9, where we explain the way we calculate the phase centers of the array sensors.

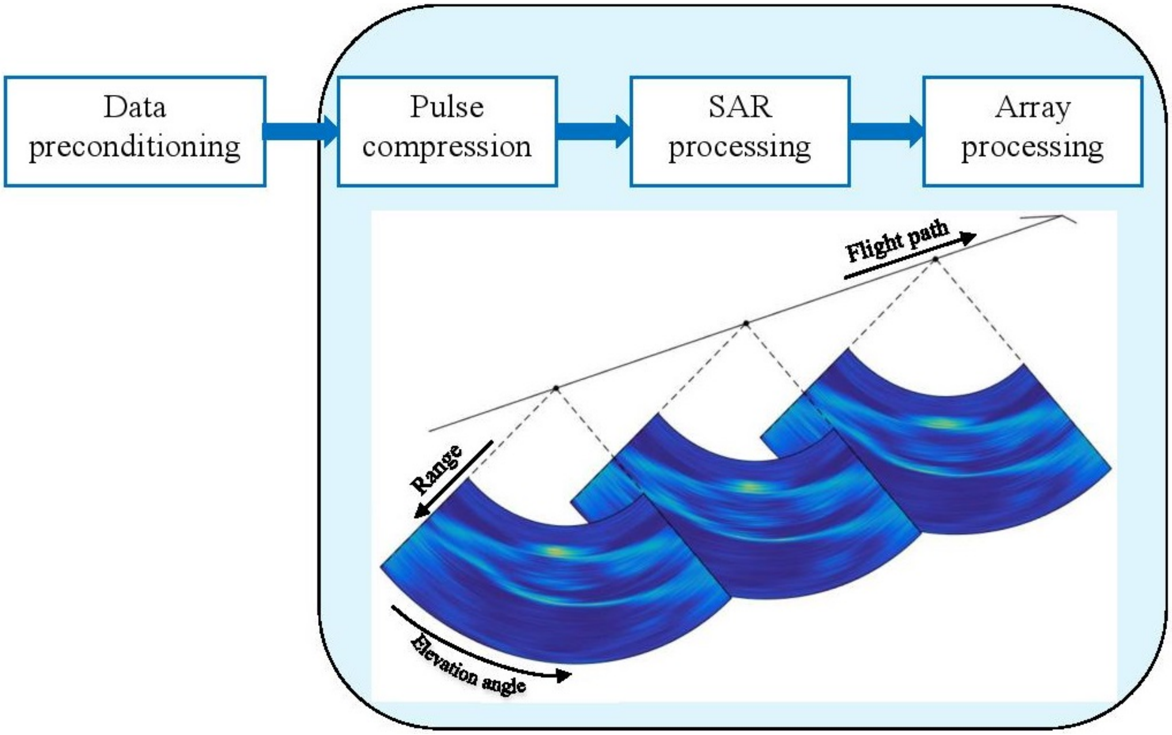

Figure 2.1: SAR data processing steps. After data preconditioning, three processing steps are applied, one for each cylindrical dimension of the collected data.

2.2 SAR Tomography

In this section we introduce the radar processing steps that lead to the formation of the 2D images of the scene. The scene in our case is an ice-sheet with thickness between 0 km (e.g. over the ocean where there is no ice) to several kilometers.

SAR images are 2D images of the scene, where the first axis represents the range dimension and the second axis represents the along-track dimension, and each pixel in the image contains the intensity information of the ground targets that are resolvable, in both these two dimensions. Figure 2.2 shows a three range-bin cross-track slice that illustrates the contents of a single range-line. The combination of the 2D slices will then produce the final 3D image of the scene. At a specific along-track location (i.e. range-line), the targets in each range-bin contain scattering from multiple targets that share the same range to the radar. These targets are resolved in the array processing step. There are typically up to four separable signals in a single range-bin: left/right ice-surface and left/right ice-bottom. However, with transmit beamforming, the beam can be steered to one side or the other so that usually only two signals dominate. For example, in the left transmit beam, the left ice-surface and left ice-bottom targets would tend to dominate.

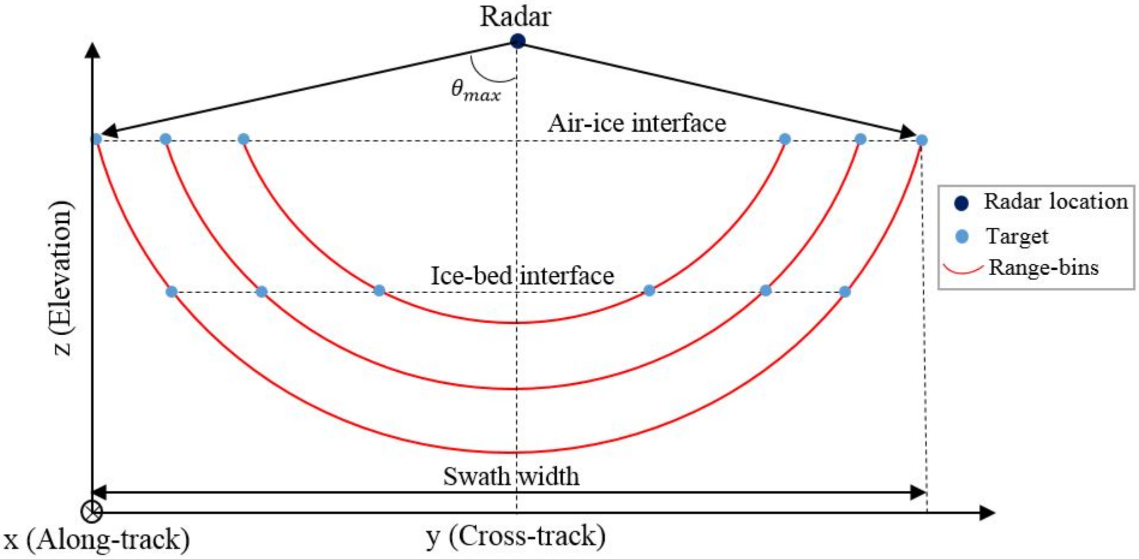

Figure 2.2: Cross-track slice that illustrates the contents of a single range line, composed of three range-bins. Array processing is then applied to resolve the ground targets. $\theta_{\max}$ is the maximum elevation angle of the targets in the array field of view.

In the range dimension, closely-spaced targets in each pixel in the SAR image can be resolved by matched-filtering the preconditioned data followed by frequency-domain windowing to reduce the side lobes of the resulting image in the range dimension. In this work, we use a fast-time Hanning window. A good example to explain the need for windowing is when there are two close targets in the scene, where one is strong and the other is weak, and we want to see them both. In this case windowing helps to reduce the correlation between these two targets by suppressing the sidelobes of the strong target's impulse response below the main lobe of the second target's impulse response.

Also, for a transmitted signal bandwidth B and pulse duration τ, the compression gain is $\tau/\tau_c = \tau B$, where τ_c is the compressed-pulse duration. Another important parameter here is the range resolution σ_r, defined as the smallest distance between two resolvable targets in the range dimension, which is given by $\sigma_r = \alpha c/2B$, where c is the speed of light, and α is a scaling factor that accounts for the windowing step.

The pulse-compressed data are then SAR-processed to focus the data in the slow-time dimension, where an FFT-implemented frequency-wavenumber (f-k) migration algorithm is applied [34]. The azimuth resolution σ_x, defined as the smallest distance between two resolvable targets on the ground in the azimuth dimension, greatly improves after SAR processing, and the effects of the azimuth clutter are reduced. The SAR resolution is mostly limited by the backscatter in the along-track dimension which is strongest around the nadir direction where the incidence angle of the scattering is near zero or normal to the surface.

Fluctuations in the platform trajectory relative to the nominal SAR aperture length are compensated for by time delaying signals along the aperture to mimic a smooth flight trajectory with a squint angle of nadir (these time delays are removed after SAR processing to preserve the actual phase centers of the measurements), while fluctuations in platform velocity are handled by uniformly re-sampling the radar data in the along-track dimension using a sinc-interpolation kernel [33].

2.2.1 Ground Range Resolution and Number of Snapshots

The relationship between the flatness of the surface and the number of snapshots used to estimate the data covariance matrix can be used to estimate the prior distribution of the targets (i.e. the ground targets), which makes it possible to use Bayesian DOA estimation, such as sequential MLE and the particle filter, rather than classical DOA estimation, such as MLE. Figure 2.3 shows the ground-range resolution, σ_g, defined as the distance on the ground between the intersection of two consecutive range bins with the surface, of a perfectly flat surface. Flat surfaces make it possible to use neighboring pixels as snapshots. For example, in figure 2.4, if the surface was flat, the ground-range resolution would have been σ_{g1}, but due to the surface undulations, the ground-range has increased to $\sigma_{g2} > \sigma_{g1}$, which makes the neighboring targets further apart and thus have different statistics. Even for smooth surfaces, there is a limit to using the snapshots because the ice-surface is usually not perfectly flat, and the range dimension, especially at nadir, is worse than the along-track dimension for collecting snapshots.

The flatness of the surface can help us do the following: 1) use prior DOA estimates to help improve future DOA estimates, and 2) track the ice-bed using simple models. To track a flat surface, we can use the position of the targets at one location to predict the position of the targets at another location with high accuracy due to the high stationarity or stability of the snapshots. This is a more different problem than tracking a single target whose angle of arrival is slowly changing, such as a rocket tracking problem where we can use the prior locations of the target to predict its future location. In other words, tracking the ice-bed is a multi-target tracking problem, where the degree of correlation between the tracked targets depend on their arrival angle and on the flatness of the surface they belong to. Additionally, for flat surfaces, it is easier to couple the DOA estimation problem with the tracking problem, as both can be formulated under Bayesian approaches, relative to very rough surfaces, which require more complex models.

The ground range resolution changes with the incident angle (θ). For a flat surface, its maximum occurs at nadir or more generally anywhere the surface is normal to the range vector, and decreases as θ increases. In other words, for a flat surface, the ground range resolution improves as incidence angle increases.

Mathematically, let $\sigma_r = c/2B$ be the range-resolution (ignoring the effect of windowing). Also, let h be the radar height, and r be the distance from the radar to the ground level where the two range-bins intersect with the ground, as shown in figure 2.5. Then, for a flat surface, the ground-range resolution can be calculated as follows:

$$\sigma_g = \sqrt{(r+\sigma_r)^2 - h^2} - r\sin(\theta_1) \tag{2.1}$$

where $r = h/\cos(\theta_1)$.

The two extremes of σ_g are:

- At nadir, $\theta_1 = 0°$ (i.e. $r = h$), and thus the ground range is $\sigma_g = \sqrt{2\sigma_r r + \sigma_r^2}$. For example, if $h = 1000$m and $B = 30$MHz, then $\sigma_g \approx 100$m.
- When $\theta_1 = 90°$, it can be shown that $\sigma_g = \sigma_r$.

Figure 2.6 shows how the ground-range changes with the incident angle for $\theta = 0°$ to $30°$ for the same parameters given above.

Note that the angle between two targets ($\Delta\theta$) on the ground also reduces as the incidence angle increases, as shown in figure 2.7. Using trigonometry and algebraic manipulations, $\Delta\theta$ can be expressed as:

$$\Delta\theta = \theta_2 - \theta_1 = \cos^{-1}(\frac{h}{r+\sigma_r}) - \cos^{-1}(\frac{h}{r}) \tag{2.2}$$

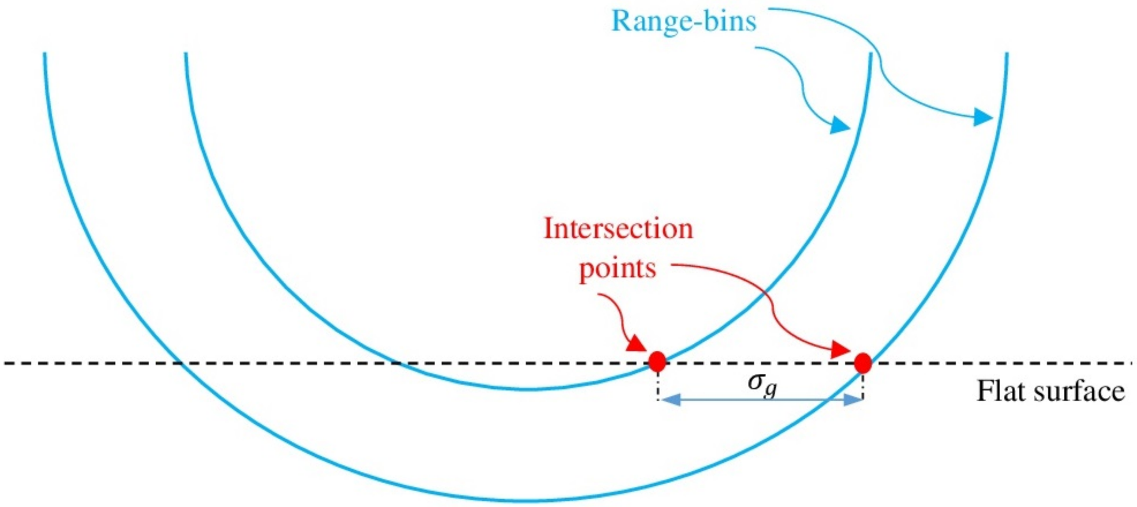

Figure 2.3: Ground range (σ_g) at off-nadir direction when the surface intersecting the two range-bins is flat.

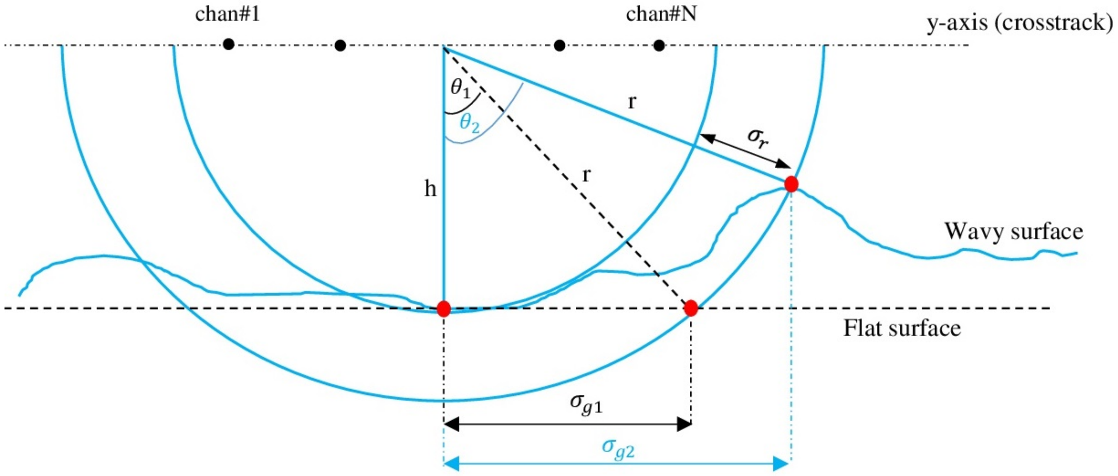

Figure 2.4: Ground-range resolution deteriorates when there is topographic relief

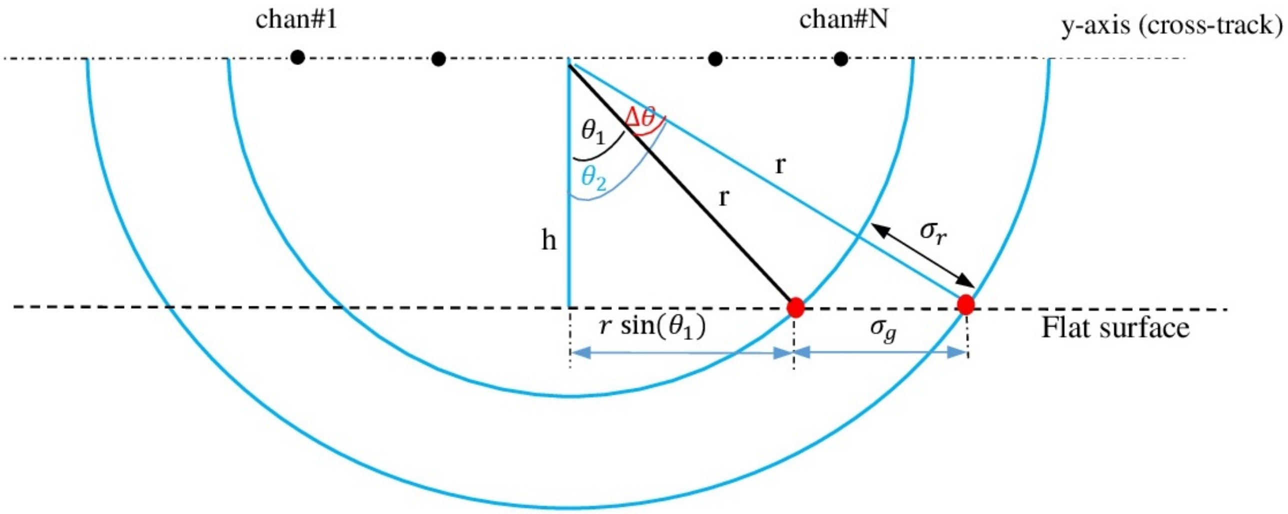

Figure 2.5: Problem geometry

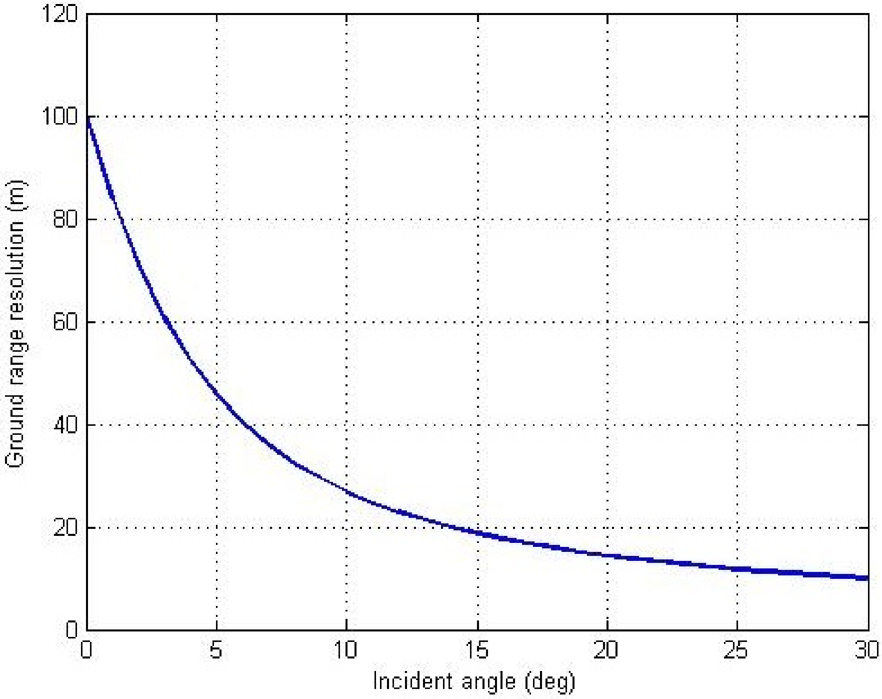

Figure 2.6: Ground-range resolution improves as the incident angle increases

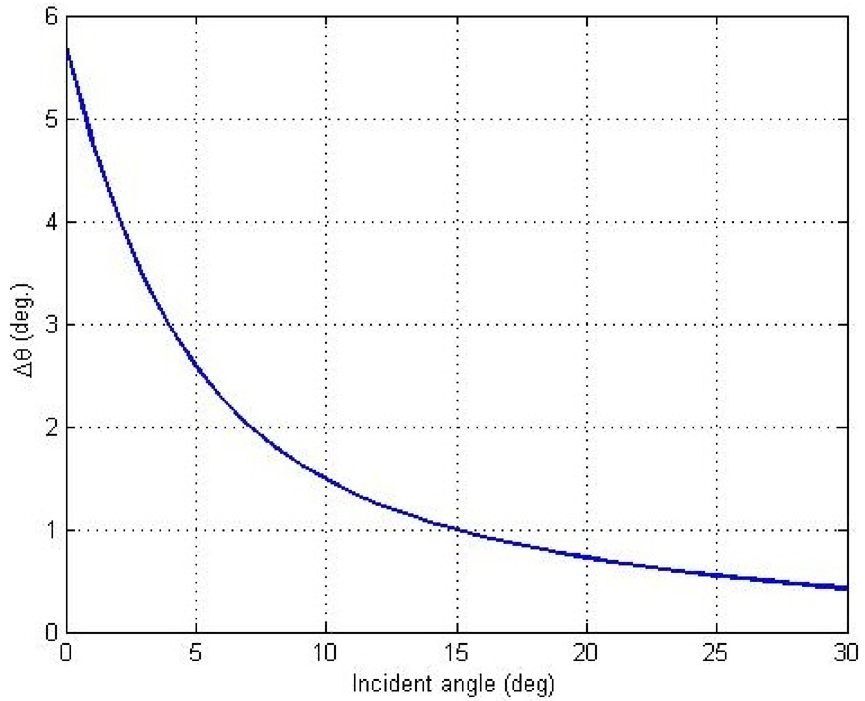

Figure 2.7: Change in angle between two targets separated by the ground range resolution as a function of the change in the incidence angle

From the above discussion, we can see that near nadir there is wide angular separation between targets in close range proximity, which has two main effects:

a. It is not recommended to use the range snapshots from near-by targets to estimate the data covariance matrix (DCM) because the snapshots are coming from targets at distinct incidence angles, especially at nadir. This makes DOA estimation worse and suggests the use of along-track snapshots rather than range snapshots for this purpose. Note that the snapshots are assumed to be uncorrelated because the noise samples are uncorrelated, but they are spatially correlated across the array. Ideal pulse compression and SAR processing should make the snapshots completely independent along the range and azimuth dimensions, but this is not true in practice due to sidelobes of the targets' response (frequency leakage).

b. Due to the large ground range resolution at nadir, the signals received from the angular-bins around nadir will appear as a distributed target in the final 3D image of the scene, which makes it difficult to recognize the exact range-bins of the ice-surface corresponding to these angular bins, as shown in figure 2.8.

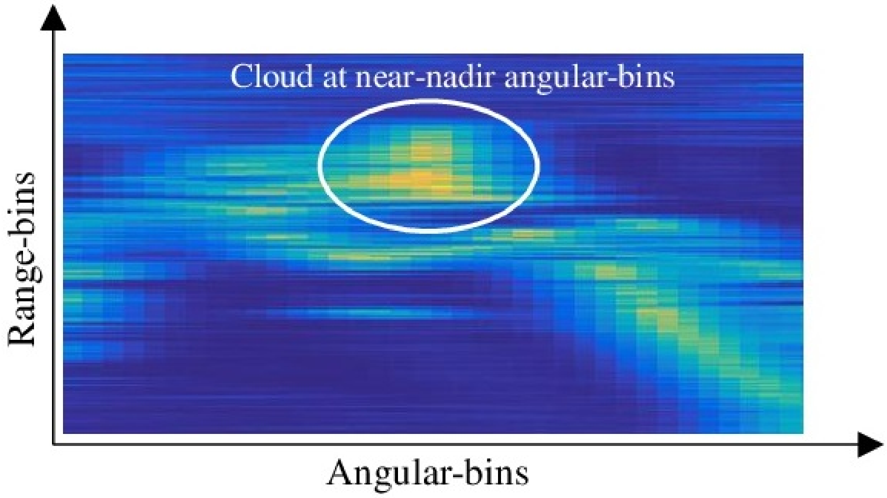

Figure 2.8: Section of a 3D image showing a point cloud near nadir that causes surface-tracking ambiguity

Now, if we increase the signal bandwidth, the ground-range resolution improves. Figure 2.9 shows the change of the ground-range as a function of the incident angle for a wideband signal ($B = 370$MHz) with $h = 1000$m. Comparing this figure with figure 2.6, it seems that the two issues mentioned above (i.e. snapshots shortage and the wide angle spread at nadir) are no longer problems in this case. However, this is only true when the surface is flat to within a single range bin, which is generally not true. Undulations in topography at nadir will cause layover. So even though $B = 370$MHz appears to have good range resolution at nadir, any topographic relief will still create the same problems mentioned above at nadir because the surface is normal to the range vector, as explained in figure 2.4.

Since range snapshots undergo a change in the direction of arrival as a function of range even for a smooth surface and this change is different for each target, in this work azimuth snapshots are preferred to form the data covariance matrix $\mathbf{R}$. In the CReSIS toolbox, we also developed a 2D array processor that utilizes both range and azimuth snapshots to form $\mathbf{R}$ rather than just the range snapshots. The snapshots are modeled, for simulation and real data processing, based on the assumption that scatterers are randomly placed in each resolution cell so that the scattering is an independent and identically distributed (iid) Gaussian random process.

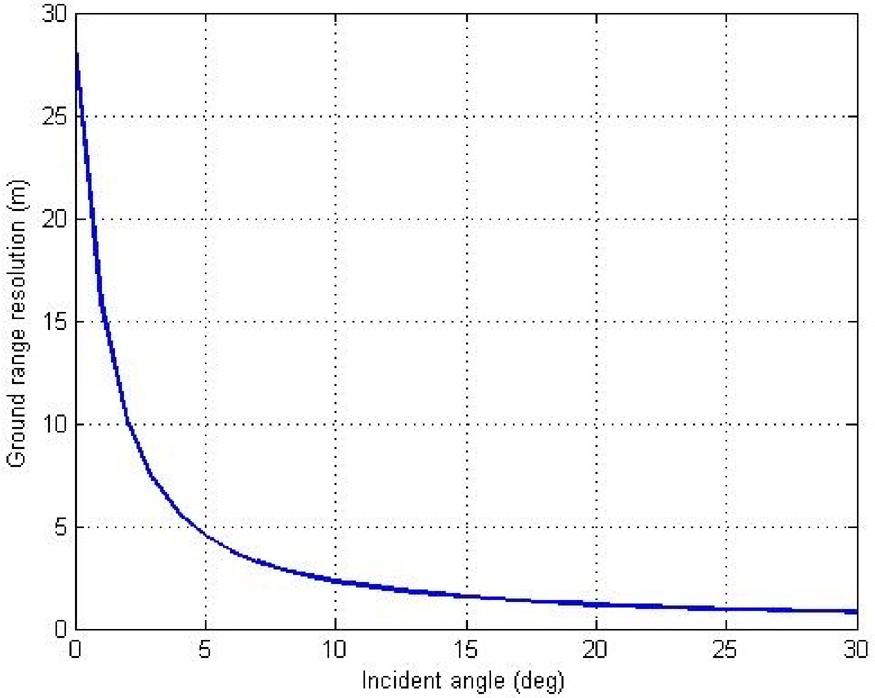

Figure 2.9: Ground-range resolution as a function of the incident angle in a wideband system with 370 MHz bandwidth

2.3 Narrowband Signal Model

In our work, we have made the following assumptions:

- There are P sensors.
- There are Q targets (aka scattering sources or targets for radar).
- The scatterers are in the far field so that only the direction of arrival matters and not the range to the target when determining the relative delays between sensors.
- The targets obey the principle of superposition or Born approximation. This allows us to neglect interactions between the targets.
- The target signals are band limited signals with a center frequency of ω_c

In general, a target's complex baseband representation, $S_w(t)$, received at a sensor with time delay, t_d, can be written in the following form:

$$S_w(t-t_d) = S(t-t_d)\ \exp\left(-j\omega_c t_d\right) \tag{2.3}$$

where $S(t)$ is the complex baseband target signal.

The signal received at sensor p, $x_p(t)$, is a linear combination of all Q targets, and is given by the following equation:

$$x_p(t) = \sum_{q=1}^{Q} S_{w,q}(t-\tau_p(\theta_q)) + n_p(t) = \sum_{q=1}^{Q} S_q(t-\tau_p(\theta_q))\ \exp\left(-j\omega_c \tau_p(\theta_q)\right) + n_p(t) \tag{2.4}$$

where, θ_q is the direction of arrival of the target q, $\tau_p(\theta_q)$ is the signal delay to sensor p for a direction of arrival of θ_q, and $n_p(t)$ is an additive noise at sensor p.

The signal model in equation 2.3 is valid for both narrow and wide bandwidths, where the received signal's envelope is not assumed to be constant across the array. This model is cumbersome to deal with because it deals with time shifted versions of the signal, $S_q(t-\tau_p(\theta_q))$. Because of the dependence on p, we cannot write the summation as a matrix equation. Under the narrowband approximation, we assume that the signal is narrowband enough (i.e. complex envelope changes slowly enough with time) so that the variation in $\tau_p(\theta_q)$ over the whole array allows for the following approximation:

$$S_{w,q}(t-\tau_p(\theta_q)) \approx S_q(t)\exp\left(-j\omega_c \tau_p(\theta_q)\right) \tag{2.5}$$

Note that we are only requiring that the relative delays between sensors be small enough so that if we look at the signals received by the array at a particular instance in time, they can be modeled across the array in this way.

Now apply the narrowband signal model discussed above on the data collected by the radar. Given a SAR image pixel at range ρ, and along-track position x, the pixel's received signal $\mathbf{x}(x,\rho)$

is modeled as a P element vector, where P is the number of sensors in the array:

$$\mathbf{x}(x,\rho) = \mathbf{A}(\boldsymbol{\theta})\ \mathbf{s}(x,\rho) + \mathbf{n}(x,\rho) \qquad \in \mathbb{C}^{P\times 1} \tag{2.6}$$

where $\mathbf{A}(\boldsymbol{\theta}) \in \mathbb{C}^{P\times Q}$ is the array steering matrix, which relates the $Q\times 1$ target echo signals $\mathbf{s}(x,\rho)$ to the P sensors for range ρ and along-track position x. The columns of $\mathbf{A}(\boldsymbol{\theta})$ are always assumed to be linearly independent in this work. $\mathbf{n}(x,\rho) \in \mathbb{C}^{P\times 1}$ is an additive white Gaussian noise vector. For narrowband signals, the elements of the array steering matrix $[\mathbf{A}(\boldsymbol{\theta})]_{p,q}$ can be expressed as a complex exponential function of the array geometric properties and the direction of the signal impinging on the array. So in the y-z plane, assuming isotropic sensors, the response of the p^{th} sensor to the q^{th} target can be described mathematically as follows:

$$[\mathbf{A}(\boldsymbol{\theta})]_{p,q} = \exp\left(j(d_{y_p}k_{y_q} - d_{z_p}k_{z_q})\right) \tag{2.7}$$

where, d_{y_p} and d_{z_p} are the spacial distance from the phase center of the p^{th} sensor to the phase center of the reference sensor along the y and z axes, respectively. $k_{y_q} = k\sin\theta_q$ and $k_{z_q} = k\cos\theta_q$ are the wavenumbers along the y and z axes, respectively, where $k = 4\pi/\lambda$ is the wavenumber, and λ is the signal wavelength. Here we used the factor 4 instead of 2 in calculating k to account for the two-way travel time (twtt) of the signal from the radar to the target and back to the radar.

Letting M be the number of snapshots, we can write the data matrix as follow:

$$\mathbf{X} = \mathbf{A}(\boldsymbol{\theta})\mathbf{S} + \mathbf{N} \tag{2.8}$$

where $\mathbf{S} \in \mathbb{C}^{Q\times M}$ and $\mathbf{N} \in \mathbb{C}^{P\times M}$ are the data and noise matrices, respectively. Assuming the noise samples to be independent and Gaussian distributed, the data vectors $\mathbf{x}$ are distributed as a multi-variate complex Gaussian random process: $\mathbf{x} \sim \mathbb{CN}(\mathbf{A}(\boldsymbol{\theta})\mathbf{s}, \sigma_n^2\mathbf{I})$, where σ_n^2 is the noise variance (unknown scalar), and $\mathbf{I}$ is the identity matrix. Thus, the conditional probability density function of **X** given $\boldsymbol{\theta}$ can be stated as:

$$p(\mathbf{X}|\boldsymbol{\theta}) = \prod_{i=1}^{M} (\pi\sigma_n^2)^{-M} \exp\big(-\frac{||\mathbf{x}(i) - \mathbf{A}(\boldsymbol{\theta})\mathbf{s}(i)||^2}{\sigma_n^2}\big) \tag{2.9}$$

where $||.||$ is the 2-norm operator.

We define **R** to be the covariance matrix of **X**. Since the signals received from nearby SAR image pixels have approximately the same direction of arrival under the assumption of a smooth surface (and hence the same statistics), they can be used as independent snapshots for estimating the data covariance matrix **R** as follows:

$$\hat{\mathbf{R}} = \frac{1}{M}\mathbf{X}\mathbf{X}^H \tag{2.10}$$

where H represents the complex-conjugate transpose operation. Using $\hat{\mathbf{R}}$ we can estimate the DOA, which is done for every pixel in the SAR image. As discussed in Section 2.2.1, neighboring pixels will likely have slightly different incidence angles. Also noted is that a greater spread is expected near nadir and when taking neighboring pixels in range rather than in the along-track dimension.

The true data covariance matrix $\boldsymbol{R}$ can be written as follows:

$$\boldsymbol{R} = \mathbb{E}(\boldsymbol{x}\boldsymbol{x}^H) = \boldsymbol{A}(\boldsymbol{\theta})\boldsymbol{R}_{ss}\boldsymbol{A}^H(\boldsymbol{\theta}) + \boldsymbol{R}_{nn} \tag{2.11}$$

where $\mathbb{E}$ is the expectation operator. The matrices $\boldsymbol{R}_{ss} = \mathbb{E}(\boldsymbol{s}\boldsymbol{s}^H)$ and $\boldsymbol{R}_{nn} = \mathbb{E}(\boldsymbol{n}\boldsymbol{n}^H)$ are the correlation matrices for signal and noise, respectively. $\boldsymbol{R}_{ss}$ and $\boldsymbol{R}_{nn}$ are positive definite matrices, where the rank of $\boldsymbol{R}_{ss}$ is Q and the rank of $\boldsymbol{R}_{nn}$ is $P-Q$ [35]. The rank of $\boldsymbol{R}$ is P, which can be shown using the positive definite properties of the constituent matrices and the linear Independence of the columns of A..

We can also analyze $\mathbf{R}$ using the singular value decomposition (SVD) technique. That is:

$$\begin{aligned}\mathbf{R} &= [\mathbf{U}_S \quad \mathbf{U}_N] \begin{bmatrix} \mathbf{\Lambda}_S & \mathbf{0} \\ \mathbf{0} & \mathbf{\Lambda}_N \end{bmatrix} \begin{bmatrix} \mathbf{V}_S^H \\ \mathbf{V}_N^H \end{bmatrix} \\ &= \mathbf{U}_S \mathbf{\Lambda}_S \mathbf{V}_S^H + \mathbf{U}_N \mathbf{\Lambda}_N \mathbf{V}_N^H \\ &= \mathbf{R}_S + \mathbf{R}_N \end{aligned} \tag{2.12}$$

where $\mathbf{R}_S$ is the signal-only covariance matrix (ideally, the signal subspace still have noise in it), and $\mathbf{R}_N$ is the noise-only covariance matrix. $\mathbf{U}_S$ contains the eigenvectors that span the signal subspace (i.e range of $\mathbf{R}_S$) , $\mathbf{U}_N$ contains the eigenvectors that span the noise subspace (i.e. range of $\mathbf{R}_N$), $\mathbf{V}_S$ is the range of $\mathbf{R}_S^T$, and $\mathbf{V}_N$ is the range of $\mathbf{R}_S^T$. $\mathbf{\Lambda}_S$ and $\mathbf{\Lambda}_N$ are diagonal matrices and contain, respectively, the signal plus noise and the noise eigenvalues. $\mathbf{\Lambda}_S$ contains the largest Q eigenvalues of $\boldsymbol{R}$, while $\mathbf{\Lambda}_N$ contains the remaining $P-Q$ eigenvalues. That is [35]:

$$\begin{aligned} \mathbf{\Lambda}_S &= \mathrm{diag}[\lambda_1, \lambda_2, \ldots, \lambda_Q] \\ \mathbf{\Lambda}_N &= \mathrm{diag}[\lambda_{Q+1}, \lambda_{Q+2}, \ldots, \lambda_P] \\ \text{with} \quad & \lambda_1 \geq \lambda_2 \ldots \lambda_Q \geq \lambda_{Q+1} \ldots \geq \lambda_P \end{aligned} \tag{2.13}$$

The eigenvectors of $\mathbf{U}_S$ and $\mathbf{U}_N$ should be sorted according to their corresponding eigenvalues in $\mathbf{\Lambda}_S$ and $\mathbf{\Lambda}_N$, respectively.

Note that $\mathbf{R}_N = \boldsymbol{R}_{nn}$ and $\boldsymbol{R}_S = \boldsymbol{A}(\boldsymbol{\theta})\boldsymbol{R}_{ss}\boldsymbol{A}^H$. So, for linearly independent targets, $\boldsymbol{A}(\boldsymbol{\theta})$ will have a full column rank of Q, which makes the rank of $\boldsymbol{R}_S$ to be Q as well. In the extreme case of left/right targets (near nadir or near grazing-angles), the columns of $\boldsymbol{A}(\boldsymbol{\theta})$ will be linearly dependent, and thus the rank of $\boldsymbol{R}_S$ will reduce, and there is no way to resolve the targets..

2.4 Wideband Signal Model

The time-bandwidth product (TBP) of the array is usually used as a metric to determine whether the system is narrowband or wideband. For small enough TBP, the envelope of the signal may be assumed constant across the entire array at any given instant in time. TBP is defined as: $\tau_{\max}B$, where $\tau_{\max}$ is the maximum difference in the time delays across the array taken over all the possible angles of arrival within the field of view (FOV). τ can be expressed as $\tau = L_a(\theta)/c$, where $L_a(\theta)$ is the length of the array projected onto the range vector in the direction of (θ). Note that L_a is a function of the DOA, where, for a linear array, the minimum array-length is for a target broadside to the array since the wavefront will impinge on all elements simultaneously, and the maximum array length is for an end fire target. Also, FOV affects whether the system is narrowband or wideband. Reducing the FOV reduces the maximum difference in time delays across the array and therefore makes the measured array signals more narrowband.

In summary, the size of the array, the bandwidth, and the FOV are the three main parameters that decide whether the system is wideband or narrowband. Van Trees [35] states that the narrowband assumption is valid when $\tau_{max}B << 1$. Based on simulations and real data using parameters which match one of the CReSIS radar systems, we noticed some degradation for a 0.4 TBP when MUSIC was used to estimate the DOAs of the received signals (due to the inherent narrowband assumption in this technique) for a 7 sensors array with $B_f \approx 0.164$ assuming FOV$= \pm 90^\circ$, but it is not severe.

In case of wideband systems, the array steering matrix will be frequency-dependent. Thus, equation 2.7 now becomes:

$$[\mathbf{A}(\boldsymbol{\theta}, f_i)]_{p,q} = \exp\Big(j\big(d_{y_p}k_{y_q}(f_i) - d_{z_p}k_{z_q}(f_i)\big)\Big) \tag{2.14}$$

where f_i is the i^{th} frequency within the signal bandwidth. $k_{y_q}(f_i)$ and $k_{z_q}(f_i)$ have the same definitions given in the previous section, except that now the wavenumber is frequency-dependent:

$k_i = 4\pi f_i / c$. Thus, the wideband data model can be written, similar to equation 2.6, as follows:

$$\mathbf{x}_i(x,\rho) = \mathbf{A}(\boldsymbol{\theta}, f_i)\ \mathbf{s}_i(x,\rho) + \mathbf{n}_i(x,\rho) \qquad \in \mathbb{C}^{P\times 1} \tag{2.15}$$

The frequency dependence of the data model makes the array processing methods more complex as we now have an additional degree of freedom. For each application of wideband array processing using subbanding, we will need to choose the number of subbands that is optimal for the specific application. This is because increased subbands leads to reduced snapshots per subband and coarser ground range resolution.

2.5 Cramer-Rao Lower Bound (CRLB)

Cramer-Rao Lower Bound (CRLB) is a measure of the amount of uncertainty in the observed data about some unknown embedded in the observation. In our case, we use the CRLB to quantify the quality of the estimated DOAs from our measured data. CRLB is independent of the type of estimator, and depends on several parameters, such as the number of sensors, the quality of the sensors, the number of targets, the number of snapshots, the degree of correlation between the targets, the amount of noise in the data, and the array imperfections (e.g. uncalibrated arrays).

The CRLB is calculated as follows [36]:

$$\mathrm{CRLB}(\boldsymbol{\theta}) = \frac{\sigma_n^2}{2N}\left[\mathrm{Re}\left\{\mathbf{D}\odot\left(\mathbf{R_s} - \left(\mathbf{R_s^{-1}} + \frac{1}{\sigma_n^2}\boldsymbol{A}^H(\boldsymbol{\theta})\boldsymbol{A}(\boldsymbol{\theta})\right)^{-1}\right)^T\right\}\right]^{-1} \tag{2.16}$$

where, $\odot$ is the Hadamard product (i.e. element-wise product). $\mathbf{D} = \dot{\boldsymbol{A}}^H(\boldsymbol{\theta})\mathbf{P}_{\mathbf{A}}^{\perp}\dot{\boldsymbol{A}}(\boldsymbol{\theta})$, and $\dot{\boldsymbol{A}}(\boldsymbol{\theta})$ is the derivative of $\boldsymbol{A}(\boldsymbol{\theta})$ w.r.t $\boldsymbol{\theta}$, where the q^{th} column of $\dot{\boldsymbol{A}}^H(\boldsymbol{\theta})$ is given by the following expression:

$$\dot{\boldsymbol{A}}_q(\boldsymbol{\theta}) = \boldsymbol{d}_q \odot \boldsymbol{A}_q(\boldsymbol{\theta}) \tag{2.17}$$

where $\boldsymbol{d}_q = [jd_{1q}, \ldots jd_{Pq}]^T \ \in \mathbb{C}^{P\times 1}$, where $d_{pq} = d_{yp}k_{yq} - d_{zp}k_{zq}$, and these variables were defined in Section 2.3. Also, $\mathbf{P}_{\mathbf{A}}^{\perp} = \boldsymbol{I} - \boldsymbol{A}(\boldsymbol{\theta})(\boldsymbol{A}^H(\boldsymbol{\theta})\boldsymbol{A}(\boldsymbol{\theta}))^{-1}\boldsymbol{A}(\boldsymbol{\theta})^H$ is the complementary projection matrix (i.e. projects onto the noise subspace, which is orthogonal to the subspace spanned by the columns of the steering-vectors).

Figure 2.10 shows the square-root of CRLB as a function of the direction of arrival for ice-bottom targets, where 2 equal-power and uncorrelated targets were assumed, with 11 snapshots and 7 sensors. The SNR was estimated from the collected data: the data at the very end of the ice-bottom were used to estimate the noise variance, while the data around the ice-bottom layer were used to estimate the signal variance, then the SNR was estimated as follows:

$$\mathrm{SNR} = \frac{\mathbb{E}_{\mathbf{x}}(||\mathbf{x}||^2)}{\mathbb{E}_{\mathbf{n}}(||\mathbf{n}||^2)} - 1 \tag{2.18}$$

where the expectation is approximated by averaging over a large number of data points. **x** represents the data within ±10 range-bins of the ice-bottom, and **n** represents the data from the last 50 range-bins, where there is no signal. Data from multiple frames (10 frames) were used to increase the accuracy of the estimated SNR, which was 14 dB for a nadir bottom target.

The DOA standard deviation is larger near nadir and near grazing angles. The first case (i.e. near nadir) is due to the small angular separation between the two targets, which results in correlated steering vectors, while the second case (near grazing angle) is due to the fact that as the arrival angle approaches ±90°, the steering vectors (for a uniform linear array with quarter wavelength spaced phase centers) also become equal and the effective aperture size reduces significantly because of the end fire geometry.

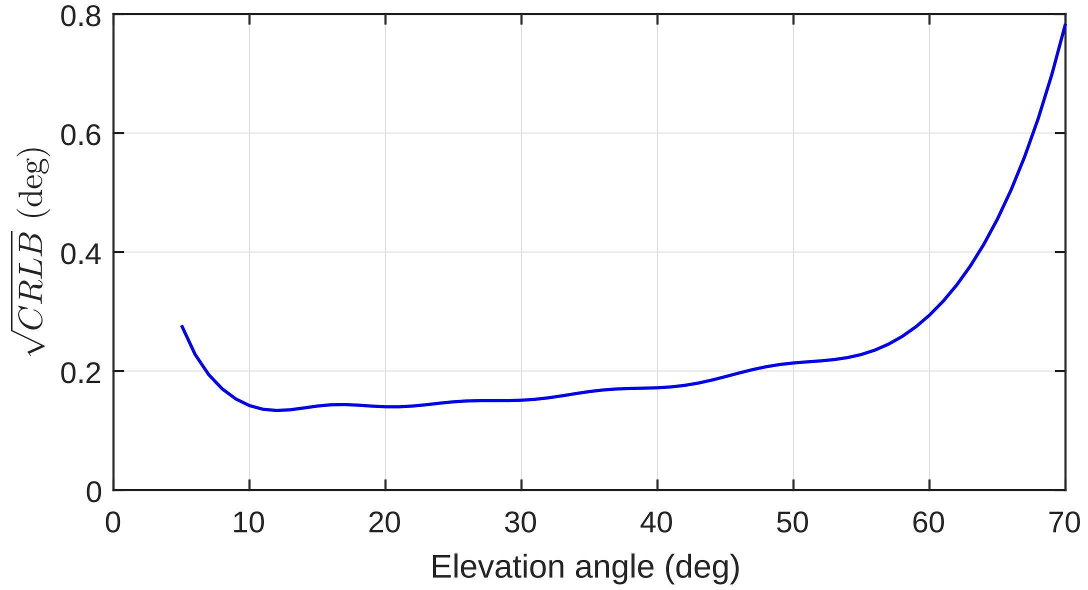

Figure 2.10: Square-root of CRLB as a function of the arrival angle for a target at the bottom of an ice-sheet assuming 2 equal-power targets with 11 along-track snapshots. One target is assumed to be on the left of the nadir and the other target is on the right of nadir.

2.6 Direction of Arrival Estimation (DOA)

After range and azimuth processing, 2D echogram images of the scene can be formulated as along-track position versus travel time or range. To obtain a 3D tomographic image of the ice-bottom, the elevation angles of the targets in each pixel need to be estimated. This problem can be formulated as a direction of arrival (DOA) estimation problem. We have applied and tested several narrowband and wideband elevation angle estimation techniques, such as MUSIC, MLE, and wideband MLE, in addition to other adaptive methods, on real and simulation data to resolve the targets in each pixel of the 2D SAR image. The theory behind these methods is introduced in this section.

2.6.1 Multiple Signal Classification (MUSIC)

MUSIC is a parametric DOA estimation technique that relies on the projection of the array steering vector at a given DOA, $\mathbf{a}(\boldsymbol{\theta})$, onto the noise subspace, $\boldsymbol{U}_N$. Ideally, $\mathbf{a}(\boldsymbol{\theta})$ is orthogonal to $\boldsymbol{U}_N$. Within the field of view, $\boldsymbol{\theta}$ that corresponds to the minimum projection result represents the estimated DOA.

The MUSIC cost function is defined as [35]:

$$\mathbf{J}_{\text{music}}(\boldsymbol{\theta}) = \frac{1}{\sum\limits_{j=Q+1}^{P} |\mathbf{a}^H(\boldsymbol{\theta})\mathbf{u}_j|^2} \tag{2.19}$$

where $\boldsymbol{u}_j$ is the j^{th} eigenvector of the noise subspace, which can be determined from the SVD of the data covariance matrix $\boldsymbol{R}$, as shown in Section 2.3. The MUSIC cost function utilizes the orthogonality between the noise subspace and the array steering vectors at the true DOAs [37]. This means that MUSIC, if used as a DOA estimator, gives the $\boldsymbol{\theta}$'s which result in the steering vectors with the lowest inner products with the noise subspace (i.e. $\boldsymbol{\theta}$ that maximizes $\mathbf{J}_{\text{music}}(\boldsymbol{\theta})$).

In this work, we use MUSIC as a beamformer (grid scan over entire field of view) rather than an estimator (returning just the peak location for each target). The latter requires the exact number of targets or targets in the range shell to be known otherwise the tracker may track false targets or miss targets all together. Note that we have fixed the dimension of the signal subspace as this is required by MUSIC to produce the output. However, there is more information in this beamformer output because it returns the result for angles spanning the whole field of view rather than just the positions of the peaks. Current efforts to estimate the model order using standard eigen-analysis of the data covariance matrices have failed due to the complicated eigen-structure of our data that may be due to issues such as the relatively large time-bandwidth product of the array and multipath effects. The output of the beamformer is a 3D image where the dimensions are along-track, range, and elevation angle. The beamformer has the advantage that even when the signal eigenspace is not precisely estimated, there is still likely to be some reduction in the null-space's correlation with the actual target's steering vector. Since MUSIC's output is based on the reduction in the null-space correlation with the steering vectors, this can aid the ice bottom tracker even though it is not the steering vector with the lowest correlation due to errors in the steering vectors or eigenspace estimation.

2.6.2 Maximum Likelihood Estimation (MLE)

MLE, for the DOA estimation problem, is an asymptotically consistent and efficient estimation technique, and is optimal to MUSIC. However, this method is more time-consuming because it requires a non-linear multidimensional search to obtain its estimates [38, 39].

Assuming that the noise variance and the target signal are unknown, but non-random, the deterministic MLE cost function to be maximized can be written as [39]:

$$\mathbf{J}_{\text{mle}} = \text{Tr}(\mathbf{P}_A\mathbf{R}) \tag{2.20}$$

where,Tr is the trace operator, and $\mathbf{P}_A = \mathbf{A}(\boldsymbol{\theta})\left(\mathbf{A}^H(\boldsymbol{\theta})\mathbf{A}(\boldsymbol{\theta})\right)^{-1}\mathbf{A}^H(\boldsymbol{\theta})$ is the projection matrix of the steering matrix. Thus, we seek the value of $\boldsymbol{\theta}$ that maximizes $\mathbf{J}_{\text{mle}}$. That is:

$$\boldsymbol{\theta} = \arg\max_{\boldsymbol{\theta}} \mathbf{J}_{\text{mle}} \tag{2.21}$$

Taking the SVD of $\boldsymbol{R}$, as shown in equation 2.12, and using the trace and projection properties, equation 2.20 can be re-written as [39]:

$$\mathbf{J}_{\text{mle}} = \sum_{p=1}^{P} \lambda_p ||\boldsymbol{P}_A \boldsymbol{u}_p||^2 \tag{2.22}$$

where $\boldsymbol{u}_p$ is the p^{th} eigenvector of $\boldsymbol{R}$ that corresponds to the eigenvalue λ_p, for $p \in \{1, \dots P\}$. Note that the MLE cost function utilizes the eigen-structure of the signal and noise subspaces, which is unlike MUSIC that only uses the noise or signal eigen-structure. The amount of contribution any eigenvector makes depends on how big its corresponding eigenvalue is.

Stochastic MLE can also be used for DOA estimation [40]. However, in this work we only use deterministic MLE due to its mathematical simplicity and the ability to estimate targets' signals (and therefore targets' power) in a straight forward method [39].

2.6.3 Wideband MLE (WBMLE)

MLE and MUSIC, as described in the previous two sections, are suitable for narrowband systems, where the time-bandwidth product is much less than 1, that is $\tau B << 1$. From an array processing stand point, wideband systems have some problems that need special treatment. For example, the narrowband array-processing techniques produce larger errors as the bandwidth of the system increases [41]. Model-order estimation is a good example of this problem, where wideband systems induce false targets [42], producing an overestimated number of targets because the signal subspace dimension is not equal to the number of targets as it is for narrowband arrays. Also, wideband systems have lower SNR relative to narrowband systems for area distributed scattering. This is due to the concomitant refinement in the resolution which results in a smaller scattering area for each radar image pixel and hence less scattered energy.

Wideband MLE (WBMLE) is a DOA estimation technique, where the signal bandwidth is sub-divided into N_f sub-bands, and then MLE is applied to all subbands at once and that for independent subbands this is just the product of the individual likelihood density functions or the sum of the individual log likelihood functions [43].

Wideband MLE has the following cost function:

$$\mathbf{J}_{\text{wbmle}} = \sum_{n=1}^{N_f} \mathbf{J}_{\text{mle}}(w_n) \tag{2.23}$$

where, $\mathbf{J}_{\text{mle}}(w_n)$ is the MLE cost function given in equation 2.20 as a function of frequency w_n. Thus, the optimization problem can be written as:

$$\boldsymbol{\theta} = \arg\max_{\boldsymbol{\theta}} \mathbf{J}_{\text{wbmle}} \tag{2.24}$$

The WBMLE method has a disadvantage [14]: it degrades the range resolution of the SAR image (due to subbanding) in order to obtain an estimate of the DOA, allowing more targets over a wider angular spread to be illuminated. The increased signal subspace and angular spread of targets within each ground range bin will result in reduced performance for our specific SAR tomography application especially for targets near nadir.

2.6.4 Focusing Matrices

Another coherent DOA estimation method is to use a focusing matrix to focus the DOA from different frequencies into the center frequency of the signal bandwidth using signal-subspace transformation matrices $\boldsymbol{T}(f)$ such that the narrowband DOA estimation techniques can be used. Even though we still have not applied the focusing matrices method to any of our data yet, we mention it here briefly for completeness.

There are several classes of this method in the literature, and here we describe the general framework given by [44], which can be summarized as follow:

1. Define $\boldsymbol{T}_i$ as the focusing matrix associated with frequency f_i, for $i \in \{1, 2, \ldots, N_f\}$. The main characteristics of $\boldsymbol{T}_i$ are described in [45]. Note that $\boldsymbol{T}_i$ transforms the array steering matrix at frequency f_i into an array steering matrix at another reference frequency, f_0, which is usually the center frequency. Thus, we can determine $\boldsymbol{T}_i$ as follow:

$$\boldsymbol{T}_i = \arg\min_{\boldsymbol{T}_i} ||\boldsymbol{A}_0(\boldsymbol{\theta}_f) - \boldsymbol{T}_i\boldsymbol{A}_i(\boldsymbol{\theta}_f)||_F \tag{2.25}$$

   where $||.||_F$ is the Frobenius-norm operator, and $\boldsymbol{A}_0$ is the array steering matrix at the reference frequency. $\boldsymbol{\theta}_f$ is the set of focusing angles, which need to be estimated a priori.

2. Using $\boldsymbol{T}_i$, determine the focused data covariance matrix $\boldsymbol{R}_{foc}$ as follow:

$$\boldsymbol{R}_{foc} = \sum_{i=0}^{N_f-1} w_i \boldsymbol{T}_i \boldsymbol{R}_i \boldsymbol{T}_i^H \tag{2.26}$$

   where w_i is a weighting factor and $\boldsymbol{R}_i$ is the data covariance matrix associated with frequency f_i.

3. Using $\boldsymbol{R}_{foc}$ and $\boldsymbol{A}_0$, estimate the DOAs using the narrowband estimation methods, such as MLE and MUSIC.

Note that the main drawback of this method is that the set of focusing angles $\boldsymbol{\theta}_f$ needs to be prepared a priori, which is not always possible. Thus, other methods were introduced in the literature to get around this problem, such as the test of orthogonality of projected sources (TOPS) introduced in [44]. On the other hand, one advantage of this method is that the subbands are used to generate more snapshots, one for each subband.

2.6.5 Sequential DOA Estimation

Unlike standard DOA estimation methods discussed above, sequential DOA estimation techniques utilize the surface geometry information to relate the estimated DOAs from neighboring pixels. This can be done by mathematically modeling the relationship between the DOAs of the neighboring range-bins. The model can also include other important prior information about the surface, such as the slope of the surface and the number of dead range-bins (i.e. range-bins that do not have targets). This model is called the transition model, the dynamics model, or the process model, and can be data-independent (i.e. only a function of the geometry of the surface).

Another important aspect of the Sequential DOA estimation is the adaptive prior probability density function or pdf. One way of updating the prior pdf is to derived it from the transition model such that it is updated at each state or range-bin based on the results from the previous range-bins. The prior pdf parameters can also be obtained from training data and then feeding the inferred parameters to the filter at each range-bin.

The bounds of the estimated DOAs should also be adaptively changing. This can be done by using the estimated DOAs from one range-bin to bound (and may be to initialize) the DOAs at the following range-bin. Accurate and tight bounds make it possible to eliminate DOA outliers and form a smooth surface in the end, but it makes the prior pdf less important to the results. Also, making an error at one range-bin may cause the following range-bins to have wrong DOAs. So, setting the tolerance in the bounds should be dependent on the geometry/flatness of the surface to be tracked, the amount of change in the DOA as a function of range-bin, and a few other physically-imposed constraints.

The results from DOA-based tracking methods can be used directly to reconstruct the ice-bottom surface, which is usually not realizable if non-sequential techniques were used to estimate the elevation angles because these techniques require a tracker to be used to extract the surface information from the estimated DOAs. Thus, here we attempt to eliminate the need for the extra tracking step by utilizing the surface geometry as a prior information.

The flat earth transition model:

In the following two sub-sections we will use the flat-earth approximation model to have an initial estimate of the change in DOA as a function of range-bin, which is defined in equation 2.2 and depicted in figure 2.5. So, the flat-earth surface will serve as the mean for estimating the actual surface.

Define N_t as the total number of range-bins and $\tilde{N}_t \leq N_t$ as the last range-bin index where the DOA, $\theta_{\tilde{N}_t}$, reaches the edges of the FOV. Also, let m and k be the range bin indices where $m,k \in \{1,\ldots,\tilde{N}_t\}$ and $m > k$. So, proceeding from equation 2.2, we can calculate θ_m as a function of θ_k and r_k, which is the range associated with range-bin index k, for a perfectly flat surface in the following way:

$$\theta_m = \pm\cos^{-1}\big(\frac{r_k}{r_m}\cos(\theta_k)\big) \tag{2.27}$$

where $r_m = r_k + (m-k)\sigma_r$. If we let θ_{ref} represent the reference DOA, which is the nadir DOA in our case, that divides the surface into two halves or modes, left and right, then $+\theta_m$ belongs to the right portion of the surface and $-\theta_m$ belongs to the left portion. Same thing holds for $\Delta\theta$.

To properly bound the estimated DOA of range-bin m, we model the prior pdf of the DOA as a truncated Gaussian random variable: $\mathscr{T}\mathscr{N}(\mu_{\theta_m}, \sigma^2_{\theta_m}, \theta_m^{(lb)}, \theta_m^{(ub)})$, where μ_{θ_m} is the mean, $\sigma^2_{\theta_m}$ is the variance, $\theta_m^{(lb)}$ is the lower bound, and $\theta_m^{(ub)}$ is the upper bound. These four parameters are derived as follows, where we show the math for the right surface mode only, which is the same for the left mode except for the sign conventions. Figure 2.11 shows a graphical view of the relationship between these four parameters.

1. Mean: let $\hat{\theta}_k$ be the estimated DOA at range-bin k. Propagating $\hat{\theta}_k$ through the transition model in equation 2.27, we can calculate the mean of the prior pdf as follows:

$$\mu_{\theta_m} = \cos^{-1}\big(\frac{r_k}{r_m}\cos(\hat{\theta}_k)\big) \tag{2.28}$$

   Note that equation 2.28 implies that the mean surface is the one produced by propagating the estimated DOAs at each range-bin to the next, and not the exact flat surface. In other words, the mean surface may not necessarily be that of the flat surface, and is usually not. This makes the tracker capable of tracking non-perfectly flat surfaces and makes the quality of the estimated surface more dependent on the quality of the data, such as SNR, than the transition model.

2. Standard deviation: define $\Delta\theta_m = \mu_{\theta_m} - \hat{\theta}_k$, then the standard deviation can be calculated as follows:

$$\sigma_{\theta_m} = \Delta\theta_m = \mu_{\theta_m} - \hat{\theta}_k \tag{2.29}$$

3. Lower bound: let a_1 be a fractional number that is close to 0, but not 0 (e.g. $a_1 = 0.1$), then the lower bound on the estimated DOA is the previously estimated DOA plus a small guard:

$$\theta_m^{(lb)} = \hat{\theta}_k + a_1\Delta\theta_m \tag{2.30}$$

   So $a_1\Delta\theta_m$ is a guard that guarantees that the estimated DOA does not turn back towards the previously estimated DOA and only expands outwards from the center (in the case of the particle filter this is true for each particle, but not for the final result). a_1 can be set to a negative value to relax this constraint.

4. Upper bound: the upper bound can be calculated as follows:

$$\theta_m^{(ub)} = \mu_{\theta_m} + f(\Delta\theta_m) \tag{2.31}$$

where

$$f(\Delta\theta_m) = -0.5569\Delta\theta_m^2 + 0.7878\Delta\theta_m + 0.0071 \tag{2.32}$$

The coefficients in equation 2.32 were derive by fitting a curve into a few reasonable points, as shown in figure 2.12. Note that the definition of $f(\Delta\theta_m)$ here is an example of how the upper guard can be st, but $f(\Delta\theta_m)$ can take any other forms, as we will see in Chapter 5.

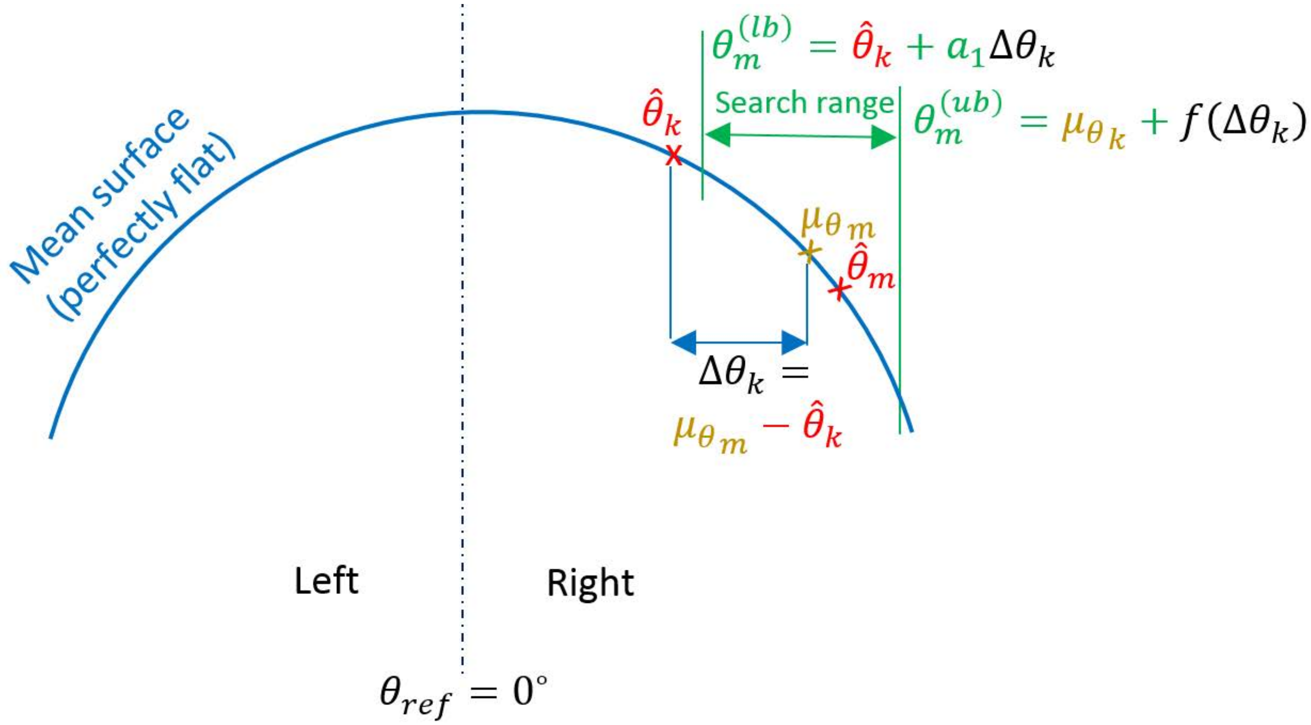
$\theta_m^{(lb)} = \hat{\theta}_k + a_1\Delta\theta_k$
$\hat{\theta}_k$
Search range
$\theta_m^{(ub)} = \mu_{\theta k} + f(\Delta\theta_k)$
Mean surface (perfectly flat)
$\mu_{\theta m}$
$\hat{\theta}_m$
$\Delta\theta_k =$
$\mu_{\theta m} - \hat{\theta}_k$
Left
Right
$\theta_{ref} = 0^\circ$

Figure 2.11: Geometric presentation of the parameters of the DOA prior pdf, which is truncated Gaussian. This figure is plotted for a perfectly flat surface for the purpose of demonstration, but this is not necessarily the case in reality.

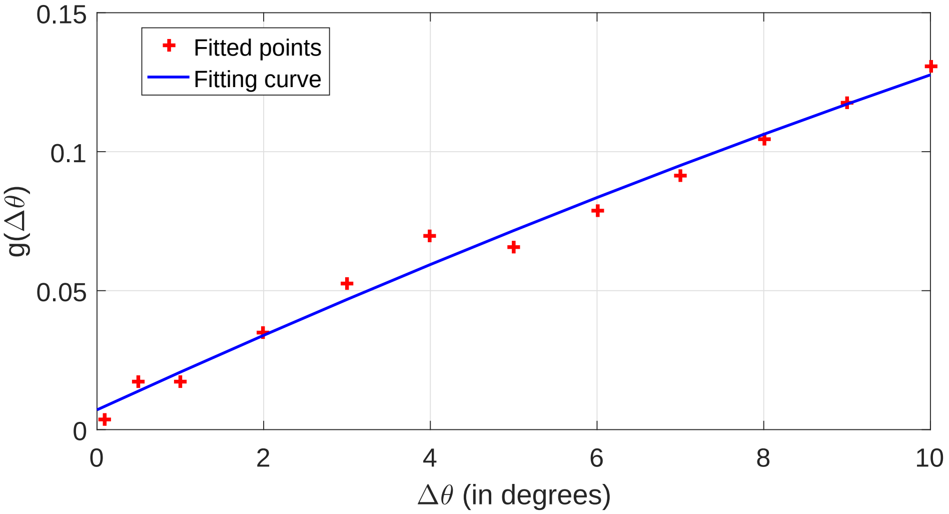

Figure 2.12: $\Delta\theta$ vs $f(\Delta\theta)$ defined in equation 2.32

To summarize, here we assume that the mean surface follows the flat earth model, where the estimated DOAs from the previous range-bin are propagated through the model in equation 2.27 to calculate the mean DOA at the next range-bin. Then, the variance and bounds of the prior pdf, which is truncated Gaussian, are calculated based on the angular distance between the mean DOA and the previously estimated DOA. In this way, the tracker can track the left and right surface modes simultaneously, but independently. Also, since the DOA bounds are determined based on $\Delta\theta$, the near-nadir DOAs (first few range-bins) will have much wider bounds than far-from-nadir DOAs (last few range-bins), which matches the physical realty, where the change in DOA reduces as a function of range (see figure 2.6). Another important point to mention here is that the suggested model can handle very low quality data scenarios (e.g. very low SNR), where the worst case scenario is that the tracker would produce a surface that is exactly the mean surface, such as in the extreme case of SNR$= -\infty$. This case is almost impossible to deal with in the case of non-iterative filters.

Note that since each range-bin has $Q \in \{0, \dots, P-1\}$ targets that share the same measurements, the ice-bottom tracking problem is an inseparable multi-target tracking problem, which is, due to the nonlinear nature of the models, a highly nonlinear problem with multimodal non-Gaussian posterior distributions. In the standard object tracking problems, each object is assumed *to send its own narrowband signal, so it is possible to decompose the problem into smaller subproblems, which is not possible in our ice-bottom tracking problem. In other words, the Q targets in each range-bin are connected via the measurements model, but separable in the transition model.*

In the following two subsections, equations 2.27 through 2.32, in addition to equation 2.8, will be used to model two Bayesian filters: the particle filter (PF) and the sequential maximum a posterior (S-MAP) filter, to estimate a radar-imaged surface at each range-line along the flight path.

2.6.5.1 Particle Filter (PF)

The Kalman filter (KF) is known for its optimality, in the mean squared-error (MSE) sense, for linear systems with a Gaussian noise distribution [46]. However, for non-linear systems, the standard KF is not guaranteed to converge due to several reasons, such as a multimodal posterior distribution that may arise from the non-linear nature of the system. The Extended Kalman filter (EKF) was introduced to handle non-linear systems, but the EKF still has the (unimodal) Gaussian noise assumption and uses a linear approximation to the non-linear system model. Because of this, it may not be able to accurately handle tracking problems for highly non-linear systems. The Unscented Kalman filter (UKF), on the other hand, can handle the non-linear systems in a better way than EKF by numerically fitting a Gaussian distribution into pregenerated samples, but it only works for unimodal noise distributions [47].

The particle filter (PF) is the most general form of a sequential filter and is capable of dealing with any mathematically defined system (i.e. linear and non-linear) and any type of posterior distribution (i.e. Gaussian and non-Gaussian, unimodal and multimodal) [48, 49]. However, unlike KF, PF approximates the posterior distribution using N samples (called particles) generated from a proposal or instrumental distribution that shares the same sample support as the actual distribution, but that is easier to draw samples from. Also, unlike the EKF, the PF uses the exact non-linear system model, which is a big advantage because it makes it possible to deal with very complex and rich dynamic models. The idea of the PF is similar to that of the UKF, but here the sample space and grid size can change adaptively over time rather than using a deterministic grid as in the case of the UKF. So, the PF sacrifices the accuracy of the posterior distribution for a better (exact) non-linear system that captures as many aspects of the problem as we want.

The PF is a sequential Monte Carlo (SMC) technique for solving the nonlinear/non-Gaussian filtering problems numerically (i.e. simulation-based method). Generally, the SMC methods are numerical solvers for integration and optimization problems [49]. But, as a sequential filter, it can also be used to adaptively track a probability distribution of a random variable, x, in signal processing problems. Given $g(x)$, $x \in \mathbb{R}^{n_x}$ for some positive integer n_x, we would like to calculate the following multidimensional integration numerically [49]:

$$I = \int g(x)dx \tag{2.33}$$

Now, if $g(x) = f(x)p(x)$ such that $p(x)$ is interpreted as a probability distribution (i.e. $p(x) \geq 0$ and $\int_{-\infty}^{\infty} p(x)dx = 1$), then equation 2.33 can be rewritten as follows:

$$I = \int g(x)dx = \int f(x)p(x)dx = \mathbb{E}_{p(x)}\{f(x)\}. \tag{2.34}$$

The Monte-Carlo (MC) estimation of the integral above is the sample mean of $f(x)$:

$$\hat{I}_N = \frac{1}{N}\sum_{i=1}^{N} f(x^{(i)}), \text{ s.t. } \{x^{(i)} : i = 1 : N\} \sim p(x), \tag{2.35}$$

where the symbol $\sim$ means 'distributed as', and i is the sample or particle index. This expression implies that $p(x)$ has the following form:

$$p(x) = \frac{1}{N}\sum_{i=1}^{N} \delta(x - x^{(i)}), \tag{2.36}$$

where $\delta(x)$ is the Dirac function.

An accurate MC estimation of the integral requires that the particles, $x^{(i)}$, be primarily drawn from regions in $f(x)$ that correspond to the high probability regions in $p(x)$. These attractive regions are called the importance sampling regions. Figure 2.13 illustrates the importance sampling region with a simple example.

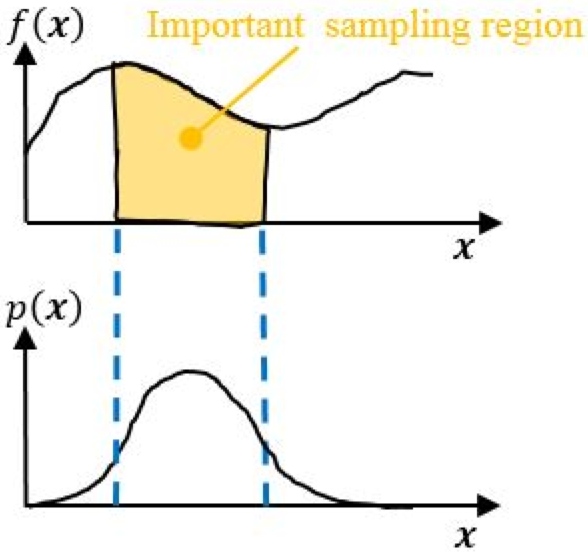

Figure 2.13: Example of an importance sampling region.

If the particles are independent, then $\hat{I}_N$ is unbiased and converges to I_N almost surely as $N \rightarrow \infty$ [49, 50]. Also, the error of MC estimates is of order $\mathscr{O}(N^{-1/2})$. This means that the rate of convergence is independent of the dimension of the integrand, n_x. This is because the particles, $x^{(i)}$, are drawn from regions of high importance to the integration result, as mentioned previously.

We separate the different concepts of the PF into sections to make the problem more tractable. We follow [49, 50] for the necessary background.

1. **Importance Sampling (IS):**

   In the Bayesian estimation context, $p(x)$ represents the posterior density. However, it is not always possible to sample effectively from $p(x)$ if it is multivariate, nonstandard, or only partially known. To solve this problem, the importance sampling (IS) technique can be used. IS suggests drawing the samples from an easy-to-sample-from proposal density $q(x)$. $q(x)$ must satisfy the following two conditions:

   (a) $q(x)$ shares the same sample support with $p(x)$ so that $q(x) > 0 \, \forall x \in \mathbb{R}^{n_x} : p(x) > 0$.

(b) $q(x)$ has a heavier tail than $p(x)$.

Starting from equation 2.33, we can proceed mathematically as follows:

$$\begin{aligned} I &= \int g(x)dx \\ &= \int f(x)p(x)dx \\ &= \int f(x)\frac{p(x)}{q(x)}q(x)dx \\ &= \int f(x)\tilde{w}(x)q(x)dx \\ &= \int \tilde{f}(x)q(x)dx \\ &= \mathbb{E}_{q(x)}\{\tilde{f}(x)\} \end{aligned} \tag{2.37}$$

such that the importance weight $0 \leq \tilde{w}(x) = \dfrac{p(x)}{q(x)} < \infty$, which can be guaranteed if the conditions on $q(x)$ are met.

Since $\int \tilde{w}(x)q(x)dx = 1$, we can estimate I and $p(x)$ as follow:

- First, rewrite I in equation 2.37 as follows:

$$I = \frac{\int f(x)\tilde{w}(x)q(x)dx}{\int \tilde{w}(x)q(x)dx} \tag{2.38}$$

- Second, estimate the numerator and denominator:

$$\begin{aligned} \hat{I}_N &= \frac{\frac{1}{N}\sum_{i=1}^{N} f(x^{(i)})\tilde{w}^{(}x^{(i)})}{\frac{1}{N}\sum_{i=1}^{N} \tilde{w}(x^{(i)})} \\ &= \sum_{i=1}^{N} f(x^{(i)})w(x^{(i)}), \text{ s.t. } \{x^{(i)} : i = 1 : N\} \sim q(x) \end{aligned} \tag{2.39}$$

where, the normalized weight $w(x^{(i)})$ is defined as:

$$w^{(i)} = \frac{\tilde{w}(x^{(i)})}{\sum_{i=1}^{N} \tilde{w}(x^{(i)})} \tag{2.40}$$

Note that since it is the ratio of two estimates, $\hat{I}_N$ is a biased estimate of I_N if N is finite, but asymptotically $\hat{I}_N$ converges to I_N almost surely.

- From equation 2.39, we can infer that the approximate (discrete) posterior density is given by the following expression:

$$p(x) = \sum_{i=1}^{N} w^{(i)} \delta(x - x^{(i)}) \tag{2.41}$$

2. **Sequential Importance Sampling (SIS)**

To apply the MC estimation method to solve nonlinear filtering problems under the Bayesian framework, the IS needs to be performed sequentially such that the particle weights at the current state are a function of the particle weights of the previous state, otherwise the filter complexity grows with each iteration. A *state* can be defined as the representation of our knowledge about tracked variables up to and including the current time step where the last received measurements are incorporated in the processing. The possible values the state variables can take are called the *state space*. Generally, every time new measurements become available, the state index is incremented by one, and the state can be updated, and thus our knowledge about the tracked variables is also updated. In our ice-bottom tracking problem, we use the PF to track the posterior density of the elevation angles given the measurements and the elevation angles estimated at the previous states. We then use this posterior density to estimate the DOAs for the current range-bin. So, these angles of arrival represent the state, which is updated over range-bins because each range bin has its own measurements and DOAs. The range-bin index is the state index. The state space, on the other hand, represents all the possible DOAs within predefined bounds (i.e. the sample support) in a given range-bin. From now on we will work on posterior probability distributions rather than general probability distributions and we will tune our discussion to our specific problem of tracking the bottom of an ice-sheet.

Let $x_{0:K} = \{x_0, \ldots, x_K\}$ represent the sensor measurements up to and including state index (or range-bin) K. x_0 is the null measurement. Also, let $\theta_{0:K} = \{\theta_0, \ldots, \theta_K\}$ represent the sequence of target states up to and including time K. θ_k is a hidden parameter inside the measurements x_k (see equation 2.6) and needs to be estimated. Then the posterior density of the target's trajectory, $p(\theta_{0:K}|x_{0:K})$ can be characterized by $\{\theta_{0:K}^{(i)}, w(\theta_{0:K}^{(i)}),\ i = 1, \ldots, N\}$:

$$p(\theta_{0:K}|x_{0:K}) = \sum_{i=1}^{N} w(\theta_{0:K}^{(i)})\ \delta(\theta_{0:K} - \theta_{0:K}^{(i)}) \tag{2.42}$$

where $w(\theta_{0:K}^{(i)}) \propto \dfrac{p(\theta_{0:K}|x_{0:K})}{q(\theta_{0:K}|x_{0:K})}$, and $\propto$ means proportional to.

If the proposal density is chosen such that

$$q(\theta_{0:K}|x_{0:K}) = q(\theta_K|\theta_{0:K-1}, x_{0:K})q(\theta_{0:K-1}|x_{0:K-1}) \tag{2.43}$$

then one can obtain samples $\theta_{0:K} \sim q(\theta_{0:K}|x_{0:K})$ by augmenting each of the existing samples $\theta_{0:K-1}^{(i)} \sim q(\theta_{0:K-1}|x_{0:K-1})$ with the new state particles $\theta_K^{(i)} \sim q(\theta_K|\theta_{0:K-1}x_{0:K})$.

The actual posterior density can also be factorized in the following way:

$$\begin{aligned} p(\theta_{0:K}|x_{0:K}) &= \frac{p(\theta_{0:K}, x_{0:K})}{p(x_{0:K})} \\ &\propto\ p(x_K|\theta_K)\ p(\theta_K|\theta_{K-1})\ p(\theta_{0:K-1}|x_{0:K-1}) \end{aligned} \tag{2.44}$$

where the normalizing constant, $p(x_{0:K})$, has been dropped. Now, by substituting the new expressions of $q(\theta_{0:K}|x_{0:K})$ and $p(\theta_{0:K}|x_{0:K})$ into $w(\theta_K)$ we obtain the following recursive update equation for the particle weights:

$$w(\theta_{0:K}^{(i)})\ \propto\ w(\theta_{0:K-1}^{(i)})\ \frac{p(x_K|\theta_K^{(i)})\ p(\theta_K^{(i)}|\theta_{K-1}^{(i)})}{q(\theta_K^{(i)}|\theta_{0:K-1}^{(i)}, x_{0:K})} \tag{2.45}$$

If we impose the Markov property, then we can assume that:

$$q(\theta_K^{(i)}|\theta_{0:K-1}^{(i)}, x_{0:K}) = q(\theta_K^{(i)}|\theta_{K-1}^{(i)}, x_K) \tag{2.46}$$

In this case, the posterior density, equation 2.42, becomes:

$$p(\theta_K|x_{0:K}) = \sum_{i=1}^{N} w(\theta_{0:K}^{(i)})\ \delta(x_K - x_K^{(i)}) \tag{2.47}$$

and the importance weight, equation 2.45, becomes:

$$w(\theta_{0:K}^{(i)})\ \propto\ w(\theta_{0:K-1}^{(i)})\ \frac{p(x_K|\theta_K^{(i)})\ p(\theta_K^{(i)}|\theta_{K-1}^{(i)})}{q(\theta_K^{(i)}|\theta_{K-1}^{(i)}, x_K)} \tag{2.48}$$

Equations 2.47 and 2.48 will be used from now on (i.e. we impose Markov assumption). Using these two equations, we can perform maximum a posterior estimation (MAP) or minimum mean squared-error (MMSE) estimation. We also consider a mixture of the two which we call quasi-MAP estimation. Note that the particles are vectors of length Q (DOAs for the number of targets in the considered range-bin) so that operations on particles by an estimator, operate on the whole vector.

- **MMSE estimation:**

  The MMSE estimator is the expected value (or weighted sum) over the sample support. Mathematically, it can be stated as follows:

  $$\hat{\theta}_K = \mathbb{E}_{p(\theta_K|x_{0:K})}(\theta_K) = \sum_{i=1}^{N} \theta_K^{(i)} w(\theta_{0:K}^{(i)}) \tag{2.49}$$

  Since MMSE estimation is the weighted sum of N particles, its result is not guaranteed to be in the sample space if the space is noncontiguous. This is not an issue for our problem because the space is contiguous. Also, if the posterior density has a multimodal nature, MMSE may give an answer that is not in the importance sampling region (low probability answer).

- **MAP estimation:**

  The MAP estimator chooses the particle that corresponds to the maximum weight among all particles of the sample support. This is equivalent to the particle with DOAs that maximize the posterior density, and can be stated as follows:

$$\hat{\theta}_K = \underset{\theta_K^{(i)}}{\arg\max}\ p(\theta_K|x_{0:K}),\ \ i \in \{1,\ldots,N\} \tag{2.50}$$

  Since only one particle is chosen out of the N particles, MAP estimation can result in a poorer answer than MMSE. However, the answer is always a sample in the sample support (i.e. it is not possible for the answer to be outside the predefined sample space because the answer is a valid particle). Also, the MAP estimator handles multimodal posterior distributions well.

- **Quasi-MAP estimation:**

  Since there are usually several particles that have large weights relative to the other particles, involving all of these highly-weighted particles in the estimation process is expected to produce a better result than MAP. We introduce the quasi-MAP estimation as a way to improve the estimated DOA of MAP and as a solution to the modal problem that MMSE estimation has. This is a very simple solution that may fail for equally weighted modal posterior distributions because it takes the (non-weighted) average of the particles that correspond to the largest n percent of the weights, where n could be any reasonably small value, such as 5 or 10.

In summary, in the PF framework, we draw samples (or particles) from a proposal distribution, then assign weights to each particle based on how important this particle is to the estimation result. As new data arrive, we update our beliefs on the importance of these particles by updating their associated weights.

Note about MAP vs MMSE for DOA estimation under the PF framework:

Since each particle has its own truncated Gaussian pdf and is propagated separately through a nonlinear dynamics model, the particles usually span a wide angular window around the mean surface, which makes it difficult or impossible to set a single DOA bound that is shared among all the particles. Because of this, the probability of having outlier particles is non-trivial. Also, it is possible that the estimated DOAs for one step could be lower in magnitude than the previously estimated DOAs (which we generally consider to be physically unrealistic since it suggests that a target is in the radar shadow of a previous target. Using S-MAP (next section), it is possible . Since in the case of MMSE all the particles participate, each based on its weight, in the calculation of the final answer, MMSE is the best option for DOA estimation with PF for our application, which will also be confirmed by the simulation results presented in Chapter 4.

Another important point to mention is that if the posterior pdf has a multimodal nature, where there is more than one peak in the pdf, then MAP is a better choice than MMSE for PF parameter estimation. This is because the MMSE estimator may give a solution that has low probability (e.g. average of two peaks). For this reason, the literature generally recommends MAP over MMSE in the PF context since PFs are often used for multimodal distributions. Although, our distribution can be multimodal, the particular parameters chosen result in distributions which are unimodal. This could be due to our specific choice of the Gaussian prior pdf and/or the angular bounds over which the posterior pdf fits are small.

3. **Sequential Importance Sampling Resampling (SISR):**

With SIS, the high-weight particles tend to be rewarded and gain more weight over time. However, low-weight particles tend to be penalized and lose weight over time until they are effectively zero weight. The extreme case is when one particle survives and all other particles die. That is $w(\theta_K^{(i)}) = 1$ and $w(\theta_K^{(j)}) = 0 \ \forall i \neq j$. This degeneracy problem is generally impossible to avoid in the SIS framework.

Since the degeneracy problem basically means that the variance of the weights increases over time, the degeneracy can be approximated by calculating the effective number of particles, N_{eff}, using the following expression:

$$N_{eff} \approx \frac{1}{\sum_{i=1}^{N} \left(w(\theta_k^{(i)})\right)^2} \tag{2.51}$$

The ideal case is when $N_{eff} = N$ (i.e. $w(x_k^{(i)}) = \frac{1}{N}$, $\forall i = 1,\dots,N$), and the worst case is when $N_{eff} = 1$ (i.e. $w(x_k^{(i)}) = 1$ and $w(x_k^{(j)}) = 0 \; \forall i \neq j$).

The sequential importance sampling resampling (SISR) is introduced in the literature as a solution to the degeneracy problem of the PF. Figure 2.14 shows how the SISR works. If the degeneracy criteria is met, then the particles are resampled such that the low weight particles are removed and the high weight particles are multiplied based on their weights. The total number of particles can be kept the same after the resampling step, where all the particles are equally weighted after this step (i.e. $w(\theta_k^{(i)}) = 1/N$, $\forall i = 1,\dots,N$).

Even though SISR solves the degeneracy problem of the PF, it introduces the following new problems:

- SISR may lead to a sample impoverishment (or lack of sample diversity) problem, where some particles are selected several times. The extreme case is when all the particles are exactly the same, which is a very poor representation of the actual posterior density. There are many solutions in the literature to this problem, such as adding a regularization step (the regularized PF) or making an informed particles move (Markov-Chain Monte Carlo (MCMC) move step PF).

- Although the weights are reset, the new distribution of particles captures the previous weights by more densely sampling particles with high weight. Nonetheless, the resampling step introduces some noise into the estimate and a drop in performance is expected after resampling. On the other hand, the PF will be able to produce better estimates in future iterations because the particles should be more densely sampled in the importance sampling region.

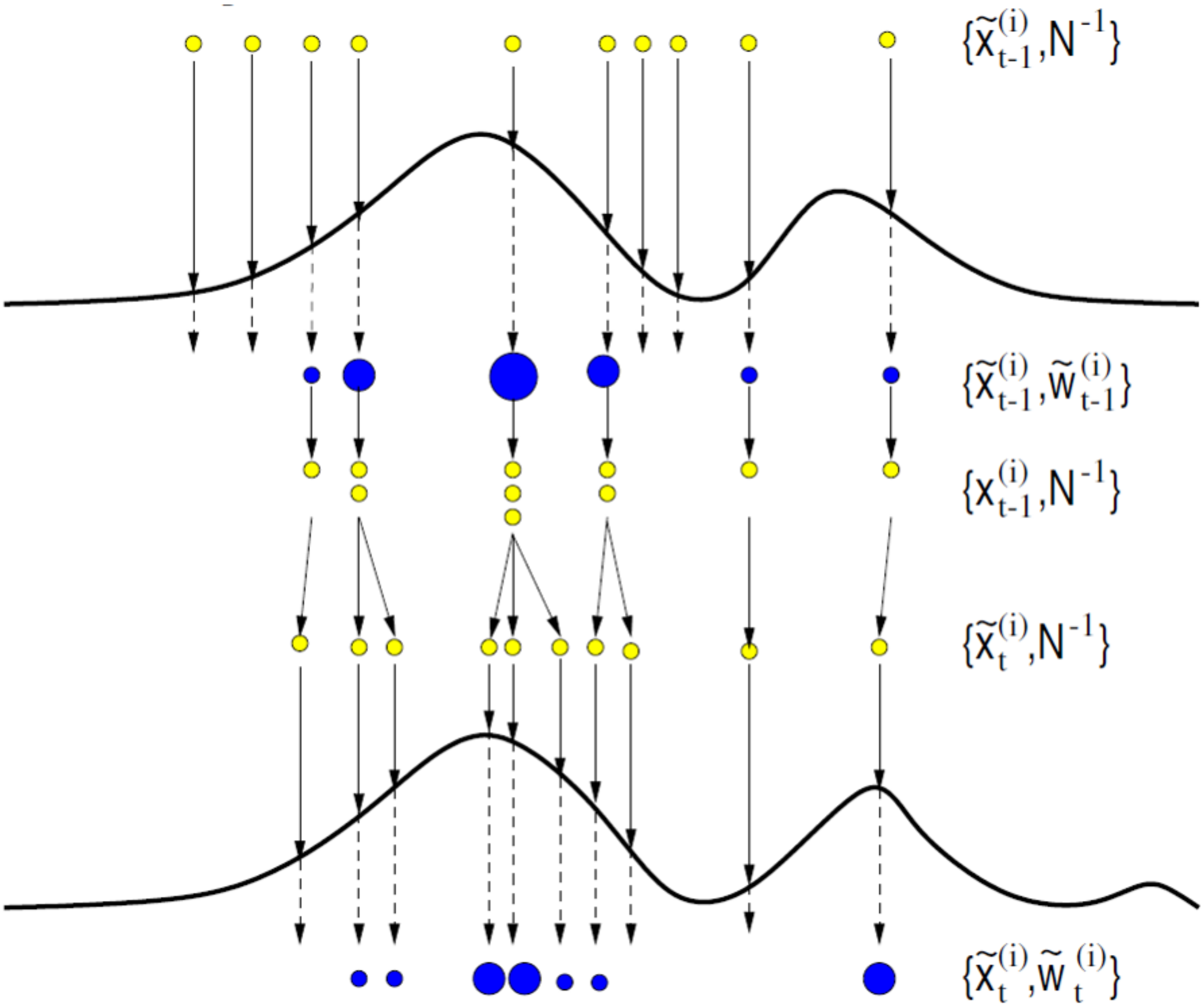
$\{\tilde{x}_{t-1}^{(i)}, N^{-1}\}$
$\{\tilde{x}_{t-1}^{(i)}, \tilde{w}_{t-1}^{(i)}\}$
$\{x_{t-1}^{(i)}, N^{-1}\}$
$\{\tilde{x}_{t}^{(i)}, N^{-1}\}$
$\{\tilde{x}_{t}^{(i)}, \tilde{w}_{t}^{(i)}\}$

Figure 2.14: Sequential importance sampling resampling (SISR) [50]

4. **PF algorithm:**

We now introduce the PF algorithm in Algorithm 1.

Algorithm 1: PF steps

```
Given the resampling threshold, $N_{thr}$, and the initial posterior density, $p(\theta_0)$.

(a) Initialization: $k = 0$
    For $i = 1 : N$
        Sample $\theta_0^{(i)} \sim p(\theta_0)$
    End for

(b) IS step:
    For $i = 1 : N$
        - Draw $\theta_0^{(i)} \sim q(\theta_k^{(i)}|\theta_{k-1}^{(i)}, x_k)$
        - Evaluate $\tilde{w}(\theta_k^{(i)}) = w(\theta_{k-1}^{(i)}) \frac{p(x_k|\theta_k^{(i)})\, p(\theta_k^{(i)}|\theta_{k-1}^{(i)})}{q(\theta_k^{(i)}|\theta_{k-1}^{(i)}, x_k)}$
    End For

(c) Normalize the importance weights:
    For $i = 1 : N$
        $w(\theta_k^{(i)}) = \frac{\tilde{w}(\theta_k^{(i)})}{\sum_{j=1}^{N} \tilde{w}(\theta_k^{(j)})}$
    End For

(d) Resampling step:
    If $N_{eff} < N_{thr}$, resample the $N$ particles with replacement according to their importance weights.

(e) Set $k \rightarrow k+1$ and go to step 2.
```

5. **Other versions of the PF:**

   There are two main extensions to the PF in the literature. These are the regularized PF (RPF) and the Markov-Chain Monte Carlo (MCMC) move-step PF. They differ from the main PF framework in the resampling step. In both extensions, a random set of samples is generated from a predefined kernel and added to the previous particle's system to generate the new one (i.e. jittering). This jittering step is called regularization. In MCMC move-step PF there is an additional step: accept the new particle only if its associated acceptance probability meets a certain threshold. The goal is to improve the sample diversity of the particle's system, where loss of diversity could happen due to the resampling step. MCMC move-step PF is, theoretically, guaranteed to converge to the true posterior, while the RPF is not. For our surface-tracking application, we use the standard PF because, by doing some tests, we did not see a noticeable difference when the modified PF is used.

6. **PF model for DOA tracking problem:**

   Like any Sequential Bayesian filtering problem, the PF requires a model for the measured data, which relates the measurements to the tracked parameter, and another model for the dynamics of the states, which relates the results of one state to the next. These equations can be described as follows:

   - The measurements model :

     The measurements model is given in equation 2.8, but we restate it here for a single range-bin, k, case:

     $$\mathbf{X}_k = \mathbf{A}(\boldsymbol{\theta}_k)\mathbf{S}_k + \mathbf{N}_k \tag{2.52}$$

     where $\boldsymbol{\theta}_k$ is bold faced to emphasize that it is a vector of length Q_k. The MLE (and also the least squares) estimation of the target's backscatter signal is given by the following expression [39]:

     $$\hat{\mathbf{s}}_k(m) = \left(\mathbf{A}(\boldsymbol{\theta}_k)^H \, \mathbf{A}(\boldsymbol{\theta}_k)\right)^{-1} \mathbf{A}(\boldsymbol{\theta}_k)^H \, \mathbf{x}_k(m) \tag{2.53}$$

where $m \in 1, 2, \ldots M$ is the m^{th} snapshot. The noise variance can be estimated as the average of the noise subspace eigenvalues [39]. From Section 2.3 we know that the noise has a complex Gaussian distribution. So, using equation 2.53, the complex likelihood density function can now be written as follows:

$$p(\mathbf{X}_k|\boldsymbol{\theta}_k) = \prod_{m=1}^{M} (\pi\sigma_n^2)^{-P} \exp\left\{ -\frac{||\mathbf{P}^{\perp}_{\mathbf{A}(\boldsymbol{\theta}_k)}\mathbf{x}_k(m)||^2}{\sigma_n^2} \right\} \tag{2.54}$$

Since the likelihood value is always ≤ 1, $p(\mathbf{X}_k|\boldsymbol{\theta}_k)$ can be extremely small if M is large. Although it is possible to represent the PF in the log domain, we take the mean of the likelihood densities for each snapshot rather than the product as follows to deal with the dynamic range problem:

$$p(\mathbf{X}_k|\boldsymbol{\theta}_k) = \frac{1}{M} \sum_{m=1}^{M} (\pi\sigma_n^2)^{-P} \exp\left\{ -\frac{||\mathbf{P}^{\perp}_{\mathbf{A}(\boldsymbol{\theta}_k)}\mathbf{x}_k(m)||^2}{\sigma_n^2} \right\} \tag{2.55}$$

- The transition model:

  The transition model was described previously in equations 2.27 through 2.32 and figure 2.11.

The PF multi-target transition algorithm:

Since the maximum number of targets is assumed to be 2 (maximum of 1 target on each side of the surface), the transition model should be able to handle the transition from 0, 1, or 2 DOAs at one state to 0, 1, or 2 DOAs at the next state. This is done using Algorithm 2, which is implemented as part of the SIS step. The main issues are 1) how to determine which side has a target when there is only one target, 2) how to update the active side (target), and 3) how to update the inactive side (no target).

Algorithm 2: PF transition algorithm

(a) If $Q_k = 1$ (cases $1 \rightarrow 1$ and $2 \rightarrow 1$)

- Define, LL_{left} and LL_{right}, to be the log likelihood sum over all particles for the left-side targets and the right-side targets respectively.
- Whichever side has a higher LL is chosen as the active side. The particle weights are updated with the likelihood function for the active side. The estimation is done with the active side targets only.
- The inactive side of each particle is still updated using the transition model, but this side has no impact on the weights or the estimation.

(b) If $Q_k = 2$ (cases $1 \rightarrow 2$ and $2 \rightarrow 2$)

- This is the nominal flow of the PF, so no additional step is required here.

Note that the particles are represented by a matrix of dimension $N \times 2$, where the first column belongs to the left-side target distribution and the second column belongs to the right-side target distribution. Also, the case of $Q_k = 0$ is skipped as no DOA estimation is required in this case. To decide on the left and right portions of the surface, we can use the nadir DOA as a reference.

Choosing the proposal density:

There are different ways to choose the proposal density. Deriving the optimal proposal density makes it too complex to draw samples when the number of snapshots, M, is more than 1. In this work we choose the prior density to be the proposal density: $q(\boldsymbol{\theta}_k|\boldsymbol{\theta}_{k-1}, \mathbf{x}_k) = p(\boldsymbol{\theta}_k|\boldsymbol{\theta}_{k-1})$. Thus, from equation 2.48, the normalized importance weights of the particles now become:

$$w(\boldsymbol{\theta}_k^{(i)}) = w(\boldsymbol{\theta}_{k-1}^{(i)})\ p(\mathbf{X}_k|\boldsymbol{\theta}_k^{(i)}) \tag{2.56}$$

2.6.5.2 Sequential Maximum A Posteriori Estimation (S-MAP)

Sequential MAP (S-MAP) is another type of sequential filters that we used to estimate the ice-bottom surface. Unlike PF, here we track the DOAs directly (in the case of PF we track the posterior pdf of the DOAs, and then estimate the DOAs using the estimated pdf) using a cost function that has two components: the MLE cost function (discussed in section 2.6.2) and the truncated Gaussian prior pdf, where the truncation of the Gaussian pdf is performed as part of a bounded minimization problem. The parameters of the truncated Gaussian pdf were discussed in equations 2.27 through 2.32 and depicted in figure 2.11. The S-MAP optimizer is initialized by the mean DOA, μ_{θ_m}, which is defined in equation 2.28.

The multivariate prior Gaussian pdf is given by the following expression:

$$f(\boldsymbol{\theta}) = \frac{1}{\sqrt{\det(2\pi\mathbf{R}_\theta)}} \exp\big(-\frac{1}{2}(\boldsymbol{\theta}-\boldsymbol{\mu}_\theta)^T\mathbf{R}_\theta^{-1}(\boldsymbol{\theta}-\boldsymbol{\mu}_\theta)\big) \tag{2.57}$$

where $\mathbf{R}_\theta \in \mathbb{R}^{Q\times Q}$ is the covariance matrix of the DOA vector, and it is diagonal because the targets are assumed to be independent in the transition model (in the measurements model, the targets of the same range-bin are not independent). Taking the natural logarithm of equation 2.57, we get the following log-prior cost function:

$$\mathbf{J}_\theta = -Q\log(2\pi) - \sum_{q=1}^{Q}\log(\sigma_{\theta_q}^2) - \frac{1}{2}(\boldsymbol{\theta}-\boldsymbol{\mu}_\theta)^T\mathbf{R}_\theta^{-1}(\boldsymbol{\theta}-\boldsymbol{\mu}_\theta) \tag{2.58}$$

The log-likelihood cost function can be obtained by taking the natural logarithm of equation 2.9 as follows:

$$\mathbf{J}_x = -M\log(\pi) - Mp\log(\sigma_n^2) - \frac{1}{\sigma_n^2}\sum_{i=1}^{M}||\mathbf{x}_i - \boldsymbol{A}(\boldsymbol{\theta})\mathbf{s}_i||^2 \tag{2.59}$$

Now, the MAP cost function is the sum of the log-prior and log likelihood cost functions. Mathematically, this can be written as follows:

$$\begin{aligned}\mathbf{J} &= \mathbf{J}_x + \mathbf{J}_\theta \\ &= c_1 - Mp\log(\sigma_n^2) - \frac{1}{\sigma_n^2}\sum_{i=1}^{M}||\mathbf{x}_i - \mathbf{A}(\boldsymbol{\theta})\mathbf{s}_i||^2 - \frac{1}{2}(\boldsymbol{\theta}-\boldsymbol{\mu}_\theta)^T\mathbf{R}_\theta^{-1}(\boldsymbol{\theta}-\boldsymbol{\mu}_\theta) \qquad (2.60)\end{aligned}$$

where $c_1 = -M\log(\pi) - Q\log(2\pi) - \sum_{q=1}^{Q}\log(\sigma_{\theta_q}^2)$ lumps together all the constants that are not function of $\boldsymbol{\theta}$.

Fixing $\boldsymbol{\theta}$ and $\mathbf{s}$, the noise variance, σ_n^2, that maximizes the cost function in equation 2.60 can be estimated as follows:

$$\hat{\sigma_n^2} = \frac{1}{MP}\sum_{i=1}^{M}||\mathbf{x}_i - \mathbf{A}(\boldsymbol{\theta})\mathbf{s}_i||^2 \qquad (2.61)$$

Now to estimate the backscatter signal, $\hat{\mathbf{s}}$, we substitute $\hat{\sigma_\theta^2}$ back into equation 2.60, and we fix $\boldsymbol{\theta}$ and minimize the MAP cost function with respect to $\mathbf{s}$. The result is as follows:

$$\hat{\mathbf{s}}_i = \left(\mathbf{A}^H(\boldsymbol{\theta})\mathbf{A}(\boldsymbol{\theta})\right)^{-1}\mathbf{A}^H(\boldsymbol{\theta})\mathbf{x}_i \qquad (2.62)$$

Note that equations 2.61 and 2.62 were also derived in [39] for the case of deterministic MLE estimation. Now our derivation and the MLE derivation starts to diverge.

Substituting equations 2.61 and 2.62 back into equation 2.60, we get the following expression:

$$\mathbf{J} = c - Mp\log\left(\frac{1}{Mp}\sum_{i=1}^{M}||\mathbf{x}_i - \mathbf{P}_A\mathbf{x}_i||^2\right) - \frac{1}{2}(\boldsymbol{\theta}-\boldsymbol{\mu}_\theta)^T\mathbf{R}_\theta^{-1}(\boldsymbol{\theta}-\boldsymbol{\mu}_\theta) \qquad (2.63)$$

where $c = c_1 - Mp$. So, the S-MAP optimization problem can be stated as follows:

$$\begin{aligned}\hat{\boldsymbol{\theta}} &= \arg\max_{\boldsymbol{\theta}}(\mathbf{J}) \\ &\text{s.t.} \quad \boldsymbol{\theta}^{(lb)} \leq \hat{\boldsymbol{\theta}} \leq \boldsymbol{\theta}^{(ub)} \qquad (2.64)\end{aligned}$$

where the bounds are updated sequentially at each state. The first part of the above equation can also be written as follows:

$$
\begin{aligned}
\hat{\boldsymbol{\theta}} &= \arg\max_{\boldsymbol{\theta}}(\mathbf{J}) \\
&= \arg\min_{\boldsymbol{\theta}}(-\mathbf{J}) \\
&= \arg\min_{\boldsymbol{\theta}}\Big\{Mp\log\Big(\frac{1}{Mp}\sum_{i=1}^{M}||\mathbf{P}_A^{\perp}\mathbf{x}_i||^2\Big)+\frac{1}{2}(\boldsymbol{\theta}-\boldsymbol{\mu}_\theta)^T\mathbf{R}_\theta^{-1}(\boldsymbol{\theta}-\boldsymbol{\mu}_\theta)\Big\} \\
&= \arg\min_{\boldsymbol{\theta}}\Big\{Mp\log\Big(\frac{1}{p}\mathrm{Tr}(\mathbf{P}_A^{\perp}\mathbf{R})\Big)+\frac{1}{2}(\boldsymbol{\theta}-\boldsymbol{\mu}_\theta)^T\mathbf{R}_\theta^{-1}(\boldsymbol{\theta}-\boldsymbol{\mu}_\theta)\Big\} \\
&= \arg\min_{\boldsymbol{\theta}}\Big\{Mp\log\Big(\mathrm{Tr}(\mathbf{P}_A^{\perp}\mathbf{R})\Big)+\frac{1}{2}(\boldsymbol{\theta}-\boldsymbol{\mu}_\theta)^T\mathbf{R}_\theta^{-1}(\boldsymbol{\theta}-\boldsymbol{\mu}_\theta)\Big\}
\end{aligned}
\tag{2.65}
$$

The first term in equation 2.65 is equivalent to the MLE cost function, $\mathbf{J}_{\text{mle}}$, which was defined in equation 2.20, while the second term is the prior cost function, $\mathbf{J}_{\text{prior}}$. So, the estimated DOA is the one that balances 1) the minimization of the projection of the measurements onto the null of the subspace spanned by the steering vectors and 2) the minimization of the angular distance between the estimated DOA and the mean DOA. Roughly speaking, $\boldsymbol{J}_{prior}$ dominates the result when the data quality are low and $\boldsymbol{J}_{mle}$ is a weak function of $\boldsymbol{\theta}$. In the extreme case of no signal, $\hat{\boldsymbol{\theta}} \approx \boldsymbol{\mu}_\theta$. If the data quality are high enough, $\boldsymbol{J}_{mle}$ will likely have a large Hessian and dominate the cost function.

There are a few other points worth mentioning. First, we assume that there is a maximum of 2 sources in each range-bin, one on the left ice-bed interface and the other on the right ice-bed interface. Second, the posterior pdf is not Gaussian in $\boldsymbol{\theta}$ so that the S-MAP and the MMSE PF results in Chapter 4 will potentially give different optimal answers from each other.

2.7 Steering Vectors Estimation and Array Calibration

Array imperfections can be divided into three categories: phase, gain, and array sensor location errors. Each of these types can have different effect on the performance of the beamformer/estimator, and thus there are different ways of handling each type. Also, different beamformers/estimators react differently to these errors. For example, the linearly-constrained minimum variance (LCMV) beamformer is very sensitive to the three types of errors [51]. For this reason, in addition to their simplicity, the performance of the LCMV-like beamformers have been extensively studied in the literature and several approaches have been presented to alleviate the effects of these errors [35, 52].

Since all of the beamformers and estimators discussed this dissertation depend on the eigenstructure of the data covariance matrix, which is a function of the array manifold matrix, these methods are affected by perturbations in the sensors and the following circuitry. So, these errors should be compensated for to improve the DOA estimation.

Most of the literature that tackles the array calibration problem focuses only on a beamformer and/or an estimator performance and behavior in the presence of array and system perturbations. Very few references address how to estimate these errors and compensate for them. Here, we classify previous work and give a summary on some example references:

1. **Estimation of (and compensation for) the perturbation errors:**

    a) [53]: Here, the authors suggest a way to estimate the array phase and gain errors, but they do not treat sensor location errors separately (i.e. treated as phase errors), and require the DOA and number of targets to be known a priori. To estimate the actual steering matrix, the authors solve the following least-squares (LS) optimization problem:

    $$\min_{\boldsymbol{\theta}} ||\mathbf{P}_{U_S}\mathbf{A}(\boldsymbol{\theta}) - \mathbf{A}(\boldsymbol{\theta})||^2 \tag{2.66}$$

    where $\mathbf{P}_{U_S} = \mathbf{U}_S(\mathbf{U}_S^H\mathbf{U}_S)^{-1}\mathbf{U}_S^H$. Also, the authors claim that the phase and gain errors can lead to the cancellation of the desired signal rather than the interference signal in the case of the LCMV beamformer.

    b) [54]: Here, the authors suggest a way to estimate the phase and gain errors and sensor location errors simultaneously through an iterative 2-step algorithm and an additional step that takes care of the residual errors. The cost function to be minimized is:

$$\mathbf{J} = \mathbf{A}^H(\boldsymbol{\theta})\mathbf{U}_N\mathbf{U}_N^H\mathbf{A}(\boldsymbol{\theta}) \tag{2.67}$$

The algorithm steps are :

1. Define the position error vector as ΔX . The estimation algorithm comprises two steps. In the first step, fixing ΔX (initial value is zero), we estimate the gain and phase errors of each array element. In the second step, using the results from the first step, i.e., holding the gain and phase errors fixed, ΔX is estimated. The algorithm iterates alternatively between the two steps until it converges.
2. Once the steering matrix, $\hat{\mathbf{A}}(\boldsymbol{\theta})$, is estimated, project it onto $\mathbf{U}_S$ to reduce the effects of the residual errors due to the inaccurate noise subspace estimation.

   As explained in section 2.6.2, MLE cost function does the projection onto the signal subspace and away from the noise subspace simultaneously rather than separately here.

c) [55]: Here the authors suggest a self-calibration algorithm based on MLE. It estimates both the DOAs and the sensor locations simultaneously. Here is how this method works: In the first step, the DOAs are estimated using the nominal sensor locations. Then using these DOAs, the sensor locations are estimated, and the process repeats until the algorithm converges.

Note that this algorithm is more robust and more complicated than the algorithms given above. However, it neglects the phase and gain errors. Also, the number of targets is assumed to be known. In addition, the algorithm is computationally expensive because for each set of sensor locations we need to iterate until the convergence condition is satisfied. Then we need to use these DOAs to iteratively estimate the sensors locations, and the process repeats. Each step in each iteration is generally a multidimensional nonlinear search.

2. **Optimal diagonal loading to handle the effect of random steering errors:**

   a) [56]: Here the authors suggest a *negative* diagonal loading to reduce the effects of array steering errors for the beamformers of the form:

   $$\mathbf{w} = (\mathbf{R} + \gamma\mathbf{I})^{-1}\mathbf{a}(\theta) \tag{2.68}$$

   where $\mathbf{w}$ is the weight vector and $\mathbf{I}$ is the identity matrix. LCMV beamformers are of this type. The optimal diagonal loading is:

   $$\gamma_{opt} = -(\sigma_n^2 + \sigma_s^2||\mathbf{a}(\theta)||^2) = -(\sigma_n^2 + \sigma_s^2 P) \tag{2.69}$$

   where σ_n^2 is the noise power, and σ_s^2 is the signal power. γ_{opt} provides a rough order of magnitude of the optimal loading level.

   b) [35]: Van Trees also suggests the use of diagonal loading to improve the sensitivity of the minimum power distortionless response (MPDR) beamformer to array perturbations. But the problem is that this loading can reduce the SINR as well.

3. **Study of the effect of array errors onto SINR and array weights (for MVDR/MPDR beamformers):**

   References [57, 58, 59], among many others, give a detailed analysis for the effect of system and array imperfections on the performance of MVDR-like beamformers. They are good for understanding the problem, but they do not offer solutions to the problem.

Note that using the MLE cost function (equation 2.19) can alleviate some of the array imperfections. This is because it does simultaneously two projections: onto the signal subspace and away from the noise subspace. Thus, we use MLE cost function not only for DOA estimation, but also for array calibration. Note that MLE is superior to MUSIC in this regard. For MUSIC, we only seek the DOAs that make the noise subspace orthogonal to the steering vectors. MUSIC cost function doesn't utilize the signal subspace and noise subspace simultaneously as MLE does. Thus, MLE is more robust to array-errors than MUSIC [55].

We have developed an MLE-based cost function to estimate the gain, phase, and location errors from the 2D data of the SAR imagery. [1] has good details on the technique, but here we will explain the method briefly and elaborate on the modifications we added to the model.

The sensors gain error is modeled as a function of the DOA using three parameters that control the shape, size, and orientation of the gain pattern of each sensor. So, the gain model for sensor p can be written, in dB, as follows:

$$\mathbf{g}_p^{(\mathrm{dB})}(\theta_q) = \alpha_{pS}\big(\sin(\theta_q) - \sin(\alpha_{p\theta})\big)^2 + \alpha_{pD} \tag{2.70}$$

where α_{pS} controls the size of the gain pattern, $\alpha_{p\theta}$, measured in radians, controls the shape and orientation (or peak location) of the gain pattern, and α_{pD} controls the deviation (up or down) of the gain pattern of the p^{th} sensor relative to the other sensors. The nominal values of these three parameters are zeros. However, to estimate $\alpha_{p\theta}$, then α_{pS} should not be set to zero and its nominal value becomes $\alpha_{pS} = 1$. In linear scale, the gain error becomes $\mathbf{g}_p(\theta_q) = 10^{\frac{\mathbf{g}_p^{(\mathrm{dB})}(\theta_q)}{20}}$.

The sensors location and phase offset (DC) errors for sensor p are modeled as a phase term in the following way (also a function of the DOA):

$$\boldsymbol{\phi}_p(\theta_q) = \exp\Big\{-j\big(k\Delta_{py}\sin(\theta_q) - k\Delta_{pz}\cos(\theta_q) + \Delta_{p\theta}\big)\Big\} \tag{2.71}$$

where Δ_{py} and Δ_{pz} are the location errors along y and z dimensions, respectively. $\Delta_{p\theta}$ is the phase deviation or DC phase offset.

Combining the gain and phase error models, the final error model of the p^{th} sensor in the direction θ_q now becomes as follows:

$$\eth_p(\theta_q) = \mathbf{g}_p(\theta_q) \times \boldsymbol{\phi}_p(\theta_q) \tag{2.72}$$

The new steering matrix can be written as the Hadamard product (i.e. element-wise product) between the ideal steering matrix, which is defined in equation 2.7, and the error matrix, which is defined above.

The cost function to be maximized is a superposition of the log-likelihood cost functions of the N_t range-bins in a given range-line. So, we seek the array errors that maximizes the following MLE-based cost function:

$$\hat{\eth} = \arg\max_{\eth} \sum_{t=1}^{N_t} \mathrm{Tr}\left(\mathbf{P}_{\mathbf{A}(\boldsymbol{\theta}_t)} \hat{\mathbf{R}}_t\right) \tag{2.73}$$

where Tr is the trace operator. Note that $\mathbf{A}(\boldsymbol{\theta}_t)$ is now the perturbed steering matrix, not the ideal.

Figures 2.15 and 2.16 show, respectively, an example of the gain and phase deviation patterns from simulation data for a practical error values of 7 linearly spaced sensors receiving 100 snapshots with 30dB SNR. Note that these errors are measured relative to the first sensor.

The gain errors represent the amount of mismatch between the isotropic pattern of the ideal sensors and the actual patters. On the other hand, the phase errors don't affect the gain pattern of the individual sensors, but rather affect the array factor.

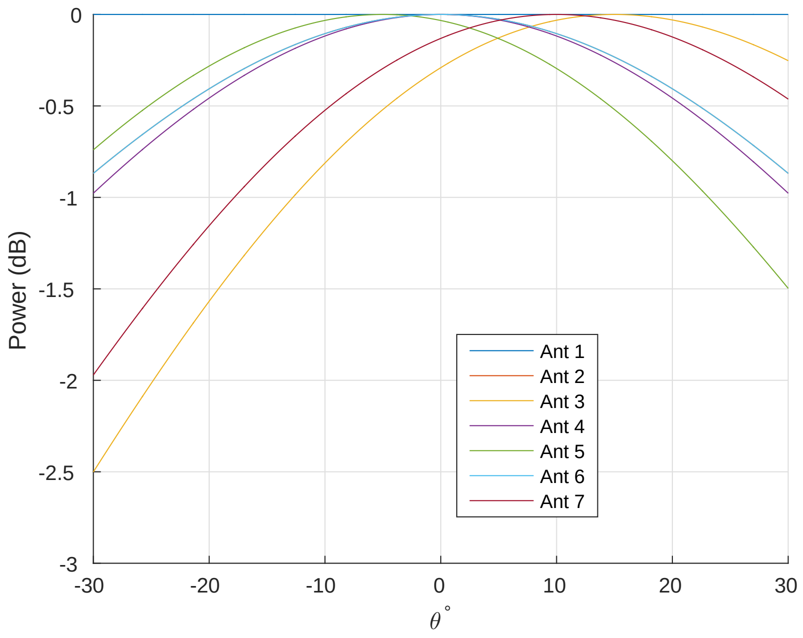

Figure 2.15: Sensors gain pattern

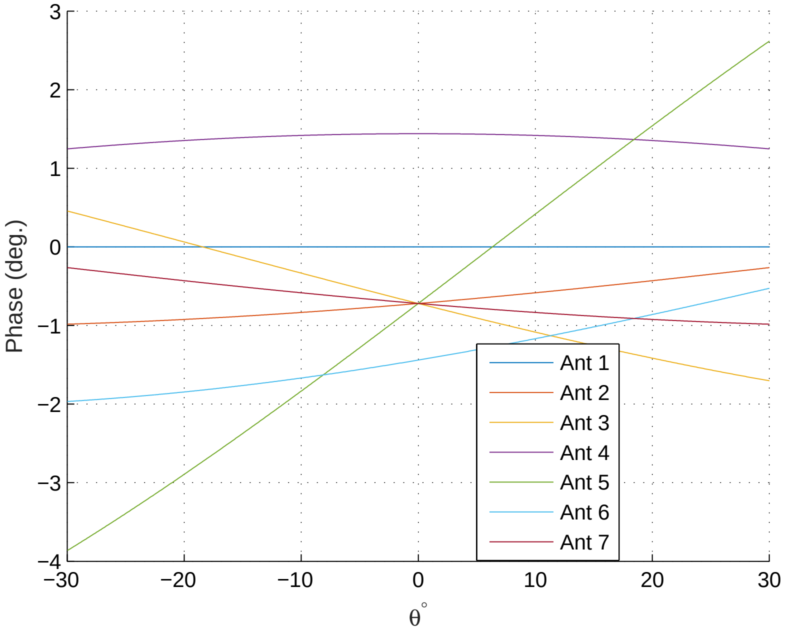

Figure 2.16: Sensors phase deviation pattern

2.8 Specifications of the Radars Used in This Work

In this section we describe the properties and parameters of the radar data used in this work.

The airborne Multichannel Coherent Radar Depth Sounder (MCoRDS), developed at the University of Kansas, was used to collect data for several of the results presented in this work. The MUSIC results in Chapter 5 were collected over the Canadian Arctic Archipelago (CAA), in 2014. Figure 2.17 a shows the transmit configuration for the CAA data collection. Three time division multiplexed beams are formed and a separate SAR image is formed for each beam. The S-MAP results in Chapter 5 are collected in a nadir-only beam configuration. Figure 2.17 b shows the 3D SAR resolution. The antenna system is composed of 15 sensors divided into three subarrays: 1) the center subarray, which is mounted on the fuselage, is composed of 7 sensors used for transmit and receive, 2) the left/right subarrays, which are mounted on the left/right wings respectively, are each composed of 4 receive-only sensors. These three subarrays are separated by substantial baselines. So, to avoid the grating lobes or ambiguities that occur when using all 15 elements, we only make use of the 7 receive elements of the center subarray, which has a length of 4.5 m. Figure

2.18 shows the geometry of this array in the y-z plane.

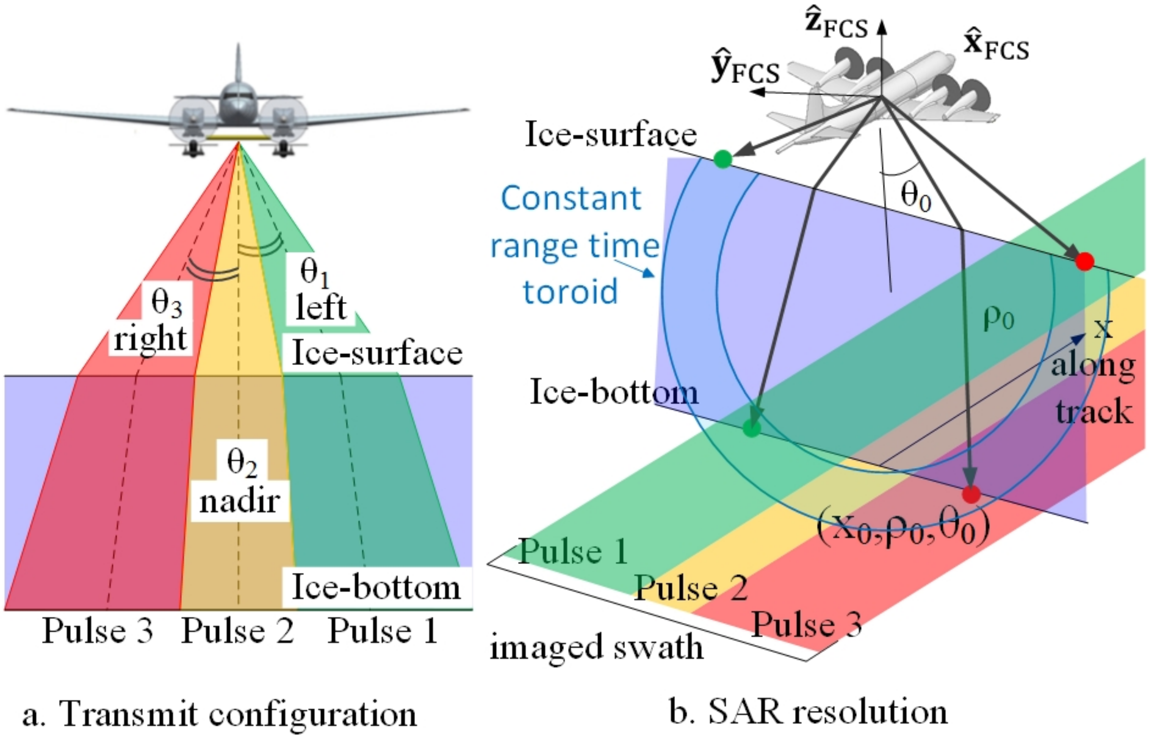

Figure 2.17: Transmit configuration of the P-3 radar. a) Shows the time multiplexed multi-beam mode of the radar, which results in a large imaged swath. b) Shows a single SAR image pixel after pulse compression and SAR processing, where the 3D scene is resolved into toroids with constant along-track and constant range that are centered on the flight path. The targets lying in a particular toroid need to be resolved by estimating their respective elevation angles.

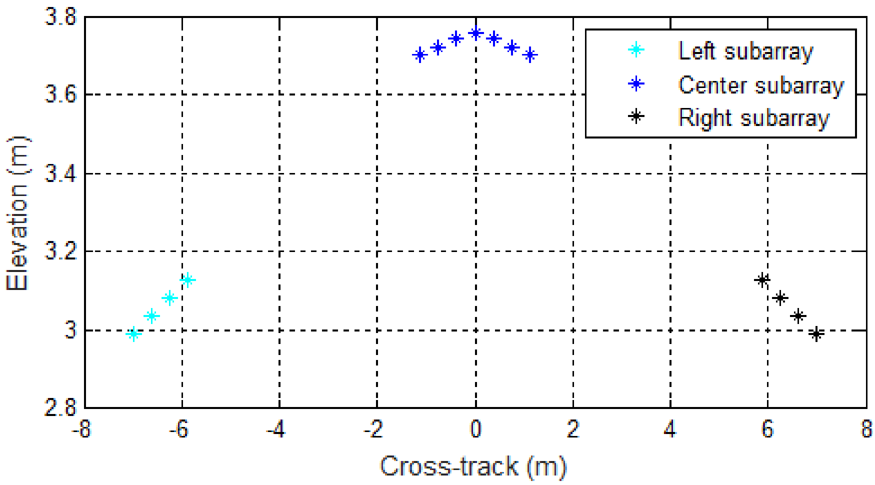

Figure 2.18: Phase centers of the three subarrays mounted on the P-3 radar plotted in the y-z plane. Each star '*' represents one sensor of the array. The y-axis points starboard/right and the z-axis points down relative to the aircraft.

MCoRDS [8] consists of three main subsystems: digital, RF, and antennas. Table 2.1 shows the radar system parameters. To increase the imaged swath for the CAA data collection, the radar was set to a multibeam transmission mode with three transmit beams steered to the left $-30°$, nadir $0°$, and right $30°$. The beam parameters are given in Table 2.2. The transmit beamwidth with the Hanning window taper produces a beam with most of the power concentrated in a $30°$ wide beamwidth.

Table 2.1: P-3 radar system parameters

Parameter	**Value**
Radar carrier-frequency	195 MHz
Signal bandwidth	30 MHz
Transmit pulse duration CAA	3 μs
Transmit pulse duration S-MAP	1 μs, 10 μs
TX antennas	7 Dipoles
RX antennas	15 Dipoles
PRF	12 KHz
Effective Storage PRF CAA 3 Beams Multiplexed, 13 stacked pulses each	307 Hz
Effective Storage PRF S-MAP 2 Nadir Beams, 32 stacked pulses total	375 Hz

The digital section consists of a waveform generator for each transmit antenna and an analog-

Table 2.2: P-3 radar beam parameters for CAA data

Waveform	**Look Angle**	**Attenuation**	**Weights**
1	$-30°$ (left)	15 dB	Hanning
2	0° (nadir)	20 dB	Hanning
3	$+30°$ (right)	15 dB	Hanning

to-digital-converter (ADC) for each receive antenna. The waveform generators are individually amplitude, phase, and time-shifted to produce a 10% Tukey-weighted linear-FM chirp, beam steered in the desired direction using true time delays. For the CAA data collection, the system cycles every 13 pulses between left, nadir, and right beams. Each batch of 13 pulses captured by an ADC, is averaged in hardware, and then stored to disk, creating 45 independent streams of data (15 ADCs $\times$ 3 beams), one for each receive-antenna and beam pairing.

The RF transmit section consists of power amplifiers, bandpass filters, and switches needed to precondition the generated pulses before radiating them into the air through the transmit antenna elements.

The duration of the transmitted pulse for the CAA data collection, 3 μs, was chosen as the longest pulse duration that would guarantee capture of the ice-surface. The minimum altitude was about 2250 ft above ground level (AGL) which allows 1.5 μs for the center 7 elements to switch from transmitting to receiving. Due to the thin ice (<1000m), the radar was operated with a single receiver gain setting for the entire range line and chose the gain to be the highest setting that still ensured that the surface return from ice would not saturate the receiver.

For a platform speed of v=124 m/s, the Nyquist criterion requires PRF=$4v/\lambda_c$ =322 Hz. The actual recording rate of 307 Hz leads to some ambiguity between forward and reverse grazing angles in the along-track dimension. However, these look angles are not used because basal ice scattering is very weak at these angles.

2.9 Processing Phase Centers

Since the transmit phase center and receive phase centers rarely align for all measurement phase centers, then by definition, CReSIS radars are bistatic even though the transmit and receive antennas are either the same or co-located. However, because monostatic geometry is much simpler than bistatic geometry, we use the monostatic radar equivalent phase centers to a bistatic radar when processing our data.

Figure 2.19 shows a graphical view of the measurement phase center calculation for a bistatic radar. The phase centers are calculated as follows. Define the following variables:

- $x_p^{tx}, y_p^{tx}, z_p^{tx}$: location of the p$^{\text{th}}$ transmit array sensor in the x, y, and z dimensions.
- $x_{pc}^{tx}, y_{pc}^{tx}, z_{pc}^{tx}$: transmit phase center (for the particular configuration) in the x, y, and z dimensions.
- $x_p^{rx}, y_p^{rx}, z_p^{rx}$: location of the p$^{\text{th}}$ receive array sensor in the x, y, and z dimensions.
- x_{pc}, y_{pc}, z_{pc}: phase center for the i$^{\text{th}}$ monostatic equivalent measurement in the x, y, and z dimensions.
- w^{tx}: transmit weights vector.

Then, we can calculate the phase centers of the transmit sensors as the inner product between the transmit sensors location and their preassigned weight, as shown in the following equation:

$$b_{pc}^{tx} = \frac{1}{\sum\limits_{p=1}^{P} w_p^{tx}} \sum_{i=p}^{P} b_p^{tx} w_p^{tx}, \qquad \text{where } b \in \{x, y, z\} \tag{2.74}$$

The phase centers of the receive sensors can be calculated as the average of the phase centers of the transmit sensors and the location of the receive sensors. This can be written mathematically as follows:

$$b_{pc} = \frac{(b^{rx} + b_{pc}^{tx})}{2}, \qquad \text{where } b \in \{x, y, z\} \tag{2.75}$$

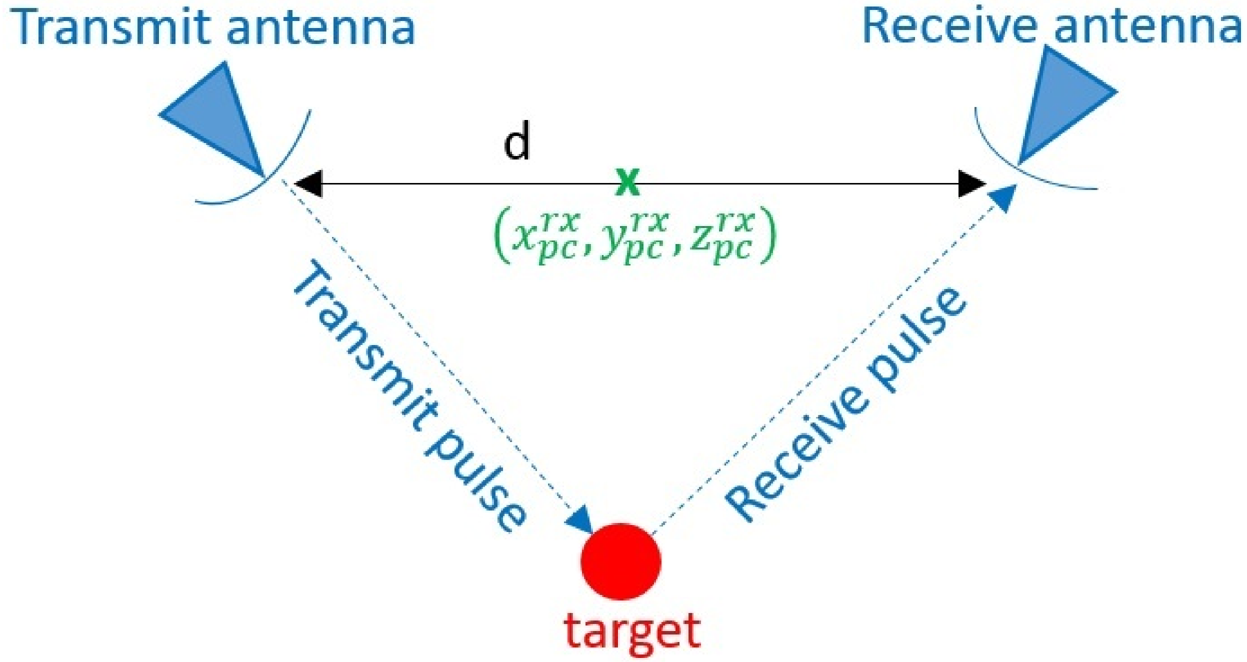

Figure 2.19: Monostatic equivalent measurement phase center for a bistatic radar geometry involving a single transmit and single receive antenna.

Chapter 3

Wideband Model Order Estimation Using Machine Learning

3.1 Introduction

Model order estimation (MOE) is the problem of estimating the number of targets, Q, that contribute to a measurement. Parametric direction of arrival (DOA) estimation techniques require the number of targets to be known a priori. Overestimating Q leads to estimating false targets, which reduces the accuracy of the estimated DOAs due to the noise being modeled incorrectly as a signal source. Similarly, underestimating Q means that the signal energy is modeled inaccurately as noise, which generally has a much more detrimental effect on the estimation accuracy than overestimation. Although overestimation does not affect the DOA as much, in the DOA-based tracking problem, such as tracking the bottom of an ice-sheet [33], overestimating Q usually leads to poor tracking results because the false targets affect the tracker's decision. Thus, it is important that Q is estimated as accurately as possible.

The classic MOE problem is solved by formulating a cost function and choosing the model order (number of targets) that minimizes the cost function. The cost function is composed of two terms: a negative log-likelihood term and a penalty term [60]. The log-likelihood term depends on the signal model used, but is always a monotonically decreasing function with model order. The reason for this is that as the model order is increased, the likelihood function is better able to match the data and so the likelihood goes up and the negative log likelihood goes down. The penalty term is a monotonically increasing function to counteract this trend so that the minimum of the combined terms occurs at the actual model order. Classic methods use analytical forms of the penalty term that are convenient because the signal model parameters are usually parameterized, which makes it easy to apply them to different scenarios (varying snapshots and number of sensors). However, in situations where the parameters are known ahead of time, [42] found that a numerically tuned penalty function outperforms all the classic methods considered in [60]. [1] has more details about this method, where optimal (number of targets and their directions are estimated jointly) and suboptimal (number of targets and their directions are estimated separately) signal models [38] are compared with each of the MOE techniques including the new numerically tuned penalty term. For the narrowband case, their results show a substantial improvement over standard methods, especially with the optimal signal model. Note that both the suboptimal and optimal signal models that the MOE techniques use are based on the narrowband signal model and they exploit the structure of the signal model's data covariance matrix (**R**) to estimate the number of targets.

For wideband signals, neither the standard MOE methods nor the numerically tuned method (NT) have good performance, especially beyond the low SNR regime and/or for large model orders up to one less than the number of sensors, P. For example, if we must estimate the number of targets, then $Q \in \{0, \ldots, P-1\}$. This is because, for wideband data, the signal subspace is no longer equal in dimension to the number of targets. It is worth noting here that higher signal-to-noise ratio (SNR) makes the MOE results worse in the wideband case because the spreading of signal energy into all the eigenvalues will be more prominent in this case. The additional signal energy in all the eigenvalues can cause a model order estimator designed around a narrowband signal model to decide these are distinct targets.

At the Center for Remote Sensing of Ice-Sheets (CReSIS), we process wideband data collected by CReSIS radars from different regions in Greenland and Antarctica with the goal of producing digital elevation models (DEMs) of the surveyed areas. But to generate these DEMs, the location of the top and bottom of the ice-sheets need to be known. The ice-top is given from the satellite imagery, but the ice-bottom should be estimated from the wideband radar data. To perform this task, the number of targets needs to be estimated per range-bin. The simple narrowband model is not effective with CReSIS radar data because the has a complicated eigen-structure for the data covariance matrix, **R**, where the dynamic range of the eigenvalues of **R** can be very large and the noise eigenvalues do not show proper multiplicity in cases where the radar scene is simple enough to enable determination of the correct model order by inspection. This suggests that there could be a violation of the narrowband assumption caused by multipath or the wider bandwidth, potential electromagnetic interference (EMI), or some combination of these. Regardless, standard MOE performs poorly.

Due to the complexity of the eigenspace for wideband data and the further complexity of the CReSIS data, we introduce a machine learning-based replacement for the simple numerical tuning model, where we apply a logistic regression method (LR-MOE) to estimate the model order under narrowband and wideband scenarios. Also, using the narrowband signal model presented in Section 2.3, we compare our results against six standard MOE methods and the former numerically tuned method (NT) compared in [1, 42]. Based on these simulations, the machine learning based MOE is able to do as well on narrowband data as the above mentioned methods and substantially outperforms all of them on wideband data.

To the best of our knowledge, this type of method and comparison are not explored in the literature and are introduced for the first time in this work. However, there are some attempts in the literature to perform this task by dividing the field of view (FOV) into multiple sectors and *detect* the presence of targets in each sector using NN techniques, and then apply DOA estimation at the sectors that have targets detected [61, 62]. A similar idea was also presented in [63] to estimate the DOA of a sound source after uniformly sampling the field of view in the elevation and azimuth dimensions and *detect* the presence of a source in each sampled direction. It is worth noting that none of these research articles dealt with the MOE problem as a multi-class classification problem or made a comparison with several other MOE methods, especially in regards to radar imagery applications, which is the focus of this work.

Although this logistic regression based technique is explored here, the MOE technique used in the remaining chapters of the dissertation is based on the minimum description length (MDL) using the optimal signal model with log-likelihood normalization method as introduced by [1, 42]. We abbreviate this method as N-MDL in this and later chapters. The log-likelihood normalization term accounts for the spread in the *estimated* noise subspace that occurs because a finite number of snapshots are used. Also, the standard MOE methods use the narrowband signal model, so in the wideband case, such as our application, the normalization term corrects for this model mismatch in the log-likelihood term of the cost function as well. By accounting for these effects, the standard algorithms perform much better. Note that the wideband results presented in [1] assume the maximum number targets is 6 for 7 sensors uniform linear array, which is why their results show that optimal and suboptimal MOE methods as well the NT method fail on wideband data, even with normalization. As we will will see in chapter 5, N-MDL works well on real wideband data when $Q = 2$ (i.e. small number targets relative to the number of sensors).

3.2 MOE Based on Logistic Regression (LR-MOE)

MOE can be viewed as a mutually exclusive multinomial classification problem, where each class represents a specific number of targets and the total number of classes is the maximum number of targets, Q, that we expect to have contributed to the measured data. Generally, for a uniform linear array, $Q = P - 1$, where P is the number of array sensors. So, in this case, there are P classes that the MOE needs to choose from, which are $Q = 0, 1, \dots, P - 1$. Each of these classes has a probability or cost associated with it and the final answer is the class that has the maximum probability or minimum cost among all other classes.

3.2.1 Logistic Regression Model

We use one versus all logistic regression to perform the classification task. Here we give a brief background on the theory of LR [64] and customize the discussion for our specific MOE problem. We start by mathematically defining the LR hypothesis model (also called sigmoid or logistic function) as follows:

$$h_{\Theta_k}(x) = \frac{1}{1+\exp(-\Theta_k^T x)} \tag{3.1}$$

$$0 \leq h_{\Theta_k}(x) \leq 1$$

where Θ_k is the LR parameter vector that is learned or optimized using the training dataset for class k, and x is the feature or input vector. Figure 3.1 shows a plot of the LR hypothesis function. $h_\Theta(x)$ maps $z = \Theta^T x$ to a probability distribution such that we can calculate the probability of each of the P classes, given z, and choose the one that has the maximum probability.

In our MOE application, we choose the features, x, to be the log of the geometric mean, $\boldsymbol{\lambda}_g(k)$, and the scaled log of the arithmetic mean, $\boldsymbol{\lambda}_a(k)$, of the eigenvalues of the data covariance matrix for $k = 0, 1 \ldots, P-1$ targets or classes. Considering this, there are a total of $2P$ features for each binary classifier. We define the i^{th} eigenvalue as $\boldsymbol{\lambda}(i)$ and sort the eigenvalues in descending order so that $\boldsymbol{\lambda}(1)$ is the largest. $\boldsymbol{\lambda}_g$ and $\boldsymbol{\lambda}_a$ are then defined as follows:

$$\boldsymbol{\lambda}_g(k) = \sum_{i=k+1}^{P} \log\big(\boldsymbol{\lambda}(i)\big) \tag{3.2}$$

$$\boldsymbol{\lambda}_a(k) = (P-k)\log\Big(\frac{1}{p-k}\sum_{i=k+1}^{P}\boldsymbol{\lambda}(i)\Big) \tag{3.3}$$

Note that $M\big(\boldsymbol{\lambda}_g - \boldsymbol{\lambda}_a\big)$ is the log-likelihood term of the standard suboptimal MOE methods where the scaling factor M is the number of snapshots. The unscaled feature vector can now be defined as follows:

$$x_{no-scale} = [\boldsymbol{\lambda}_g(0), \ldots, \boldsymbol{\lambda}_g(P-1), \boldsymbol{\lambda}_a(0), \ldots, \boldsymbol{\lambda}_a(P-1)]^T \tag{3.4}$$

Note that the dependence on the particular feature vector example has been dropped. When we refer to a particular training or testing example, we will use a subscript; for example x_i is the i^{th} training example. To make the feature vectors robust against scaling and to prevent large-value features from dominating the cost function, which can slow the training down, we normalize each feature vector or training example x_i by subtracting its mean, μ_{x_i}, and dividing by its standard deviation, σ_{x_i}, before feeding the data to the classifier. Note that the feature vectors for each example are normalized independently from each other, which is not the standard normalization method used in machine learning with logistic regression which generally normalizes each feature across the whole training set. The scaled feature vector, again with the training example index dropped, is

$$x = \frac{x_{no-scale} - \boldsymbol{\mu}_x}{\boldsymbol{\sigma}_x} \tag{3.5}$$

where $\boldsymbol{\mu}_x \in \mathbb{R}^{2P}$ with all of its entries equal to μ_{x_i}. Similarly, $\boldsymbol{\sigma}_x \in \mathbb{R}^{2P}$ with all of its entries equal to σ_{x_i} .

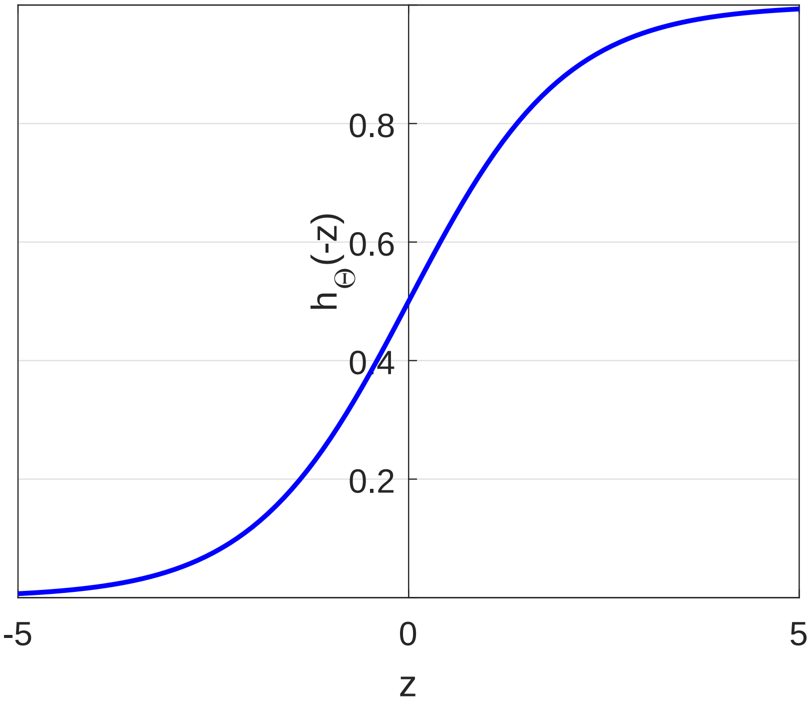

Figure 3.1: The sigmoid function with $z = \Theta^T x$.

3.2.2 Logistic Regression Cost Function

In our classification problem we are seeking the parameter Θ_k, which is obtained by minimizing a cost function, $J_{LR,k}$, that has two main terms: the first is the cost when the training example is in the class and the second is the cost when the training example is not in the class. For m training examples, this can be written as follows [64]:

$$\begin{aligned} J_{LR,k} = &-\frac{1}{m}\sum_{i=1}^{m}\Big(\mathbf{1}_{\boldsymbol{k}}(y_i)\log\left(h_{\Theta_k}(x_i)\right) \\ &+\mathbf{1}_{\mathbf{not}\,\boldsymbol{k}}(y_i)\log\left(1-h_{\Theta_k}(x_i)\right)\Big)+\alpha\Theta_k^T\Theta_k \end{aligned} \tag{3.6}$$

where x_i is the i^{th} example (or feature vector) and y_i is the corresponding label or class (the model order). Here we use indicator functions to control the first two terms. $\mathbf{1}_{\boldsymbol{k}}(y_i)$ is 1 when y_i is equal to k and is zero otherwise. Conversely, $\mathbf{1}_{\mathbf{not}\,\boldsymbol{k}}(y_i)$ is 1 when y_1 is not equal to k and zero otherwise. α is the learning rate and $\alpha\Theta_k^T\Theta_k$ is the regularization term that is added to avoid overfitting on the training set, which is an issue that usually arises from having too many features relative to the training set size. In other words, α can be used to keep all the features in the model by reducing the variability of the parameter vector Θ_k. In our application, we found through a grid search that setting $\alpha = 10^{-5}$ helps to slightly improve the percentage of correctly estimating the true number of targets.

The optimization problem can now be stated, for each class k, as follows:

$$\hat{\Theta}_k = \arg\min_{\Theta_k} J_{LR,k} \tag{3.7}$$

Because the logistic regression cost function is convex, we use a steepest gradient based algorithm to minimize the cost function to find the MOE classification parameters. A grid search on the regularization coefficient was also performed to find the optimal regularization constant.

3.2.3 Testing and Training Modes

In supervised machine learning, we first train the algorithm using a training data set to obtain the parameters, Θ. Once we are satisfied with the results, usually based on some application-dependent metrics, we take Θ associated with the best or lowest cost and apply this to a test set, which is mutually exclusive of the training set, to obtain the final results and can then move on to actual operation.

For our MOE application, we train and test for a given number of snapshots, M, and sensors, P. This implies that if either the number snapshots or sensors change, then we should again re-train to obtain the best possible results. For a particular number of snapshots and sensors, we generate training and testing data sets for a range of SNR scenarios and for all possible numbers of targets, $Q = 0, 1, \ldots, P-1$, using a one dimensional (1D) DOA simulator, where the snapshots are generated along the azimuth (along-track) dimension only and are assumed to be temporally independent, which simulates an ideal synthetic aperture radar (SAR) processor. The number of training examples for each possible combination of SNR and number of targets is 10000. Therefore, if there are 3 SNRs and $P = 7$, there are $3 \times 7 \times 10000 = 210{,}000$ training examples in total. Similarly, we used 105,000 testing examples. The generated data snapshots used in each training and test example are independent.

3.2.4 LR-MOE Algorithm

The LR-MOE problem is a multi-class classification problem, where each class has its own parameter vector $\Theta_k \in \mathbb{R}^{2P}$, and the parameters of the P classes are arranged in a single parameter matrix, $\boldsymbol{\Theta} \in \mathbb{R}^{2P \times P}$, that is then fed into the testing phase along with the testing dataset. In the training phase, the optimizer considers each class independently, where the label vector, y, has m entries with individual values $y_i \in \{0, \ldots, P-1\}$.

In the testing phase, we apply the estimated parameters of the P classes, one class at a time, to the testing dataset, and the final answer for the estimated number of targets, $\hat{q}$ (i.e. the estimated class) corresponds to the binary class function that has minimum cost. Mathematically, this can be written as follows:

$$\hat{q} = \arg\max_{k} h_{\hat{\Theta}_k}(x) \tag{3.8}$$

where $h_{\hat{\Theta}_k}(x)$ is the sigmoid function for class k.

We use the percentage correct metric to evaluate our results. This metric represents the average number of times the model order is estimated correctly relative to the total number of input examples. We use this metric to compare the LR-MOE results to seven other MOE methods.

3.2.5 Results: Comparison Between LR-MOE and Other Methods

Now we present our results of the LR-MOE. The training and testing data were generated from a $P = 7$ sensor uniform linear array with $M = 11$ snapshots and different SNR values. We are particularly interested in the low snapshots case because the radar scene often allows for only a small number of snapshots because of the requirement that the snapshots are stationary. The data were generated for narrowband and wideband scenarios with fractional bandwidths of $\sim 0\%$ and $\sim 15\%$, respectively, and for $Q = 0, 1, \ldots, 6$ targets. Figures 3.2 and 3.3 show the normalized geometric and arithmetic means of the eigenvalues of a wideband data covariance matrix (averaged over 5000 Monte Carlo runs). We can see that there is good separation between the different curves (each belongs to a specific number of targets), which justifies choosing the geometric and arithmetic means of the eigenvalues as features to perform classification. But the boundary between the different classes becomes less clear as the number of targets increases. As we will see next, the LR-MOE method performs better in the narrowband case than in the wideband case, especially when the number of targets is large, due to the clearer boundary between the different classes in the narrowband case. For the wideband case, the LR-MOE outperforms all the other methods even though all methods, including the LR-MOE method, use the arithmetic and geometric means of the eigenvalues as the main component in their cost functions. The following results demonstrate this.

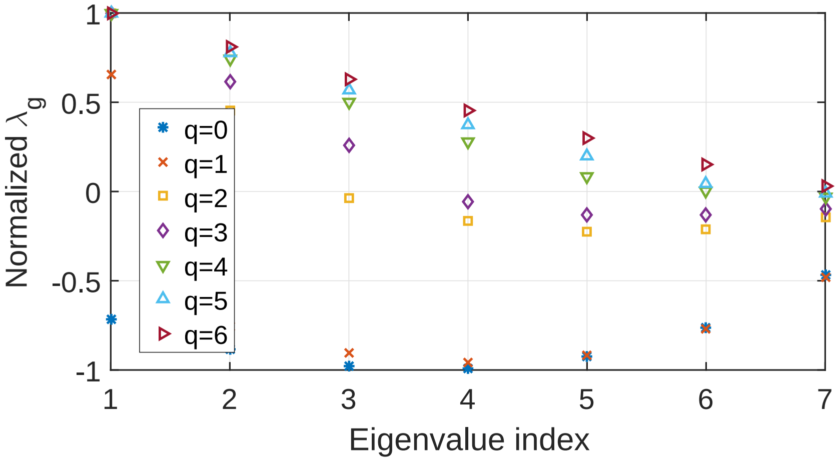

Figure 3.2: Normalized geometric means of the eigenvalues of the data covariance matrix averaged over 5000 Monte Carlo runs.

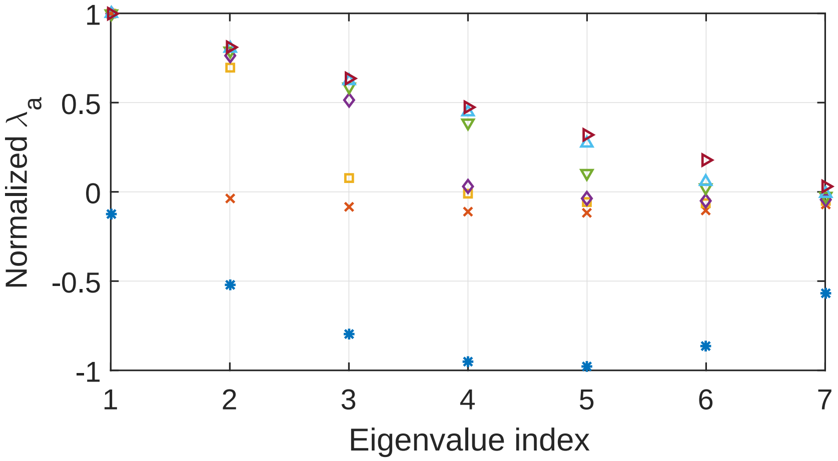

Figure 3.3: Normalized arithmetic means of the eigenvalues of the data covariance matrix averaged over 5000 Monte Carlo runs. The legend matches the previous plot.

Seven MOE methods were used to compare against the suggested logistic regression MOE method, which are [42, 1]: Akaike Information Criterion (AIC), Hannan and Quinn Criterion (HQ), Minimum Description Length (MDL), Corrected AIC (AICc), Vector Corrected Kullback Information Criterion (KICvc), Weighted-Average Information Criterion (WIC), and numerical tuning (NT). In the plot results presented below we present the LR-MOE results in a separate plot while keeping all other methods in a single plot for better visualization.

We start the comparison with the narrowband case. Figures 3.4 and 3.5 show the percentage correct results of the LR-MOE method and the other compared methods, respectively. The data is a mix of 3 SNRs: 10 dB, 20 dB, and 30 dB. The suboptimal signal model is used in all these methods. The results are evaluated for each SNR separately and with all SNRs at once, including the LR method.

We can conclude from these results that the LR-MOE method has better performance than all other methods at low SNRs and at large numbers of targets, which is a more challenging scenario in the narrowband case. It is worth noting that the log-likelihood term, in all of the compared methods except the LR method, is normalized using the method described in [1]. Without the normalization, the results are much worse. Note that the percentage correct of the WIC and KICvc methods is 0 for some numbers of targets because the penalty term of their cost function has a denominator that is not positive due to our specific choice of the number of snapshots and number of sensors, which causes these methods to give nonphysical values for the model order.

Now we perform the same comparison as before, but for the wideband scenario. Figures 3.6 and 3.7 show the percentage correct results of the compared methods. As expected, all the standard MOE methods as well as the NT method fail almost completely at medium and high SNRs even when the measurement snapshots result from a small number of targets. Increasing the number of snapshots from 11 to 101 does not help improve the performance of these methods, as shown in figure 3.8. These results are discussed in [1]. However, the logistic regression results are much more robust and have comparable performance at all SNRs and numbers of targets and with a small number of snapshots, which is the main conclusion from this study. Note that we did not include the machine learning results for the 101 snapshots because it already performs well with only 11 snapshots and increasing snapshots increases the performance since it reduces the noise in the estimation of the eigenvalues.

To test the SNR range over which the LR-MOE method still performs well, we did a separate experiment where we trained and tested the machine learning algorithm on 1D wideband data generated for 3 dB, 40 dB and 50 dB SNRs (i.e. skipped medium SNR). The percentage correct results are shown in figure 3.9. Also, figure 3.10 shows the results for the case of SNR = 50 dB narrowband and wideband data (the LR algorithm is trained and tested separately for each bandwidth scenario). We can see that the LR-MOE method still has acceptable performance, where the percentage correct is more that 80% in all test cases, given the wide dynamic range of the SNRs with no mid-range SNRs used in tuning for figure 3.9. These results support our conclusions regarding the robustness of the machine learning technique when applied to the MOE problem. Also, the results of this section unveil a promising solution for the MOE problem in the case of wideband data, especially in the high SNR regime and high model order applications.

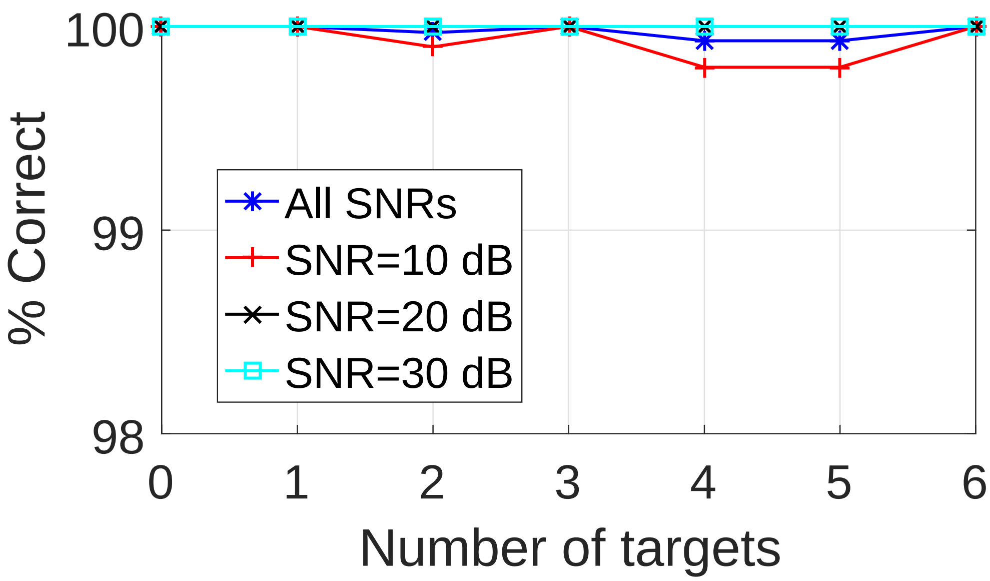

Figure 3.4: LR-MOE results for narrowband scenario. It shows the number of times the model order is estimated correctly relative to the total number of examples contributed in the test.

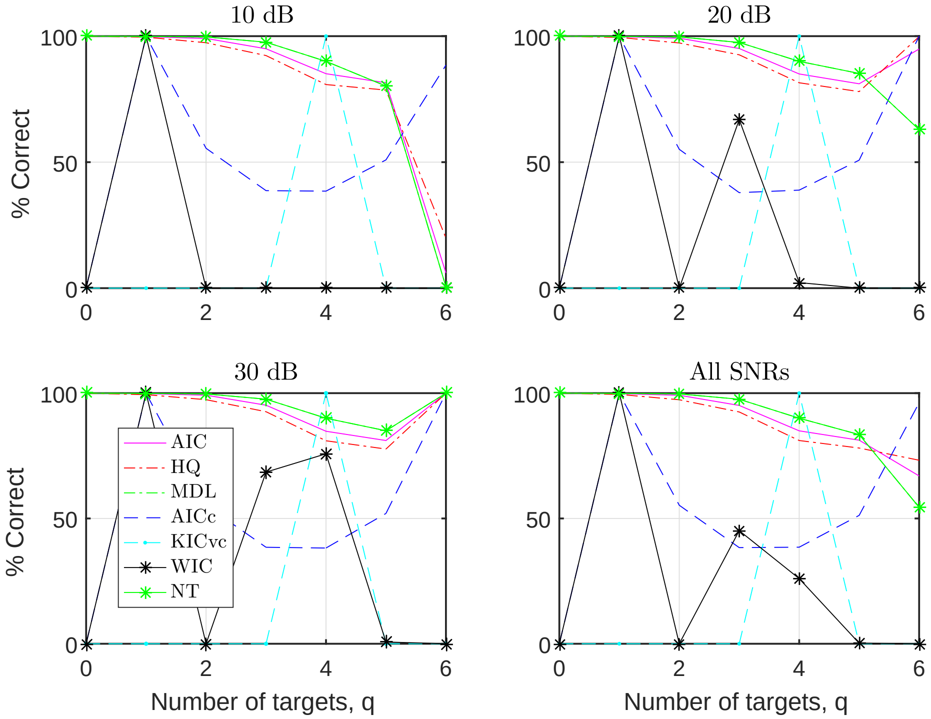

Figure 3.5: Results of seven compared methods for a narrowband scenario[1].

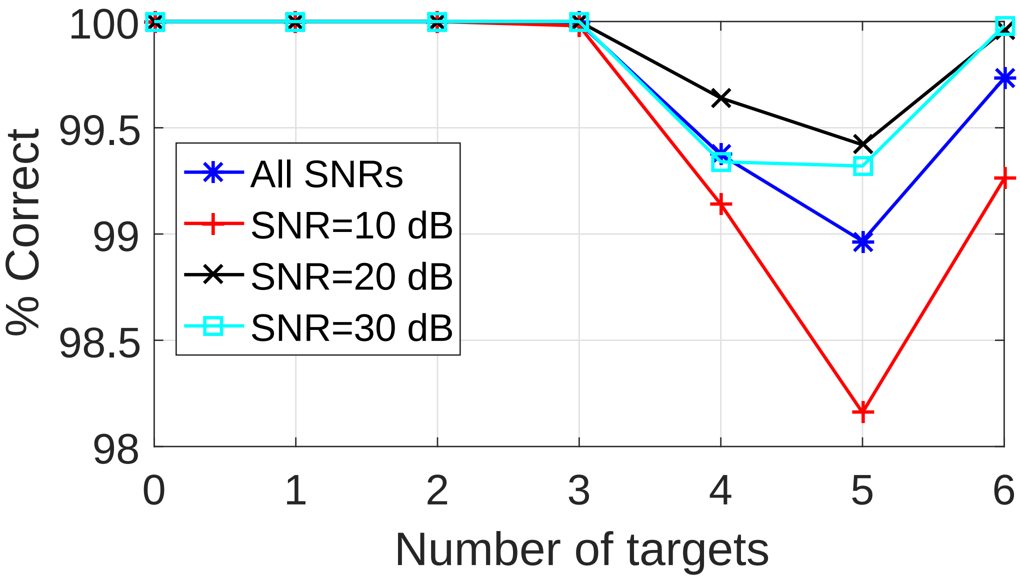

Figure 3.6: LR-MOE results for wideband scenario.

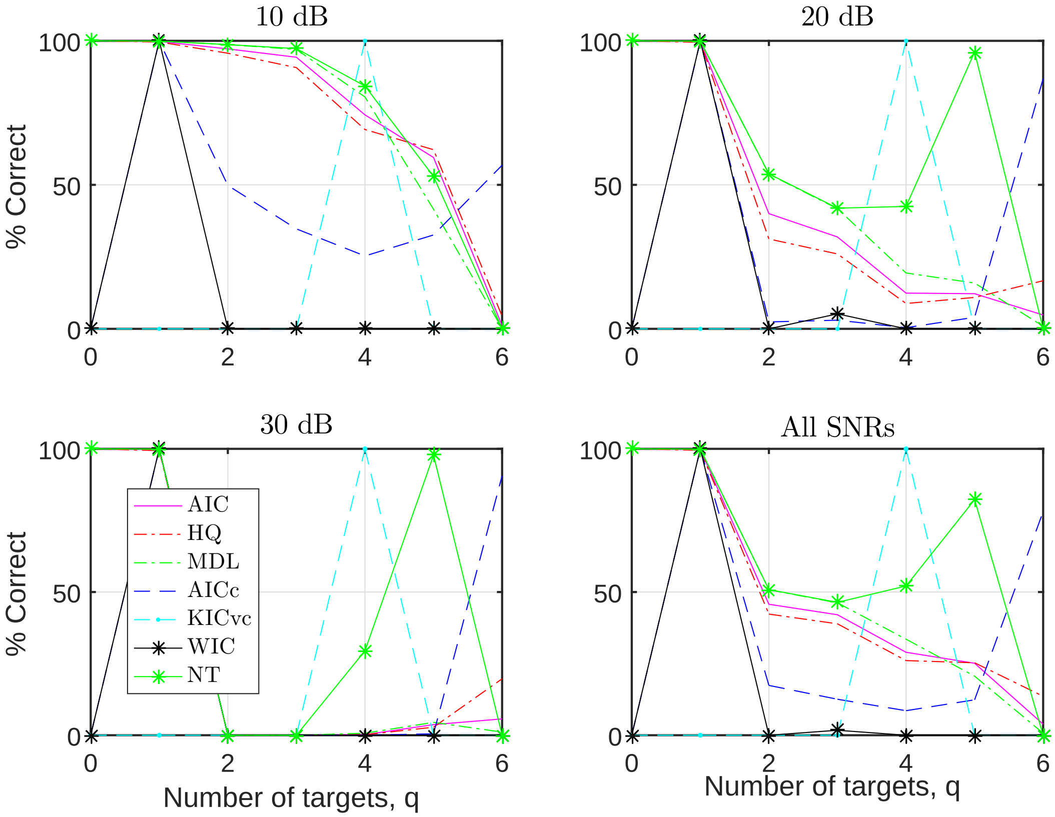

Figure 3.7: Results of seven compared methods for wideband scenario [1].

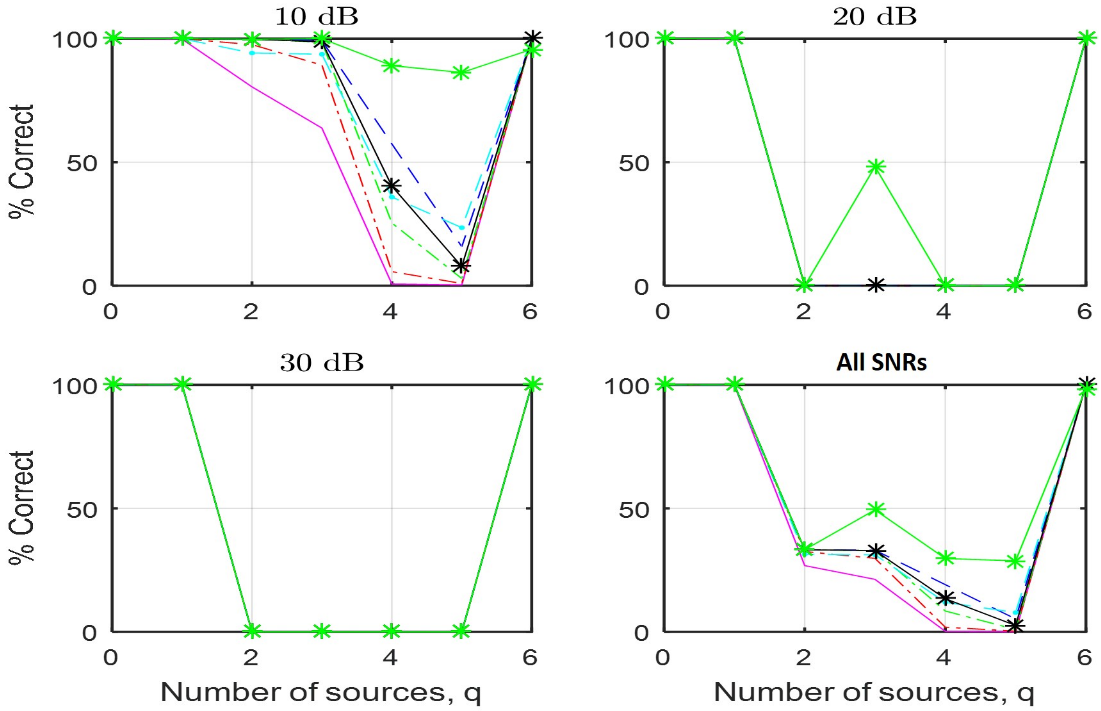

Figure 3.8: Results of seven compared methods for wideband scenario with 101 snapshots [1]. The legend matches the previous plot.

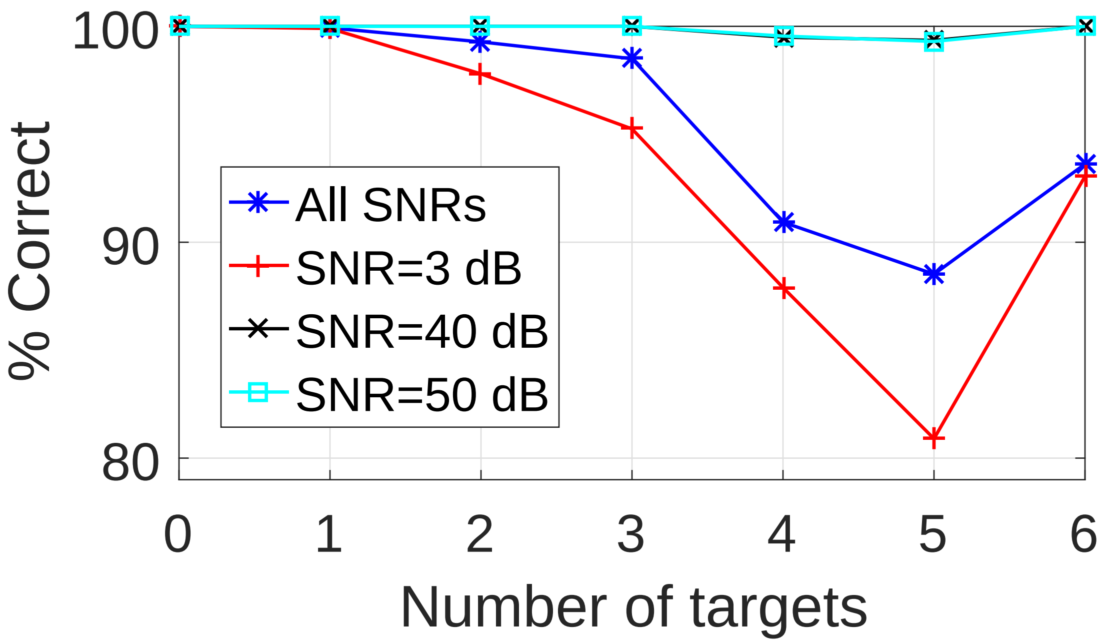

Figure 3.9: LR-MOE results for wideband scenario using wide dynamic range of training SNRs.

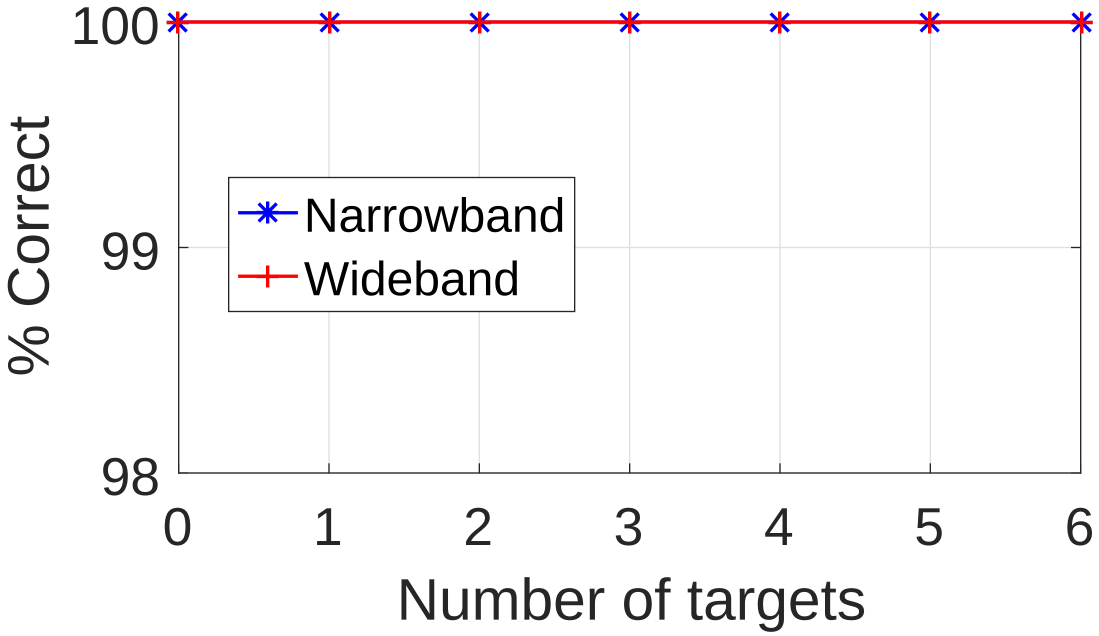

Figure 3.10: LR-MOE results for narrowband and wideband scenarios for 50 dB SNR.

Chapter 4

Comparison Between Particle Filter and Sequential MAP for Surface Tracking

4.1 Introduction

In this chapter we perform a 2D simulation-based study to evaluate the sequential surface trackers suggested and discussed in chapter 2 (namely, the PF and S-MAP). First, we investigate the performance of each of the two filters separately, and then compare them together and draw some conclusions. So, the goal here is to form a more in-depth understanding of the theoretical bounds of these filters when applied to the problem under consideration (surface tracking). For the best of our knowledge, this is the first study that is performed for this type of application, which we think that it will open the door for a new research direction to where these sequential filters can be applied, including the point cloud-based ice-bottom tracking problem.

4.2 Simulation Setup

The results presented in the following sections are produced using a 2D simulator, where the data are generated for each range-bin and each range-line as opposed to the standard 1D simulator that works along one dimension only. The 2D simulator is built to generate surfaces and evaluate the performance of different DOA estimation methods. All simulations assume a flat earth and point targets (a target that can be characterized by its radar cross section, RCS, only). Since we are interested in cross-track slices, no interaction between the data collected across range-lines is assumed, which mimics an ideal SAR processor. All snapshots are along-track snapshots, and thus independent. However, the frequency leakage between range-bins is captured in the 2D simulator, where the range to each target is calculated with respect to each phase center of the radar array sensors and a received sinusoidal signal is generated for that target at the predefined center frequency and bandwidth. The signals from the different targets are then combined together after being multiplied by their radar cross-section, which is modeled as a complex Gaussian random variable with predefined mean and variance. A Hanning window is then applied to reduce the interaction between neighboring range-bins. Thus, targets that share the same range to the radar are added together to form the measurements data received from their respective range-bin. The different relative delays from each target to the array sensors are then utilized by the DOA estimator to estimate the elevation angle of the targets.

We simulate a 7 sensor uniform linear array (ULA) in this chapter. The transmit beamforming and array perturbations can also be incorporated in the data generation, but for the simulations in this chapter we assume the array is ideal and no transmit beamforming is applied. So, all targets are assumed to have the same SNR (omni-directional array) to avoid averaging high SNR results (near nadir) with low SNR results (outside the 3 dB beamwidth of the radiation pattern). The FOV is restricted to be ±30°. Also, SNR is defined to be per channel everywhere in this chapter. Note that there is an SNR gain of 8.5 dB from the 7 sensors, assuming coherent integration of the returns.

We do our simulations for 2 fractional bandwidth scenarios: $f_c = 195$ GHz at $B = 30$ MHz (narrowband case) and $f_c = 195$ MHz at $B = 30$ MHz (wideband case, which matches real data fractional bandwidth). 1000 Monte Carlo runs are used in both simulation scenarios.

The model order, Q, is assumed to be known exactly, even though we will discuss the case of the estimated model order at the end of the chapter. Also, for the sequential trackers to work properly, tight initial bounds are necessary. But, for the purpose of this theoretical study, we relax this requirement and set the bounds to be ±15° (for the first active range-bin only) to better understand the behavior of the sequential trackers under unfavorable conditions. One issue withe these loose initial bounds is the possibility that the tracker may diverge and not be able to recover and come back on track. We found issue is less sever in the case of the PF than S-MAP, as we will see later in this chapter.

We use the root mean squared-error (RMSE) as a qualitative statistic to evaluate the performance of the studied DOA estimation methods. We chose the RMSE because it is a combination of the variance and the bias of the estimator. Note that the RMSE curves in this chapter are averaged over the number of simulated targets and number of active range-bins, so it is the average RMSE. Also, to measure the quality of the RMSE results, we use $\sqrt{\mathrm{CRLB}}$ as a reference. Figure 4.1 shows a plot of the $\sqrt{\mathrm{CRLB}}$ as a function of DOA for 3 different SNRs (3 dB, 10 dB, and 20 dB) and 21 snapshots for the case of a single range-bin with 2 equal SNR targets. The higher the SNR is, the more linear the $\sqrt{\mathrm{CRLB}}$ curve becomes over the considered FOV, and also less dependent on the elevation angle of the target. Also, as the two targets both approach nadir, there angular separation decreases, making it harder to distinguish the two targets, and thus higher SNR is important to separate them. Note that figure 4.1 is the only CRLB curve in this chapter and we put it separate for better visualization.

4.3 Particle Filter As a Surface Tracker

In this section we evaluate the performance of the PF, where we use the sequentially tracked (approximate) posterior pdf to perform Bayesian DOA estimation. One of the important parameters in the PF implementation is the resampling threshold, N_{thr}, where, as mentioned in chapter 2, if the effective number of particles, N_{eff}, is less than N_{thr}, then resampling is performed. This parameter is application-dependent. Setting the threshold too low makes the resampling happens more often, which leads to a loss of the information that is accumulated over time. Also, setting the threshold too high can lead to the degeneracy problem. In our PF simulations, we set $N_{thr} = 0.2N$ (or 20%

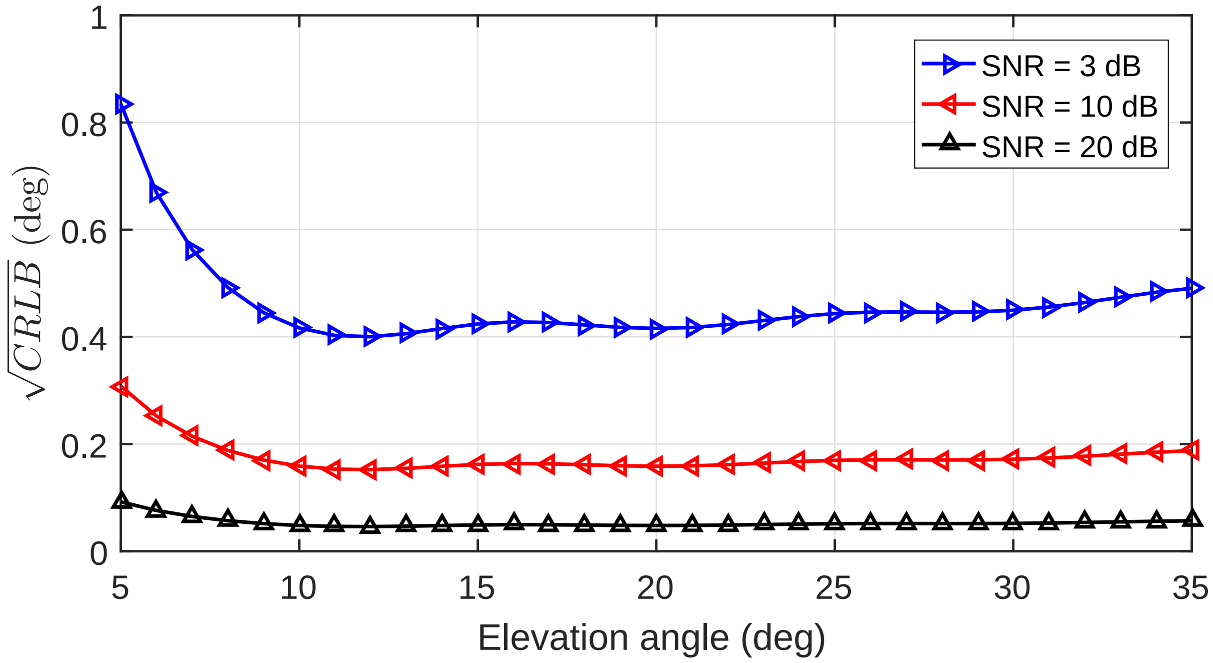

Figure 4.1: Elevation angle vs $\sqrt{\text{CRLB}}$, in degrees, for 3 SNRs with M = 21 snapshots.

of the total number of particles), and use the 'systematic' resampling method [47].

The PF algorithm is initialized with a uniform prior pdf within the predefined initial DOA bounds. For the following states, the particles are drawn from a truncated Gaussian pdf, as detailed in chapter 2. Also, to calculate the likelihood of each particle from the measured data, the noise variance is estimated using the measurement model for each particle separately, which requires the model order to be known a priori.

The PF is setup to start from the center of the surface, which is nadir for the case of a flat surface, and tracks outwards one range-bin or state at a time, until it reaches the limits of the FOV. After the forward PF tracking, a smoothing step can be applied in the backward direction to refine the results. One of the optimal backward smoothing methods is the Viterbi smoother [65], which is based on the MAP trajectory estimation. However, since we use the minimum mean-squared error (MMSE) estimator for DOA estimation under the PF framework, the Viterbi smoother is not relevant for our application. Other forms of PF smoothers are also available in the literature. But, smoothing, in general, is more suited for low quality data, so it is better applied for real data with low SNR. Also, for a large number of particles, smoothing is time consuming and requires extra memory for storing some of the parameters and results during the forward filtering stage to be used in the backward smoothing stage. Even though Viterbi smoother, in addition to another suboptimal smoother, were integrated with our implementation of the PF, but we didn't use smoothing in the results of this chapter.

4.3.1 DOA estimation under the PF framework

Since the output of the PF is the posterior pdf, we can apply several types of Bayesian DOA estimation methods using this pdf. So, the goal here is to choose the best DOA estimation method (in RMSE sense) under the PF framework for the surface-tracking problem, which was also discussed in chapter 2. Also, we are interested in choosing the relevant number of particles, N, for our application. Since the rate of convergence of the PF is dependent on N (the error of MC estimates is $\mathscr{O}(N^{-1/2})$), large N is preferred for any PF application, but large N can make the processing time too large to be practical. On the other hand, small N increases convergence time, but it makes the PF more practical. To resolve this issue, which is application-dependent, we plot the RMSE vs N for MMSE, MAP, and quasi-MAP DOA estimators in figure 4.2 for the case of a single range-bin and in figure 4.3 for the case of multiple range-bins or a surface for the narrowband scenario with SNR $= 5$ dB and $M = 21$ snapshots. Since multiple range-bins are used in figure 4.3, the tracked posterior pdf converges to the actual posterior pdf as the tracker steps through the range-bins, which improves the estimation accuracy. For this reason, in addition to the smaller angular separation between the targets in the single range-bin case ($\pm 5^\circ$), the RMSE in figure 4.3 is lower than that of figure 4.2.

Since the MAP and quasi-MAP methods have the possibility of choosing an outlier particle as an answer, we pass the particles set through an angular smoothing filter before DOA estimation. It starts by binning the particles into equally-spaced angular ranges (here, the window length is 0.5°), and then average the particles within each window. The same is done for the weights of the binned particles. So, *for the purpose of DOA estimation*, the new number of particles, N_b, will be less than N, but smoother (i.e. less outliers). The value of N_b is more dependent on the spread of the particles than on the actual number of particles, N. It is worth noting that applying the MMSE estimator within each angular window is not possible here because the result could be outside the window limits (MMSE is a weighted sum over all the N particles in the sample space). Choosing the length of the smoothing window is a compromise between smoothness and number of particles that should efficiently represent the posterior pdf in the DOA estimation step.

Figures 4.2 and 4.3 confirm our conclusion in chapter 2 that the MMSE DOA estimator performs much better than MAP and quasi-MAP estimators under the PF framework in terms of RMSE. We can also see that the MMSE is more stable and steady than the other two methods. In addition, both the single and multiple range-bin simulations show that, for MMSE estimator, $N > 100$ is sufficient for our application. But, to keep the PF more stable and to avoid resampling at each state, we choose $N = 1000$ and $N_{thr} = 200$ for all the simulations in this chapter. We think that this choice is a good compromise between accuracy, convergence speed, and efficiency.

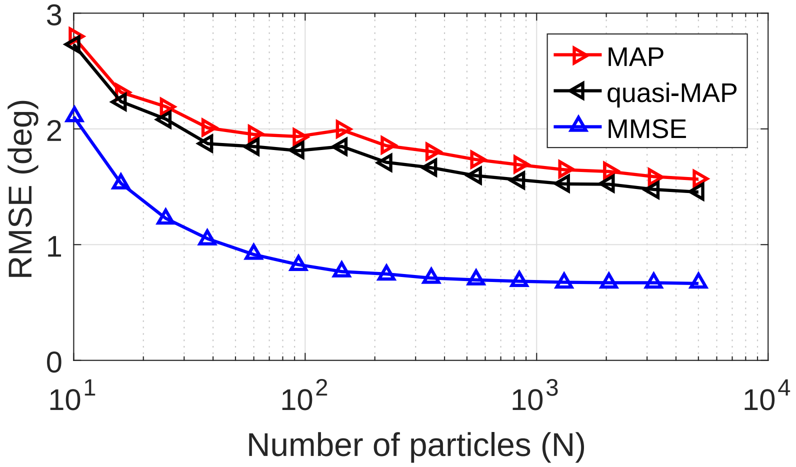

Figure 4.2: RMSE vs number of particles for 3 DOA estimation methods under the PF framework. 0.5° window length is used for the angular smoothing filter applied on the particles before MAP and quasi-MAP DOA estimation. These curves were generated for the narrowband case with SNR $= 5$ dB, $M = 21$ snapshots, and actual DOAs are $[-5^\circ \quad +5^\circ]$ (i.e. single range-bin).

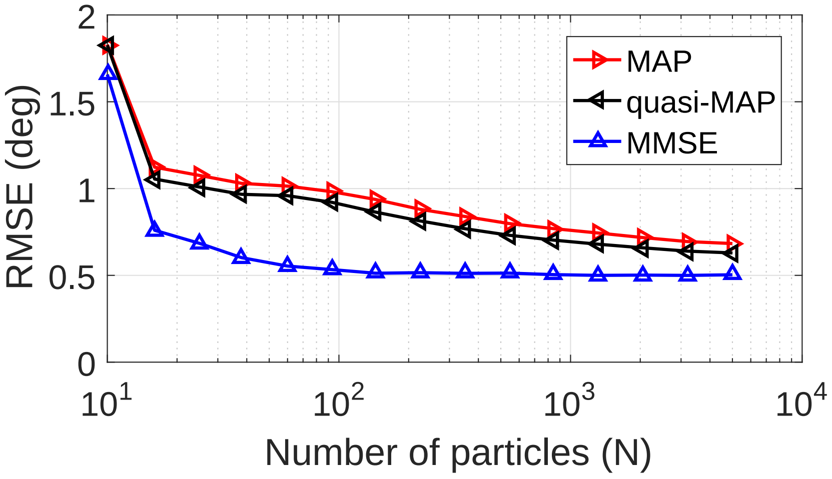

Figure 4.3: Same as figure 4.2, but here we simulate a flat surface with several range-bins. The range of the actual DOAs extends over the whole FOV, which is ±30°.

4.3.2 PF vs MLE and MUSIC: a Qualified Validation

The PF framework is set to work as a tracker, where the posterior pdf is updated sequentially and adaptively over time. But, before running the whole PF, we want to test the PF for the single-state case and compare its performance against MLE and MUSIC because the performance of these methods is well studied in the literature, so they can serve as a reference for validation or comparison against the MMSE PF. Figures 4.4 and 4.5 show, respectively, the RMSE vs SNR and RMSE vs number of snapshots for MLE, MUSIC, and PF for the narrowband scenario. Figures 4.6 and 4.7 show the same curves for the wideband scenario. The 1D simulator curves of the MLE and MUSIC are also included for reference against the MLE and MUSIC curves of the 2D simulator. It is also worth noting that due to outliers, some of the SNR curves seem to be increasing between SNR = 5 dB and SNR = 10 dB. Removing these outliers (e.g. using 3σ rule) makes the curves smoother, but we did not investigate this further.

1D and 2D simulator curves don't exactly match because in the 2D simulator case we simulate $N_t = 300$ range-bins, but in the 1D simulator case there is no sense of range bins. But we can consider the number of snapshots as the number of range-bins in the 1D simulator case. Thus, in the 2D simulator case the fast time Hanning window has a length of $N_t = 300$ here, but in the 1D simulator case it is $N_t = M = 21$.

From these results, we can observe that the PF is better than MLE at the low SNR and/or low snapshots regimes because the PF solution is a brute force solution in this case, where the likelihood of each of the N particles is calculated and either the best particle is chosen (in case of MAP) or all the particles participate, each based on its own weight, in the final answer (in case of MMSE). However, in the case of MLE, an optimizer walks towards the answer in steps starting from some initial point. Also, the shape of the cost function, which is dependent on the quality of the data, is a key factor in the optimizer's decision. To further support our conclusion, we plot the PF vs MLE and MUSIC in figure 4.8 for the 2D narrowband scenario when $M = 3$ (low snapshots regime). We can see that the PF is performing much better than MLE in this scenario.

The results of the wideband scenario ($B_f = B/f_c = 0.1538 \approx 15\%$) have almost no difference from the narrowband scenario ($B_f = B/f_c = 0.1538 \times 10^{-3} \approx 0\%$). To see a difference, we need to increase the fractional bandwidth to $B_f > 15\%$ (from simulations, we noticed a difference at $B_f \geq 30\%$). This seems to be the case for many subspace-based DOA estimation and beamforming methods [66], but still more investigation is required to generalize this fact. Interestingly, for model order estimation problem, $B_f = 15\%$ is large enough to make almost all the standard model order estimation techniques fail when the number of targets is large relative to the number of array sensors, as shown in [1], because this is a classification or detection problem rather than estimation problem.

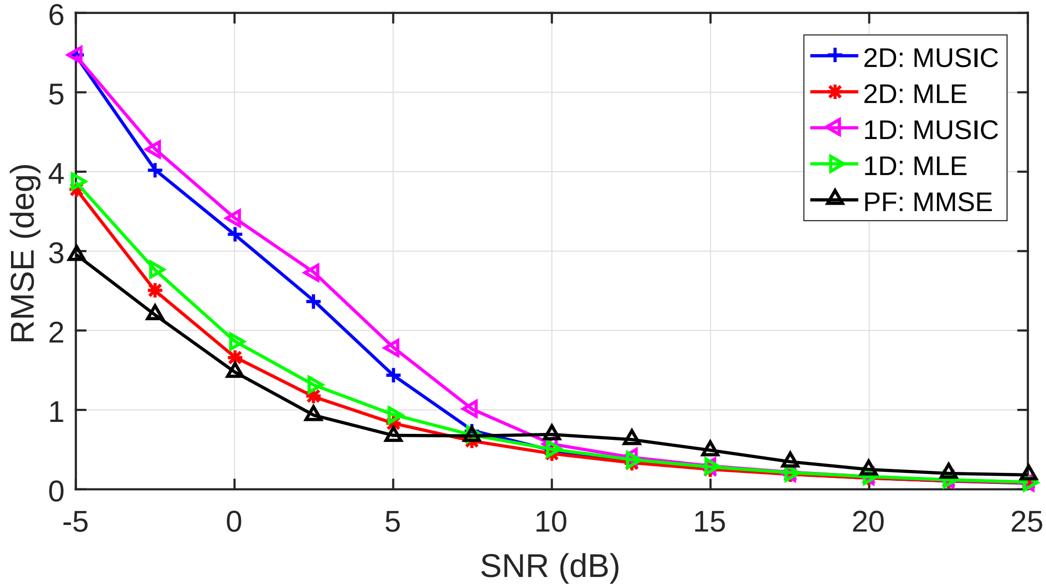

Figure 4.4: Two equal SNR targets, located at ±5°, are simulated for a narrowband scenario with $M = 21$ snapshots.

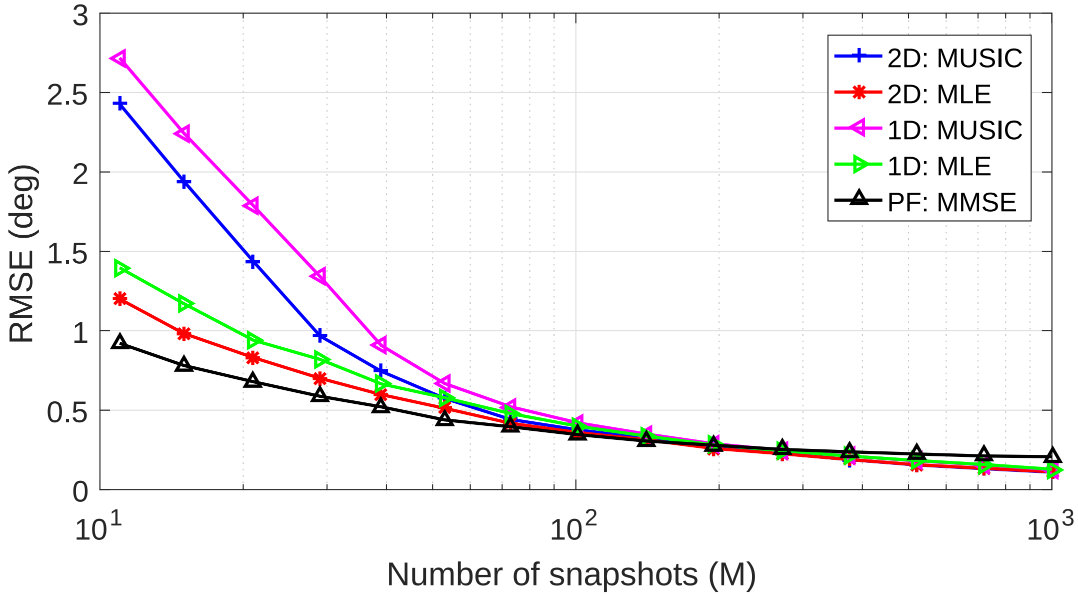

Figure 4.5: Same scenario as in figure 4.4. SNR = 5 dB.

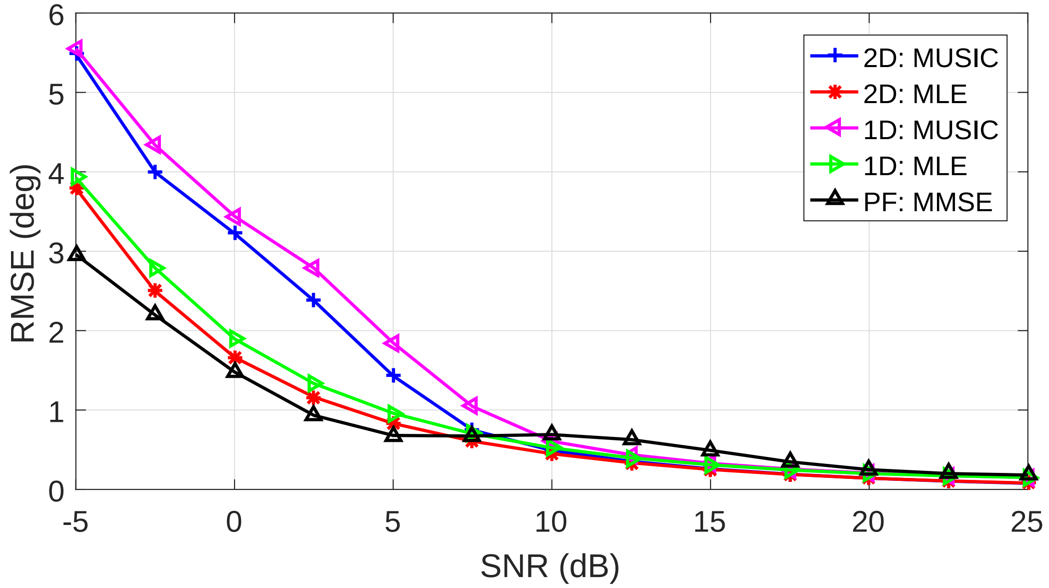

Figure 4.6: Same scenario as in figure 4.4, but for wideband case.

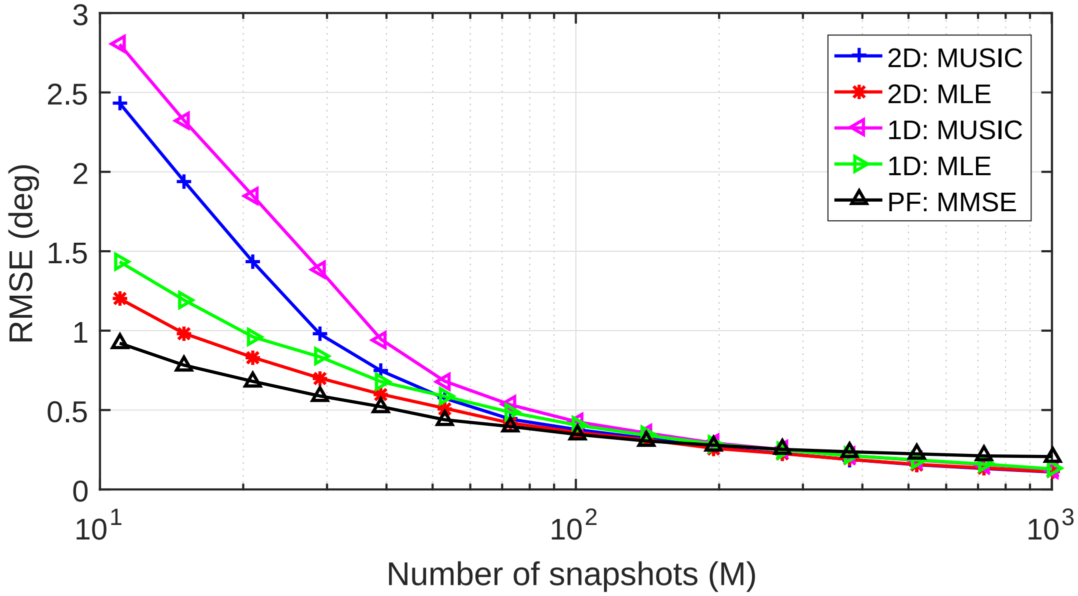

Figure 4.7: Same scenario as in figure 4.6. SNR = 5 dB.

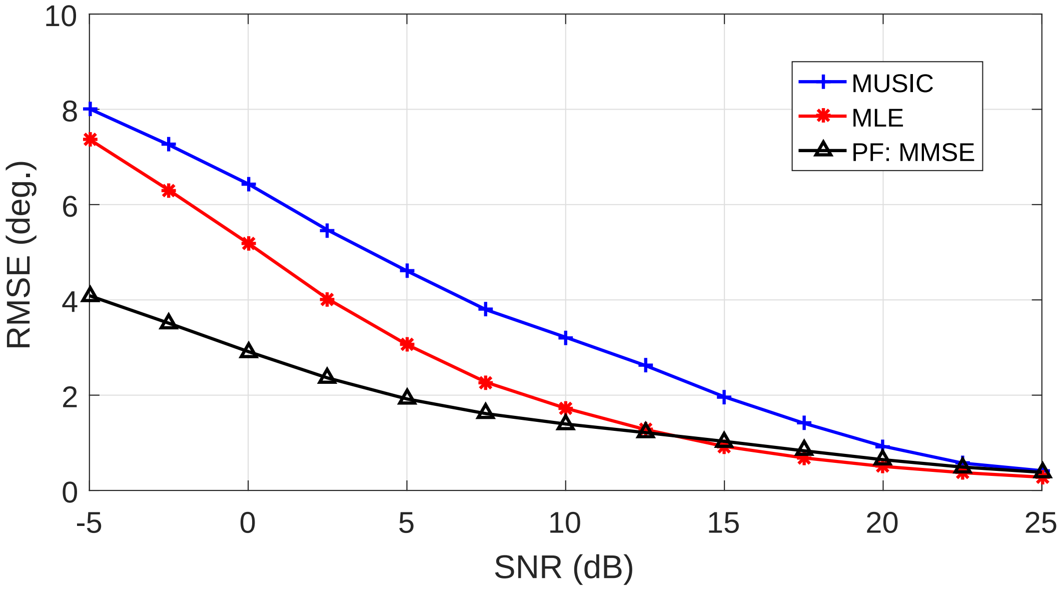

Figure 4.8: Same scenario as in figure 4.4. Low snapshots support, $M = 3$.

4.3.3 Surface Tracking: Step by Step Explanation

Here we explain the sequential part of the PF and how it starts and converges to the true posterior pdf as it passes from one range-bin to the next. The simulation scenarios are the same as those presented in Section 4.3.2, except that here we simulate a flat surface with multiple range-bins, each has either 2 targets (one on the left and one on the right) or no targets.

Figure 4.9 shows the estimated posterior pdf in a 3D scatter plot, where the particles are plotted on the x-and-y axes (each particle is a vector of length 2) and the weights are color coded. Two scenarios are simulated : a) low/medium number of snapshots (the left sub-figures), and b) high number of snapshots (the right sub-figures). Another view of the same plots is also presented in figure 4.10 in the form of empirical density plots. Five states were skipped in between the presented states (total of 21 states were simulated). These plots represent the outputs of the labeled states, which are then propagated into the next state after the DOAs are estimated. In other words, these plots show how the importance sampling work, which is the heart of the PF algorithm. The actual DOAs are also shown in the scatter plots as a red '+' symbol. We can see that even though the particles are initially uniformly distributed (two dimensional), the importance region of the posterior density is quickly approached after few iterations, which improves the estimation of the

DOA by a large amount relative to the first few states. It is worth noting that ‘state 1’ here is not the initial state, which is state 0 (initially, all the weights are $1/N$).

The purpose of presenting low and high sample support scenarios is to show an interesting fact about the PF, where in the case of $M = 1001$ the high-quality particles (i.e. particles with high weight) quickly accumulate around the true solution starting from the first state (i.e. smaller uncertainty region). After passing through the few following states, the high-weight particles start to collapse into a very small region, and thus very small importance sampling area. This behavior can be confusing and might lead to wrong conclusions because we might think that there is a degeneracy problem (particles collapse into a very small importance region, which results in a bad representation of the actual posterior pdf). However, in our application, due to the fast decrease of the change in DOA over range (see figure 2.7 in Chapter 2), the region over which the actual posterior pdf fits narrows down as the tracker steps through the range-bins. In addition to this, increasing the number of snapshots improves the estimation of the data covariance matrix, which makes the particles less noisy (smaller spread around the true solution). Thus *the PF performance saturates with increasing number of snapshots*, and to get out of this situation we need to either re-distribute the particles, which may only work for the first few states, or expand the region over which the particles are distributed, which means losing some prior information. Also, note that this issue was not very clear from the results of the previous section because we estimated the DOA for a single range-bin with $\pm 20^\circ$ initial bounds (i.e. the posterior pdf is fit into a wide region) It is also worth noting that *the PF does not saturate with increasing SNR* because the noise variance will go down, which improves the selection of the particles that most contribute to the final results. This fact will be elaborated on in section 4.5.

Moreover, because the particles are sequentially accumulating around a single mode that is the true solution, MMSE makes more sense than MAP and quasi-MAP for our surface-tracking application. Another thing to note here is that if the number of states is large, the PF will soon run into the sample impoverishment problem, which means two things: 1) a more sophisticated PF needs to be used, such as MCMC move-step, and 2) because, generally, there are more range-lines than range-bins in SAR imaging problems, tracking along the azimuth direction is not practical on a large scale, especially when the PF will need to resample every few states to stay stable (resampling means loss of the previously accumulated information represented by the sequentially-updated weights).

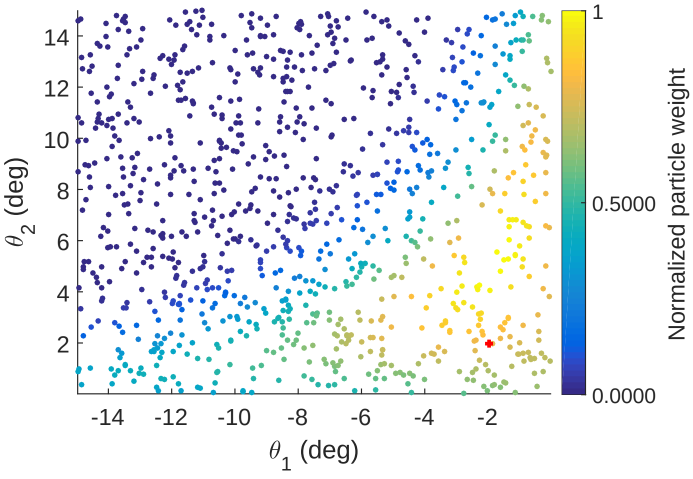

a) State 1: $M = 21$

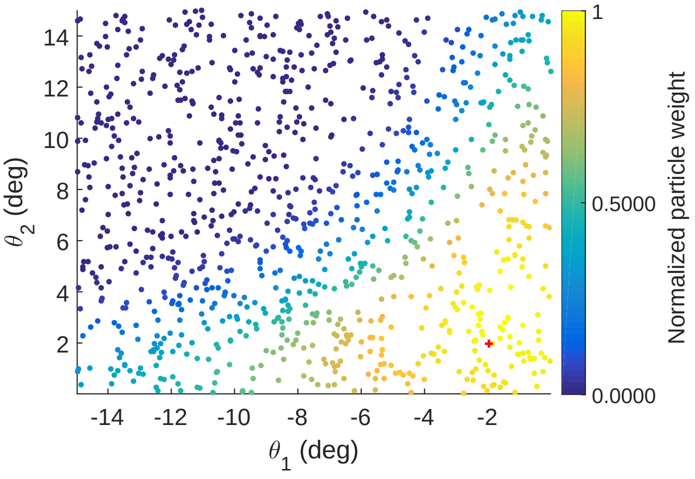

b) State 1: $M = 1001$

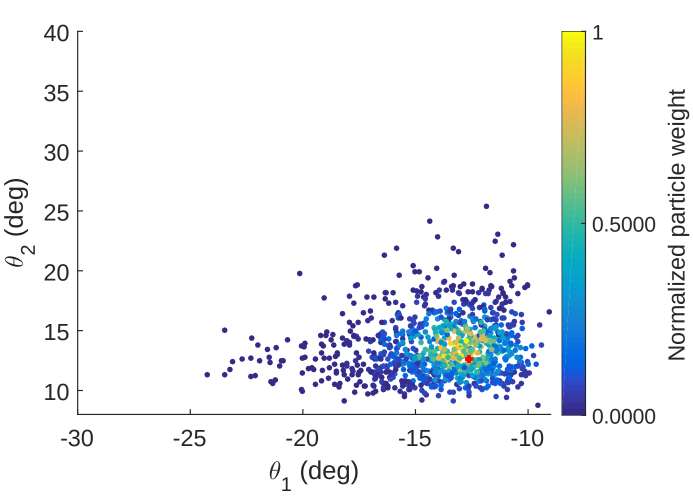

c) State 5: $M = 21$

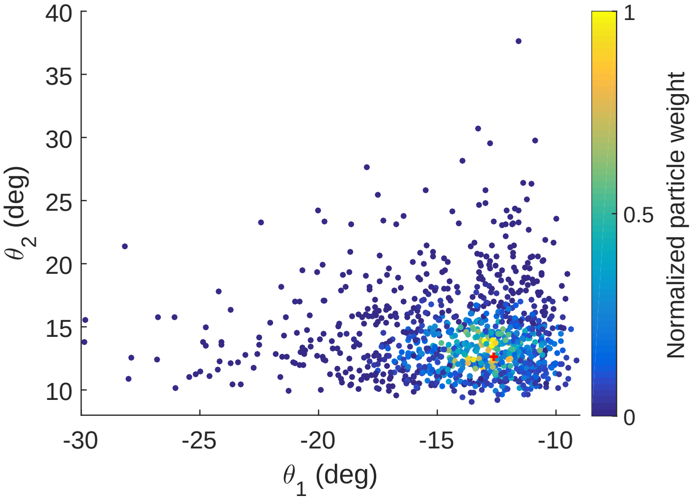

d) State 5: $M = 1001$

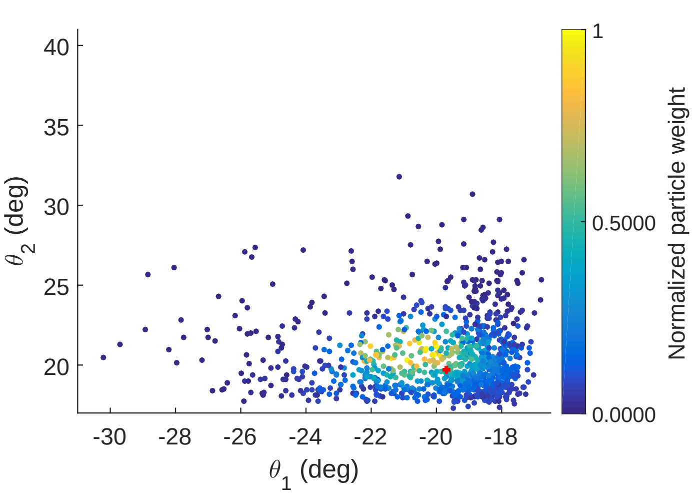

e) State 10: $M = 21$

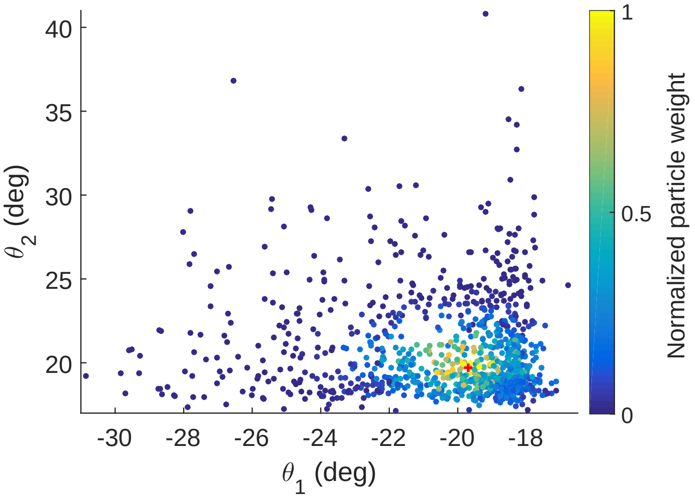

f) State 10: $M = 1001$

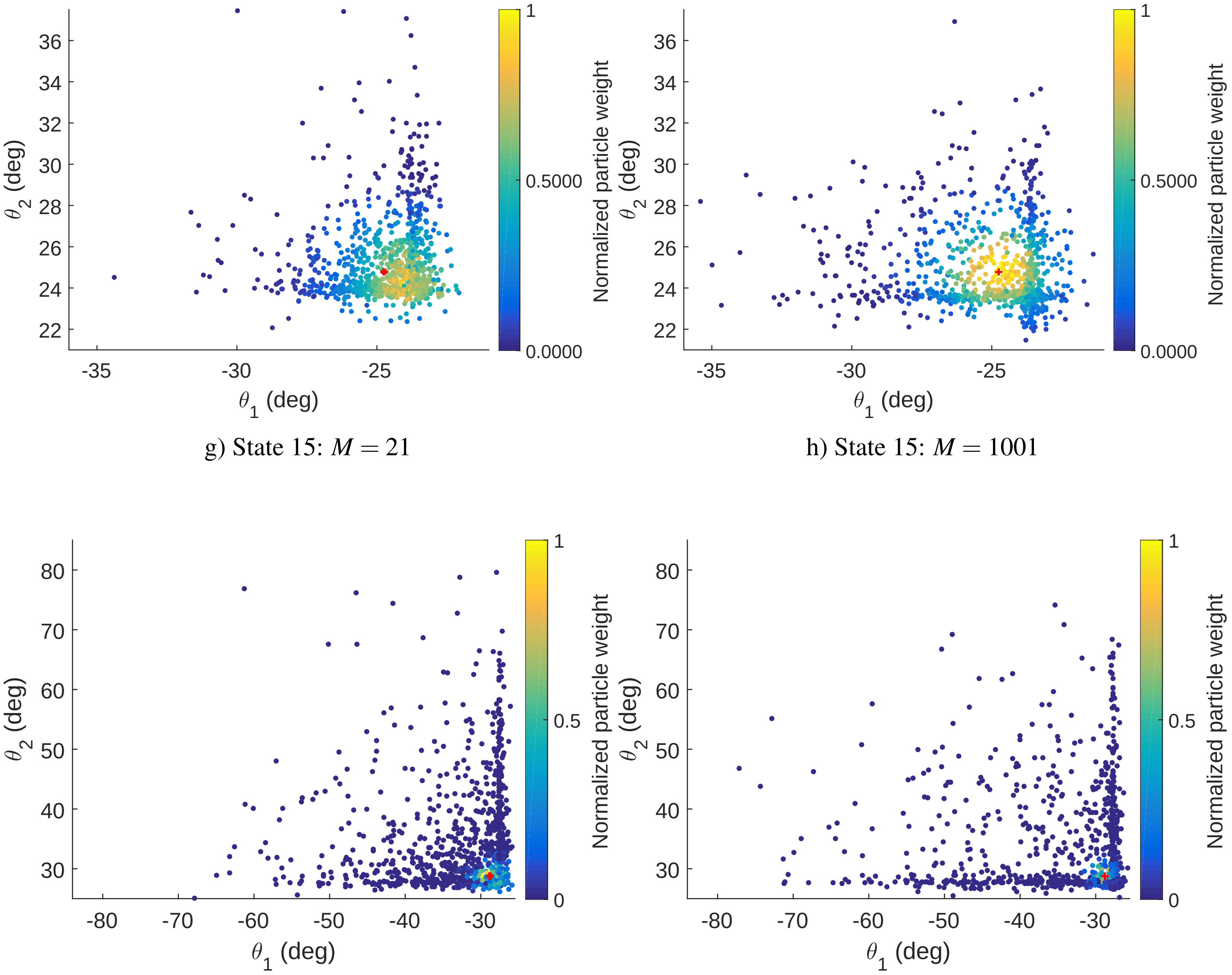

g) State 15: $M = 21$

h) State 15: $M = 1001$

i) State 20: $M = 21$

j) State 20: $M = 1001$

Figure 4.9: Tracking the importance sampling region using PF: 3D scatter plots, which show the two dimensional posterior pdf. Two scenarios are presented here: $M = 21$ snapshots (left sub-figures) and $M = 1001$ snapshots (right sub-figures). These plots are the outputs of the labeled states, which are passed into the DOA estimator and then to the input of the following state. The red '+' symbol represents the location of the actual DOA. Note that the weights of the particles are normalized relative to the maximum weight for better visualization.

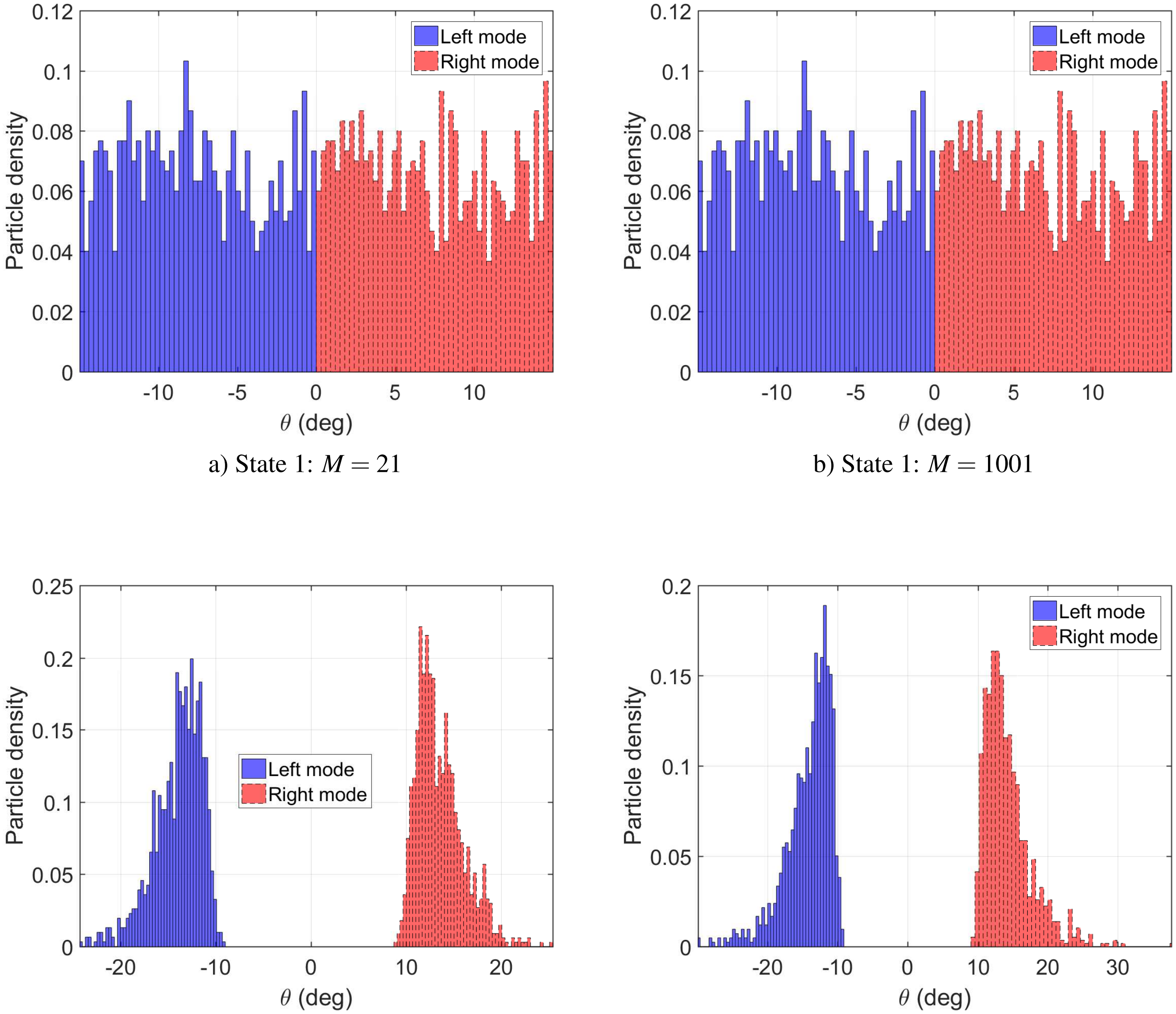

a) State 1: $M = 21$

b) State 1: $M = 1001$

c) State 5: $M = 21$

d) State 5: $M = 1001$

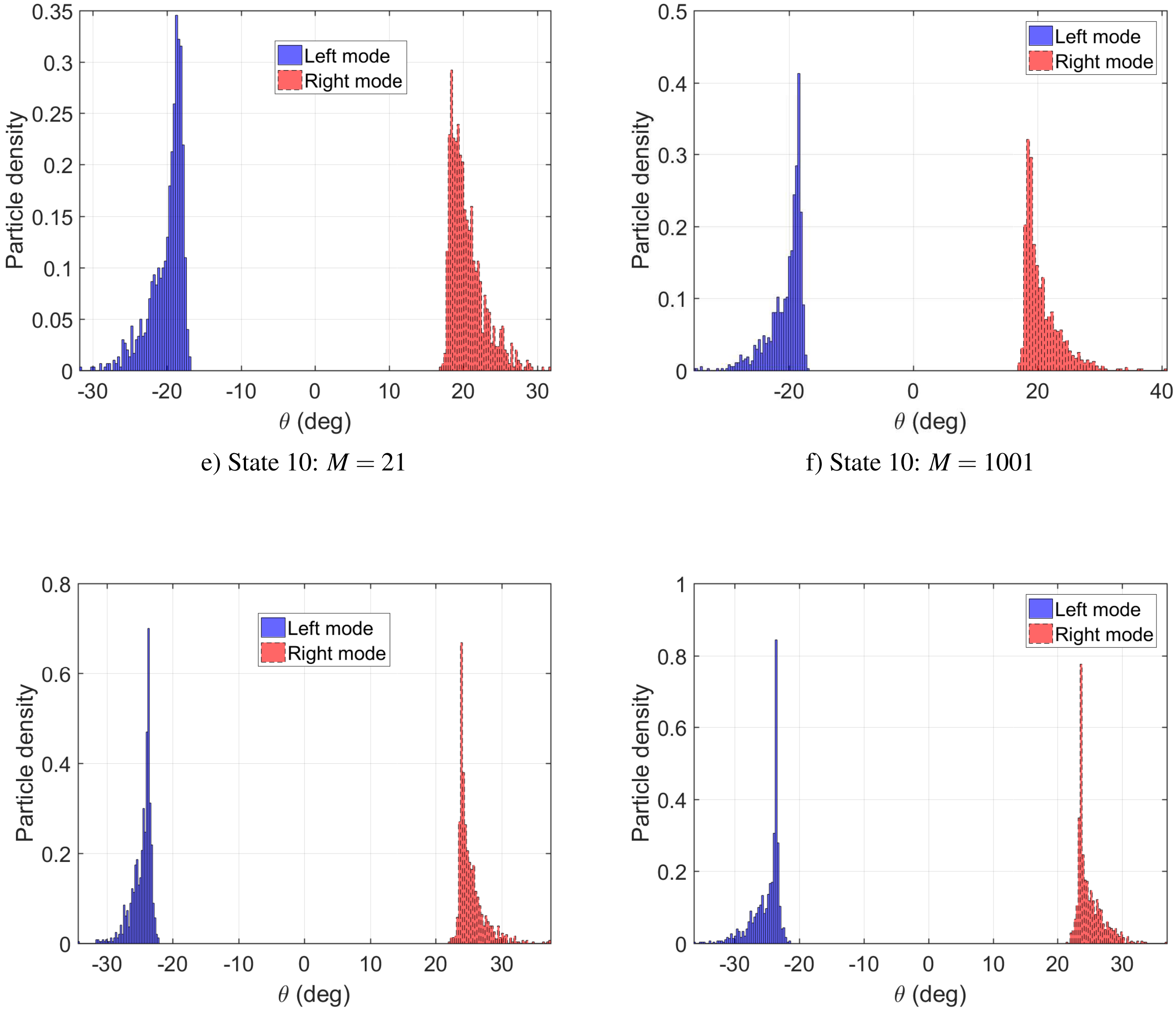

e) State 10: $M = 21$

f) State 10: $M = 1001$

g) State 15: $M = 21$

h) State 15: $M = 1001$

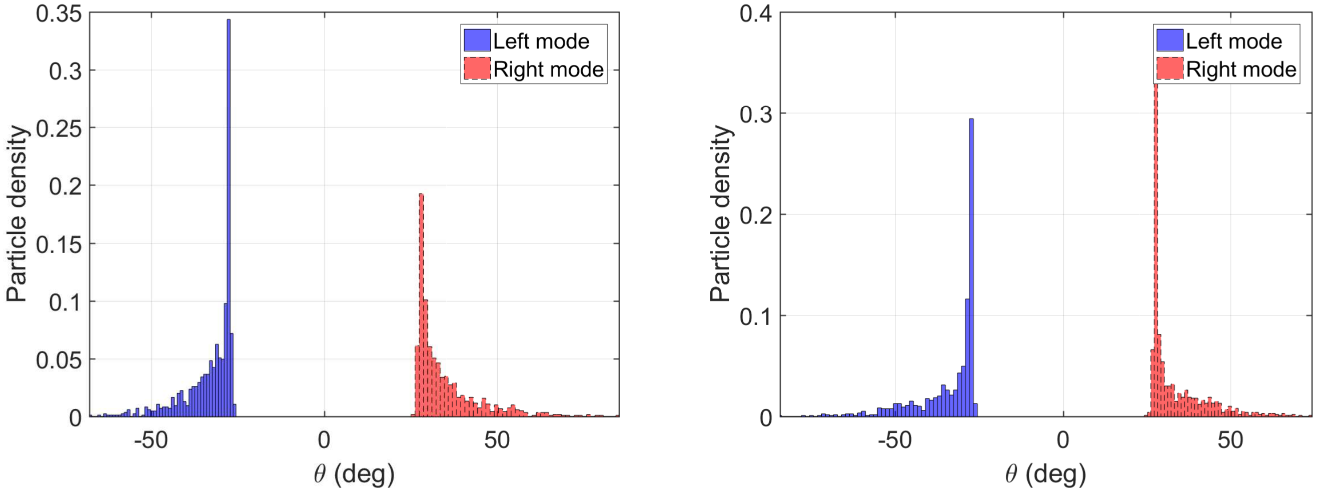

i) State 20: $M = 21$

j) State 20: $M = 1001$

Figure 4.10: Tracking the importance sampling region using PF: 2D empirical density plots. Same simulation scenarios as in figure 4.9, but here we show the bi-modal empirical posterior pdf in a histogram-like plots.

4.4 Sequential MAP Filter As a Surface Tracker

The details of the S-MAP surface-tracker were presented in Chapter 2. So, here we look closely at the operation of the S-MAP as it steps through the range-bins of each cross-track slice, following a similar approach to that introduced in section 4.3.3.

4.4.1 Surface Tracking: Step By Step Explanation

Unlike PF, S-MAP has an analytical form, which was given by equation 2.64. So, here we plot the actual surface, the estimated surface, the mean surface, and the bounds in figure 4.11 for three SNR scenarios: -100 dB, 100 dB, and 5 dB, with 21 snapshots for the narrowband case. These specific examples are chosen to show the main tracking habits, and they all share the exact same input data set, but different SNRs. We can see that when the SNR is very low (-100 dB here), the estimated surface is the mean surface because the data quality is too low and, thus, the prior cost function dominates the MAP cost function, which is an expected result. Thus, *the worst result we could get in the case of S-MAP is the mean surface*. This is not necessarily true for PF. However, when the SNR is very high (100 dB here), the estimated surface matches the actual surface almost exactly, where the likelihood cost function dominates the MAP cost function in this case. Finally, when the SNR is in between these two extremes (5 dB here), the estimated surface results from a combination of the prior information and the measurements data. These conclusions match our expectations based on the mathematical equation of the S-MAP cost function in chapter 2. Also, note that there is no mean DOA in the first range-bin, but there are initial DOA bounds, because the DOAs are assumed to be initially uniformly distributed (see the dynamics model in chapter 2). In addition, S-MAP tracker (as well as PF) put a heavy weight on the results of the first state, where if the estimated DOA of the first state is far from the actual DOA, the estimated surface may not match the actual surface, as seen by figure 4.11-a. The probability of this event is inversely proportional to the SNR. However, PF is more robust to this problem than S-MAP because its mathematical model is built to handle randomness.

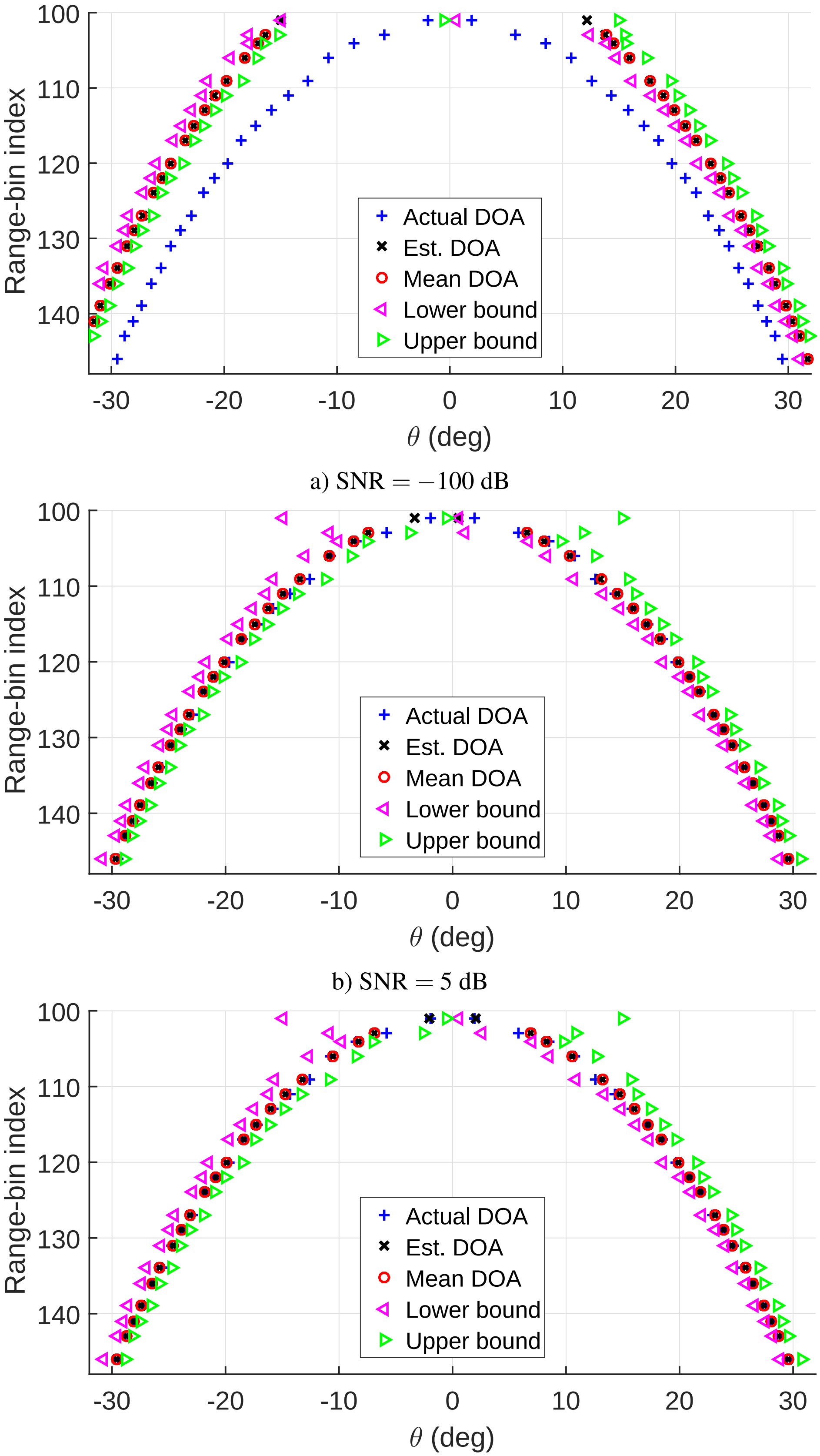

a) SNR $= -100$ dB

b) SNR $= 5$ dB

c) SNR $= 100$ dB

Figure 4.11: S-MAP surface for 3 different SNR scenarios: -100 dB, 5 dB, and 100 dB. $M = 21$ snapshots.

4.5 Performance Comparison of PF vs S-MAP

In this section we compare the performance of S-MAP vs PF as surface-trackers for narrowband and wideband scenarios. The simulation setup is the same as that of section 4.3.2, but here we simulate a surface that has 21 active range-bins, each has 2 targets (one on each side of the surface).

Figures 4.12 through 4.15 show the performance of these two sequential trackers, measured by the color-coded RMSE (deg), over a wide range of SNR and snapshots support for the narrowband scenario. The SNR plots are generated with $M = 21$ snapshots, while the snapshots plots are generated with SNR $=$ 5 dB. The following main points can be drawn from these plots:

- The PF converges, over range, SNR, and number of snapshots, faster than S-MAP. This is due to two reasons:

  a. The PF has a brute force-like nature, and thus it is not limited by the shape of the cost function and/or the performance of the optimization method used to solve the problem.

  b. The PF is limited by the number and the spread of the particles over the importance sampling region, as well as the bounds of the DOAs (remember (the error of Monte Carlo-based estimates of the pdf is $\mathscr{O}(N^{-1/2})$, which is 0.0316 in our case, but increases to 0.0707 when PF enters into a resampling mode) .

- Unlike S-MAP, the PF performance saturates with high number of snapshots.

- For both trackers, the main source of the high RMSE is the first 1 or 2 range-bins, which shows how much these trackers rely on the initial states and on the initial DOA bounds. The tighter the initial DOA bounds, the better the performance of the S-MAP and PF is, given that there is good-quality data within the preset initial bounds.

- On average, the PF has a better performance, in terms of RMSE, than S-MAP due to the same reasons mentioned in the first point above.

Also, to provide an average look at the performance of the compared trackers, we plot the average RMSE vs SNR in figures 4.16 and 4.18 and the average RMSE vs number of snapshots in figures 4.17 and 4.19 for the narrowband and wideband cases, respectively. As we have seen in section 4.3.2, wideband scenario has almost the same results as the narrowband scenario. In addition, the PF is much better than the S-MAP at low SNR and/or low snapshots support regions, and the reason for this was discussed when we compared the PF against MLE.

The saturation of the PF with increasing M is also clear in figures 4.17 and 4.19, which was discussed in section 4.3.2. The PF is, again, limited by N, angular spread of the particles, and the bounds of the DOA, and not by M. Higher SNR *decreases* the noise variance relative to the signal power, which improves the selection of the important region within the posterior pdf, and so result in better importance sampling. However, increasing *M improves* the estimation of the noise variance, but does not necessarily make it smaller as in the case of increasing SNR. So, since the particles are concentrate around the true solution over time, small improvements in the noise variance estimation become less important for the final result. In the case of S-MAP (and MLE and MUSIC), we set the tolerance of the optimizer to 10^{-6}, so any improvement in the data covariance matrix (or the estimation of the noise variance) matters. But in the case of PF, there is no way to set a tolerance on the accuracy of the estimated DOA in this way. *In summary, the PF is better suited for the case of limited data quality, where the SNR is very low and/or with low snapshots support.*

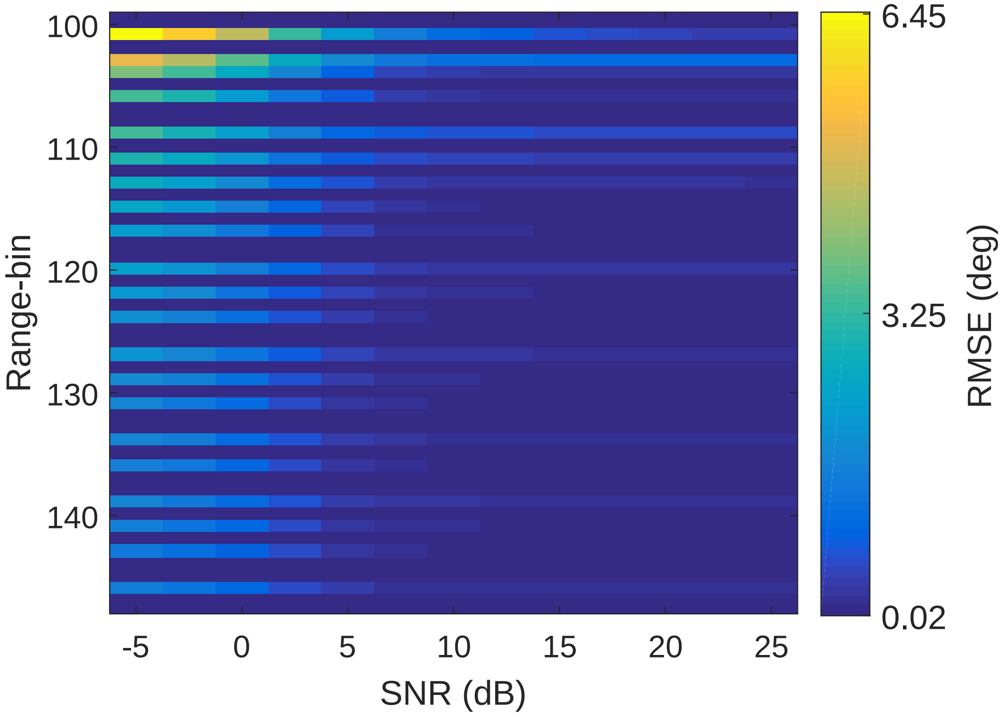

Figure 4.12: **S-MAP**: surface tracking assessment result. Narrowband scenario with $M = 21$ snapshots.

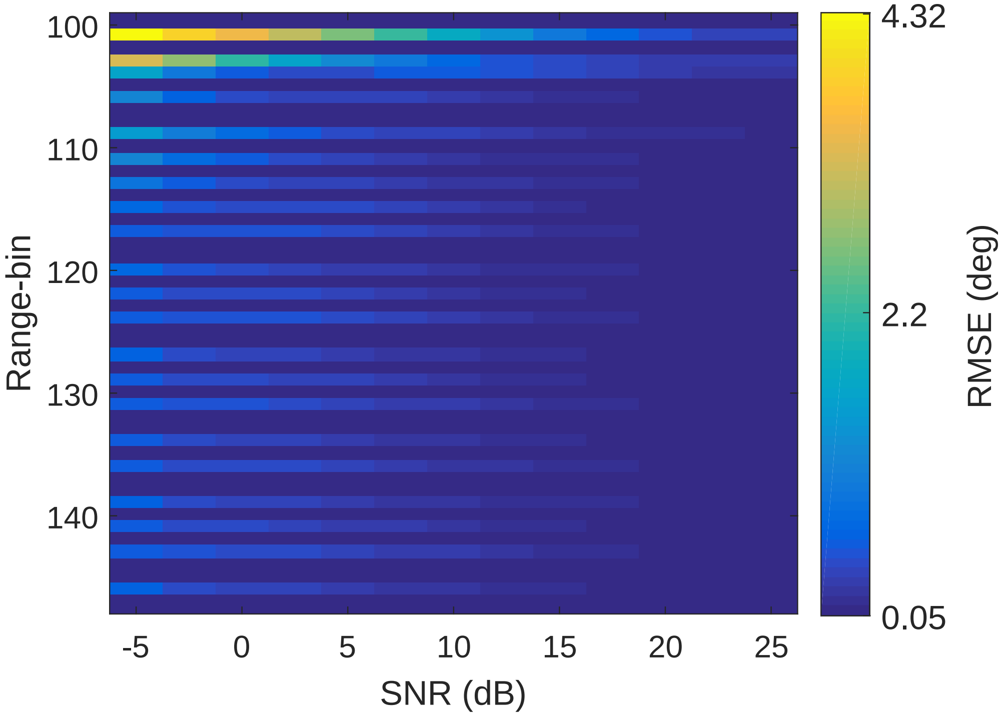

Figure 4.13: **PF (MMSE)**: surface tracking assessment result. Narrowband scenario with $M = 21$ snapshots.

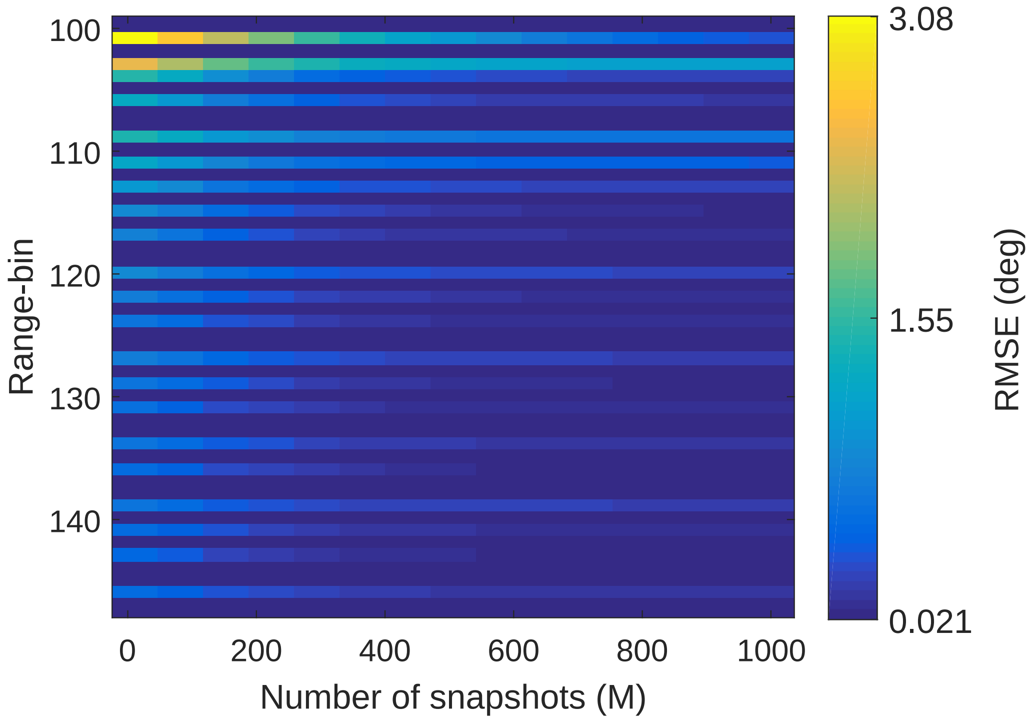

Figure 4.14: **S-MAP**: surface tracking assessment result. Narrowband scenario with SNR = 5 dB.

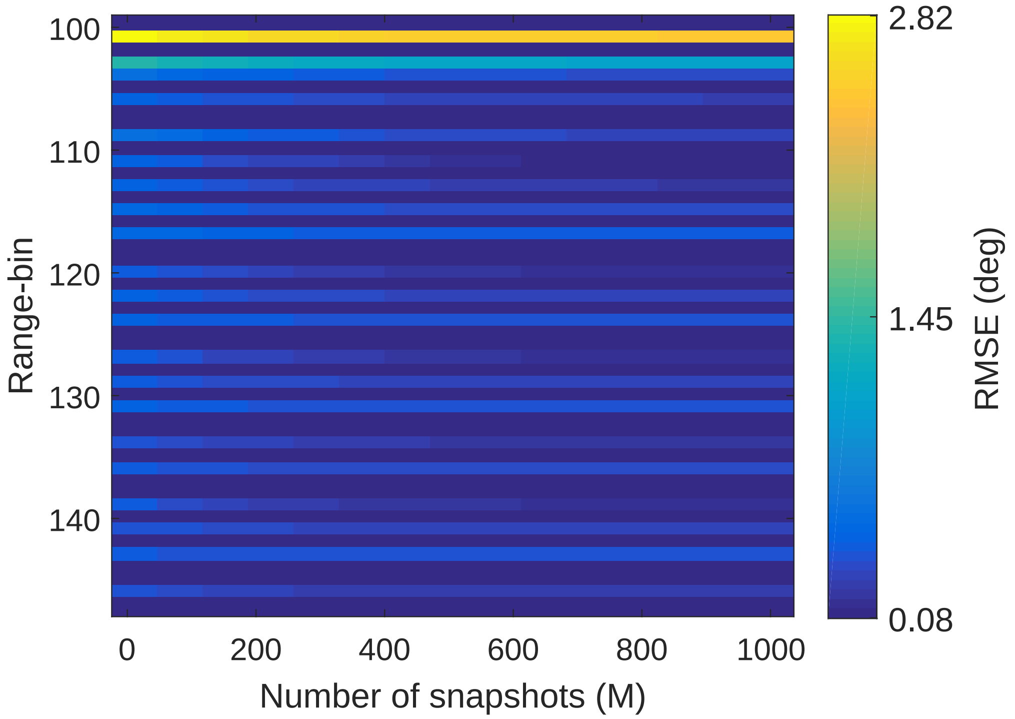

Figure 4.15: **PF (MMSE)**: surface tracking assessment result. Narrowband scenario with SNR = 5 dB.

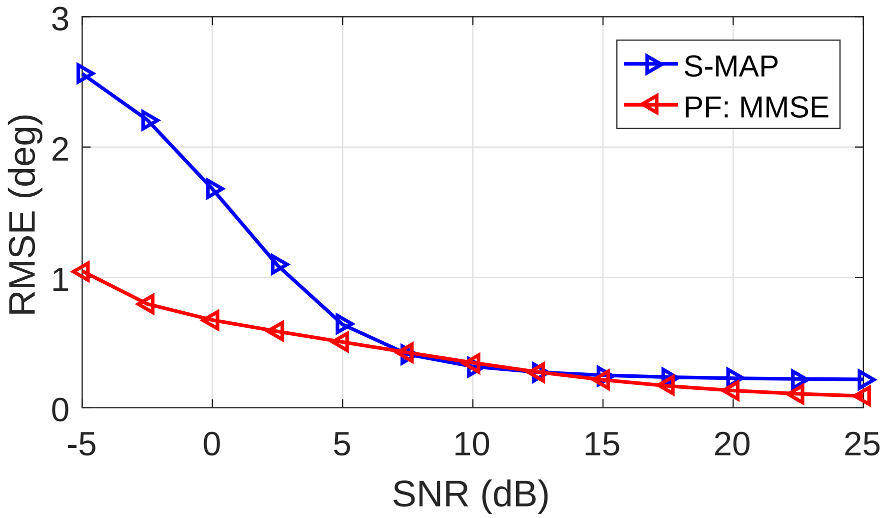

Figure 4.16: Surface tracking assessment result: narrowband scenario with $M = 21$ snapshots.

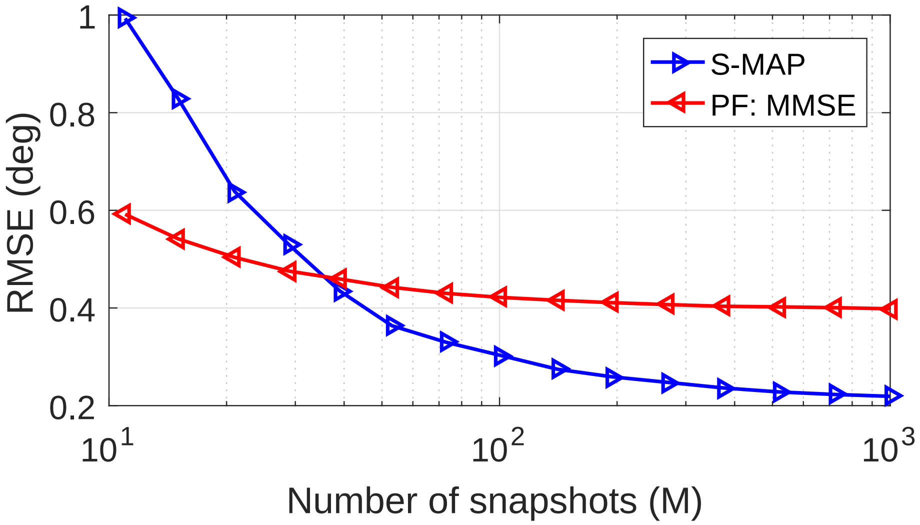

Figure 4.17: Surface tracking assessment result: narrowband scenario with SNR $= 5$ dB.

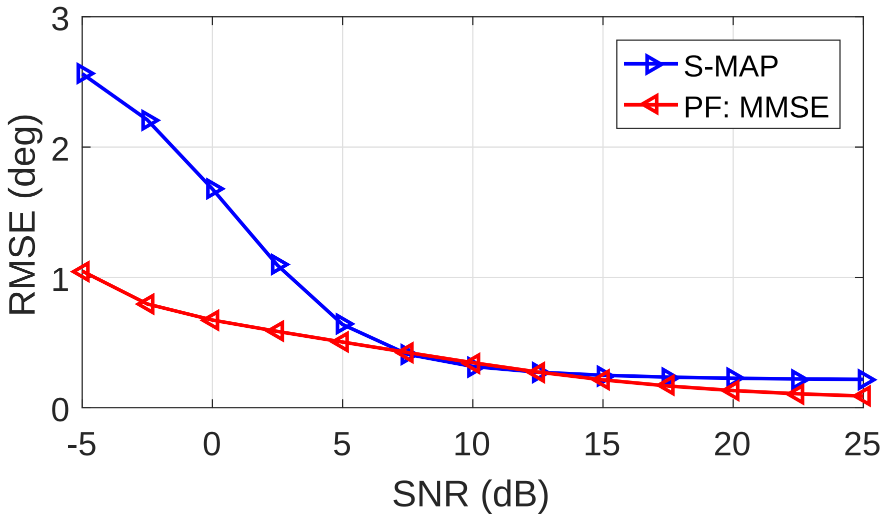

Figure 4.18: Surface tracking assessment result: wideband scenario with $M = 21$ snapshots.

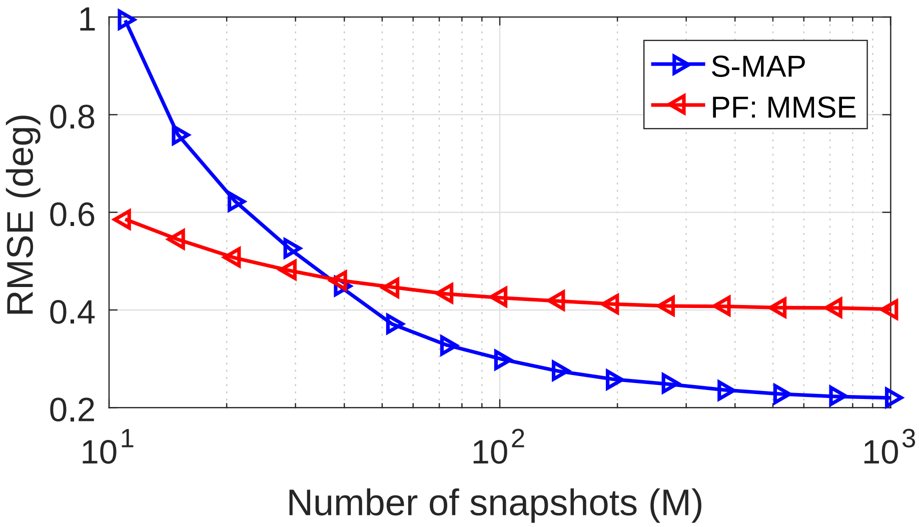

Figure 4.19: Surface tracking assessment result: wideband scenario with SNR = 5 dB.

4.6 Discussion

The goal of this section is to answer three questions about the two trackers discussed in this chapter:

- Can PF and S-MAP track non-flat surfaces?
- How do PF and S-MAP perform if the model order is not exactly known?
- Can PF and S-MAP track distributed targets surface?

We now discuss these three questions separately with a reasonable amount of details, but leave a more comprehensive study for future work.

1. **Can PF and S-MAP track non-flat surfaces?** Since all the tracking results in this section are generated for a perfectly-flat surface, here we discuss the case of tracking non-flat surfaces. Generally, the ability to track moving targets using any tracking technique relies heavily on the dynamics model, which connects, mathematically, the different states of the state space of the problem based on our understanding of the physical world. For our surface tracking problem, even though we use the flat-earth assumption as our transition model to estimate the mean surface, this *estimated mean surface is dynamic and does not represent a perfect surface (i.e. not static)*. This is because the mean surface is obtained from the mean DOAs based on a posterior pdf that is sequentially updated over time. In other words, how well it matches the actual surface depends on the quality of the measurements (e.g. SNR and M).

   The bounds of the search region is another important factor. Tracking surfaces that are narrower or wider than a flat surface is possible if we can set the DOA bounds appropriately to be around the mean DOA at each state. This is a design problem that is surface geometry dependent. So, the mathematical model of the bounds introduced in equations 2.30 and 2.31 can still be applied to any surface geometry, but the limits of the DOA bounds need to be adapted to allow for different types of surfaces (e.g. change a_1 in equation 2.30 and $f(\Delta\theta_m)$

in equation 2.31). We will present several bounding models in Chapter 5 when we apply S-MAP to real radar data.

Statistics and mean surfaces drawn from geostatistical analysis of real tracked surfaces can also be used to modify the transition model and the bounds. For example, figure 4.20 shows the mean and variance of the DOAs from the 2014 Canadian Arctic Archipelago (CAA) training data set. The FOV (±90°) is quantized into 64 bins (here we clipped the first and last DOA bins), where bin 1 corresponds to the far right DOA, bin 64 corresponds to the far left DOA, and nadir corresponds bin 33. The horizontal axis is the index of the DOA bin and the vertical axis is the DOA step size per range-bin measured in DOA bins. These means and variances can be used to calculate the prior pdf of the DOA, the search bounds, and assign costs to separate left from right DOAs in case the model order is $Q = 1$. Other information about the use of geostatistical analysis to help in tracking surfaces can be found in [67].

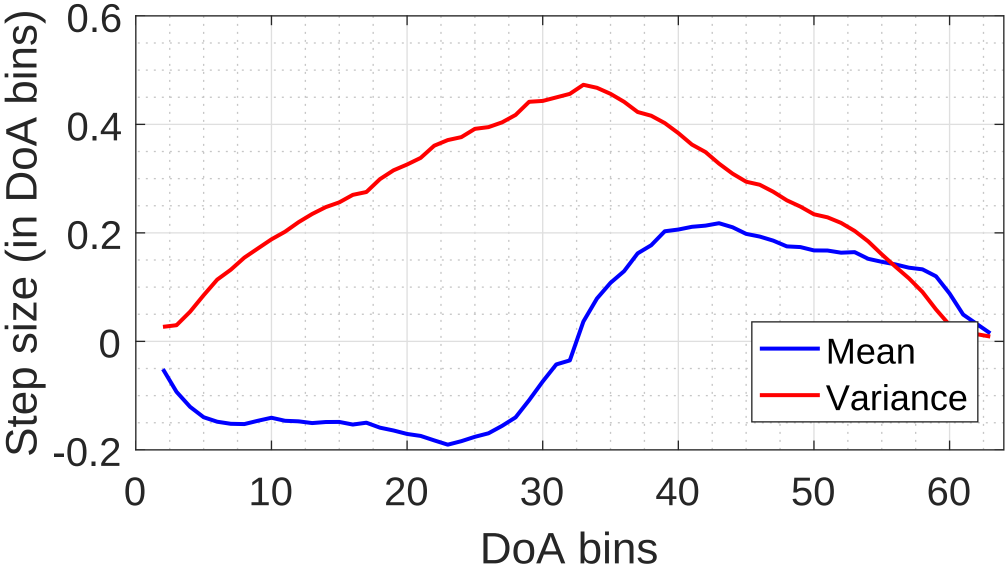

Figure 4.20: Mean and variance of the quantized DOA range (64 bins) generated from the 2014 Canadian Arctic Archipelago (CAA) training data set.

2. **How do PF and S-MAP perform if MOE is not exactly known?**

The main assumption in this work is that there is a maximum of $Q = 2$ DOAs per range-bin, one on each side of the surface. With MLE and MUSIC, we assume that there is either $Q = 0$

or $Q = 2$ targets per range-bin. But, S-MAP and PF have a transition model that can handle the transition between range-bins that have different numbers of targets (for example, see Algorithm 2 in Section 2.6.5.1). The main idea of these multi-target transition algorithms is that we use a transition model to keep track of the DOAs such that there is always $Q = 2$ DOAs at each state. These DOAs need not represent an actual target. This is useful in the case of $Q = 1$, where we should know whether this target is on the left or on the right side of the surface. If the model order is completely unknown, then MUSIC beamformer is our next option. However, for point-cloud trackers, the model order must be provided, even if it is not very accurate.

Since our real data are relatively wideband (about 15% fractional bandwidth), non of the standard model order estimation (MOE) methods can give a reasonable performance in the case of large number of targets relative to the number of array sensors. This problem was discussed in Chapter 3. The results in [1, 42] confirmed that the numerical tunning (NT) method also fails to handle the MOE problem in wideband systems. In addition, the authors in [1, 42] conducted all of their experiments for the case of $Q = 6$ targets. However, repeating the same experiments on the case of $Q = 2$ targets showed very satisfactory performance of the NT method in the wideband case. Moreover, normalizing the log-likelihood function with respect to the case of SNR $= -\infty$ (effectively, this is a no-target scenario) does help make most of the standard MOE methods perform as well as the NT method in the wideband case.

Figure 4.21 shows the eigenvalues of a data covariance matrix for the 15% fractional bandwidth scenario for $q = 0$, $q = 1$, and $q = 2$ targets. The simulation parameters are: $M = 21$, 100 Monte Carlo runs, and the training and testing data were generated for three SNRs: 10 dB, 20 dB, and 30 dB. We can see that the eigenvalue spread starts to show up at $q = 2$, especially at high SNR, which is why most of the standard MOE methods fail in these scenarios. Also, figure 4.22 shows the percentage correct (i.e. number of times the MOE is estimated correctly relative to the total number of simulated examples) plots of 7 MOE methods, which are: Akaike Information Criterion (AIC), Hannan and Quinn Criterion (HQ), Minimum Description Length (MDL), Corrected AIC (AICc), Vector Corrected Kullback Information Criterion (KICvc), Weighted-Average Information Criterion (WIC), and numerical tuning (NT). In the case of optimal MOE, the number of targets and their directions are estimated simultaneously. Color-coded plots are also shown in figure 4.23 for the estimated number of targets at each simulated range-bin for each of the 7 MOE methods, in addition to the actual number of targets, Q, in the worst simulated case scenario , which is when SNR $= 30$ dB and the data is wideband. All of these plots show that *most of the tested MOE methods can be used successfully for MOE in the wideband scenario if the log-likelihood values are normalized and the number of targets is small relative to the number of sensors*. Also, AICc and KIVvc methods failed here due to our specific choice of $M = 21$ and $p = 7$, which makes the denominator of their mathematical formula go to 0 in some cases.

In the next chapter, we will apply the MDL method with normalized log-likelihood values (N-MDL) under the optimal MOE formulation to estimate the number of targets and their direction, which will be integrated with the sequential surface-tracking methods introduced in this chapter, at each range-bin of the real radar-collected wideband data.

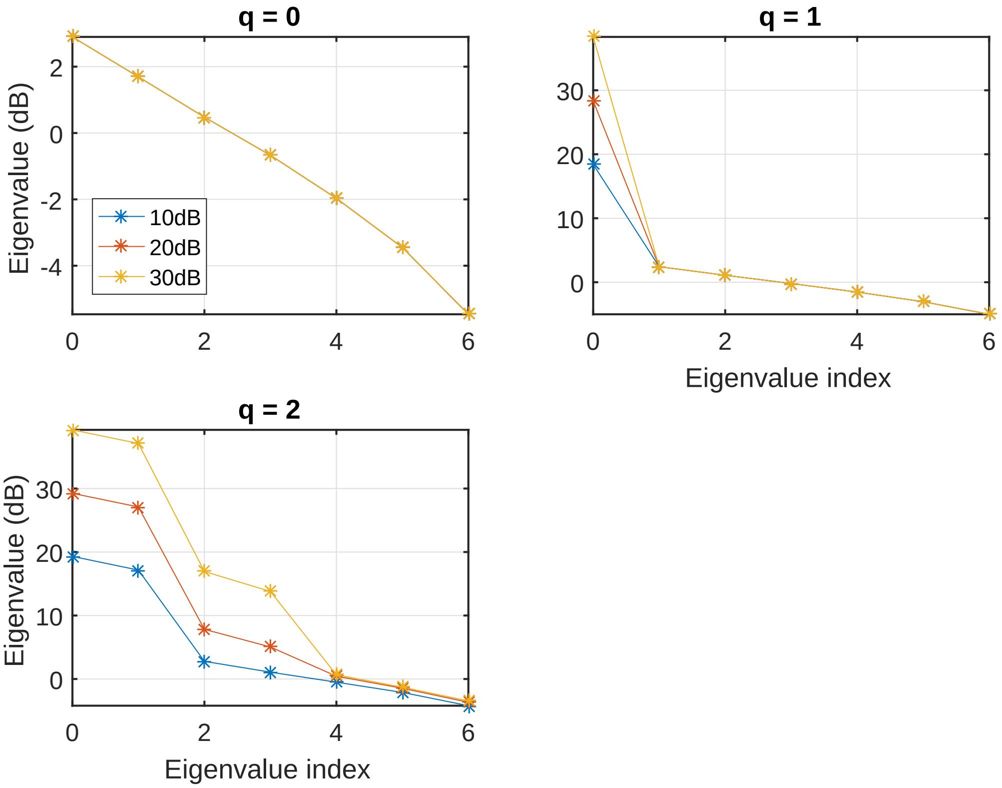

Figure 4.21: Eigenvalues of a data covariance matrix generated by simulating $M = 21$ snapshots and $p = 7$ sensors for the 15% fractional bandwidth scenario.

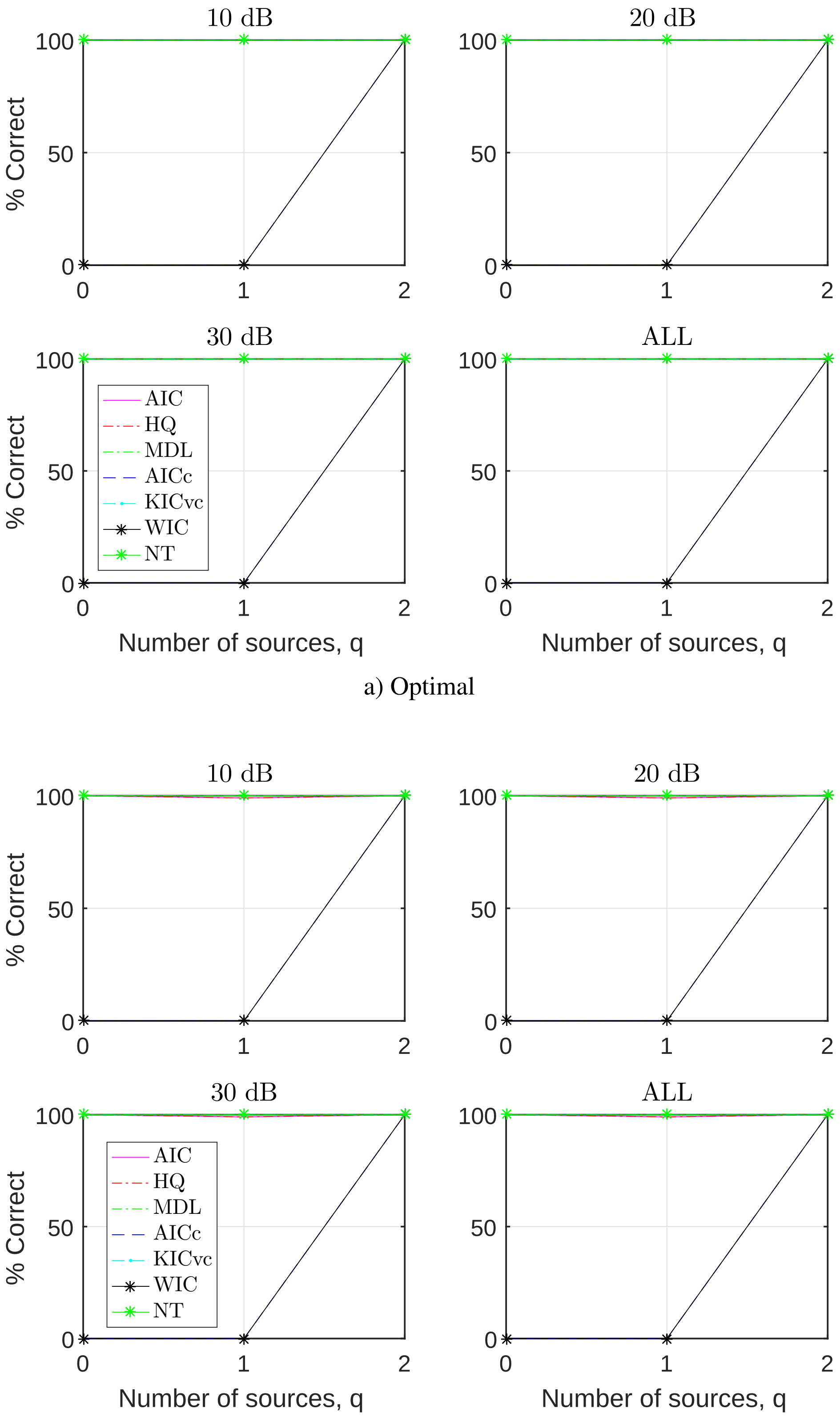

a) Optimal

b) Suboptimal

Figure 4.22: Percentage correct plots of the estimated number of targets for the 15% fractional bandwidth scenario.

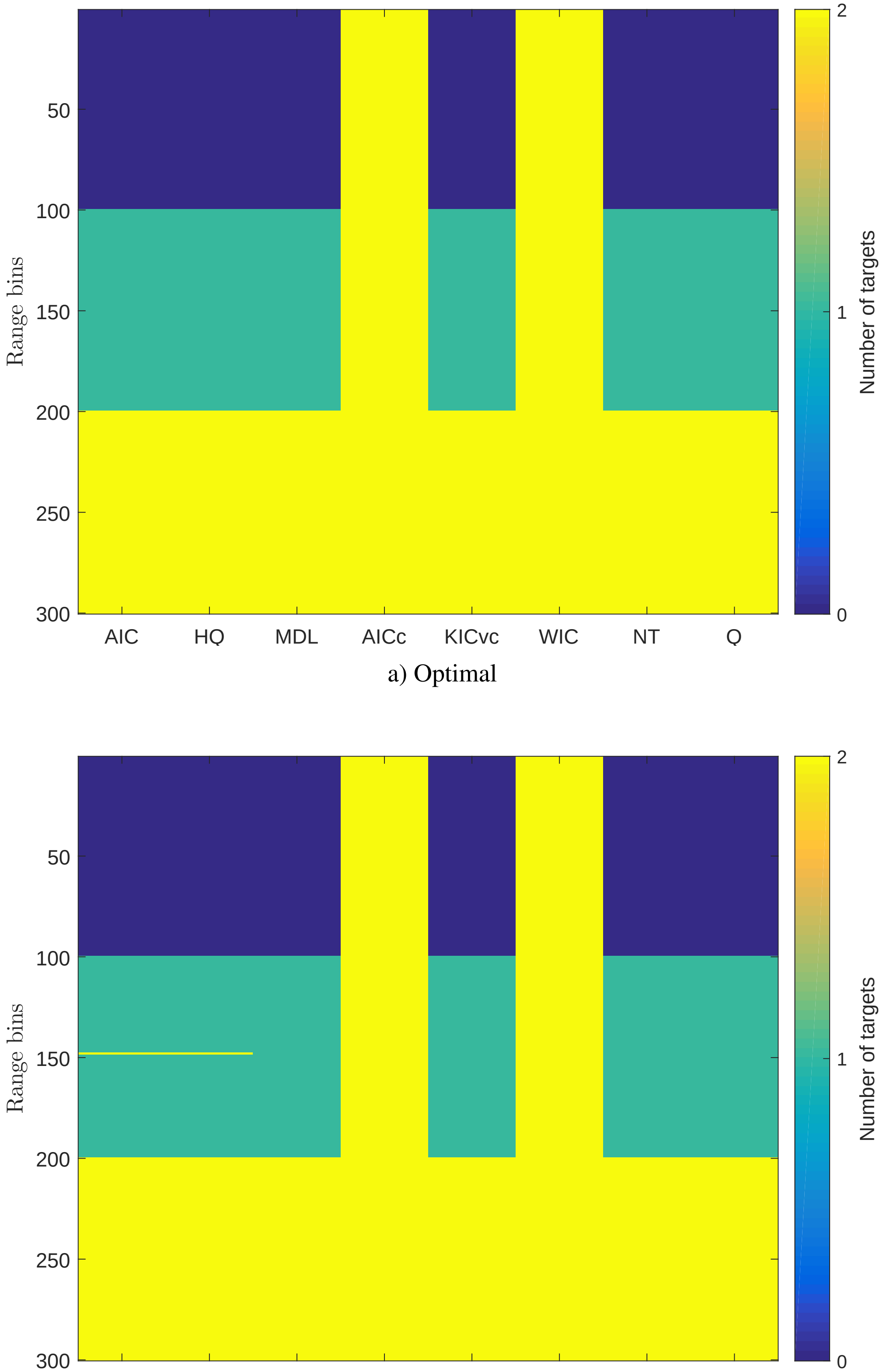

a) Optimal

b) Suboptimal

Figure 4.23: Number of estimated targets per range-bin for each of the 7 tested MOE methods, in addition to the actual number of targets, Q, for the 15% fractional bandwidth scenario with SNR = 30 dB.

3. **Can PF and S-MAP track distributed targets surface?**

   All of the simulations above assume point targets. But, for a distributed target scenario, where N_{D} point targets are collocated and separated by a small angular distance, $\Delta\theta_{\mathrm{D}}$, we expect $\Delta\theta_{\mathrm{D}}$ to be a new limiting factor of the tracking performance. Because our PF and S-MAP trackers are built around the assumption of having a maximum of $Q = 1$ target on each side of the surface, the larger $\Delta\theta_{\mathrm{D}}$ gets, the worse the estimation. So, this is a limitation of the mathematical model, and not of the estimation techniques. A more general mathematical model would either deal with more than just 2 sides of the surface (left and right) or relax the assumption of having a maximum of 1 target per surface side. But, these types of generalizations require first solving the wideband MOE problem for the distributed target scenario, which is not available at this point (open research problem). Also, dealing with distributed targets might require a new measurements model than that used in this dissertation, which is the standard model used in the literature. Thus, we do not tackle the distributed targets problem in this work and leave it as a future project.

Chapter 5

3D Image Formation Results of Ice-Sheets

5.1 Introduction

In this chapter, we describe the processing steps that led to the generation of the digital elevation models (DEMs) of the ice-bottom from the different data sets that were collected using CReSIS radars. We applied MUSIC to generate a 3D image and tracked the ice bottom in this image with the sequential tree reweighted (TRW-S) belief propagation algorithm to generate DEMs of the CAA. We also used the S-MAP algorithm to generate a few sample results for sea ice near Thule, Greenland and for ice-free land near Russell Glacier.

The quality of the MUSIC/TRW-S tracking algorithm is statistically evaluated by comparing the tracked ice-bottom layers from each range-line before and after applying manual corrections. In addition, the generated DEMs are self-assessed using crossover analysis where two flight paths intersect. The ice-surface DEMs, which are already available from the satellite imagery, were also used to provide a simple calibration of the steering vectors and to aid the tracker.

The collected data are partitioned into segments, where each data segment corresponds to the data collected over the time from turning the radar on until turning it off again. Then each segment is divided into frames, where each frame is, roughly, 50 km along the flight path. Each frame has an identifier or ID associated with it, which has the following format: yyyymmdd_ss_fff, which refers to the year (yyyy), month (mm), day (dd), segment number (ss), and frame number (fff). For example, the frame ID 20140401_03_037 provides the following information about the DEM: the DEM is created using the data collected on April 1st, 2014 from the 37th frame in segment 3. This naming style will be used from now on.

The DEMs were generated per frame in the following way. Assuming the dielectric constant of the ice to be 3.15 and using the derived surface range to determine the point of refraction, each tracked ice-bottom point is geolocated. Then, we perform Delaunay triangulation to tessellate the ice-bottom points. The final gridded product is a linear interpolation of all the points in the swath after removing the gridded points outside the boundary of the valid SAR pixels.

5.2 Ice-Bottom Tracking Using MUSIC and TRWS

The Canadian Arctic Archipelago (CAA) contains one-third of the global volume of land ice outside the ice sheets. But the basal topography of the outlet glaciers draining the CAA ice caps and its contribution to sea-level change is largely unknown. To measure the basal topography, the MCoRDS radar was used to collect data over the CAA islands (Ellesmere, Axel Heiberg, and Devon) during the NASA Operation IceBridge 2014 arctic campaign. Figure 5.1 shows the location of the CAA islands and the flight-paths of this mission.

To create the DEMs, we use MUSIC array processing to estimate the pseudo-spectrum (a value loosely related to the scattering intensity for the corresponding DOA) for a uniform grid of 64 cross-track wavenumbers that correspond to DOAs from -90° to $+90^\circ$ [11]. Figure 5.2 illustrates the beamformer output at one along-track location for 5 range-bins, $Q = 2$ targets per range-bin, and the FOV is quantized into 10 angular-bins. In this example, the beamformer output is a 5×10 matrix, where each row contains the pseudo-spectrum information from a single range-bin. The pseudo-spectrum is the inverse of the correlation between the array steering vector and the noise subspace at each angular-bin and is roughly related to the scattered energy. Then, the ice-bottom tracker tracks or estimates the row corresponding to the surface in each column. The estimate balances a cost function that considers a number of inputs including the pseudo-spectrum and the smoothness of the surface.

The characteristics of this work can be summarized as follow:

- We used the narrowband signal model.
- Only the center subarray of the P-3 radar array was used.
- We used a fixed model order for each range bin (i.e. number of targets) of 2.
- We applied a simple array calibration step to calibrate the center subarray using the surface DEMs.
- The ice-bottom tracker is used to track the surface from one elevation angle bin to the next (64 bins total) rather than tracking targets from one range bin to the next. In this way, solutions are forced to be single valued with respect to elevation angle.
- Three array beams were collected (left, center, and right). They were array processed separately, but then combined before tracking.
- The tracking is based on computer vision algorithms and not coupled with DoA estimation.

After array processing is done, we have a 3D image for each of the 3 beams, as shown in figure 5.3. Then, the three images are merged using a Gaussian-weighted sum of the three images to synthesize a single wide swath beam. The Gaussian weights are proportioned according to the transmit beam direction of the particular image. We call the image formed by taking the 3D pixels at a constant along-track position, a "*slice*". A slice contains information about the surface and bottom of the ice at a single range-line (i.e. along-track position), making it possible to visualize the ice surface and bottom simultaneously. An example slice is shown in figure 5.3. Note that the slices are in cylindrical coordinates with the vertical axis corresponding to the range and the horizontal axis corresponding to the elevation angle. Figure 5.4 illustrates the actual (Cartesian) geometry of a sequence of slices.

To improve the accuracy of the steering vectors, the ice-surface DEM, which is obtained from the ArcticDEM [68], was used to calibrate the steering vectors by adjusting the angular dependence using a low-order polynomial least squares fit between the radar-derived ice-surface and the ice-surface DEM [33, 69]. A region of data was used where the radar surface returns were very clear and the ice-surface scattering could be tracked accurately with a simple routine and then compared to the ArcticDEM surface elevation. The polynomial fit adjustment from the surface is then applied to the ice bottom for which there is no similar a priori information.

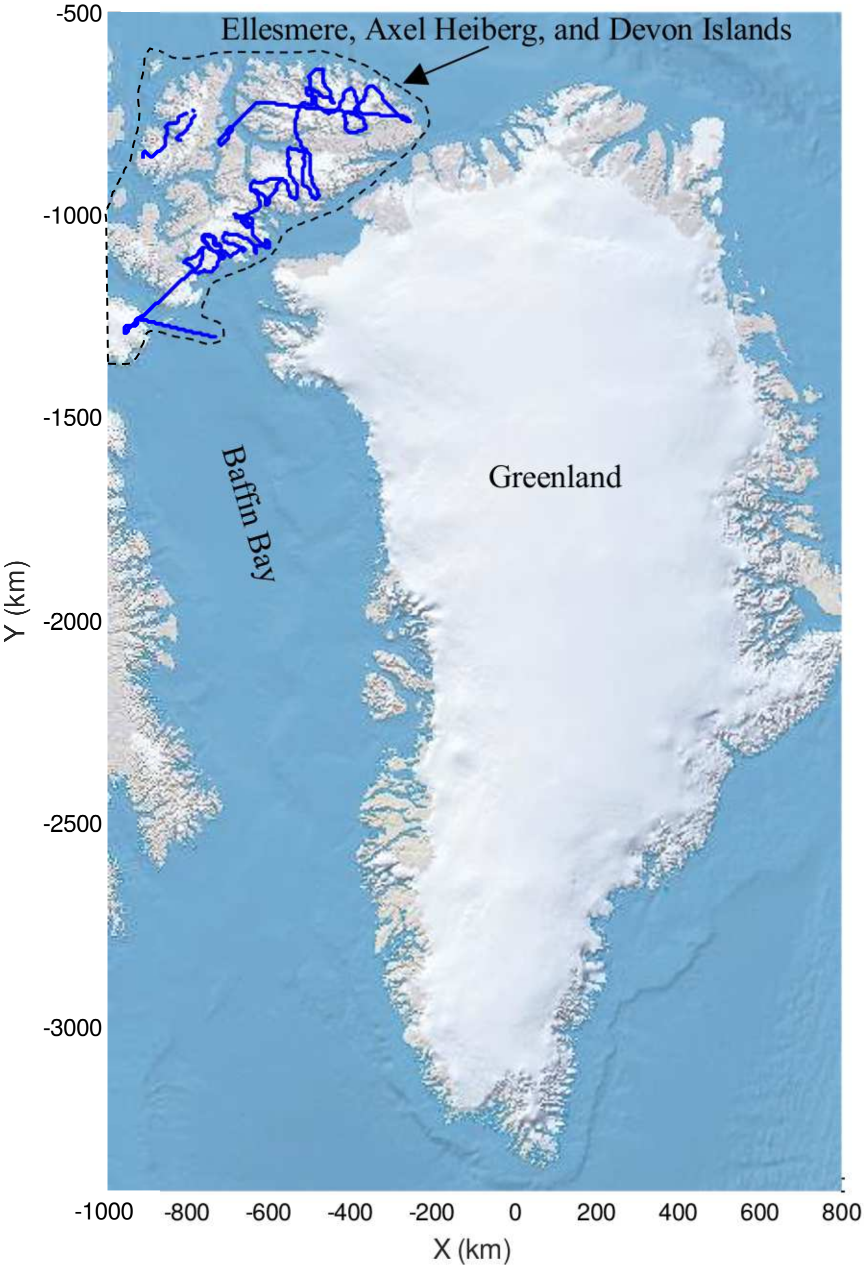

Figure 5.1: Canadian Arctic Archipelago islands along with the flight paths (the blue curve) for the radar data used in this work. Background raster image from NASA Natural Earth.

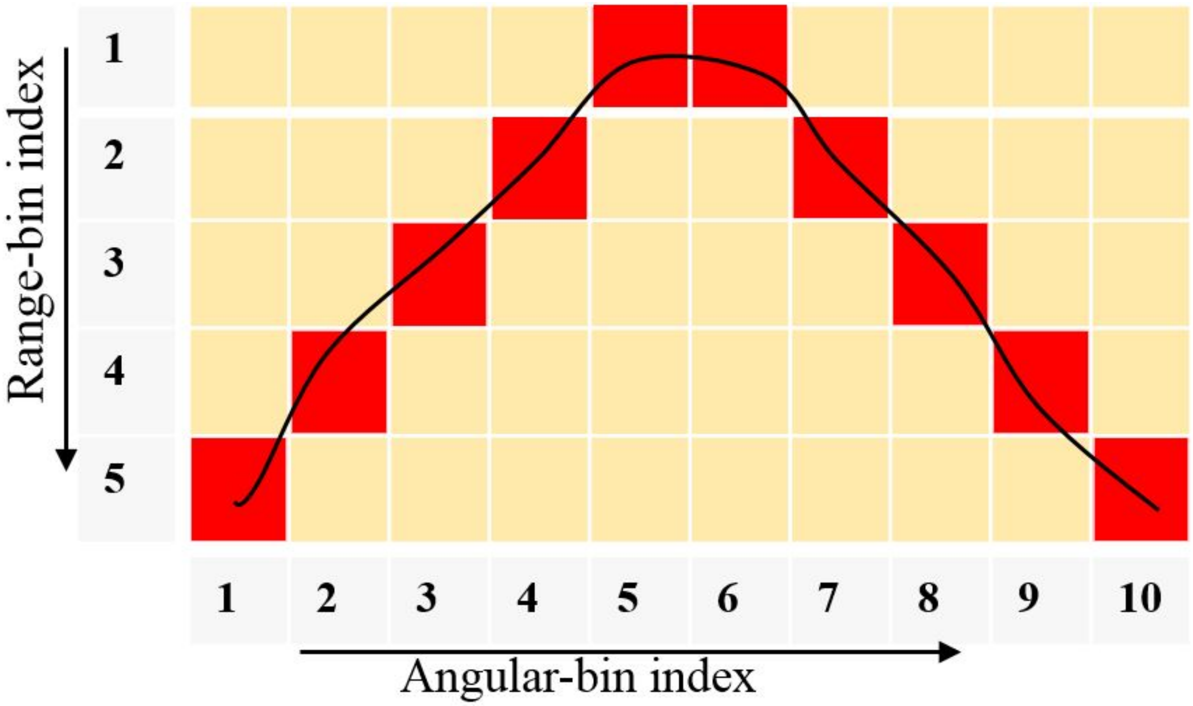

Figure 5.2: Illustration of the beamformer output for a single range line. In this example, we grid the FOV into 10 angular-bins and, assuming $Q = 2$ targets per range-bin, we use the MUSIC pseudospectrum from all these angular-bins to form an image, where each square represents one image pixel. The red squares are the pixels where the pseudo spectrum is highest. The tracked surface (the black curve) is formed by connecting these pixels such that the surface is smooth.

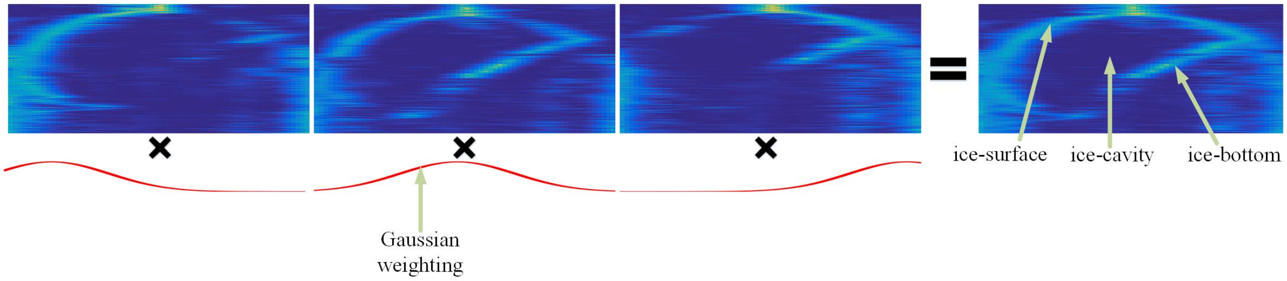

Figure 5.3: The merged image composed of three separate left-beam, nadir-beam, and right-beam images. The red curves represent the Gaussian weighting associated with each input image. The labeled output is shown on the right.

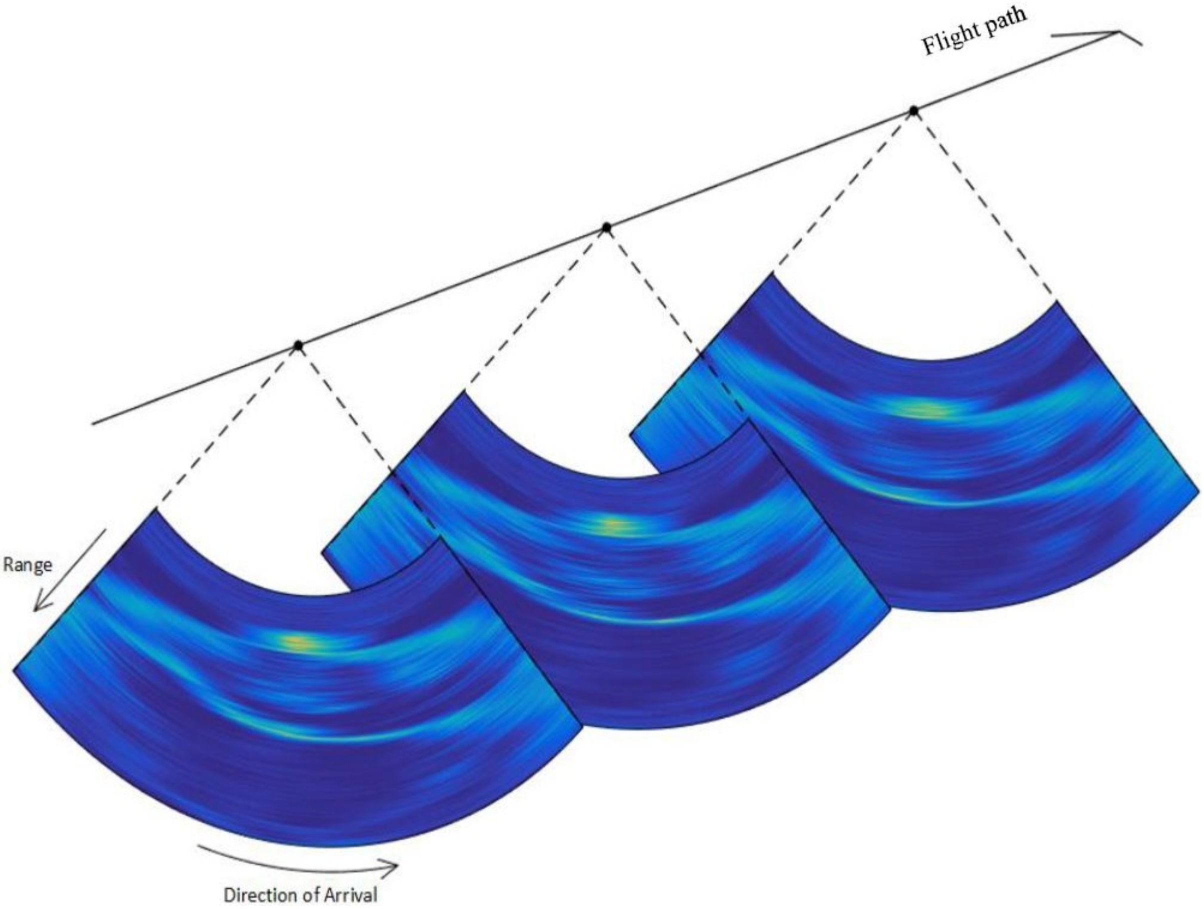

Figure 5.4: Along-track slices shown in cylindrical coordinates. Each slice represents the scattered power at a single range-line along the flight path.

5.2.1 MUSIC: Ice-Bottom Tracking Algorithm and DEM Generation Process

Since manual tracking of the ice-bottom is impractical on a large scale, we have implemented an automated technique for extracting the ice-bottom surface as well as a browser to visualize the 3D images [33, 70, 67]. We used the sequential tree-reweighted (TRW-S) algorithm [71] for this purpose. The particular algorithm used is described in detail in [67]. A brief review of the algorithm is also provided here, but is not the focus of this work.

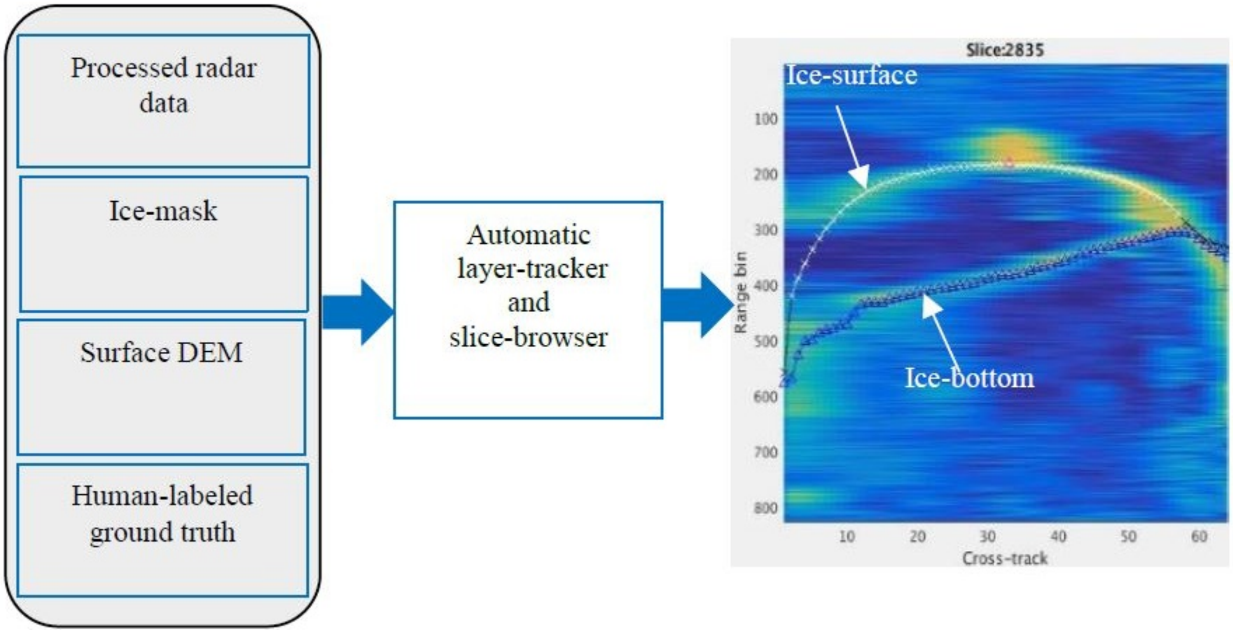

Figure 5.5: Input/output of the automatic ice-layer tracker

There are four main inputs to the layer-tracker (see figure 5.5):

1. The radar-processed data is the 3D image where the ice-surface and bottom needs to be tracked.

2. The ice-mask [72] is a binary raster that is used to determine at each DoA whether there is ice or not. This is useful to force the automatic layer-tracker to alter the cost calculation accordingly and forces the ice-surface and ice-bottom to merge where there is no ice.

3. For each angle of incidence in the 3D image, the a priori surface DEM from ArcticDEM is used to find an estimate of the range-time to the ice-surface.

4. Ground truth points indicate where the ice-bottom layer should pass through. These are human labeled and only available for the nadir direction when the tracker is first run. The tracker does not assume these points are perfect, but the cost function is lower for layers that pass through them.

The TRW-S tracker optimization is a message passing algorithm that performs inference on a Markov Random Field (MRF) by iteratively propagating messages between the nodes. The nodes in the MRF are the columns of the 3D image. Columns are aligned with the range dimension. Therefore, for every range line and elevation angle pair, there is a node and associated column of range bins. The estimated surface is single valued for each node so that the surface is only allowed to pass through a node once and the tracker's job is to determine which range bin this occurs at. For each node, connections are made to each of the four neighboring nodes. These connections are left and right (elevation angle dimension) and forward and backward (along-track dimension) as shown in figure 5.6. Each node stores a unary cost for each range bin and a set of four binary messages for each range bin. The four binary messages are the last messages passed to that range bin from the four neighboring nodes. A new cost message, J_{TRWS}, from range bin d_i of node i to range bin d_j of a neighboring node j is given by:

$$J_{\mathrm{TRWS}} = J_{\mathrm{U}} + J_{\mathrm{B}} + J_{\mathrm{I}}. \tag{5.1}$$

J_{U} is the unary cost for range bin d_i of node i that is sending the message. It is composed of three terms:

$$J_{\mathrm{U}} = J_{\mathrm{U}_i} + J_{\mathrm{U}_g} + J_{\mathrm{U}_b}, \tag{5.2}$$

where J_{U_i} is a pixel intensity related cost, J_{U_g} is a ground-truth related cost, and J_{U_b} ensures that the bottom does not go above the surface. The unary cost for each pixel is only computed one time and is not updated. J_{B} is the binary cost and depends on how the surface transitions from one node to the next and is used to control the smoothness of the surface. This allows the tracker to work through low quality regions where several pixel choices might be equally likely based on the unary cost only. The binary cost increases the likelihood that the range bin that produces the smoothest surface overall will have the lowest cost by applying a quadratic distance cost. The distance is the absolute value of the change in range bins, $|d_i - d_j|$. J_{I} is the summation of the most recent incoming messages to range bin d_i of node i from the other three nodes that are connected to node i (so *not* including from node j). The messages are updated on each iteration of the algorithm. They are a mix of unary and binary costs. The incoming messages are all initialized to the prior.

In general, the cost message to bin d_j of node j from node i is taken to be the minimum cost message from node i where the minimum is taken over all of the range bins d_i of node i. Therefore, many cost messages to bin d_j on node j are computed, but only the minimum cost message will be used. Due to symmetry properties of the quadratic distance used in the binary cost, only a subset of the possible transitions require the cost messages to be computed. As the algorithm iterates, the most recent cost messages, J_{TRWS}, are stored and they represent the state of inference.

In our implementation, once a fixed number of iterations have been reached, the algorithm is stopped and the final answer for any node i is taken to be the range bin, d_i, with the lowest cost. This cost is defined as $J_{\text{U}} + J_{\text{I}}$ where J_{U} is the unary cost for bin d_i of node i and J_{I} is the summation of the most recent messages from the (four) neighboring nodes of node i for range bin d_i.

The tracker [70] was modified in several ways to improve its performance. In [70], although messages are passed in all directions on each iteration, there is a preferential direction where the most recent message is taken from the current iteration rather than the previous iteration. The message costs in the preferential direction propagate across the entire field or graph in a single iteration. This causes a strong bias towards the side of the image that the preferential direction starts from. For example, when the preferential direction is left to right, the left-most side of the image has a stronger effect on the updated messages than all other columns because its message would be passed to all nodes in a single iteration. [70] dealt with this by alternating the preferential direction on each loop from left to right and then right to left and from up to down and then down to up. The issue with this solution was that the most extreme directions of arrival (far-left and far-right), where the signal quality is worst, were being given too much influence. Since we have ground truth at nadir and the signal quality is often best at nadir, the preferential direction was changed to be always outward from nadir. So on the left side of the image, the preferential direction is always toward the left and on the right side of the image, the preferential direction is always toward the right. These are shown by the green arrows in figure 5.6). In this way, the nadir column asserts the greatest influence. No change was made to the alternation between up and down directions so that each is the preferential direction 50% of the time.

The cost function has been updated from [70]. The unary term includes several components that we modified to improve the tracking. The first term is the template energy which was set by the mean squared difference between a template peak waveform and the image intensity surrounding the pixel in question. A single template was used on all pixels and was not scaled with the pixel intensity: a peak waveform that exactly matches the template intensity scores the lowest cost of zero while a peak waveform with a larger peak value than the template (and presumably higher quality) would score a higher cost because the mean squared difference is used. Instead of using the mean squared difference, we now use the negative of the correlation between the template and the waveform around the image pixel to set the cost.

Another term in the unary cost is the bottom location or bin in the nadir direction which is a priori information available at each along-track position. In [70] this was constructed to ensure the ice bottom layer passed beneath this bottom bin. The bottom bin cost was modified to force the ice bottom layer to pass within a 20-pixel neighborhood of the bottom bin rather than strictly beneath. This improved results when the bottom bin was too low due to errors in the human labeling of the nadir bottom bin. Although the bottom bin tends to be fairly accurate, the previous tracker implementation would allow the bottom layer to pass far beneath the bottom bin with no cost penalty.

The final term that was modified is a surface repulsion term that increases the ice bottom layer cost if it approaches the ice surface. This was necessary because the ice surface is often stronger and more consistent than the bottom and there is no other mechanism in the cost function to keep the tracker from choosing the surface instead of the bottom. Combined in this term, but not fully described in [70], was an ice mask term that overrode this term when there was no ice present. In this case the ice bottom was forced to be equal to the ice surface to indicate zero ice thickness. The issue is that at the boundaries between ice and no-ice, the ice bottom often gradually separates from the ice surface. To accommodate this, the surface repulsion term was modified to gradually increase away from no ice edges and another term was added to attract the layers together as they approach a no ice region. This modification helped remove artificial discontinuities at the no-ice/ice transitions.

The binary cost was also improved, where in [70], the smoothing was set to produce a constant range layer in the cylindrical coordinate system of the image. The problem is that a constant range layer in the cylindrical coordinate system is a circle in Cartesian space. The smoothing term was modified to set to lowest cost an ice bottom layer with the same range-slope as the ice surface. Although this is still not a flat surface, it is generally flatter and more realistic than the circle and was simpler computationally than calculating a flat ice bottom in Cartesian space which must account for ice refraction from a non-flat ice surface layer.

After the layer tracker is run, the layers are visualized by viewing the layer overlaid on the radar image in three dimensions along with a corresponding satellite image map and ice mask map that shows the flight track and image pixel locations. Where needed, the bottom layer is manually corrected by adding additional ground truth points to the 3D image and corrections are made to the ice mask. The tracker is then rerun in small neighborhoods with this new information to correct issues. Poor data quality areas are also tagged so that they are not included in the final output.

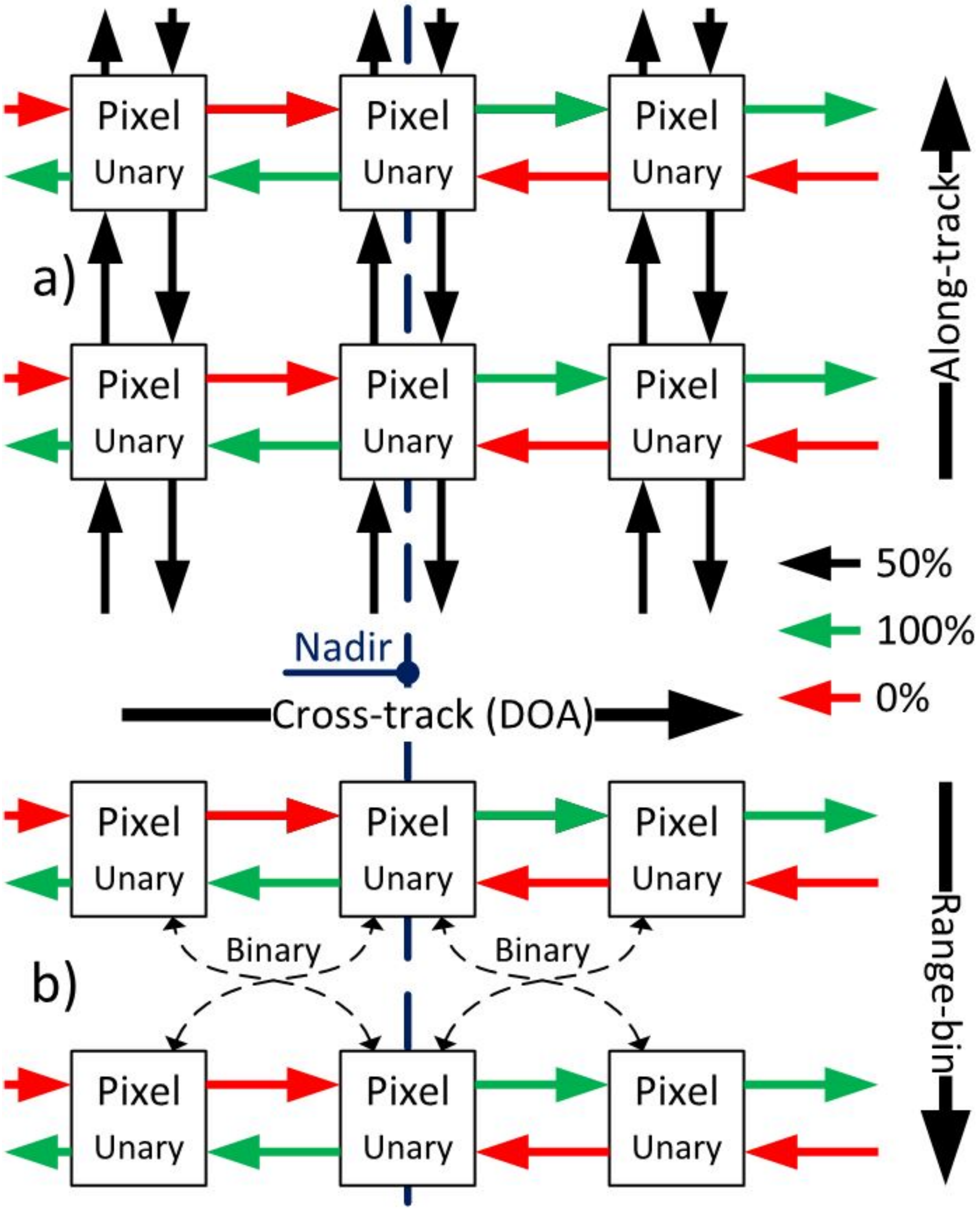

Figure 5.6: Flow diagram showing how TRW-S algorithm works by passing cost messages to and from neighboring pixels. The arrows represent the preferred direction of information flow. The colors of the arrows indicate the frequency of the preferred direction aligning with the arrow.

5.2.2 MUSIC: DEM Generation Results

After the cross-track slices have been processed and tracked at every range-line along the flight-path, we are ready to combine them to form the ice-bed tomography images of the scene, where the x-axis and y-axis represent the location of the imaged ice-bottom, and the z-axis is color-coded to convey the elevation information referenced to the WGS-84 ellipsoid.

Using MUSIC and TRW-S, we have processed 102 DEMs from the Canadian Arctic Archipelago in Greenland from 5 segments: 20140325_05 (2 DEMs), 20140325_06 (1 DEM), 20140325_07 (5 DEMs), 20140401_03 (48 DEMs), and 20140506_01 (46 DEMs). The complete set of the generated DEMs can be found here [31], which contains all the ice-surface and ice-bottom DEMs that we have processed. An example DEMs are shown in figure 5.7.

In the next two sub-sections, we will assess the quality of the generated DEMs from two perspectives. First, we self-assess our results by generating the DEMs of the overlapped areas from the crossing tracks (crossovers), and second, we present and discuss several statistics of the error between the output of the automatic layer-tracker before and after manual corrections (MC) are applied. By MC we mean the manual correction by adding more ground truth, fixing the ice mask, and the data quality labeling step.

5.2.3 MUSIC: DEM Crossover Analysis

Here, we evaluate the self-consistency of the generated DEMs where flight paths cross over each other and two measurements are made at the same location. Quality control has been applied to all the results in this section; most importantly this includes the manual corrections.

We have a total of 20 crossovers from this data set, but here we have only illustrated two, and the complete set of crossovers can be found here [31]. Figure 5.7 shows two crossover examples over ice, which are also representative of the types of error patterns seen in the 20 crossovers. Each example has four plots, which are the zoomed version of the original DEMs with the intersection marked in red along with an inset showing the error map, and a sample slice from each DEM at the intersection of the two flight lines showing the ice-surface and ice-bottom after applying the automatic tracker (detailed in the previous subsection) in addition to manual corrections. The flight line for each DEM is shown in black. The location of the 3D slice at the intersection of the flight lines is shown in the error map and marked to indicate the left and right DoA portions. In the slice view, the left and right DoA portions are marked in red and white, respectively. The difference between the DEMs is the crossover error since, from a self-consistency standpoint, the two DEMs would ideally be the same and the difference would be zero. Table 5.1 shows the statistics of the overlapped DEM errors for the crossovers in figure 5.7. Over all 20 crossovers, the mean absolute error is 23 m, the median absolute error is 11 m, and the root mean square-error (RMSE) is 38 ± 7 m (average RMSE$\pm\sqrt{\sigma^2_{\text{rmse}}/N}$, where σ^2_{rmse} is the variance of the RMSEs and $N = 20$). If we assume Gaussian statistics for the errors in each of the individual DEMs, then the RMSE for the crossovers that are shown here should be $\sqrt{2}$ larger than the RMSE of the individual images. This accuracy is acceptable since the ice thickness is about 1000 m.

Figure 5.8 shows the change of the average RMSE over all 20 crossovers as the largest errors are removed. This plot shows that the lower 70% of the errors have an RMSE of 10m. Table 5.2 gives the same results as in Table 5.1, but with the largest 10% of errors removed. The resultant reduction in error statistics is larger than what would be expected for Gaussian distributed errors. Also, in figure 5.9 we plot the RMSE of the errors of the 20 DEM crossovers before and after trimming the largest 10% of the errors. The RMSE values were sorted in a descending order for better visualization. We see that 15 of the 20 crossovers have an RMSE $<$ 50m before trimming, which goes down to less than 25m after trimming. Also, there are 5 crossovers with RMSE $<$ 5m before and after trimming. The main source of the larger error statistics comes from the 5 crossovers with RMSE $>$ 60m, including the crossover example presented in figure 5.7-B, which is the one with the largest RMSE error among all the 20 crossovers. These results tell us that there is usually a good match between the overlapped DEMs, but there are few large errors that are causing the mean statistics to be large (i.e. a heavy tail distribution due to outliers). From examining figure 5.7-B, if the tracker fails to track the correct surface, a whole region may have a very large error and creates a heavy tail distribution.

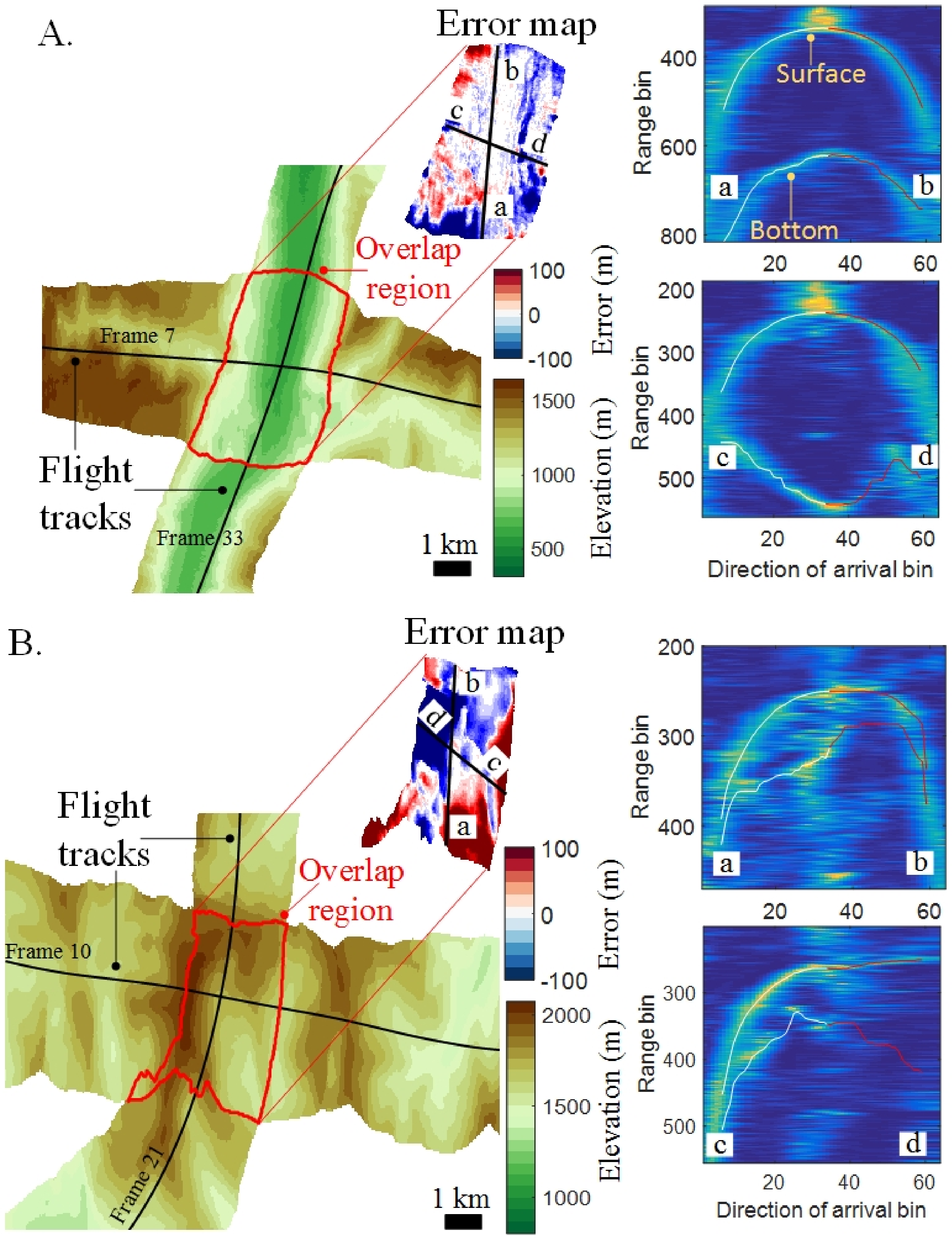

Figure 5.7: Examples of a consistent (A) and inconsistent (B) crossovers. The inconsistent crossover is caused by weak basal scattering for which the tracker fails. The DEM for each flight line is shown along with the difference between the two. Example slices from the 3D images used to construct the DEMs are also given.

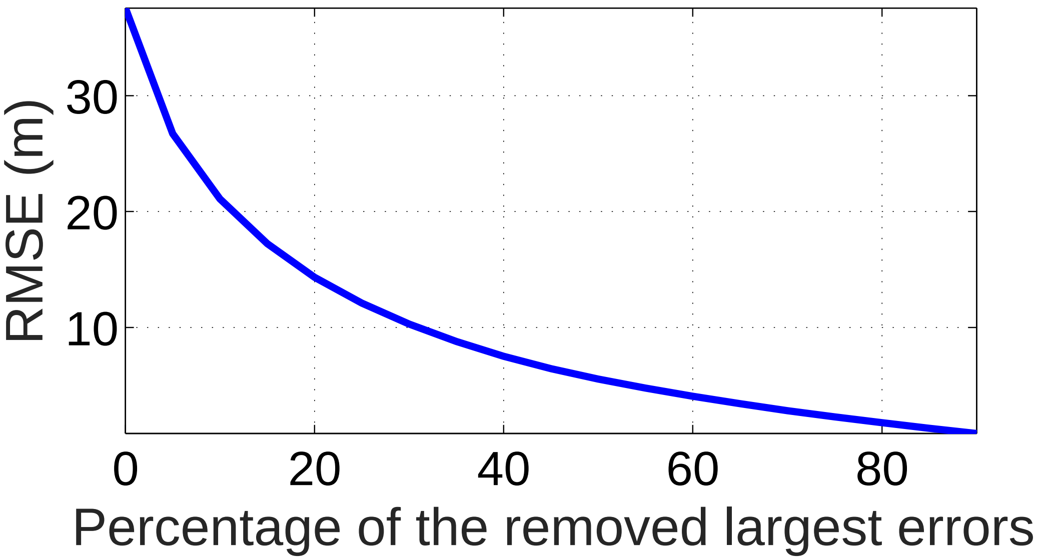

Figure 5.8: Change of the average RMSE as we remove a percentage of the largest errors.

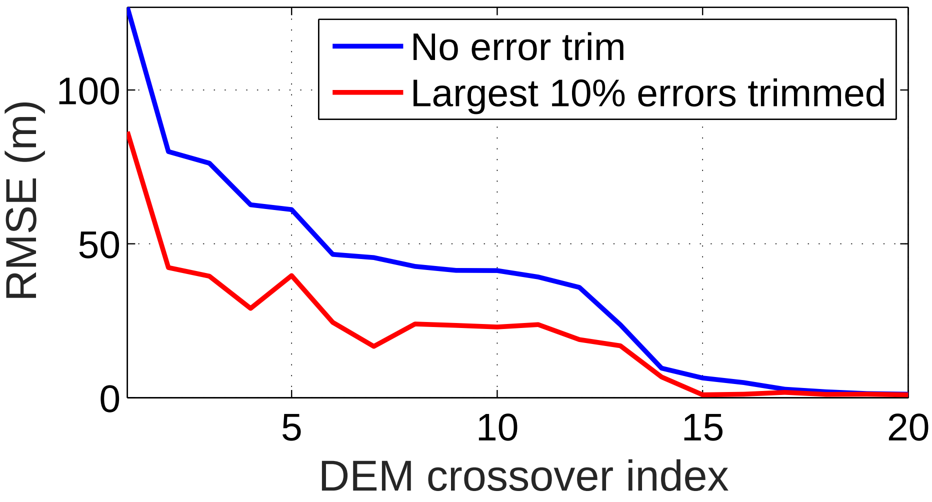

Figure 5.9: Sorted RMSE of the differences of the 20 DEM crossovers before and after trimming the largest 10% of the errors.

The DEM errors can result from several causes. We divide these into four categories:

1. **Poor data quality**: This is the most severe type of errors. It is due to shadowing and weak backscatter, or data recording issues. Different flight paths and improved instrument parameters may improve this category, but these causes cannot be changed in post processing. For example, in figure 5.7-B, there seems to be no bottom data in the rightmost angular bins of the 3D slice example of frame 10. In this case, there is no guarantee that this portion of the ice-bottom layer is correct.

2. **Errors due to suboptimal array processing**: The MUSIC method is known to be suboptimal to MLE [73] and we assume a fixed model order of 2 even though the scene in general may have more or less than 2 scattering sources. The beamformer was setup to scan through 64 DoA bins with uniform sampling in wavenumber domain. This DoA sample spacing limits the accuracy of the DoA resolution. For example, in figure 5.7-B we can see that there

are several targets near the first half of the bottom layer of frame 21.

3. **Tracking error**s: The tracker does not perform an exhaustive search of all paths (NP-hard problem) and therefore the ice-bottom result may not be the best regardless of other deficiencies. In areas where there are no data, even a trained analyst cannot predict for sure where the ice-bottom layer should pass through. This problem is clearly evident in figure 5.7-B.

4. **Radar view angle**s: The radar look angle or view is different for the two overlapped DEMs, which makes the imaged surface look different to the radar in each case.

As a sanity check, we have also performed the crossover analysis on the surface DEMs that were generated using the radar collected data and found that the error statistics are almost zero for all the tested crossovers. This is expected because the surfaces are all pulled from the ArcticDEM and should be the same within the interpolation errors of the software (the surface is linearly interpolated onto the radar data and then linearly interpolated again to form the crossover DEMs used to check the software).

Table 5.1: Statistics of the errors of the overlapped DEMs in figure 5.7.

Figure 5.7	**A**	**B**
Mean error [m]	29	86
Median error [m]	16	45
RMSE [m]	47	127

Table 5.2: Statistics of the errors of the overlapped DEMs in figure 5.7 when the largest 10% of the errors were removed.

Figure 5.7	**A**	**B**
Mean error [m]	19	62
Median error [m]	13	37
RMSE [m]	25	87

5.2.4 MUSIC: Layer Tracking Assessment

Here we assess the ice-bottom tracking results by looking at statistics of the difference (measured in range-bins) between the MC output, which has been manually corrected, and the result with no MC (NMC), which is the direct output from the automatic layer-tracker. Results are averaged over all 102 frames in this CAA data set, where each frame contains approximately 3332 slices. The reference layer is the MC ice-bottom layer. Thus, when the error is positive it represents the number of range-bins the NMC tracking result is above the MC tracking result. Note that the layer data from the first and last 5 DOA-bins, which correspond to the near-grazing angles, were removed in this comparison and in the generated DEM crossovers, as shown in the slice plots in figure 5.7. At these angles, the effective array aperture is very small and the received echoes are weak, which can reduce the quality of the data.

Table 5.3 shows the average mean, median, and RMSE of the absolute error. Based on our previous published results [70], the old algorithm had an average mean error of 11.9 range bins over seven test frames, whereas the new algorithm has an average mean error of 4.5 range bins over the same test frames. Figure 5.10 shows the cumulative distribution function of these errors. We see that $\sim 52\%$ of the errors are 0 (i.e. identical), $\sim 85\%$ of the errors are within 5 range-bins from the MC results, and $\sim 95\%$ of the errors are within 25 range-bins from the MC results. Also, figure 5.11 shows the RMSE of the 102 frames that we have in the CAA data set. The RMSE values were sorted in a descending order for better visualization. We see that there are 89 frames of the 102 frames with RMSE $<$ 30 range-bins, 46 frames with RMSE $<$ 10 range-bins, and 26 frames with RMSE $<$ 5 range-bins.

These errors arise from different factors related to the error types mentioned in the previous subsection. From a qualitative inspection, the largest errors occur when the wrong layer is tracked, which often means a few manually placed ground truth points allow the algorithm to track the correct layer.

The error statistics discussed in this section show a good tracking capability, but with limitations where data quality is poor. In some cases, the MC result will also have errors, even for a trained analyst, especially in the places where the data quality is low (e.g. due to weak target echoes).

Table 5.3: Statistics of the layer-tracker errors (measured in range-bins).

Average mean error	Average median error	Average RMSE
10	6	19.5

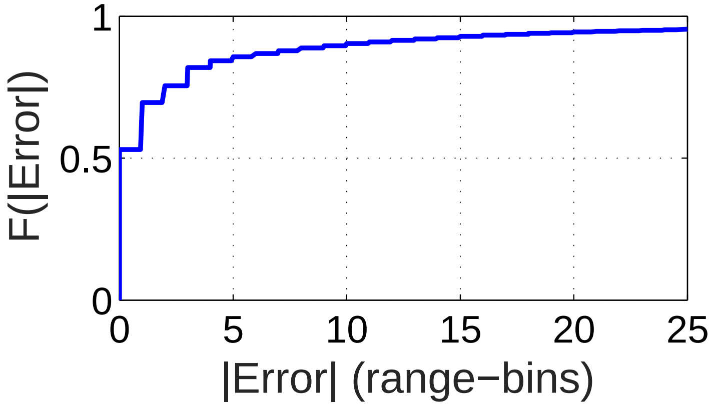

Figure 5.10: Cumulative distribution function of the distance, measured in range-bins, between the tracked ice-bottom layers before and after manual corrections have been applied.

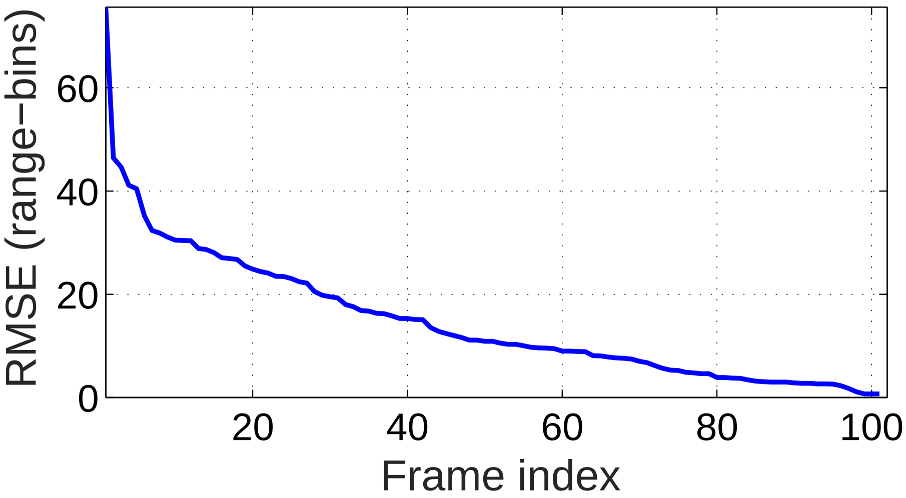

Figure 5.11: Sorted RMSE of all the frames in the CAA data set that we processed.

5.3 Ice-Bottom Tracking Using Sequential MAP

In this section we present our results of the S-MAP tracker applied to real wideband data collected by the MCoRDS CReSIS radar from Russell glacier in Greenland during the 2011 arctic campaign. As we did in the beamforming-based tracker, we only process the data collected by the center 7 sensors (i.e. the middle subarray) mounted on the fuselage of the P-3 aircraft used in this campaign. Signal bandwidth and center frequency are same as before as well. However, rather than operating the radar in a 3-beam mode (left/center/right) with a single medium-gain setting as in the CAA 2014 campaign, here the radar was operated in a single beam mode with two receiver gain settings: a low gain mode for imaging the ice-top and a high gain mode for imaging the ice-bottom. Thus, here we do a vertical fusing of the two tracked images as opposed to a horizontal fusing in the case of the CAA 2014 dataset.

The S-MAP tracker tracks the ice-bottom along range-bins and no tracking information is passed from one range-line to the next (i.e. 1D tracker). *From now on we will use the term 'slice' to refer to the 2D cross-section at one specific range-line*. (The tracker tracks one slice at a time.) The initial range-bin in each slice comes from a nadir ground truth, which are obtained by expert human annotators aided by automatic tracking methods [67]. Since these ground truth points are not always accurate to the pixel level, the tracker is set to start searching for the initial point three range-bins before the ground truth point.

Each range-bin is assumed to have a maximum of $Q = 2$ targets, one on each side of nadir. The continuous FOV is restricted to ±70°. The number of targets and their directions are estimated jointly (i.e. optimal model order estimation) using optimal normalized MDL (N-MDL), which was explained in Chapter 3. Since, usually, nadir data have the best quality (unless the receiver is saturated by the strong nadir echoes), we start the tracker at ±2° around nadir at the initial range-bin. The tracker decides that the tracking task is complete for each slice once it reaches either end of the FOV.

In the following sections, we present and assess the quality of our S-MAP tracking results from different perspectives.

5.3.1 S-MAP Tracker: Bounding Models and Prior pdf

The first piece of prior information that is given to the S-MAP tracker is the bounds over which the optimizer searches for the answer. Here we suggest four methods (models) to perform this task.

1. **Model 1: Default bounds**:

   Here, we use the flat-earth model given in Section 2.6.5. This is the basic model used in all the simulations of Chapter 4. So, applying this model to real data helps us to understand how practical our tracking results and conclusions are that were presented in the Chapter 4.

2. **Model 2: Fixed wide bounds**:

   Here, we fix the bounds to be ±5° around the mean DOA defined in equation 2.28. The goal of this model is to test the tracker's behavior in too wide bounds scenarios.

3. **Model 3: Slightly wider bounds**:

   Here, we set the the upper bound (or lower bound for left targets),θ^{ub}, to 3 times the default value whenever it drops below some threshold. In other words, for right the hand side of the surface, $\theta^{ub}_{\text{new}} = \mu_\theta + 3f(\Delta\theta)$ if $f(\Delta\theta) \leq \theta^{ub}_{\text{t}}$, where θ^{ub}_{new} is the new upper bound and θ^{ub}_{t} is the threshold value, which is 0.5° in our case. Usually, the DOA bounds drop to a fraction of a degree soon after the tracker starts in case of high altitude radar imaging as well as far-from-nadir elevation angles. A continuous version of this model is also implemented based on a heuristic mathematical formula.

4. **Model 4: Geometry-based bounds**:

   This model is derived from the geometry shown in figure 5.12 and the bounds, around the mean value, are given as follows:

   $$\theta_{\text{geom}} = \pi/2 - \theta - \sin^{-1}\left(\frac{r_1}{r_2}\sin(\pi/2+\theta)\right) \tag{5.3}$$

   where all the symbols are defined in figure 5.12. The effect of refraction of ice-bottom targets is accounted for in the implementation of this model.

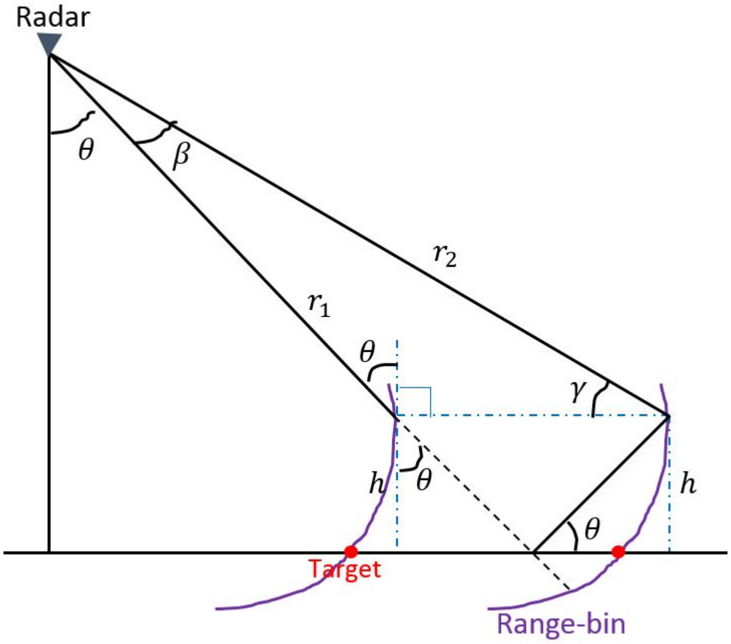

Figure 5.12: Geometry of Model 5 for bounding the S-MAP tracker (used for deriving equation 5.3).

These models sever as an upper bound for the right target and a lower bound for the left target. These models are meant to study the effect of the bounds on the quality of the tracked slices.

The tracked layers in all of the following results are laid over a MUSIC pseudo-spectrum background (64 DOA bins and fixed $Q = 2$ targets are assumed) to better visualize and understand the traced layers and to guide us in our visual assessments. We generated results for two layers: ice-top, where we used sea ice data frame 20110417_04_001 (this is high altitude relative to other some frames), and ice-bottom, where we used data frame 20110313_01_001. We chose these two specific frames among others to generate our results and do our assessments because the data of image 2 are not affected by receiver saturation in almost all of the slices, which is a major problem in this 2011 campaign data, and also have reasonably good data quality. However, here we present sample results for an ice-bottom only since it is the focus of this work. Note that the tracked surfaces are plotted in the DOA-range domain, where the elevation angle axis (the x-axis) is restricted to ±70° and the range axis (y-axes) are forced to be matched for each plot for fair assessment even though the curves may start and end at different range-bins depending on the bounding and prior pdf used in generating these plots. Thus, we stamp the DOA tracking results with the used bounding model and prior pdf for storage and for comparison against other tracking techniques or ground truth.

N-MDL is used for model order estimation. Few examples will be presented at the end of this section to show the performance of N-MDL on real data, which is not presented in [1] where this method was first suggested (the N-MDL is tested using 1D and 2D simulation data only and for 0 to 6 targets in [1]).

From the many tests we performed, we realized that the geometry-based model (Model 4) is the best in most scenarios. Thus, here we presents our tracking results using Model 4 and two types of prior pdfs, Gaussian and uniform. The results are intended to show different tracking behaviors based on the prior information, which includes both of the prior bounds and the prior pdf. These results are presented in figures 5.13 to 5.19 for 7 different scenarios. In each example, there are two plots: the one plot shows the whole tracked slice and the other plot shows a zoomed-in cross-section of the slice to show the tracking behavior at different stages of the tracking process.

Define σ_θ as the standard deviation of the prior Gaussian pdf, k_σ as a scaling factor of σ_θ to test the effect of larger and smaller values of σ_θ, and k_b as a scaling factor of the bounds to test the effect of wider and narrower bounds on the tracking performance. Default values are $k_\sigma = 1$ and $k_b = 1$. Now we list the different tested scenarios and give our observations and conclusions in the end.

1. **Scenario 1**: *Gaussian prior pdf with default bounds and default standard deviation*. In this scenario, we use the default values of the bounds and σ_θ defined in equations 5.3 and 2.29, respectively. Figure 5.13 shows the result of this scenario.

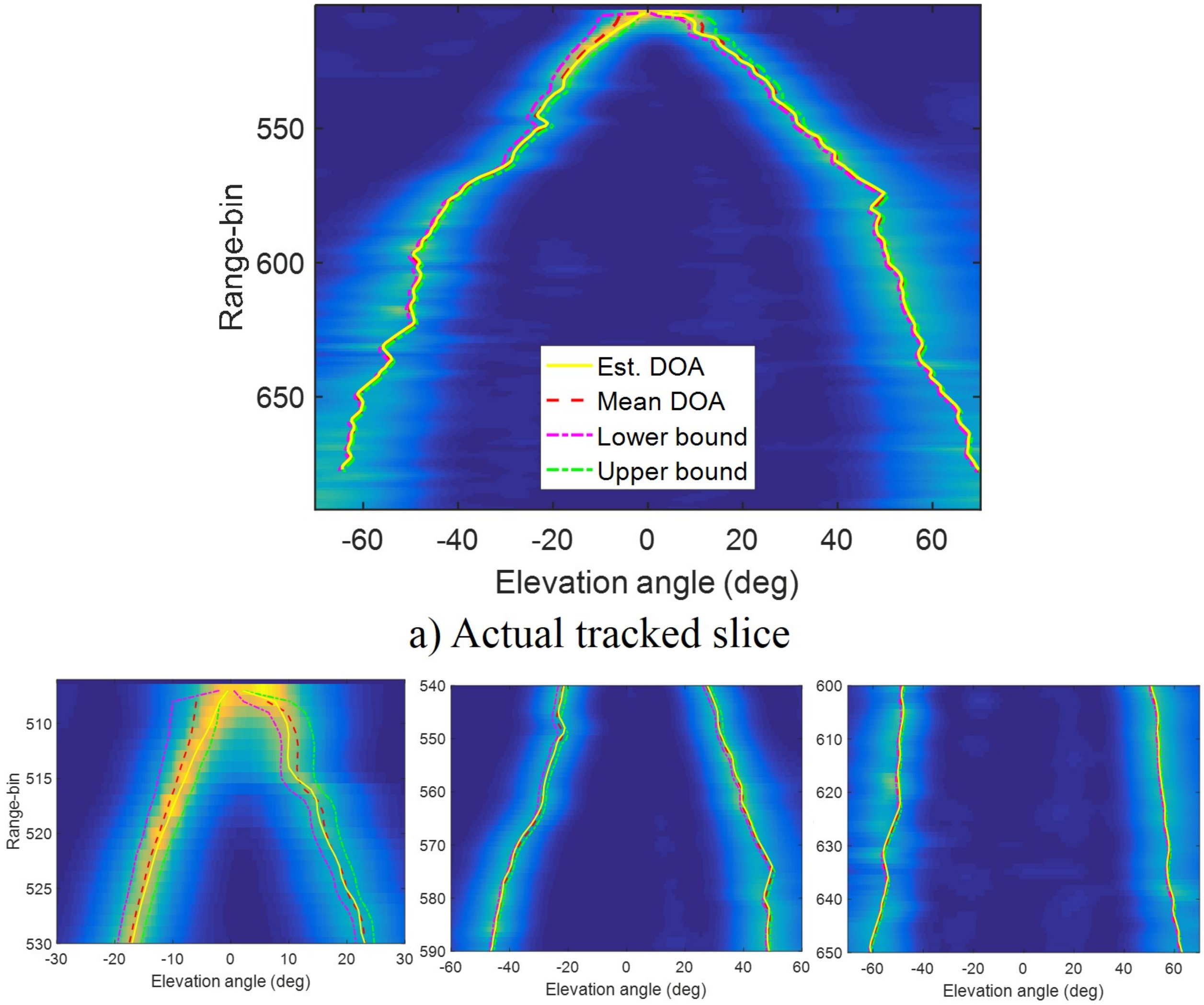

a) Actual tracked slice

b) Zoomed-in cross-sections

Figure 5.13: S-MAP result for Scenario 1: Gaussian prior pdf with default bounds and default standard deviation.

2. **Scenario 2**: *Gaussian prior pdf with narrow bounds and default standard deviation*. In this scenario, we scale the default value of the bound down by $k_b = 1/2$, but kept the default value of σ_θ. Figure 5.14 shows the result of this scenario.

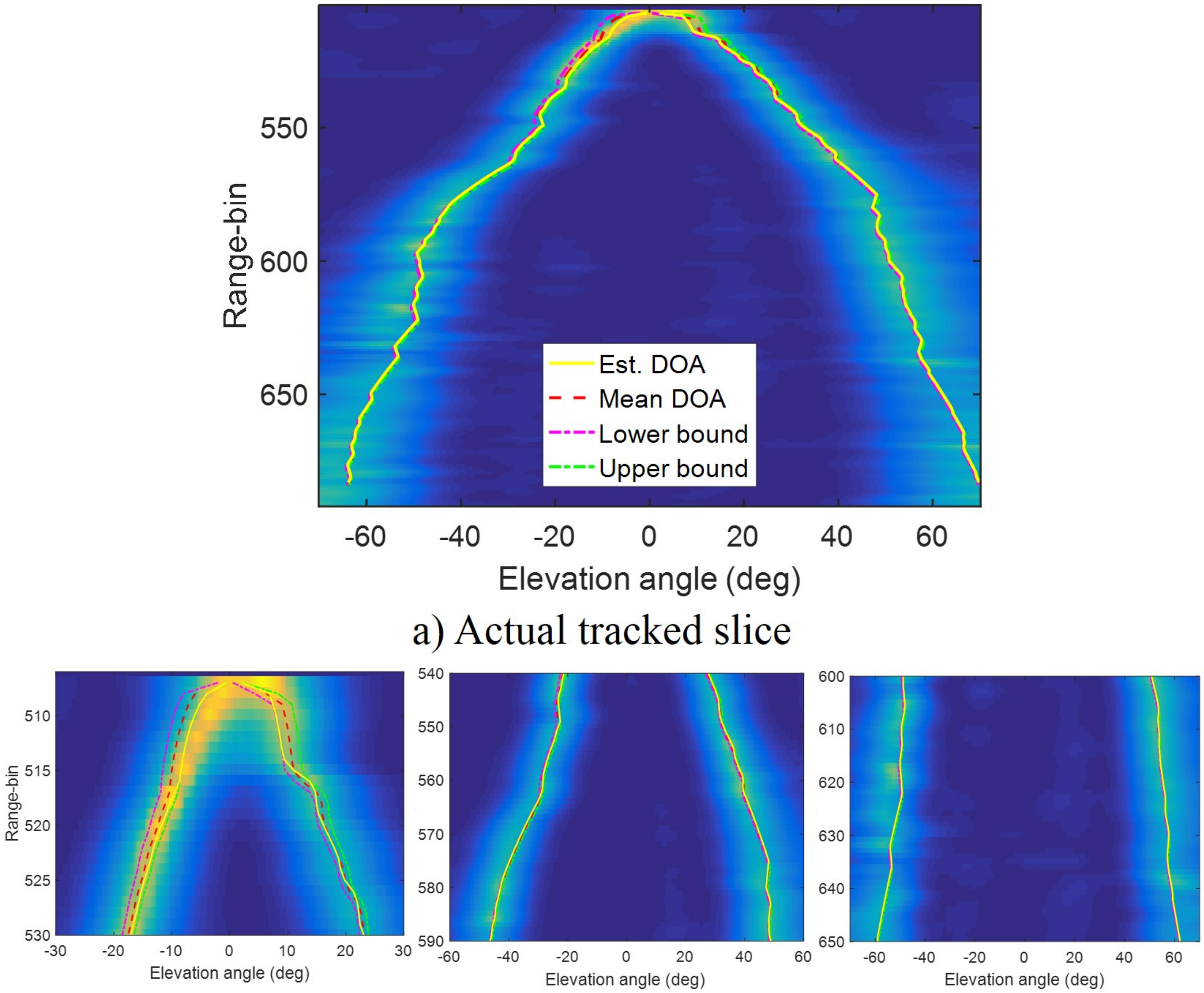

a) Actual tracked slice

b) Zoomed-in cross-sections

Figure 5.14: S-MAP result for Scenario 2: Gaussian prior pdf with narrow bounds and default standard deviation.

3. **Scenario 3**: *Gaussian prior pdf with wide bounds and narrow standard deviation*. In this scenario, we set the bounds to be ±5° around the mean, and we scale σ_θ down by $k_\sigma = 1/4$. Note that ±5° bounds are much more than the standard values of the bounds, especially far from nadir where σ_θ drops to a fraction of a degree. Figure 5.15 shows the result of this scenario.

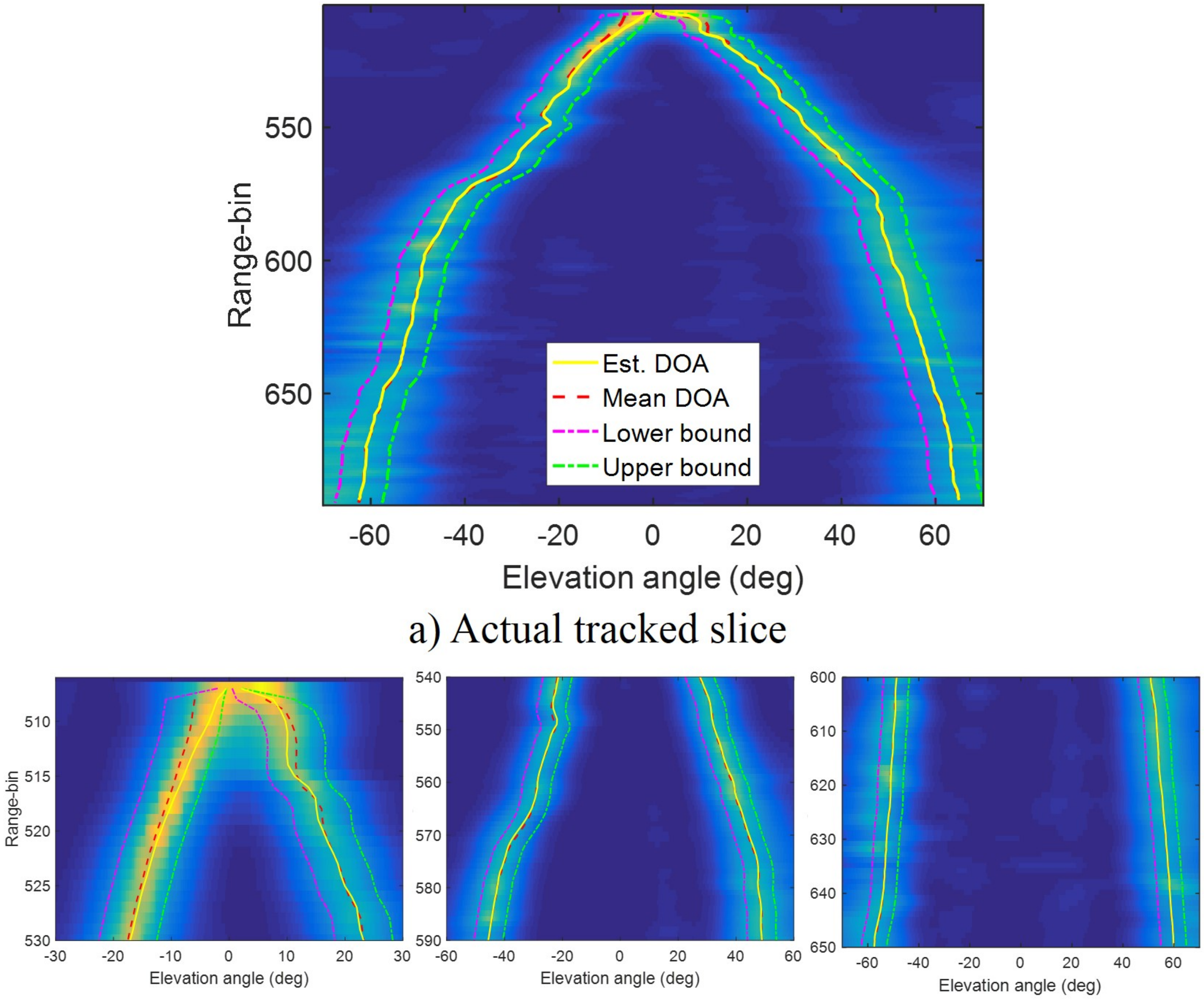

a) Actual tracked slice

b) Zoomed-in cross-sections

Figure 5.15: S-MAP result for Scenario 3: Gaussian prior pdf with wide bounds and narrow standard deviation.

4. **Scenario 4**: *Gaussian prior pdf with wide bounds and wide standard deviation*. In this scenario, we set the bounds to be ±5° around the mean, and we scale σ_θ up by $k_\sigma = 4$. Figure 5.16 shows the result of this scenario.

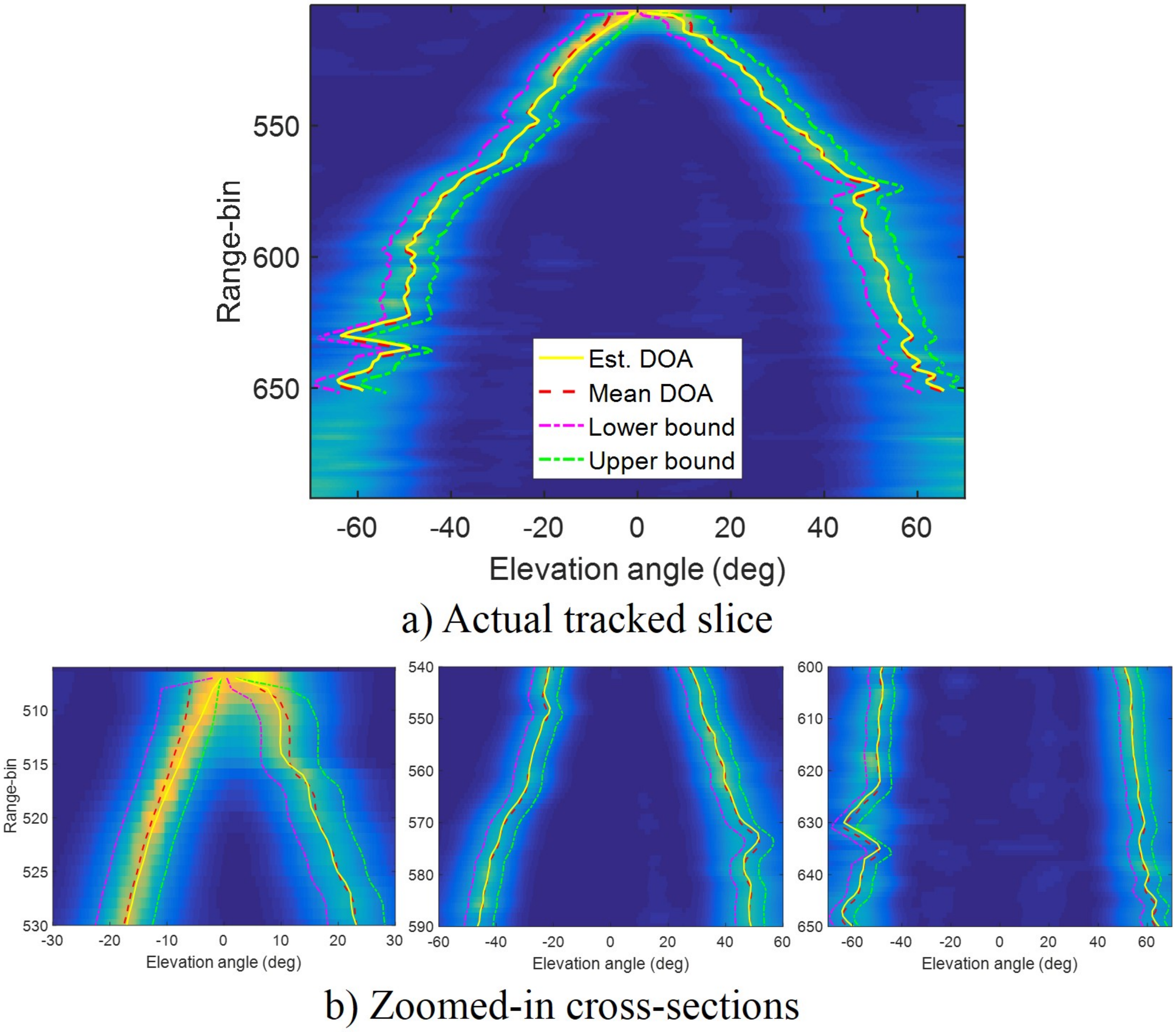

Figure 5.16: S-MAP result for Scenario 4: Gaussian prior pdf with wide bounds and wide standard deviation.

5. **Scenario 5**: *Uniform prior pdf with default bounds*. In this scenario, we use the default values of the bounds defined in equation 5.3. Figure 5.17 shows the result of this scenario.

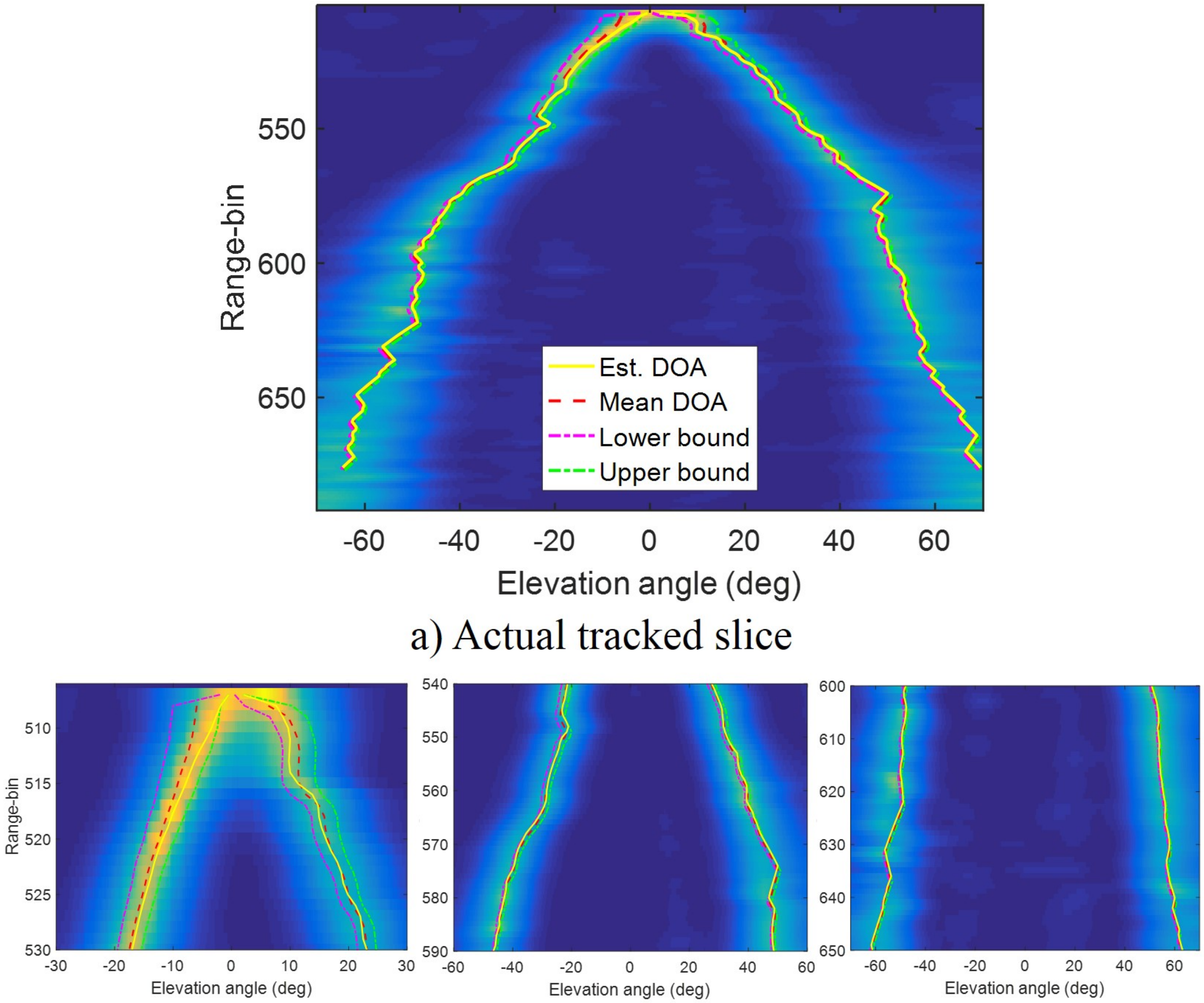

a) Actual tracked slice

b) Zoomed-in cross-sections

Figure 5.17: S-MAP result for Scenario 5: Uniform prior pdf with default bounds.

6. **Scenario 6**: *Uniform prior pdf with narrow bounds*. In this scenario, we scale the default value of the bound down by $k_b = 1/2$. Figure 5.18 shows the result of this scenario.

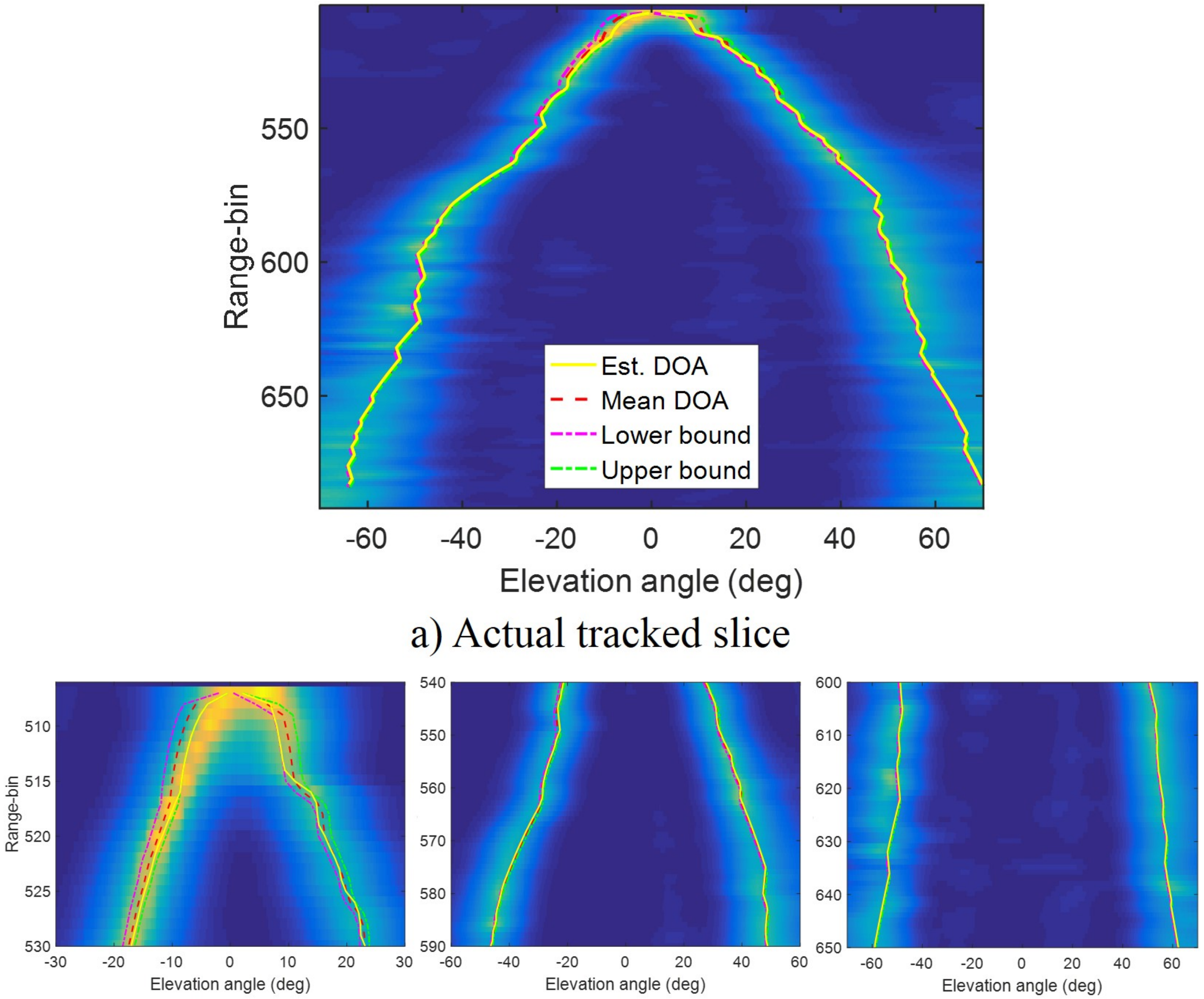

a) Actual tracked slice

b) Zoomed-in cross-sections

Figure 5.18: S-MAP result for Scenario 6: Uniform prior pdf with narrow bounds.

7. **Scenario 7**: *Uniform prior pdf with wide bounds*. In this scenario, we set the bounds to be ±5° around the mean. Figure 5.19 shows the result of this scenario.

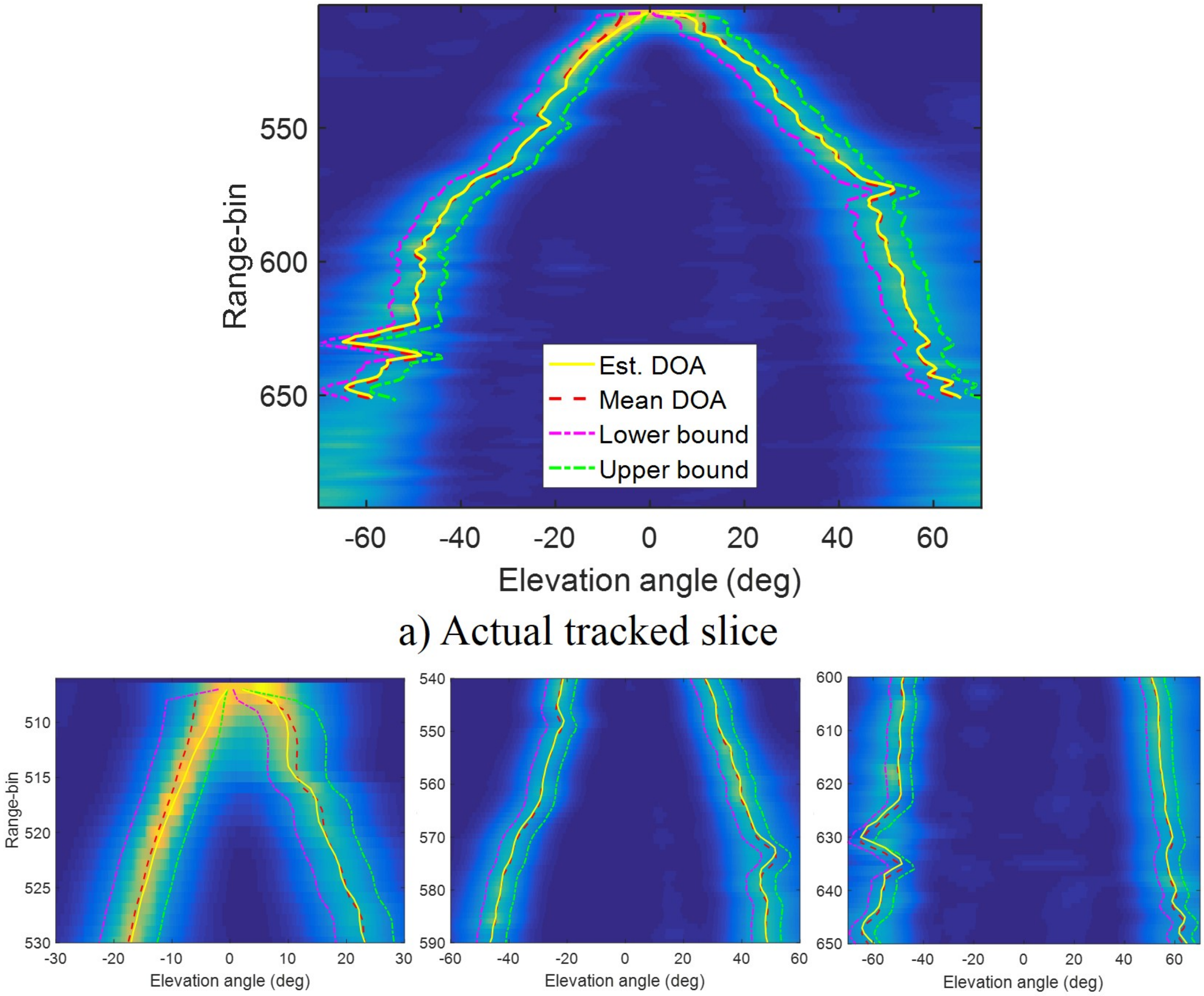

a) Actual tracked slice

b) Zoomed-in cross-sections

Figure 5.19: S-MAP result for Scenario 7: Uniform prior pdf with wide bounds.

Main observations:

The main observations and conclusions from these examples are listed below:

1. **Effect of bounds**:

   Choosing the right bounds depends mainly on the ice-surface topography and the quality of the data. Narrowing the bounds down serves as a smoother to the tracked slice. But it doesn't give the tracker a good chance to make a good use of the measured data to guide its decision (i.e. the narrower the bounds are, the less the tracker relies on the measured data). Figures 5.13, 5.14, 5.17, and 5.18 confirm this observation.

   Wide bounds, on the other hand, give the tracker the chance to rely more on the log-likelihood part of the cost function. Also, tight bounds make the prior pdf less important for the answer.

   But wide bounds also make the tracker behave in a strange way in regions of low quality data. The blips around range-bins 550 and 635 on the left side of the slice and range-bin 575 on right side of the slice in figures 5.16 and 5.19 show this observation.

   In addition, making the bounds too wide or leaving the bounds open mean that the tracker is loosing an important piece of prior information that can be efficiently used to improve the results.

2. **Effect of the prior pdf**:

   Gaussian prior pdf has an extra benefit over uniform prior pdf, which is the possibility of adjusting the standard deviation to improve the tracking results. Figure 5.15 shows an interesting example if the effect of narrowing the standard deviation down. We can see that the blips near range-bins 575 and 635 are almost completely gone and that near range-bin 550 is greatly reduced when the standard deviation is reduced, even though the bounds are too wide.

   Figure 5.20 shows an ice-bottom example of a uniform prior pdf and another example of a Gaussian prior pdf aligned with the corresponding range-bin for which these priors are calculated as well as the log-likelihood cost for. The location of the estimated targets and bounds are different in the two examples because the priors are not exactly the same, even though both of them use Model 4 to bound the DOA. These plots show, visually, the effect of the prior pdf on the tracking performance.

In the case of uniform prior pdf, the decision is completely made based on the measured data within the bounds. However, in the case of Gaussian prior, the prior pdf also affects the trackers decision, even though the Gaussian pdf is acting similar to a uniform pdf in the presented example because the standard deviation is wide.

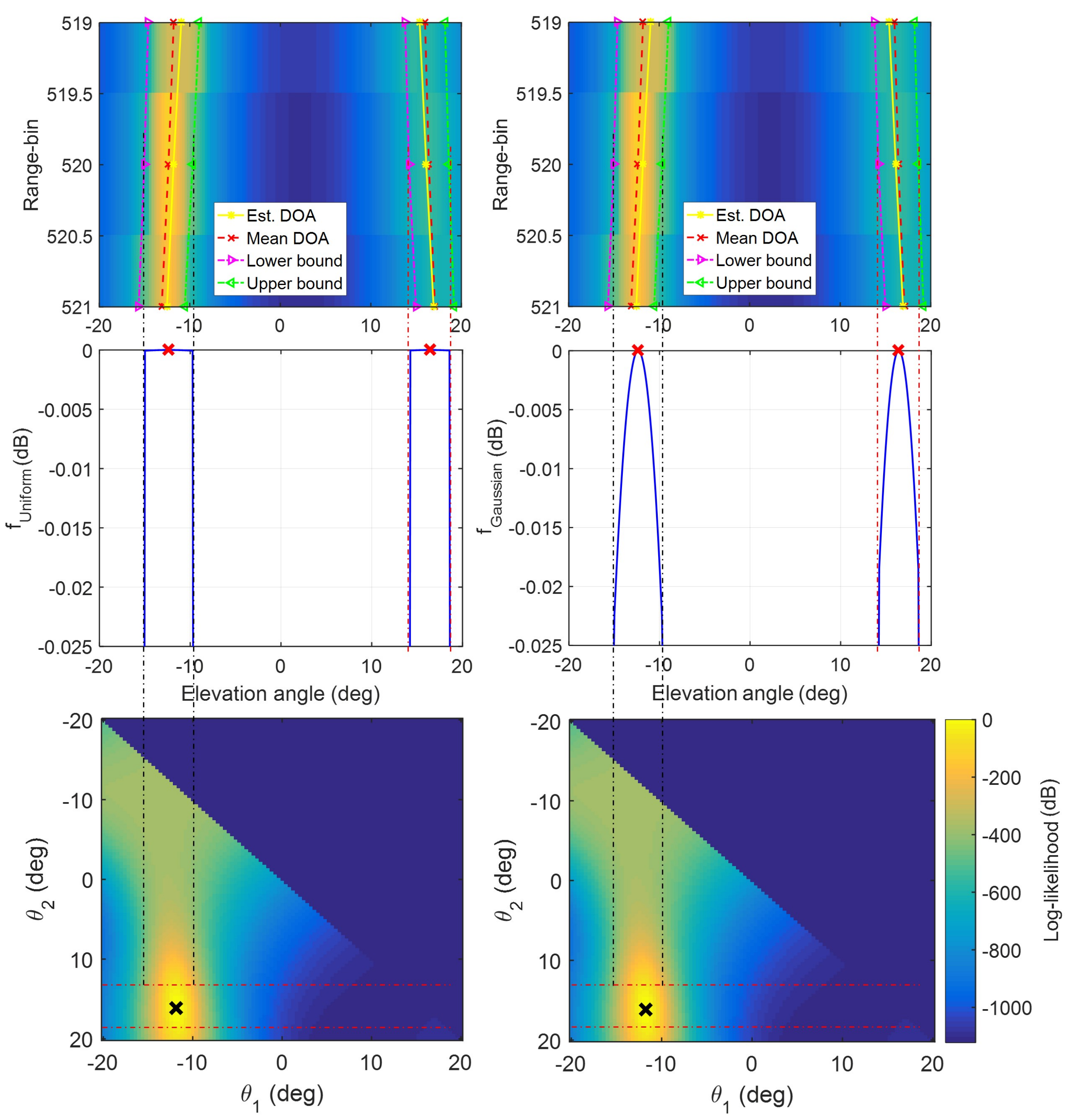

a) Uniform prior

b) Gaussian prior

Figure 5.20: Uniform (left) and Gaussian (right) priors of S-MAP for a specific range-bin (range-bin 520) of an ice-bottom example (Model 4 is used here for bounding). The red cross on the top of the priors is the mean DOA, which is calculated from the transition model presented in chapter 2. The black cross on the log-likelihood plot is the estimated DOAs at this range-bin. f_{Uniform} and f_{Gaussian} are the uniform and Gaussian probability density functions, respectively. All cost values are in normalized and in dB scale.

The net conclusion from this discussion is that Gaussian prior pdf is always a better option for our application than uniform prior because it has an extra degree of freedom that comes from controlling its standard deviation. Also, since the prior and standard deviation are both important to the tracking result, the best solution is the one that uses them both. Our recommendation is to use wider bounds than the default, but narrower standard deviation than the default.

Bad tracking example:

In Figure 5.21 we show a bad-tracking example of an ice-bottom layer using uniform prior pdf with bounding Model 3. We can see that the tracking is good over elevation angles $\sim 10^\circ$ to 60°, but it didn't track anything on the left side of the slice. The reason for this is a) the starting range bin comes too early (around 510 instead of 525), b) the confusing nadir data, which extends from about range-bins 520 to 540, and c) the weak-scattering region (most severe on the left) centered on range bin 540, which makes the model order estimator estimate zero targets, and thus no DOA is estimated by the tracker. Possible solutions in this case include the use of wider bounds (e.g. $\pm 20^\circ$) on the left side of the slice, or having a human annotator add a few ground truth points on the edge between the bad-data zone and the following good-data zone and force the tracker to start from these points rather than from its default nadir point.

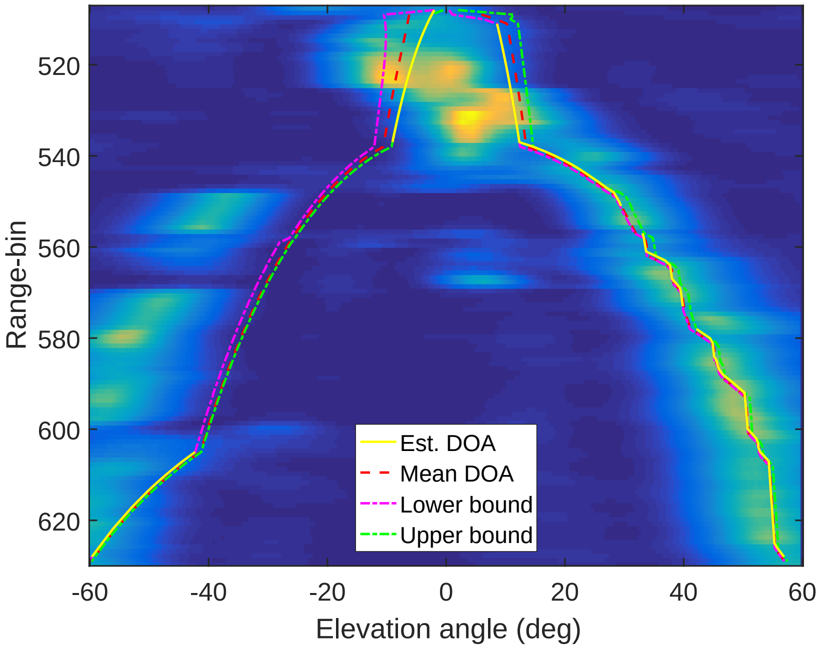

Figure 5.21: Bad tracking example of an ice-bottom layer using uniform prior pdf.

MLE tracking examples:

In addition to the presented S-MAP examples, in figure 5.22 we also show examples of the standard MLE applied to estimate the DOA of an ice-top and ice-bottom surfaces for the purpose of comparison. We can see that MLE traced the ice-bottom better than the ice-top. This is due to the effect of signal multiple (i.e. the nadir signal reflects off the aircraft and make another nadir target that is received later in time), in addition to the low data quality off to the side.

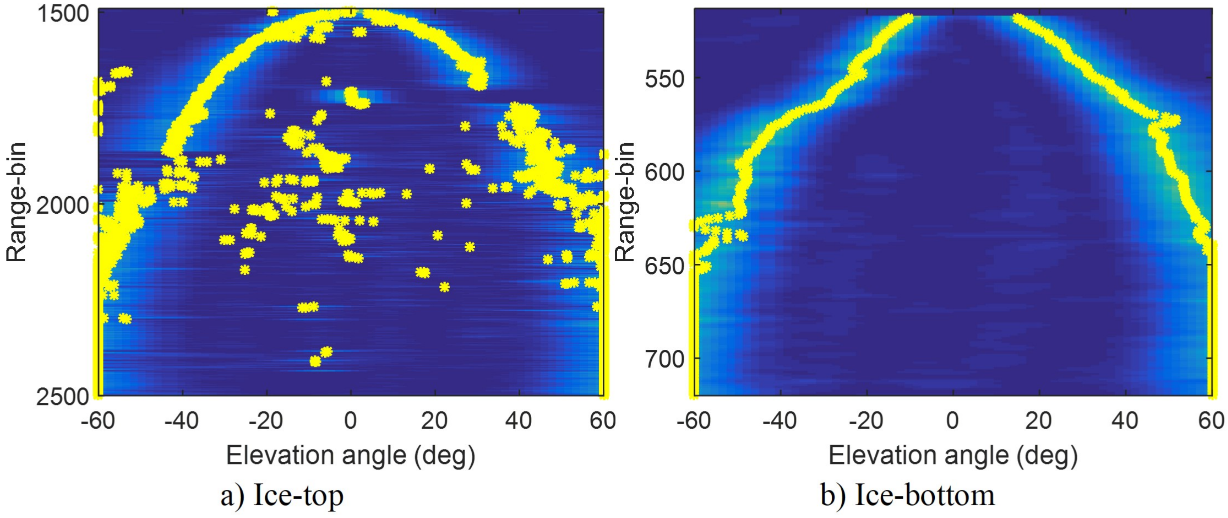

a) Ice-top

b) Ice-bottom

Figure 5.22: Ice-top and ice-bottom examples when MLE is used to estimate the DOA (i.e. no bounds and no prior information).

5.3.2 S-MAP Tracker: Layer Tracking Assessment

In addition to the basic tracking evaluation presented in the previous section, in this section we assess the performance of the proposed DOA tracker in two ways. First, we evaluate the effect of the model order estimation on the S-MAP tracking results and compare that to a reference MLE DOA estimator. Second, we compare our tracked surfaces against the surface data provided by the satellite imagery, which are usually very accurate. We use sea-ice data frames 20110417_03_001 and 20110417_04_001 in this evaluation study.

5.3.2.1 Tracking Assessment: MOE

Unlike beamformer-based trackers, DOA-based trackers require a good estimation of the model order in most of the tracked range-bins. The tracker can loose track of the ice-surface if there are big chunks of data missing or have 0 model order, unless the bounds are set too wide, which means loosing a great deal of prior information.

In this section we apply the MLE and S-MAP to a sea-ice example (i.e. ice-top surface) and investigate the performance of the MOE method (N-MDL) under both processors. The log-likelihood is normalized using data generated from a 1D simulator, following the method described in [1]. Figures 5.23 and 5.24 show a processed slice (the left figure) and a zoomed-in cross-section of the processed slice (the right figure) for MLE and S-MAP, respectively.

The eigen-analysis of three specific range-bins from this example are shown in figures 5.25, 5.26, and 5.27. The data covariance matrix, $\boldsymbol{R}$, is estimated using 63 snapshots (± 10 range-lines and ± 1 range-bins). Also, the eigenvalues are normalized by subtracting their mean and dividing by their standard deviation. However, the eigenvectors pseudo-spectrum and $|\boldsymbol{R}|$ are normalized relative to their maximum values (i.e. maximum relative value is 1). Now we look closely into each of these range-bins:

- Figure 5.25: This range-bin has two targets with similar SNR and are both inside the bounds of the S-MAP. So the model order is estimated correctly as 2 in S-MAP as well as MLE cases. The two big peaks in the MUSIC pseudo-spectrum and the first two eigenvalues confirm this observation.

- Figure 5.26: This range bin is at the beginning of a nadir multiple, which is clear in the nadir peak of the MUSIC pseudo-spectrum and the second biggest eigenvalue. But this nadir target is outside the S-MAP bounds. The other target, $\sim -38^\circ$, is inside the S-MAP bounds. Thus the model order should be 1 in the case of S-MAP and 2 in the case of MLE, which is what the model order estimated.

- Figure 5.27: This range-bin is right at the strong nadir multiple, which dominates the other targets in this range-bin. This is clear in the sharp nadir peak of the MUSIC pseudo-spectrum. Again, since this target is outside the S-MAP bounds, then the model order is correctly estimated as 0. However, it is 2 in the case of MLE since it is not bounded.

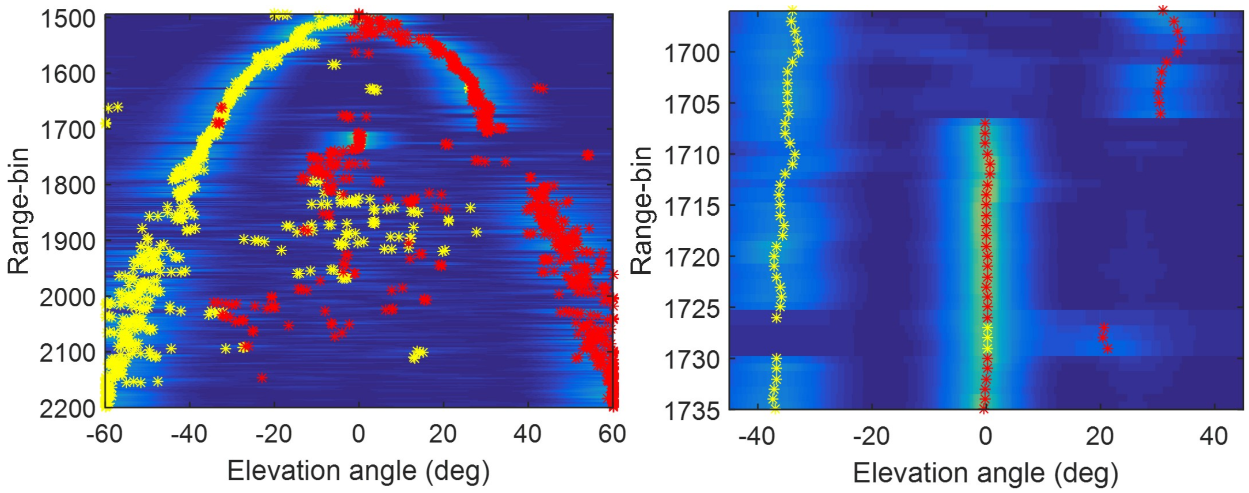

a) Actual slice

b) Zoomed-in cross-section

Figure 5.23: Sea-ice example showing the behavior of N-MDL when used with MLE DOA estimator, applied to real data. DOA 1 (yellow) and DOA 2 (red) are the elevation angles of the left and right targets, respectively.

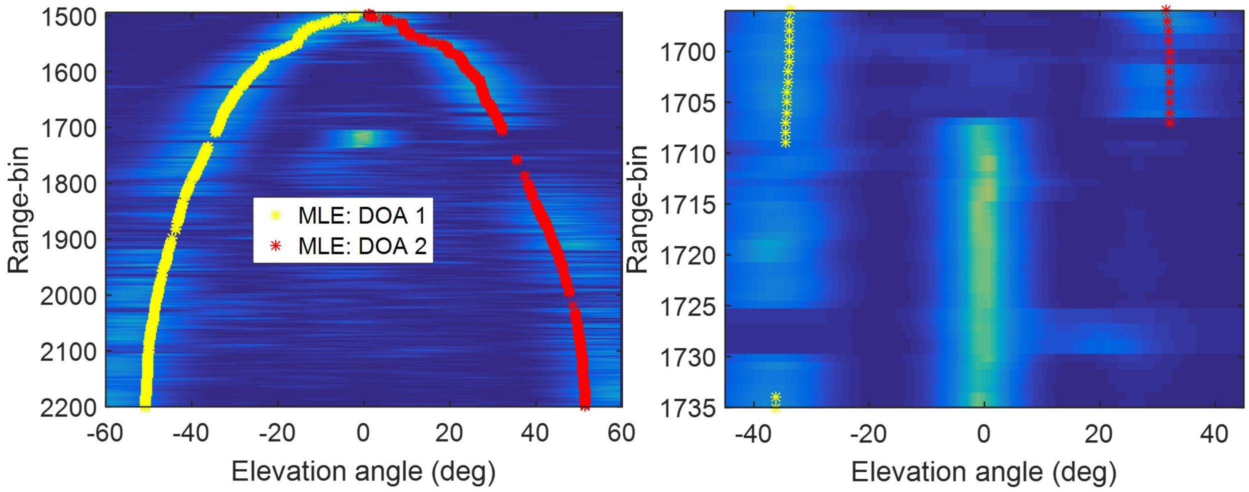

a) Actual slice

b) Zoomed-in cross-section

Figure 5.24: Sea-ice example showing the behavior of N-MDL when used with S-MAP tracker (Gaussian prior pdf and bounding Model 1 are used here), applied to real data. DOA 1 and DOA 2 are defined in figure 5.23.

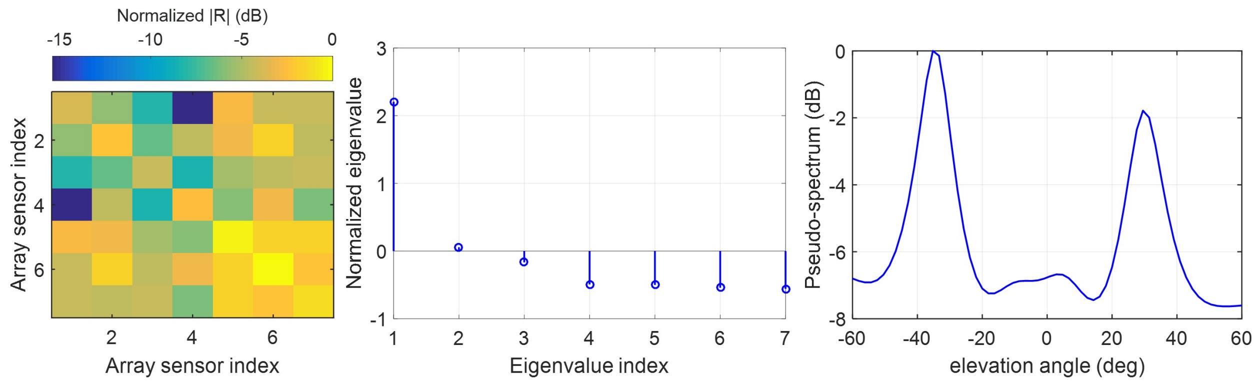

a) Normalized $|R|$ b) Normalized eigenvalues c) Normalized MUSIC pseudo-spectrum

Figure 5.25: Eigen analysis of range-bin 1706 of the sea-ice example shown in figures 5.23 and 5.24.

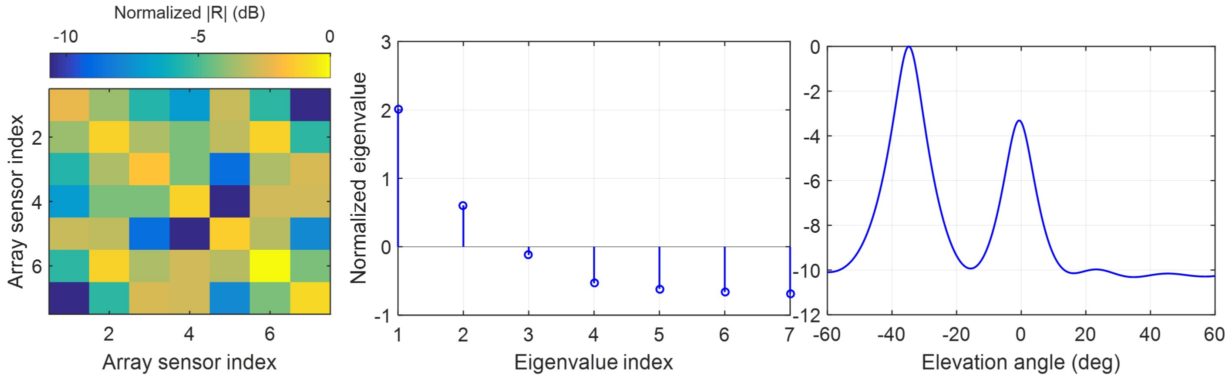

a) Normalized $|R|$ b) Normalized eigenvalues c) Normalized MUSIC pseudo-spectrum

Figure 5.26: Eigen analysis of range-bin 1708 of the sea-ice example shown in figures 5.23 and 5.24.

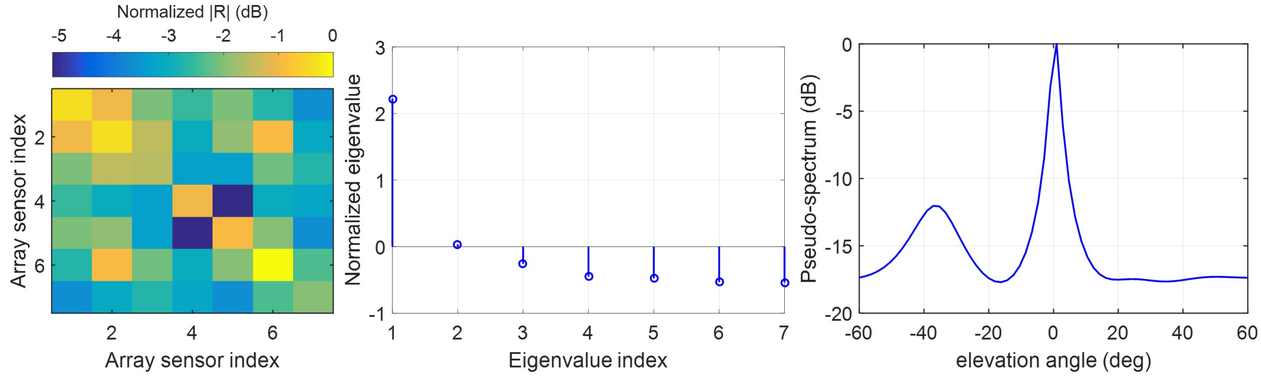

a) Normalized $|R|$ b) Normalized eigenvalues c) Normalized MUSIC pseudo-spectrum

Figure 5.27: Eigen analysis of range-bin 1712 of the sea-ice example shown in figures 5.23 and 5.24.

5.3.2.2 Tracking Assessment: S-MAP tracked layers vs ground truth

In this section, we compare S-MAP tracking results against ground truth for two sea-ice frames 20110417_03_001 and 20110417_04_001 (i.e. no ice-bottom, just ice-top), which are ideal frames for assessment and calibration. The first frame has 2012 slices, while the second frame has 2929 slices. The FOV is restricted to ±25°. Also, S-MAP bounding Model 3 with uniform prior pdf is used in generating the results of this section.

Figure 5.28 shows the empirical cumulative distribution function (CDF) of the absolute difference between the S-MAP tracked ice-top layer data and the ground-truth layer data. We can see that 73% of the errors are less than 5 range-bins and 85% are less than 10 range-bins. Over all range-bins and range-lines of the testing data frames, the mean of the absolute error is 4.65 range-bins and the root mean-squared error (RMSE) is 6.5 range-bins.

The reason for these errors, as well as the elevation errors in the next section, can be attributed to the following reasons:

1. S-MAP tracker doesn't usually start from the same initial point provided by the nadir ground truth (i.e. it could start before, after, or at the nadir ground-truth). As we mentioned before, S-MAP searches for the initial range-bin around the ground truth point because the ground truth points are usually provided by human annotators, which makes the ground truth not accurate to the pixel level. However, the ground-truth surfaces start exactly at the nadir ground truth. Since nadir strong echo signals may contaminate the near-by range-bins, the S-MAP initial range-bin is usually difficult to determine exactly. Thus, large percentage of these error statistics are attributed to this initial point mismatch.

2. Unlike S-MAP surface, the ground truth surface doesn't depend on the quality of the measured data. This fact is clear in figure 5.29, which shows a slice example of an S-MAP surface and the corresponding ground truth surface.

So, these statistics show a good S-MAP tracking performance.

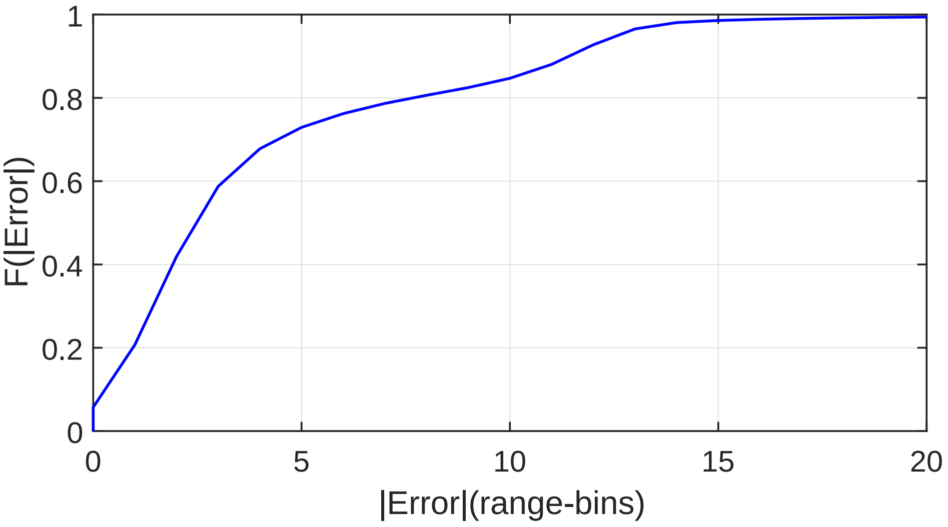

Figure 5.28: CDF of the error in S-MAP layer tracking relative to the ground truth.

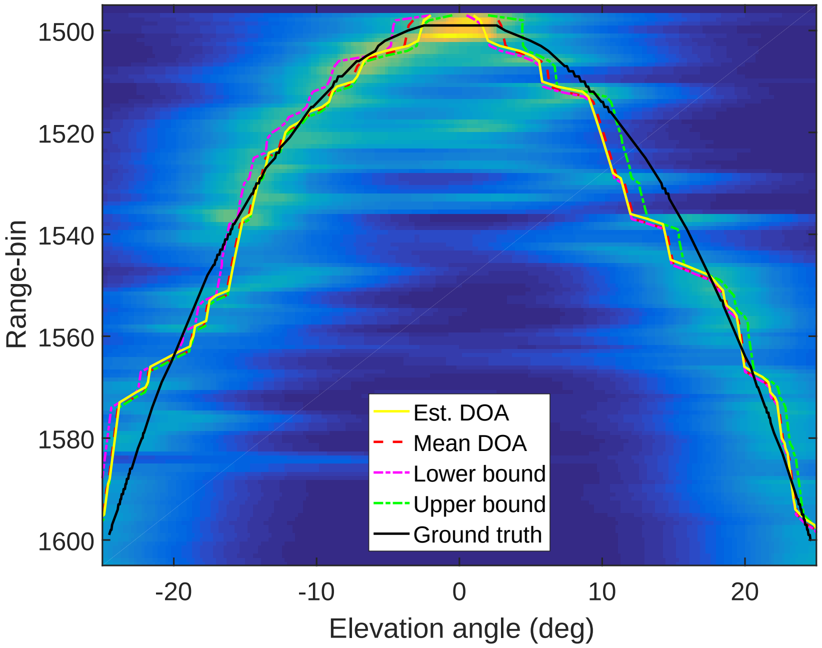

Figure 5.29: A slice example from data frame 20110417_03_001. It shows the S-MAP tracked surface (yellow) as well as the ground truth surface (black). Clearly, S-MAP surface if tracking correctly based on its bounds, prior pdf, and the quality of the measured data. However, the ground truth surface is not affected by these parameters.

5.3.3 S-MAP Tracker: DEM Generation Results and Assessments

The goal of tracking the bottom of an ice-sheet is to generate a DEM by geocoding and gridding the DOA points of the tracked slices.

Figures 5.30 and 5.31 show two versions of the DEM for each of the testing frames used in Section 5.3.2.2: the upper plot is the DEM generated from the ground truth layers (i.e. ground-truth DEM), and the lower plot shows the DEM generated from the S-MAP tracked slices. The ice-top elevation information are color-coded and referenced to the WGS-84 ellipsoid.

To assess the quality of the S-MAP DEM, we present the error DEMs for the same considered testing frames in figures 5.32 and 5.33. These error DEMs represent the error between the S-MAP DEM and the ground-truth DEM, which is the reference (i.e. negative errors mean that the elevation value from S-MAP is less than that of the ground truth).

Also, figure 5.34 shows the CDF of the elevation absolute error. We can see that 56% of the errors are less than 10 m and 80% of the errors are less than 20 m. In addition, over all the points in the error DEM, the mean absolute error is 15.2 m and the RMSE is 21.76 m. No error outliers were removed in these statistics. In addition, figure 5.35 shows the RMSE of the elevation errors after trimming the largest *n*% of the errors, where *n* is a number between 0 and 95 with steps of 5. This plot shows that trimming the largest 20% of the errors reduces the RMSE from 21.76 m to 9.83 m (i.e. 57% reduction in the RMSE). The reasons for these errors were discussed in the previous section. These results show good S-MAP tracking performance, but there seems to be a systematic tracking or steering vector error that is affecting one side of both the swaths.

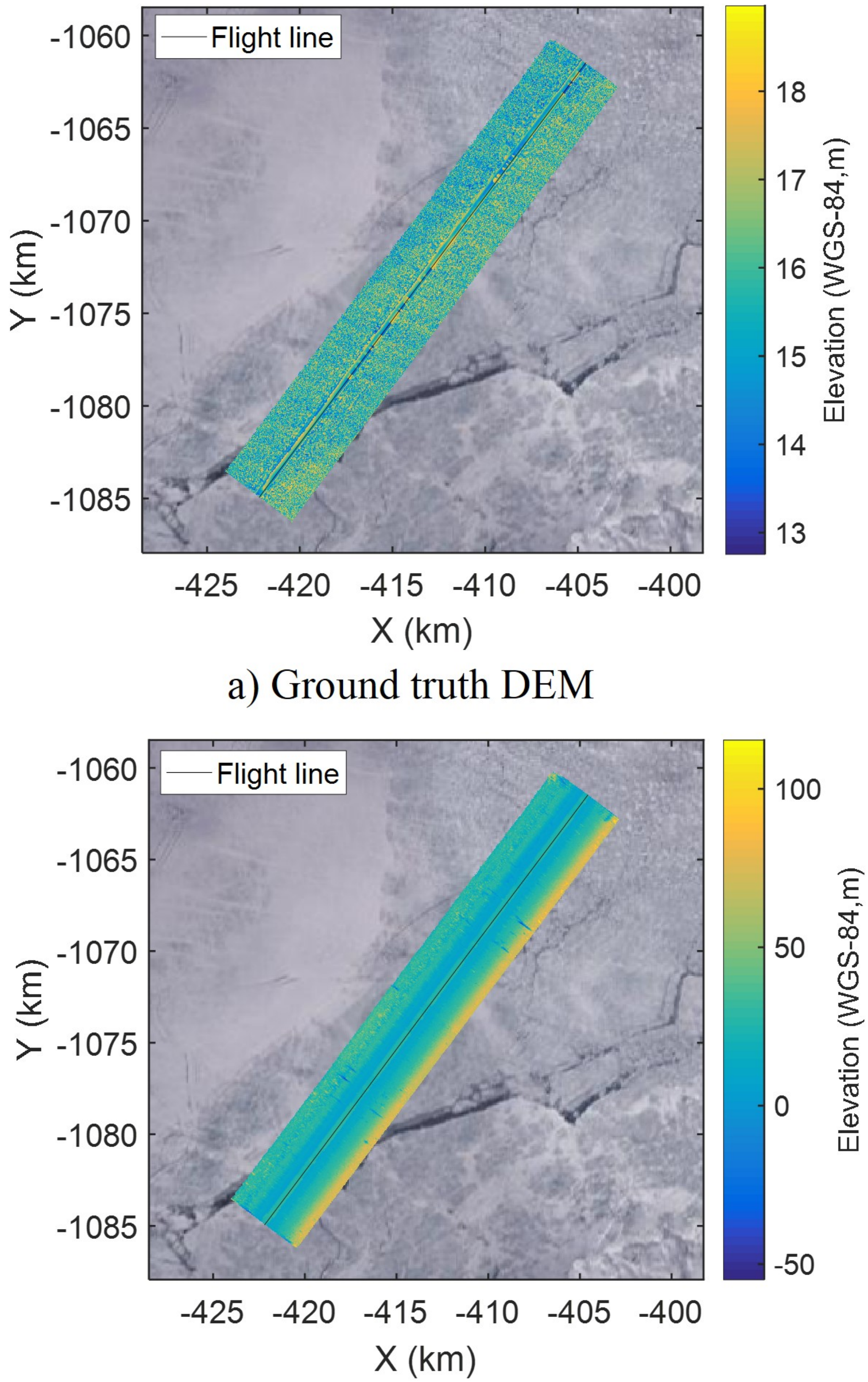

a) Ground truth DEM

b) S-MAP DEM

Figure 5.30: Digital elevation models of the ice-top of sea-ice frame 20110417_03_001. a) is the ground truth DEM and b) is the DEM resulting from S-MAP tracker. Nadir is right at the flight line, negative elevation angles extend from nadir towards positive x-axis, and positive elevation angles extend from nadir towards negative x-axis.

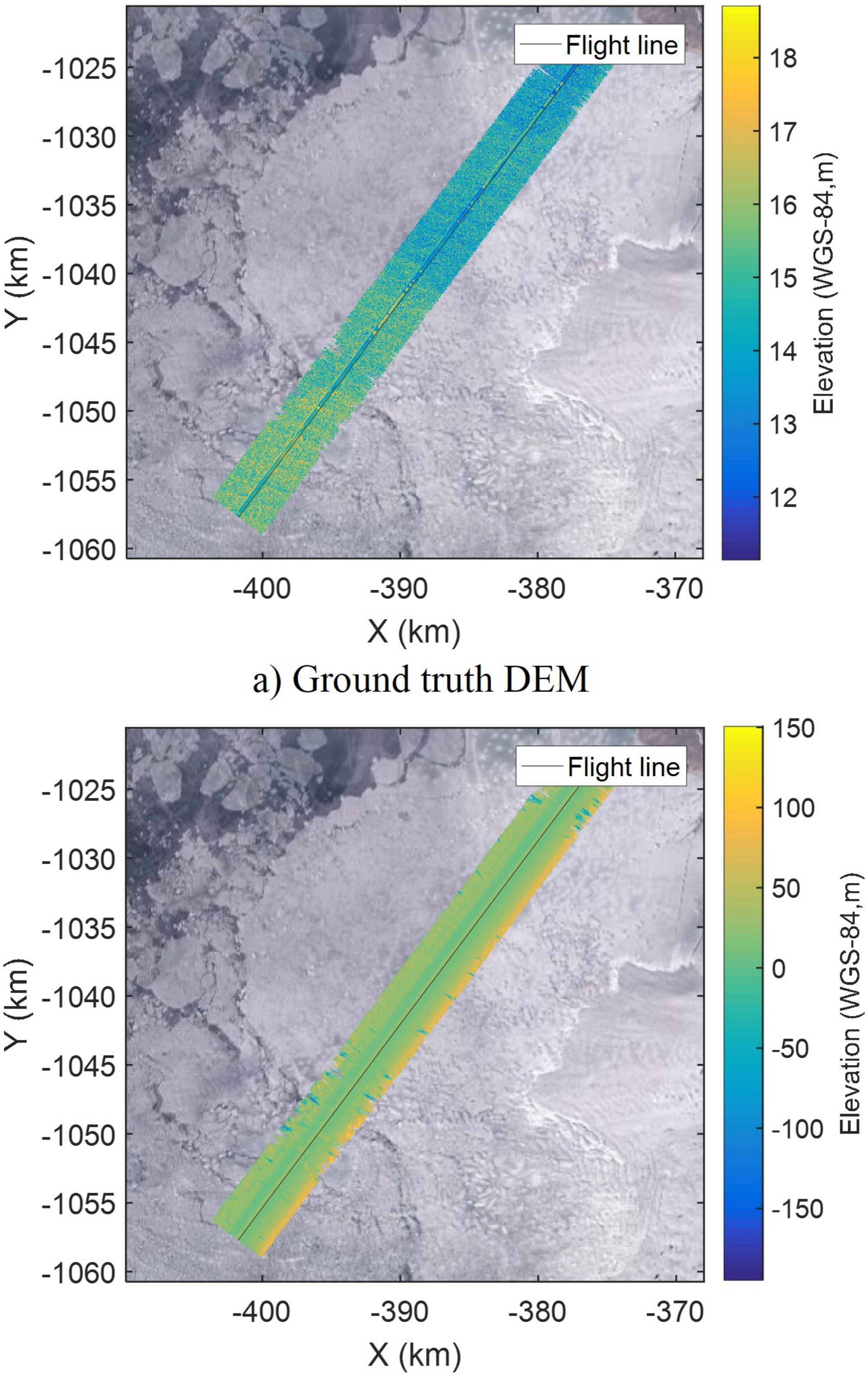

a) Ground truth DEM

b) S-MAP DEM

Figure 5.31: Same as figure 5.30 but for frame 20110417_04_001.

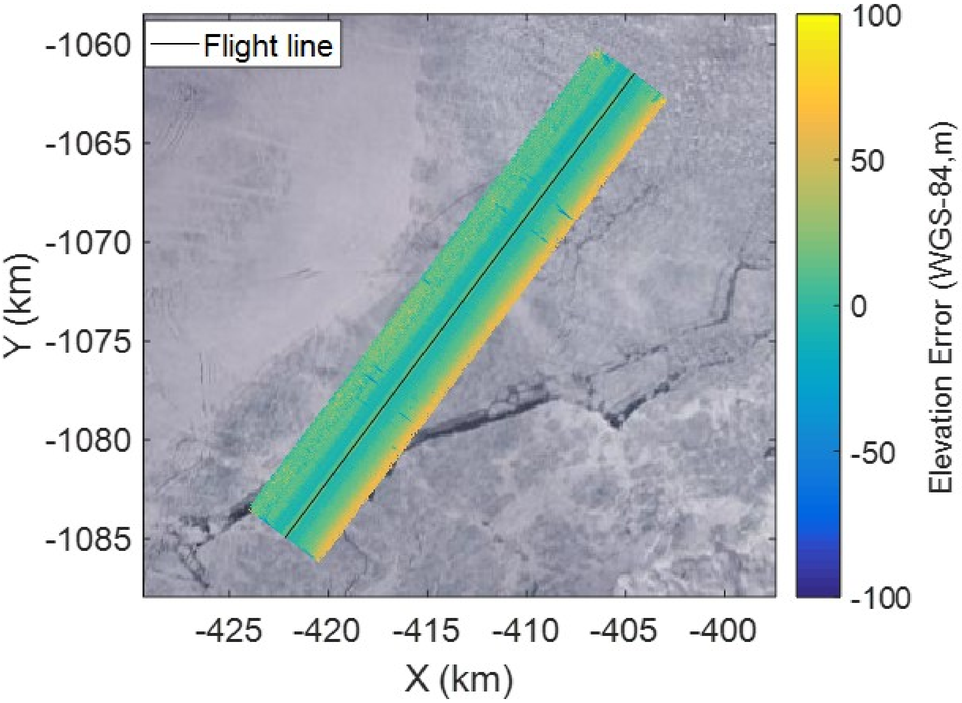

Figure 5.32: Digital elevation model of the error between S-MAP DEM and the ground-truth DEM for data frame 20110417_03_001.

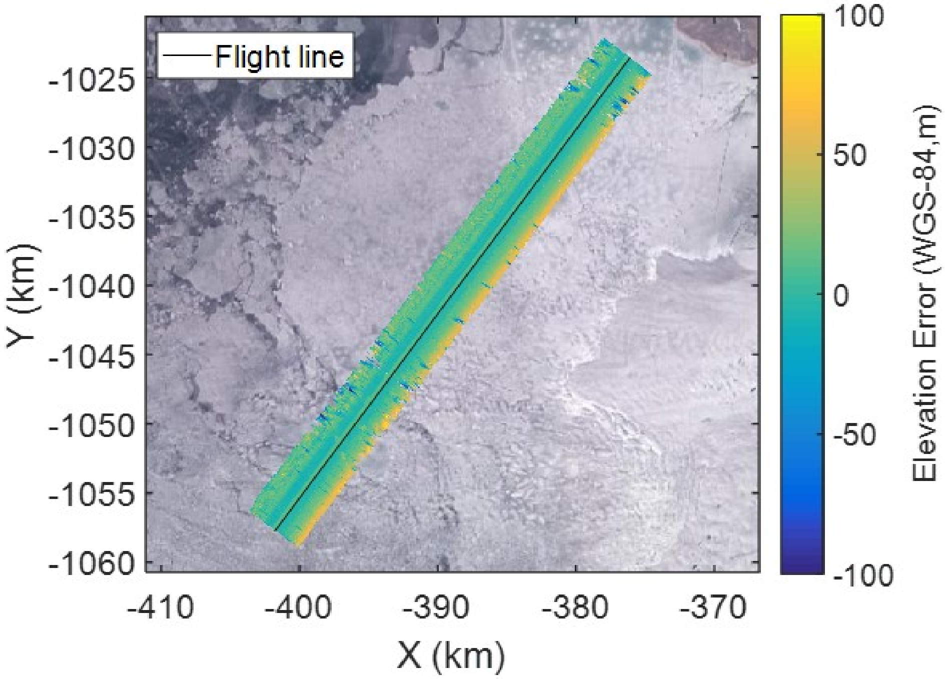

Figure 5.33: Digital elevation model of the error between S-MAP DEM and the ground truth DEM for data frame 20110417_04_001.

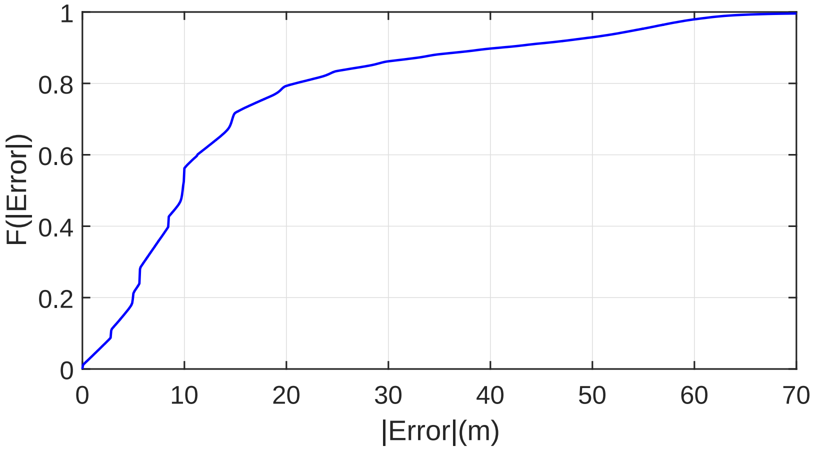

Figure 5.34: CDF of the ice-top elevation error of S-MAP DEM relative to the ground truth DEM.

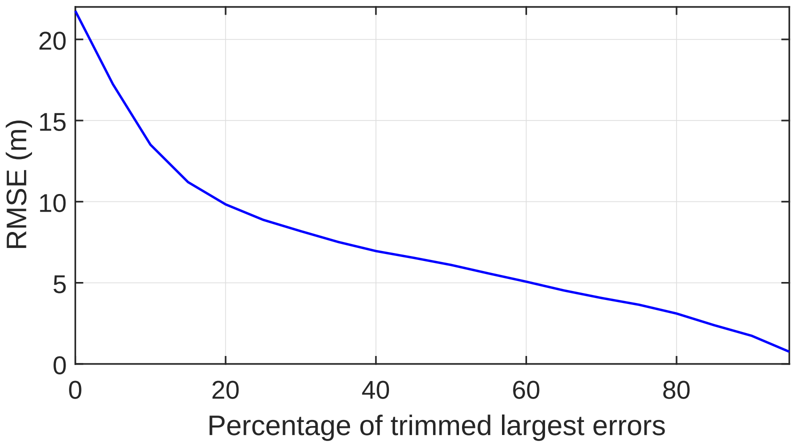

Figure 5.35: RMSE of the trimmed largest elevation errors. Each point on the horizontal axis represents a specific percentage of trimmed errors before the RMSE is calculated.

Chapter 6

Conclusions and Future Work

6.1 Concluding Remarks

In this work, we addressed the problem of estimating the location of the ice-bottom of an ice-sheet. We started by investigating the problem of estimating the signal subspace dimension, which is an essential part of our tracking model. Seven methods were tested in this work and compared against a machine learning (ML) based technique. We found that the ML method outperforms all other compared methods, especially in the more challenging scenario of wideband data with a large number of targets. Also, we found that normalizing the log-likelihood term of the MOE cost function can make the standard methods, such as MDL, work well in the wideband case with $Q = 2$ maximum number of targets. The normalized MDL was applied successfully to real wideband radar data.

Several methods were studied to solve the problem of surface tracking in the radar imaging application. This problem was formulated as an ice-bottom tracking problem and two main categories of solutions were proposed.

The first solution was beamforming-based, where we used the MUSIC beamformer to create images of the radar scene (in the elevation angle-range domain) that are fed into a sequential tree-reweighted message passing (TRW-S) belief propagation tracker to estimate the location of the bottom of the ice-sheet. This technique was successfully applied to process 102 frames collected from the Canadian Arctic Archipelago during the 2014 Arctic campaign.

The second category of solutions to the ice-bottom tracking problem is DOA-estimator based. Here, two types of trackers were proposed: one is based on the particle filter (PF) and the other is based on the sequential maximum a posterior (S-MAP) which is numerically solved the maximum likelihood estimator with a prior added. These two algorithms were compared using a 2D simulator under narrowband and wideband scenarios. In performing these simulations we assumed equal power point targets and a flat surface. We found that the PF solution is more suitable for low snapshots and/or low SNR scenarios than S-MAP. Also, the PF, in our specific application, saturates quickly with increasing number of snapshots relative to S-MAP. The model order was assumed to be known in this comparison. In addition, we discussed the performance of these two methods in other scenarios, such as estimating model order (i.e. effect of model order errors) and tracking non-flat surfaces.

We successfully applied the S-MAP tracker to process real wideband data collected from Russell glacier collected during the 2011 Arctic campaign. Also, we proposed several models to bound the S-MAP tracker and compared these models under different scenarios with uniform and Gaussian prior distributions. We found that the prior bounds and pdf affect the tracking results in different ways, where the best option is to use relatively wide bounds with narrow standard deviation with the Gaussian prior.

6.2 Future Work

The DOA-based ice-bottom tracking problem presented in this dissertation is still in its early stages. We laid the groundwork for this problem, but there are still several open problems that are not covered.

In this work we assumed that there are $Q = 2$ maximum number of targets in each range-bin; one on the left side of the platform and the other on the right side of the platform, with nadir being the reference. This could be extended to a more general framework that can handle an arbitrary number of targets, arbitrary starting angles, and the ability to handle the birth and death of targets. This proposal also opens a new problem, which is how to accurately estimate the model order in the high order wideband scenario with real data. Machine learning is a powerful solution, but preparing training and testing datasets from *real data is a major bottleneck.*

Also, some of the S-MAP bounding models tested in this work were not chosen based on mathematically rigorous derivations or tuning. It is difficult to choose one set of parameters that works for all scenarios. Machine learning may be used here to learn some of the parameters of S-MAP, such as the standard deviation of the Gaussian prior. This is another promising research direction.

In addition, we did not apply the particle filter-based DOA tracker to process real data in this work. So, exploring this ice-bottom tracking solution with real data along with other Kalman filter-based solutions are good research problems that should be addressed in the future. From our analysis in this dissertation, we expect that the particle filter based solution will be a competitive solution to the S-MAP tracker because it can handle low quality data scenarios and difficult surface shapes better.

References

[1] *Sravya Athinarapu. Model order estimation and array calibration for synthetic aperture radar tomography. Master's thesis, University of Kansas, 2018.*

[2] *Bruce C. Douglas, Michael S. Kearney, and Stephen P. Leatherman. Sea level rise: History and consequences.* International Geophysics Series*, 75(34), 2001.*

[3] *Bruce C. Douglas and W. Richard Peltier. The puzzle of global sea-level rise.* Physics Today*, 55(3):35–40, May 2002.*

[4] *Wesley Van Wychen, Jamie Davis, David O. Burgess, Luke Copland, Laurence Gray, Martin Sharp, and Colleen Mortimer. Characterizing interannual variability of glacier dynamics and dynamic discharge (1999–2015) for the ice masses of Ellesmere and Axel Heiberg Islands, Nunavut, Canada.* Journal of Geophysical Research: Earth Surface*, 121(1):39–63, 2016.*

[5] *Climate Change IPCC. The scientific basis.* IPCC, Geneva, Switzerland*, 2001.*

[6] *Ice bottom DEMs, 2018.* `https://climate.nasa.gov/vital-signs/ice-sheets/` *[Accessed: 2018-08-07].*

[7] *John Paden.* Synthetic aperture radar for imaging the basal conditions of the polar ice sheets. *PhD thesis, University of Kansas, 2006.*

[8] *F. Rodriguez-Morales, S. Gogineni, C. J. Leuschen, J. D. Paden, J. Li, C. C. Lewis, B. Panzer, D. Gomez-Garcia Alvestegui, A. Patel, K. Byers, R. Crowe, K. Player, R. D. Hale, E. J.*

Arnold, L. Smith, C. M. Gifford, D. Braaten, and C. Panton. Advanced multifrequency radar instrumentation for polar research. IEEE Transactions on Geoscience and Remote Sensing*, 52(5):2824–2842, May 2014.*

[9] R.W. MCNABB, R. HOCK, S. O'NEEL, L.A. RASMUSSEN, Y. AHN, M. BRAUN, H. CONWAY, S. HERREID, I. JOUGHIN, W.T. PFEFFER, B.E. SMITH, and M. TRUFFER. Using surface velocities to calculate ice thickness and bed topography: a case study at Columbia Glacier, Alaska, Usa. Journal of Glaciology*, 58(212):1151–1164, 2012.*

[10] Huilin Li, Felix Ng, Zhongqin Li, Dahe Qin, and Guodong Cheng. An extended "perfect-plasticity" method for estimating icethickness along the flow line of mountain glaciers. OURNAL OF GEOPHYSICAL RESEARCH*, 17, 2012.*

[11] J. Paden, T. Akins, D. Dunson, C. Allen, and P. Gogineni. Ice-sheet bed 3D tomography. Journal of Glaciology*, 56(195):3–11, 2010.*

[12] W. A. Blake. Interferometric synthetic aperture radar (INSAR) for fine-resolution basal icesheet imaging. *PhD thesis, University of Kansas, 2010.*

[13] X. Wu, K. C. Jezek, E. Rodriguez, S. Gogineni, F. Rodriguez-Morales, and A. Freeman. Ice sheet bed mapping with airborne SAR tomography. IEEE Transactions on Geoscience and Remote Sensing*, 49(10):3791–3802, Oct 2011.*

[14] Theresa Stumpf. A wideband direction of arrival technique for multibeam, wide-swath imaging of ice sheet basal morphology. Master's thesis, University of Kansas, 2015.

[15] U. Nielsen. Tomographic techniques for radar ice sounding. *PhD thesis, Technical University of Denmark, 2015.*

[16] D. Kirkland. Compressive sensing for RADARSAT-2 tomography. In 3rd International Workshop on Compressed Sensing Theory and its Applications to Radar, Sonar, and Remote Sensing (CoSeRa), Pisa, Italy. *IEEE, July 2015.*

[17] X. X. Zhu and R. Bamler. Superresolving SAR tomography for multidimensional imaging of urban areas: Compressive sensing-based tomosar inversion. IEEE Signal Processing Magazine*, 31(4):51–58, July 2014.*

[18] X. X. Zhu and R. Bamler. Tomographic SAR inversion by l_1-norm regularization—the compressive sensing approach. IEEE Transactions on Geoscience and Remote Sensing*, 48(10):3839–3846, Oct 2010.*

[19] D. J. Crandall, G. C. Fox, and J. D. Paden. Layer-finding in radar echograms using probabilistic graphical models. In Proceedings of the 21st International Conference on Pattern Recognition (ICPR2012)*, pages 1530–1533, Nov 2012.*

[20] S. Lee, J. Mitchell, D. J. Crandall, and G. C. Fox. Estimating bedrock and surface layer boundaries and confidence intervals in ice sheet radar imagery using MCMC. In 2014 IEEE International Conference on Image Processing (ICIP)*, pages 111–115, Oct 2014.*

[21] M. Xu, D. J. Crandall, G. C. Fox, and J. D. Paden. Automatic estimation of ice bottom surfaces from radar imagery. In 2017 IEEE International Conference on Image Processing (ICIP)*, pages 340–344, Sept 2017.*

[22] J. E. Mitchell, D. J. Crandall, G. C. Fox, and J. D. Paden. A semi-automatic approach for estimating near surface internal layers from snow radar imagery. In 2013 IEEE International Geoscience and Remote Sensing Symposium - IGARSS*, pages 4110–4113, July 2013.*

[23] Victor Berger, Mingze Xu, Shane Chu, David Crandall, John Paden, and Geoffrey C. Fox. Automated tracking of 2D and 3D ice radar imagery using Viterbi and TRW-S. In 2018 IEEE International Geoscience and Remote Sensing Symposium - IGARS*, July 2018.*

[24] X. X. Zhu and M. Shahzad. Facade reconstruction using multiview spaceborne TomoSAR point clouds. IEEE Transactions on Geoscience and Remote Sensing*, 52(6):3541–3552, June 2014.*

[25] *M. Shahzad and X. X. Zhu. Robust reconstruction of building facades for large areas using spaceborne TomoSAR point clouds.* IEEE Transactions on Geoscience and Remote Sensing*, 53(2):752–769, Feb 2015.*

[26] *M. Shahzad, M. Maurer, F. Fraundorfer, Y. Wang, and X. X. Zhu. Extraction of buildings in vhr sar images using fully convolution neural networks. In* 2018 IEEE International Geoscience and Remote Sensing Symposium - IGARS*, July 2018.*

[27] *X. X. Zhu, F. Fraundorfer, F. Kurz, and P. Reinartz. Building detection and segmentation using a CNN with automatically generated training data. In* 2018 IEEE International Geoscience and Remote Sensing Symposium - IGARS*, July 2018.*

[28] *M. Rahnemoonfar, G. C. Fox, M. Yari, and J. Paden. Automatic ice surface and bottom boundaries estimation in radar imagery based on level-set approach.* IEEE Transactions on Geoscience and Remote Sensing*, 55(9):5115–5122, Sept 2017.*

[29] *Mingze Xu, Chenyou Fan, John D. Paden, Geoffrey C. Fox, and David J. Crandall. Multi-task spatiotemporal neural networks for structured surface reconstruction.* IEEE Winter Conference on Applications of Computer Vision (WACV)*, March 2018.*

[30] *Hamid Kamangir, Maryam Rahnemoonfar, Dugan Dobbs, John Paden, and Geoffrey Fox. Deep hybrid wavelet network for ice boundary detection in radra imagery. In* 2018 IEEE International Geoscience and Remote Sensing Symposium - IGARS*, July 2018.*

[31] *Ice bottom DEMs, 2018. https://data.cresis.ku.edu/data/rds/2014_Greenland_P3/CSARP_DEM/ [Accessed: 2018-08-12].*

[32] *Z. Wang, S. Gogineni, F. Rodriguez-Morales, J. B. Yan, J. Paden, C. Leuschen, R. D. Hale, J. Li, C. L. Carabajal, D. Gomez-Garcia, B. Townley, R. Willer, L. Stearns, S. Child, and D. Braaten. Multichannel wideband synthetic aperture radar for ice sheet remote sensing: Development and the first deployment in antarctica.* IEEE Journal of Selected Topics in Applied Earth Observations and Remote Sensing*, 9(3):980–993, March 2016.*

[33] *M Al-Ibadi, J Sprick, S Athinarapu, T Stumpf, J Paden, C Leuschen, F Rodríguez, M Xu, D Crandall, G Fox, D Burgess, M Sharp, L Copland, and W Van Wychen. DEM extraction of the basal topography of the Canadian Archipelago ice caps via 2D automated layer-tracker. In* International Geoscience and Remote Sensing Symposium (IGARSS)*, pages 965–968. IEEE, July 2017.*

[34] *C. Leuschen, S. Gogineni, and D. Tammana. SAR processing of radar echo sounder data. In* International Geoscience and Remote Sensing Symposium (IGARSS)*, 2000.*

[35] *H. Van Trees.* Optimum Array Processing. Part IV of Detection, Estimation, and Modulation Theory*. John Wily and Sons Inc., 2002.*

[36] *M. A. Doron and E. Doron. Wavefield modeling and array processing,Part III-resolution capacity.* IEEE Transactions on Signal Processing*, 42(10):2571–2580, Oct 1994.*

[37] *T. B. Lavate, V. K. Kokate, and A. M. Sapkal. Performance analysis of MUSIC and ESPRIT DOA estimation algorithms for adaptive array smart antenna in mobile communication. In* 2010 Second International Conference on Computer and Network Technology*, pages 308–311, April 2010.*

[38] *Mati Wax.* Detection and Estimation of Superimposed Signals*. PhD thesis, Stanford University, 1985.*

[39] *I. Ziskind and M. Wax. Maximum likelihood localization of multiple sources by alternating projection.* IEEE Transactions on Acoustics, Speech, and Signal Processing*, 36(10):1553–1560, Oct 1988.*

[40] *M Wax, T. J. Shan, and T. Kailath. Location and the spectral density estimation of multiple sources. In* Proc. 16th Asiloma conference on signals, systems, and computers*, 1982.*

[41] *J. Paden, T. Stumpf, and M. Al-Ibadi. Wideband DOA estimation for ice sheet bed mapping. In*

IEEE International Symposium on Phased Array Systems and Technology (PAST)*, October 2016.*

[42] S. Athinarapu, J. Paden, M. Al-Ibadi, and T. Stumpf. Model order estimators using optimal and suboptimal methods with numerical tuning. In IEEE Radar Conference*, 2018.*

[43] M. A. Doron, A. J. Weiss, and H. Messer. Maximum-likelihood direction finding of wide-band sources. IEEE Transactions on Signal Processing*, 41(1):411–, Jan 1993.*

[44] Yeo-Sun Yoon, L. M. Kaplan, and J. H. McClellan. TOPS: new DOA estimator for wideband signals. IEEE Transactions on Signal Processing*, 54(6):1977–1989, June 2006.*

[45] M. A. Doron and A. J. Weiss. On focusing matrices for wide-band array processing. IEEE Transactions on Signal Processing*, 40(6):1295–1302, Jun 1992.*

[46] Steven M. Kay. Fundamentals of Statistical Signal Processing: Estimation Theory. *Prentice-Hall Inc., 1993.*

[47] F. Gustafsson. Particle filter theory and practice with positioning applications. IEEE Aerospace and Electronic Systems Magazine*, 25(7):53–82, July 2010.*

[48] A. Doucet and A. Johansen. A tutorial on particle filters for online nonlinear/non-gaussian bayesian tracking. in The Oxford Handbook of Nonlinear Filtering. New York: Oxford Univ. Press*, 2009.*

[49] B. Ristic, S. Arulampala, and N. Gordon. Beyond the Kalman Filter: Particle Filters for Tracking Applications. *Artech House, 2004.*

[50] A. Doucet, N. de Freitas, and N. Gordon. Sequential Monte Carlo Methods in Practice. *Springer, 2001.*

[51] Won Sik Youn and Chong Kwan Un. Robust adaptive beamforming based on the eigenstructure method. IEEE Transactions on Signal Processing*, 42(6):1543–1547, Jun 1994.*

[52] *A. Young, M. V. Ivashina, R. Maaskant, O. A. Iupikov, and D. B. Davidson. Improving the calibration efficiency of an array fed reflector antenna through constrained beamforming.* IEEE Transactions on Antennas and Propagation*, 61(7):3538–3545, July 2013.*

[53] *Won Sik Youn and Chong Kwan Un. Robust adaptive beamforming based on the eigenstructure method.* IEEE Transactions on Signal Processing*, 42(6):1543–1547, Jun 1994.*

[54] *L. Ma, Z.F. Li, and G.S. Liao. System error analysis and calibration methods for multichannel SAR.* Progress In Electromagnetics Research*, 112(6):309–327, 2011.*

[55] *A. J. Weiss and B. Friedlander. Array shape calibration using sources in unknown locations-a maximum likelihood approach.* IEEE Transactions on Acoustics, Speech, and Signal Processing*, 37(12):1958–1966, Dec 1989.*

[56] *F. Vincent and O. Besson. Steering vector errors and diagonal loading.* IEE Proceedings - Radar, Sonar and Navigation*, 151(6):337–343, Dec 2004.*

[57] *M. Wax and Y. Anu. Performance analysis of the minimum variance beamformer in the presence of steering vector errors.* IEEE Transactions on Signal Processing*, 44(4):938–947, Apr 1996.*

[58] *Azizul H. Quazi. Array beam response in the presence of amplitude and phase fluctuations.* The Journal of the Acoustical Society of America*, 72(1):171–180, June 1998.*

[59] *B. Friedlander. Sensitivity analysis of the maximum likelihood direction finding algorithm. In* Twenty-Third Asilomar Conference on Signals, Systems and Computers, 1989.*, volume 2, pages 594–598, Oct 1989.*

[60] *P. Chen, T. J. Wu, and J. Yang. A comparative study of model selection criteria for the number of signals.* IET Radar, Sonar and Navigation*, 2(3):180–188, 2008.*

[61] *S. Caylar.* A novel neural network based approach for direction of arrival estimation. *PhD thesis, Middle East Technical University, 2007.*

[62] *M. Agatonovic, Z. Stankovic, N. Doncov, L. Sit, B. Milovanovic, and T. Zwick. Application of artificial neural networks for efficient high-resolution 2d doa estimation.* Radioengineering*, 21(4):1178–1186, 2012.*

[63] *S. Adavanne, A. Politis, and T. Virtanen. Direction of arrival estimation for multiple sound sources using convolutional recurrent neural networ.* [Online]. available: https://arxiv.org/abs/1710.10059*, Aug 2018.*

[64] *Kevin P Murphy.* Machine learning: a probabilistic perspective. *MIT press, 2012.*

[65] *A. Doucet and A. Johansen. A tutorial on particle filtering and smoothing: Fifteen years later.* Handbook of Nonlinear Filtering, Oxford Univ. Press*, 2009.*

[66] *M. Zatman. How narrow is narrowband?* Proc. IEEE-Radar, Sonar and Navin*, 145(2), 1998.*

[67] *Victor Berger, Mingze Xu, Mohanad Al-Ibadi, Shane Chu, David Crandall, John Paden, and Geoffrey Fox. Automated tracking of 2D and 3D ice radar imagery using Viterbi and TRW-S.* Submitted to IEEE J. Sel. Topics Appl. Earth Observ (JSTARS)*, 2019.*

[68] *ArcticDEM, 2018.* `https://www.pgc.umn.edu/data/arcticdem/`.

[69] *Jérôme Korona, Etienne Berthier, Marc Bernard, Frédérique Rémy, and Eric Thouvenot. SPIRIT. SPOT 5 stereoscopic survey of polar ice: Reference images and topographies during the fourth international polar year (2007–2009).* ISPRS Journal of Photogrammetry and Remote Sensing*, 64(2):204 – 212, 2009.*

[70] *M.Xu, D.Crandall, G.Fox, and J.Paden. Automatic estimation of ice bottom surfaces from radar imagery. In* IEEE International Conference on Image Processing (ICIP) 2017*, 2017.*

[71] *V. Kolmogorov. Convergent tree-reweighted message passing for energy minimization.* IEEE Transactions on Pattern Analysis and Machine Intelligence*, 28(10):1568–1583, Oct 2006.*

[72] *A. Arendt and et.al. Randolph glacier inventory [v2.0]: A dataset of global glacier outlines.* Global Land Ice Measurements from Space, Boulder Colorado, USA, Digital Media*, 2012.*

[73] P. Stoica and A. Nehorai. Music, maximum likelihood, and cramer-rao bound. IEEE Transactions on Acoustics, Speech, and Signal Processing*, 37(5):720–741, May 1989.*